Galaxy clustering and feedback

Bielby, Richard

GALAXY CLUSTERING AND FEEDBACK

RICHARD BIELBY

A thesis submitted to the University of Durham
in accordance with the regulations for admission to the
Degree of Doctor of Philosophy.

DURHAM UNIVERSITY

2008

ABSTRACT: GALAXY CLUSTERING AND FEEDBACK

I cross-correlate the WMAP third year data with the ACO, APM and 2MASS galaxy and cluster catalogues, confirming the presence of the SZ effect in the WMAP 3rd year data around ACO, APM and 2MASS clusters, showing an increase in detection significance compared to previous analyses of the 1-year WMAP data release. I compare the cross-correlation results for a number of clusters to their SZ β-model profiles estimated from ROSAT and Chandra X-ray data. I conclude that the SZ profiles estimated from the β-model over-predict the observed SZ effect in the cluster samples. Additionally, I develop colour cuts using the SDSS optical bands to photometrically select emission line galaxies at redshifts of $z < 0.35$, $0.35 < z < 0.55$ and $z > 0.55$. The selections have been calibrated using a combination of photometric redshifts from the COMBO-17 survey and spectroscopic observations. I estimate correlation lengths of $r_0 = 2.64^{+0.05}_{-0.08} h^{-1} Mpc$, $r_0 = 3.62 \pm 0.06 h^{-1} Mpc$ and $r_0 = 5.88 \pm 0.12 h^{-1} Mpc$ for the low, mid and high redshift samples respectively. Using these photometric samples I search for the Integrated Sachs-Wolfe signal in the WMAP 5yr data, but find no significant detection. I also present a survey of star-forming galaxies at $z \approx 3$. Using Lyman Break and U-dropout photometric selections, we identify a total of $\approx 21,000$ candidate $z > 2$ galaxies and perform spectroscopic observations of a selection of these candidates with integration times of 10,000s with the VLT VIMOS. In total this survey has so far produced a total of 1149 LBGs at redshifts of $2 < z < 3.5$ over a total area of $1.18 deg^2$, with a mean redshift of $\bar{z} = 2.87 \pm 0.34$. Using both the photometric and spectroscopic LBG catalogues, I investigate the clustering properties of the $z > 2$ galaxy sample using the angular correlation function, measuring a clustering amplitude of $r_0 = 4.32^{+0.13}_{-0.12} h^{-1} Mpc$ with a slope of $\gamma_2 = 1.90^{+0.09}_{-0.14}$ at separations of $r > 0.4 h^{-1} Mpc$. We then measure the redshift space clustering based on the spectroscopically observed sample and estimate the infall parameter, β, of the sample by fitting a redshift space distortion model to the $\xi(\sigma, \pi)$. To conclude this work, I analyze the correlation of LBGs with the Lyα forest transmissivity of a number of $z \sim 3$ QSOs, with the aim of looking for the imprint of high velocity winds on the IGM. The data show a fall in the transmissivity in the Lyα forest at scales of $5 h^{-1} Mpc < r < 10 h^{-1} Mpc$ away from LBGs, indicating an increase in gas densities at these scales. However we find no significant change from the mean transmissivity at scales of $< 3 h^{-1} Mpc$, potentially signifying the presence of low density ionised regions close to LBGs.

PREFACE

GALAXY CLUSTERING AND FEEDBACK

The work described in this thesis was undertaken between October 2005 and November 2008 whilst the author was a research student under the supervision of Prof. Tom Shanks in the Department of Physics at the University of Durham. This work has not been submitted for any other degree at this (or any other) university.

The main collaborators involved in this thesis are Prof. T. Shanks, Dr. N. Crighton & Dr. N. Metcalfe.

Results from this thesis have appeared (or will appear) in the following papers:

- Bielby, R. & Shanks, T., 2007, MNRAS, 382, 1196
- Bielby, R., Shanks, T., Sawangwit, U. & Ross, N., 2009, Submitted to MNRAS
- Bielby, R., Crighton, N., Shanks, T., Bouché, N., Infante, L., Metcalfe N., Morris, S. L., & Theuns, T., 2009, In Prep.
- Crighton, N., Bielby, R., Shanks, T., Bouché, N., Infante, L., Morris, S. L., & Theuns, T., 2009, In Prep.

ACKNOWLEDGEMENTS

I would like to begin by thanking Prof. Tom Shanks, my PhD supervisor, whose guidance, enthusiasm and encouragement has led to the breadth and diversity of the work described herein. Further to this, I acknowledge the funding of PPARC/STFC during the course of this PhD. Also, I would like to thank Dr N. Crighton, Dr N. Ross, Utane Sawangwit, Michael Hill and Dr. N Metcalfe for the constructive discussion they have provided and for their collaboration at various times during my PhD. I would also like to thank a number of my contemporaries who have prompted a range of thougtful and interesting discusions. In particular, I would like to thank Dr R Crain, Dr N. Schurch, J. Gladstone and Dr G. Davies. Similarly, a special thanks goes to Dr W. Frith who as well as enthusiastically drawing out discussions on our subject, prompted me to embark upon this PhD. I also thank Dr I. McCarthy, Dr A. Edge, Dr R. Lieu, Dr R. Fong and G. Worseck for challenging, useful and interesting discussions. Finally, I reserve thanks for my family and Lisa, whose support has been a key ingredient in this work.

Dedicated to Lisa

Contents

List of Figures

List of Tables

CHAPTER 1

INTRODUCTION

1.1 Overview

This thesis presents a review of a number of strands of research related to galaxy clustering and feedback that have been covered in the three years of my PhD from 2005-2008. These consist of the following:

- Observations of galaxy clusters via the Sunyaev Zel'Dovich effect in 3rd year WMAP data;
- The photometric selection and clustering properties of emission line galaxies at $z < 1$;
- A search for the presence of the ISW effect in WMAP 5 year data using photometrically selected emission line galaxies;
- A survey of $z \approx 3$ galaxies and the study of their clustering properties;
- An investigation of the interactions between galaxies and the inter-galactic medium at $z \approx 3$ using the above galaxy survey and the Lyα forest of bright $z > 3$ QSOs.

The structure of this thesis is as follows. In this current Chapter, I provide the necessary background to the topics listed above, covering all the topics covered in this thesis. In Chapter 2, I present research on the presence of Sunyaev-Zel'Dovich effect signals in the WMAP 3rd year data release based on cross-correlation with clusters of galaxies out to $z \approx 0.3$. I then discuss methods for simple photometric selection of emission line galaxies at $z < 1$, analyse their clustering properties and apply these selections to the investigation of the presence of the Integrated Sachs-Wolfe effect in WMAP CMB data in Chapter 3. I then move on to the primary work of this thesis, the VLT LBG Survey. In Chapter 4, I discuss the imaging observations, photometric selection and spectroscopic observation. In Chapter 5 I investigate the clustering properties of the LBG data. I then go on to use the

LBG data in combination with QSO spectroscopic data to investigate the interactions between galaxies and the surrounding inter-galactic medium at $z \approx 3$ in Chapter 6. Finally, Chapter 7 provides a summary and conclusion to this work.

Unless stated otherwise, I assume a ΛCDM cosmology with $\Omega_m = 0.3$, $\Omega_\Lambda = 0.7$ and $H_0 = 70 kms^{-1} Mpc^{-1}$ throughout this thesis.

1.2 The Cosmic Microwave Background and the Growth of Large Scale Structure

1.2.1 The Cosmic Microwave Background

The postulation and discovery of the Cosmic Microwave Background (CMB) has been one of the most influential discoveries in modern cosmology. CMB theory was developed in the 1940s and 1950s as a by product of the early work on the big-bang model (Lemaître, 1931; Gamow, 1946), whereby the CMB is a natural result of the cooling of the Universe with the expansion of the Universe (Alpher et al., 1953). Although the CMB is now recognized as being detected in the 1950s (Shmaonov, 1957), it wasn't until the observations of Penzias & Wilson (1965) that this uniform background signal was allied with the earlier theories pointing to its cosmological origins (Dicke et al., 1965)

The CMB is a thermal black-body signal with a temperature of 2.725K originating from the time of recombination in the early Universe. Prior to recombination, with the temperatures too high for electrons and protons to bind together, the Universe was opaque to the radiation background, however once the Universe cooled sufficiently for the protons and electrons to stably exist in bound states, photons could then pass freely through space. This point of decoupling of the radiation background from the ionised plasma is termed the surface of last scattering. From these origins the CMB contains the imprint of early structure in the form of anisotropies which are the result of oscillations of the photon-baryon fluid in the gravitational potential wells created by total density perturbations. These fluctuations, which seed the growth of large scale structure in the Universe, were predicted in the early 1970s (Harrison, 1970; Peebles & Yu, 1970; Zel'Dovich, 1970) and have fuelled the work to observe the CMB with greater and greater accuracy.

The primordial anisotropies were not however measured until the space bourne instruments Relikt-1 (Strukov, 1992) and COBE produced measurements during the 1980s

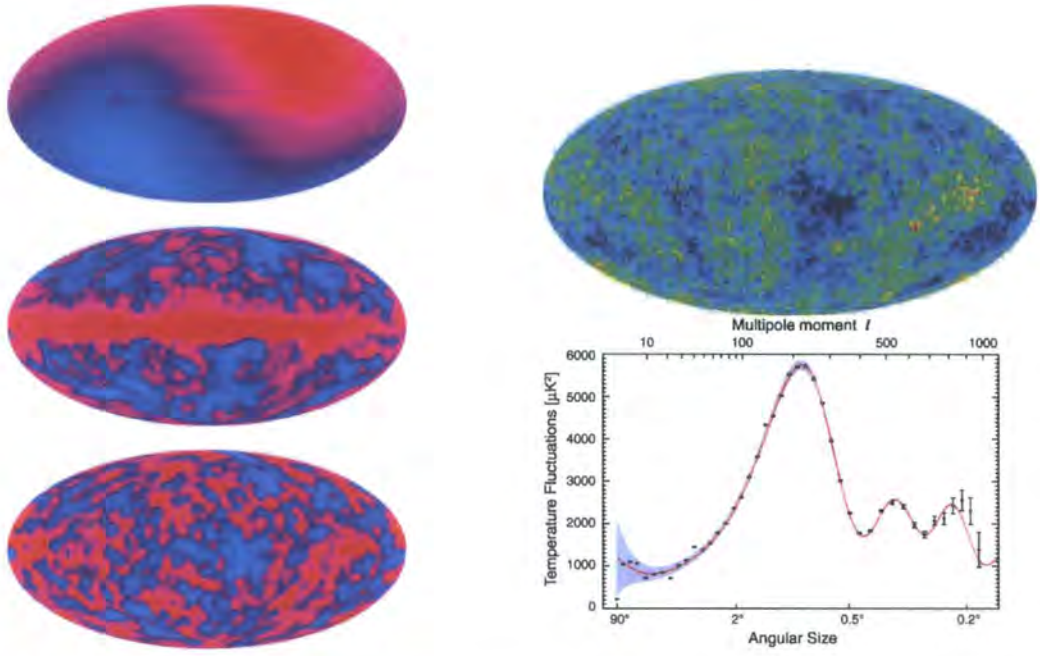

Figure 1.1: Left: Physics Today cover image (1992) showing the COBE measurements of the CMB (Credit: NASA/COBE Science Team). The top image shows the CMB dipole, the middle image shows the dipole subtracted image in which the galactic plane is visible, whilst the bottom image shows the dipole and galactic foreground subtracted image. Right: The WMAP 5-year data all-sky map (top, Credit: NASA/WMAP Science Team) and derived power spectrum (bottom, Credit: NASA/WMAP Science Team).

and early 1990s. The Relikt-1 team successfully detected the dipole and quadrupole moments of the CMB, whilst COBE took the important extra step of observing the CMB anisotropies using its Differential Microwave Radiometers (DMR) Experiment (Smoot et al., 1990; Bennett et al., 1992a).

Sky maps from the DMR on COBE are shown in figure 1.1 (Smoot et al., 1992). The top left panel shows the CMB dipole signal, which results from the motion of the Solar System relative to the local rest-frame and has a magnitude of $\Delta T \approx 3$mK (Conklin, 1969; Henry, 1971; Corey & Wilkinson, 1976). The middle-left panel shows the COBE data with the dipole removed, revealing the galactic plane emission that consists of synchrotron, free-free and dust emission at the level of ~ 0.1mK (Bennett et al., 1992b). Finally the dipole and galactic emission subtracted map is shown in the lower-left panel, where the CMB anisotropies are clearly evident with an amplitude range up to $\Delta T \sim 10\mu$K.

The next step in the study of the CMB was to produce higher signal-to-noise and higher

resolution maps. With this aim, the Wilkinson Microwave Anisotropy Probe (WMAP) was launched in 2001 and observed the CMB in 5 bands: 23, 33, 41, 61 and 93GHz. The 5-year ILC map (a combination of the separate wavebands) is shown in the top-right panel of figure 1.1, with the CMB dipole and galactic foreground emission subtracted. WMAP mapped the whole sky with a minimum beam-width of $13.2'$, significantly improving on the earlier COBE measurements. The key result from the WMAP data was the precise measurement of the CMB power spectrum, clearly showing the primary anisotropy peak, as well as (by the 5-year data release) detecting the second and third peaks (lower-right panel of figure 1.1).

1.2.2 Foregrounds in the Cosmic Microwave Background

Beyond the primary science of the study of the primordial density fluctuations, the CMB data also has a range of useful information on the more recent Universe, between us and the surface of last scattering. This information is in the form of secondary anisotropies, which are the result of CMB photons interacting with structures they have passed through since escaping the primordial plasma. The key secondary anisotropies of interest are:

- Sunyaev-Zel'Dovich Effect
- Sachs-Wolfe Effect
- Rees-Sciama Effect

These contribute their own signals to the measured CMB data and are important to understand in terms of using CMB data to determine cosmological parameters and also as measures of cosmological and astrophysical phenomenon themselves. I now discuss the background and recent work regarding the first two of these.

1.2.2.1 The Sunyaev-Zel'Dovich Effect

The Sunyaev-Zel'Dovich (SZ) effect is the process by which CMB photons passing through clusters interact with the hot intracluster medium (ICM) via inverse Compton scattering and results from both the thermal (thermal SZ effect) and bulk motion (kinetic SZ effect) of cluster gas. It was first postulated by Sunyaev & Zel'dovich (1972) and suggested as an important method for studying the properties of the hot cluster gas. Under the interaction,

CMB photons receive an energy boost, gaining energy from the hot intra-cluster gas. This effectively results in an overall frequency shift in the CMB blackbody spectrum. Depending on the frequency band that an observer uses to measure the temperature of the CMB, either a temperature decrement (at frequencies below the blackbody peak) or temperature increment (at frequencies above the peak) will be measured.

In terms of the cluster properties the temperature decrement/increment that is observed is proportional to both the gas temperature (T_e) and the gas density (n_e) within the cluster. Ultimately, as the quantity $n_e T_e$ is effectively proportional to the gas pressure, the SZ effect is approximately proportional to overall cluster mass. Further details of the effect are given in Chapter 2. Finally, a key advantage of using the SZ in this way is that the magnitude of the effect is independent of the cluster redshift, given that it is simply a distortion of the CMB signal.

The first successful measurements of the SZ effect in local clusters was made at the single dish Chilbolton radio observatory of the SRC Appleton Laboratory by Gull & Northover (1976) and Birkinshaw et al. (1978). These observations recorded temperature decrements of $\approx$-0.5 to -1.5mK in the microwave signal at 10.6GHz in several local large clusters. Since these original detections, many further measurements of the SZ effect have been made with increasingly sensitive radio telescopes and interferometers (Carlstrom et al., 1996) and the SZ effect has ultimately become an extremely useful cosmological tool as well as a method for investigating the properties of clusters (Carlstrom et al., 2002).

Firstly, a number of studies have been performed using the cluster SZ effect in combination with cluster X-ray data to make estimates of H_0 (Birkinshaw, 1979, 1991; Jones et al., 2005; Bonamente et al., 2006; Cunha et al., 2007). Further to this, the SZ effect provides a useful tool for mapping the large-scale structure of the universe as traced by massive clusters of galaxies. Being insensitive to the redshift of the galaxy cluster, it is well-suited to studies of clusters at all redshifts.

The production of the WMAP first-year maps sparked a number of studies into the SZ effect and the detection of clusters using it. Predictions for contamination of the CMB data from the SZ effect were made by several authors (Komatsu & Kitayama, 1999; Refregier et al., 2000), most of whom concluded that the contaminating effects to the WMAP data were small. Indeed very few individual clusters can be detected directly using the SZ effect in the WMAP data. However, much progress has been made with the application of

cross-correlation methods, whereby existing cluster samples are cross-correlated with the WMAP all-sky maps to evaluate the contribution of the SZ signal to the WMAP data. Hernández-Monteagudo & Rubiño-Martn (2004) cross-correlated cluster samples from the Northern ROSAT All Sky Galaxy Cluster Survey (NORAS) and the ROSAT Brightest Cluster Sample (BCS) and published detections of 2-5σ. Afshordi et al. (2004) claimed the detection of the SZ signal in a power-spectrum analysis of WMAP data and the 2MASS galaxy catalogue. Myers et al. (2004) performed the cross-correlation with ACO clusters, limiting their sample to clusters with richness $R \geq 2$, and found a decremental correlation with an extended profile and also claimed detections of the SZ signal using 2MASS and APM data.

Finally, the next major advance for using the SZ as a cosmological tool will be the launch of the Planck Surveyor instrument (Bartlett et al., 2008). This is expected to yield a cluster catalogue that will greatly exceed any current cluster catalogue in terms of numbers, depth and sky coverage. The current consensus is an expected total number of $\approx 10^4$ clusters out to redshifts of $z \approx 1$.

1.2.2.2 Integrated Sachs-Wolfe Effect

The Sachs-Wolfe effect was first postulated by Sachs & Wolfe (1967). It follows from general relativity that as a photon passes through a gravitational field it may be either blueshifted or redshifted (i.e. gain or lose energy) as it falls into or escapes from a potential well. As a photon passes through a cluster or a galaxy halo, it will first be blueshifted as it enters the object and then redshifted by an equal amount as it leaves, regaining its original energy/frequency. However, now suppose that the object's potential well is changing significantly on the timescale of the photons crossing of the potential well. The photon will no longer leave with the same amount of energy as it entered with, but will now have gained or lost energy depending on whether the potential well became weaker or stronger during the crossing period. In an accelerating Universe therefore the Sachs-Wolfe effect can become an important and measurable effect as photons now receive an overall shift in energy from this effect. In this instance, when considering the combined effect of many potential wells as photons travel from the surface of last scattering to the present day, the phenomenon is termed the Integrated Sachs-Wolfe effect.

With the first data release from the WMAP project, it became possible to study this

large scale phenomenon using the full sky CMB maps now available. As with the SZ effect the prime tool to do so was the cross-correlation of the CMB maps with galaxy density maps from large scale galaxy surveys such as the SDSS and APM. By cross-correlating the two datasets, it is possible to better isolate the ISW signal within the primordial density fluctuations of the CMB. The first detections of the Integrated Sachs-Wolfe effect came with the correlation of the WMAP data with SDSS LRGs by Fosalba et al. (2003) and Scranton et al. (2003). This was followed by further positive measurements using the APM survey data (Fosalba & Gaztañaga, 2004) and updated data releases of both the WMAP data and SDSS data by (Padmanabhan et al., 2005b; Cabré et al., 2006). However, Rassat et al. (2007) performed an updated analysis using clusters identified in the 2MASS data, finding an achromatic signal across the WMAP frequency bands. However, they find that the signal is not statistically significant and is still consistent with the null hypothesis.

With the tentative detections of the ISW so far, Douspis et al. (2008) discuss the optimisation of large galaxy surveys for ISW detection. Such surveys may ultimately provide significant insights into the nature of the Universe through the measurement of the ISW effect, placing important constraints on the cosmological constant.

1.2.3 The Growth of Large Scale Structure

The observations of the CMB described above have allowed astronomers to see the initial density perturbations, those initial conditions from which the entirety of the large scale structure in the Universe has formed. By studying the properties of the resultant large scale structure through observations we can learn more about not just the components of the structure, but also the nature and history of the Universe itself.

We can describe the distribution of mass in the Universe via the dimensionless perturbation field, defined as:

$$\delta \equiv \frac{\rho(x) - \langle\rho\rangle}{\langle\rho\rangle} \tag{1.1}$$

where ρ is the mass density. Given linear adiabatic density perturbations, in a matter dominated Universe, the perturbations scale as:

$$\delta \propto a(t) \tag{1.2}$$

where $a(t)$ is simply the expansion scale factor. Over time gravity causes the amplitude of the perturbations to increase, i.e. structure begins to collapse into clumps leading eventually to the formation of stars, galaxies and clusters. Of course the situation is more complicated than a simple collapse and as the density peaks increase to the levels seen in galaxies and clusters, more complicated, non-linear, processes come into play.

In order to study these processes we need both detailed and complex computational analysis and the observations against which to test the resultant predictions. A key test therefore, is the measurement of the density field and its evolution over time. This is often best measured via the clustering properties of the visible components of the density field (i.e. galaxy populations and clusters) measured by the mass power spectrum or its fourier transform the correlation function:

$$\xi(r) \equiv \langle \delta(x)\delta(x+r) \rangle \tag{1.3}$$

Although it is difficult to measure the density perturbations of the underlying dark matter, of which $\approx 85\%$ of the matter in the Universe is inferred to be, we can measure the clustering of the luminous components with the correlation function. From this we may develop a greater understanding of the evolution and nature of different galaxy types, tracing their clustering history back through time. As it is in the highest density peaks that the luminous components must form, these must inherently tell us something about the dominant mass component: the dark matter. The relation between a given galaxy or cluster population's clustering and that of the underlying dark matter density field is then parametrised by the bias parameter, b, such that:

$$\xi_g(r) = b^2 \xi_{DM}(r) \tag{1.4}$$

1.3 Galaxy Photometric Selection at $z < 1$

1.3.1 Overview

Although galaxies vary significantly in their luminosities and spectral energy distributions (SEDs), there remain enough consistent features that it is a feasible goal to be able to estimate the redshifts of galaxies from their colours (Baum, 1962; Koo, 1985; Loh & Spillar, 1986; Connolly et al., 1995; Eisenstein et al., 2001). This photometric selection of galaxies

is a key tool in modern astronomy for narrowing large surveys to focus on distinct galaxy populations. This is particularly the case in large spectroscopic surveys where telescope time is limited and observing a single population over a larger area can be far more efficient and provide more information than a magnitude limited approach.

Such photometric samples can be applied to a number of scientific objectives, some of which I now explore using two populations used in large photometrically selected surveys: Luminous Red Galaxies and Emission Line Galaxies.

1.3.2 Luminous Red Galaxies

A galaxy population that has provided much success for large spectroscopic surveys are Luminous Red Galaxies (LRGs) at $z < 1$ (Eisenstein et al., 2001; Cannon et al., 2006). LRGs are ideal candidates for spectroscopic galaxy redshift surveys since they are intrinsically bright and so can be seen to large cosmological distances. Their colours and therefore the associated photometric selections are heavily dominated by the 4000Å break, which moves through the optical bands out to z=1. This dominant feature is the key that allows relatively clean and complete photometric selections of LRGs at these redshifts.

LRGs are an excellent tracer of large scale structure, making them ideal as the basis of large spectroscopic and photometric surveys of galaxies. A key application of this has been the measurement of the Baryonic Acoustic Oscillations (BAOs) using LRGs selected from SDSS optical imaging data (Eisenstein et al., 2005). Here, a sample of >46,000 LRGs over a volume of $0.72h^{-3}\mathrm{Gpc}^3$ was used to detect the BAO signal at $100h^{-1}\mathrm{Mpc}$ (figure 1.2). This result, along with the 2dFGRS BAO result (Cole et al., 2005), provided further confirmation of the cosmological model being developed through the COBE and WMAP measurements of the CMB acoustic peaks (Smoot et al., 1992; Bennett et al., 2003) and the Supernova standard candle data of Riess et al. (1998) and Perlmutter et al. (1999).

A further example is the 2dF-SDSS LRG and QSO survey (2SLAQ, Cannon et al. 2006), which extended LRG studies from $z \approx 0.45$ upto $z \approx 0.7$. Photometric selection was again performed using the SDSS imaging, whilst spectroscopic observations were performed using the Two-Degree Field (2dF) instrument on the 3.9m AAT. This project had two key aims: to reveal the large scale structure and clustering of matter when the Universe was about two-thirds its present age and to understand the evolution of LRGs. Wake

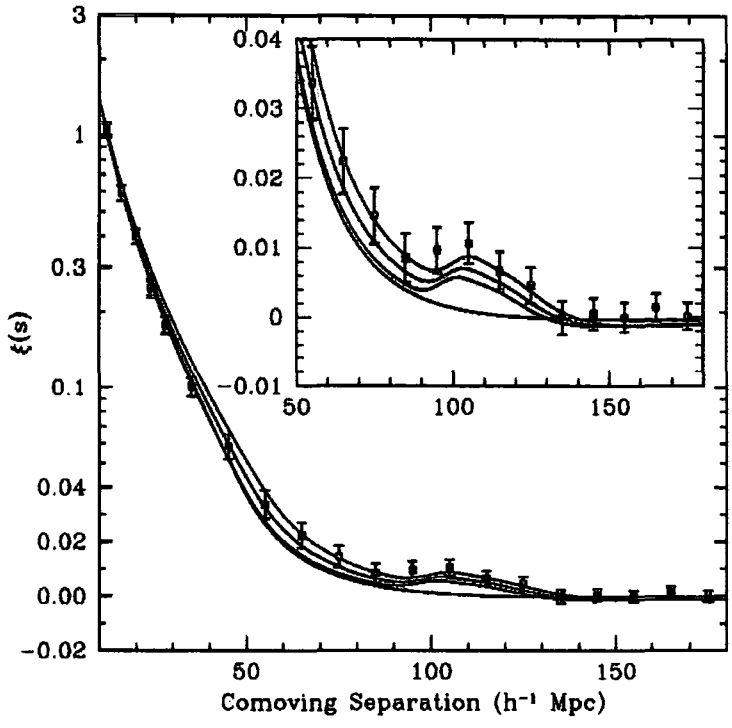

Figure 1.2: Redshift space correlation function as measured by Eisenstein et al. (2005) using $> 46,000$ LRGs (square points). The lines show four models, these being (from top to bottom): $\Omega_M h^2 = 0.12$, 0.13 and 0.14 (all with $\Omega_b = 0.024$) and a pure CDM model with $\Omega_M h^2 = 0.105$. The BAO signal is clearly seen as an increase in the clustering strength at comoving separation of $s \approx 100 h^{-1} Mpc$.

et al. (2008) used the 2SLAQ LRG sample to investigate the evolution of LRG clustering from $z = 0.19$ to $z = 0.55$ and found no evidence for any significant evolution of the clustering amplitude of the correlation function with redshift. Further to this, they found their results rejected a passive evolution model in which there are no mergers between LRGs and concluded that a merger rate of $7.5 \pm 2.3\%$ over the above redshift range is predicted by their data, providing an important observational constraint for galaxy formation models.

1.3.3 Emission Line Galaxies

A key alternative to LRGs as candidates for large scale galaxy surveys are blue star-forming galaxies. These offer the key advantage that redshifts can be obtained spectroscopically using relatively short exposures ($\approx$1-2hrs on a typical 4m telescope) due to the prominence of their emission features. At optical wavelengths the nebular emission lines, OII, Hβ, OIII 5007Å and Hα, facilitate straightforward redshift determination for galaxies at $z < 1$. A trade-off exists however between star forming galaxies and LRGs, as star forming galaxies require the shorter exposure times, but LRGs are more strongly biased and as such trace the peaks in the matter density distribution more closely, giving larger more easily measured clustering amplitudes.

An example of the use of star forming galaxies for the study of large scale clustering is the WiggleZ project (Blake et al., 2009), which aims to measure the BAO signal at $z \approx 0.7$. Their selection is firstly based on GALEX UV imaging, with which they can use the Lyman Break spectral feature at $\lambda = 912$Å to identify galaxies with redshifts of $z > 0.5$. They then use SDSS gri photometry to isolate star-forming galaxies within their $z > 0.5$ UV selection based on their intrinsically blue colours. Using this selection, they then obtain spectroscopic redshifts using low-resolution spectroscopy with the AAOmega instrument on the 3.9m AAT. Aside from the measurement of the BAO signal at $z \approx 0.7$, the WiggleZ survey has several other key goals. Firstly, the survey will yield an accurate measurement of the shape of the galaxy clustering power spectrum on large scales, which in conjunction with CMB data can provide accurate estimates of the composition of the Universe, such as estimating the absolute neutrino mass. Also, the survey aims to map the growth of structure with redshift via the study of galaxy dynamics and redshift-space distortions and also perform detailed analysis of star-formation rates, environments, morphologies

and luminosity functions, providing information on many aspects of galaxy evolution.

1.4 QSOs, Galaxies and Gas at $z \approx 3$

1.4.1 Surveying the $z \approx 3$ Galaxy Population

At redshifts of $z < 1$, the Universe can be relatively simply explored using large scale optical imaging and spectroscopic surveys. At optical wavelengths galaxies at $z < 1$ have both strong continuum emission, enabling straightforward broadband surveys, and strong absorption and emission features, enabling straightforward spectroscopic surveys. Combined with this, the $4000\mathring{A}$ H-break enables the simple photometric selection of galaxies in desired redshift ranges out to $z < 1$, acting as a crucial enabler for large scale spectroscopic surveys of galaxies at such redshifts. However, as we move out in redshift beyond $z > 1$, not only do galaxies appear fainter, but also these important absorption and line emission features move beyond the optical range and into the infrared where our ability to perform 'quick and easy' identification for large scale surveys is inhibited by both strong atmospheric absorption/emission and instrument capability.

The situation improves however as we reach the $z > 2$ epoch. At such redshifts, key features of the UV galaxy spectrum begin to reach optical wavelengths and the most important of these is in terms of galaxy surveys is the $912\mathring{A}$ Lyα-break. Below $912\mathring{A}$, the Universe is opaque to photons and so a break at this wavelength should be a ubiquitous feature in galaxy spectra. Thus the $912\mathring{A}$ Lyα-break provides a comparable tool to the $4000\mathring{A}$ H-break, with which we can photometrically select galaxies at $z > 2$ using broadband optical filters. At redshifts of $2 < z < 4$, the break falls into the U band optical filter and so this selection method can be referred to as the U-dropout technique. The galaxies selected using this method are referred to as Lyman Break Galaxies (LBGs).

The Lyman Break selection method was pioneered in the 1990s, early examples being Guhathakurta, Tyson & Majewski (1990), Steidel & Hamilton (1992), Steidel & Hamilton (1993) and Steidel et al. (1995), in which searches were made for $z \approx 3$ galaxies by looking close to the line of sight of QSOs with observed optically thick Lyman limit absorption systems. Their aim was to either observe or rule out the existence of "normal" galaxies (i.e. similar to the $z = 0$ population) at $z > 3$. Using the Lyman Break selection method, they identified $z > 3$ galaxy candidates using deep optical imaging in the U, G and R

bands in 5 separate QSO fields, estimating a surface density for their LBG populations to $R \approx 25$ of $\approx 0.5 arcmin^{-2}$. Further, Giavalisco et al. (1996) reported HST observations in the Hubble Deep Field investigating the morphology of LBGs. These observations showed that the LBGs exhibit cores of size $\approx 0.5 - 1''$ $(6 - 12kpc)$, comparable to the scales of the cores of present day galaxies. Halo structures were also observed, which were often irregular and asymmetric. The surface brightness of the LBG cores was estimated at $22 - 23$ $mag\ arcsec^{-2}$, of the order of $10\times$ the central surface brightness of typical spiral disks at the present epoch. The cores dominate the UV flux of the galaxies and so dominate the star-formation in these galaxies.

The next step came with the use of the LRIS instrument at the Keck Observatory. Using this, Steidel et al. (1996) and Madau et al. (1996) were able to provide spectroscopic confirmation of the high-redshift nature of LBG candidates. They added to their previous imaging using the Palomar 5m telescope (allowing a field of view of $9.7' \times 9.7'$) and obtained a more accurate estimate of the sky density for $z > 3$ $R < 25$ LBGs of $0.40 \pm 0.07 arcmin^{-2}$. They estimated that their U-dropout sample forms 1.3% of all $R < 25$ objects and 2% of all $23.5 < R < 25$ objects. Given these numbers and the spectral confirmation, the importance of the Lyman Break selection technique is clearly apparent.

From the small numbers of objects spectroscopically confirmed in these early stages a large program was embarked upon, the results of which were published in Steidel et al. (2003). This took advantage of the 10m Keck Telescope to provide a large catalogue of galaxies at $z \approx 3$. The LBG selection criteria was extended to isolate galaxies in the redshift range $2.5 < z < 3.5$ and went to a depth of $R < 25.5$. This gave a candidate density of $\approx 1.8 arcmin^{-2}$. Over 17 separate fields (with fields of view in the range $18 - 250 arcmin^2$), covering a combined area of $0.38 deg^2$ they identified 2347 LBG candidates and were able to observe $\approx 55\%$ of these using Keck. 76% of those were identified and 73% were galaxies at $z \approx 3$ (the remainder being stars and AGN). A redshift distribution was obtained with $z = 2.96 \pm 0.29$.

The work of Steidel et al. (2003) has therefore successfully opened up a window to the $z \approx 3$ Universe. Interestingly however, Le Fèvre et al. (2005) indicated that Steidel et al. (2003) underestimate the galaxy population at $z \sim 3$, providing an indication of the numbers of galaxies missed by the Lyman-Break selection using data from the VLT VIMOS Deep Survey (VVDS). They find a galaxy surface density in the redshift range

$2.7 < z < 3.4$ of $\Sigma = 0.235 \pm 0.025/arcmin^2$ at $I_{AB} < 24$, a factor of ≈ 2 higher than the Steidel et al. (2003) colour selected samples. Despite this, Steidel et al. (2003) have shown the feasibility of performing redshift surveys of large numbers of LBGs using the U-dropout selection method and low-resolution spectroscopy. This method enabled the opportunity to study the $z \approx 3$ Universe efficiently opening a number of avenues for scientific work.

1.4.2 Galaxy Structure

Early work on the structure and dynamics of the LBG population was based on low-resolution optical and infra-red spectroscopy (Steidel et al., 1996; Madau et al., 1996; Giavalisco et al., 1996; Lownethal et al., 1997; Pettini et al, 1998). Key absorption and emission features that were observed included Lyα in emission and absorption, a range of interstellar absorption lines (e.g. OI, CII, SiIV) and a range of nebular emission lines including the prominent Hα, [O III] λ5007, 4959, Hβ and [O II] λ3727 lines. From these observations a key observation was that these the nebular emission lines and interstellar absorption lines were found to be offset by velocities of $\approx 200 kms^{-1}$ (Pettini et al, 1998). This suggested that the sources of these lines are not at rest with respect to each other and are instead dynamically different regions.

A further advancement was the discovery of a lensed high-redshift galaxy MS 1512-cB58, which was discovered by Yee et al. (1996) and is a typical $\sim L^*$ galaxy at z=2.73. It is magnified by a factor of $\approx$30 by the z=0.37 foreground cluster, MS1512+36 (Seitz et al., 1998), making it an ideal subject for the study of galaxy properties and formation at these high redshifts. Teplitz et al. (2000) presented the rest-frame optical spectrum of MS 1512-cB58, taken using the NIRSPEC during the instruments commissioning. With this data, they detected several nebular emission lines indicative of star-formation, including Hα, [O III] λ5007, 4959, Hβ and [O II] λ3727 as well as detecting the optical continuum. From the line-strength data, they estimated a star-formation rate of $\approx 620 M_{\odot} yr^{-1}$ and concluded that MS 1512-cB58 is an evolved galaxy with significant metals and that it is consistent with LBGs being the progenitors of modern-day elliptical galaxies.

In tandem with these near infrared observations using NIRSPEC, Pettini et al (2000) and Pettini et al (2002) performed optical spectroscopy of MS 1512-cB58 using the Low Resolution Imaging Spectrograph (LRIS) and Echelle Spectrograph and Imager (EIS) on the Keck II telescope respectively. Pettini et al (2002) found that the $z = 2.72$ galaxy is

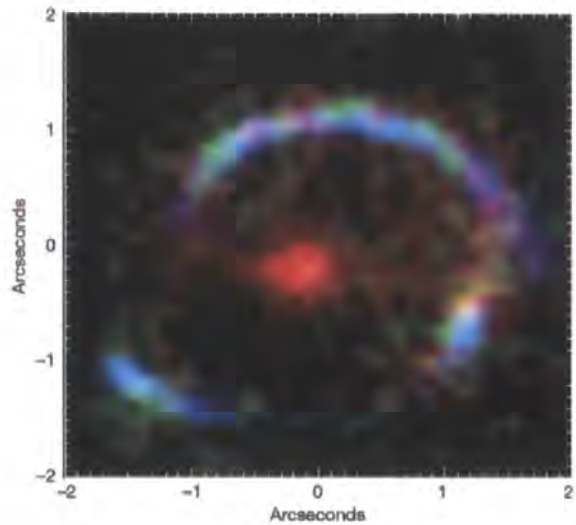

Figure 1.3: Colour image of J2135-0102 (blue Einstein ring) taken from Stark et al. (2008). J2135-0102 is a z=3.07 galaxy magnified $\approx 28\times$ by the foreground cluster galaxy at z=0.7 (central red object).

'highly enriched by the chemical elements released by Type II supernovae' and, based on the measured abundances, indicate that this particular galaxy has already processed a large proportion of its gas into stars. At the same time they note that it is also relatively deficient in elements (e.g. N, Mn, Fe and Ni) produced by intermediate-mass stars. Combining these two observations, they suggested that this particular LBG is in the process of converting its interstellar medium (ISM) into stars and that it may be in the process of forming a bulge or elliptical galaxy. Further to this, both Pettini et al (2000) and Pettini et al (2002) concluded that the ISM has been 'stirred and accelerated to high velocities', based on measurements of the line-widths of the ISM lines of $\sim 500 kms^{-1}$.

A significant addition to the study of the properties of $z \approx 3$ galaxies has come with the discovery of another highly lensed $z \sim 3$ galaxy, LBG J2135-0102 (Smail et al., 2007). Coppin et al. (2007) performed millimeter interferometry and mid-IR imaging of this object, measuring CO line-widths and inferring stellar mass and star-formation rates. From this data, Coppin et al. (2007) concluded that LBG J2135-0102 is a high-redshift, gas-rich analog of a local luminous infrared galaxy. Additionally to this, Stark et al. (2008) took IFU observations of the J2135-0102 (figure 1.3), with a linear resolution of $\sim 100pc$. From these high-resolution observations, Stark et al. (2008) investigate the dynamics of the galaxy and find strong evidence for clear rotation. Combining their data with that

of Coppin et al. (2007), they determine the ratio between the CO luminosity and the molecular gas mass in order to distinguish the mode of star formation and conclude that the star-formation occurs in an extended single region across the high-redshift galaxy.

From the numerous observations of LBGs at $z \approx 3$, a picture of the nature of galaxies at these high redshifts is being constructed. They typically have half-light radii of $\approx 1.6h^{-1}kpc$ within which significant levels of star-formation are found. Further to this, there appear to be negligible velocity offsets between nebular emission lines and stellar photospheric absorption features, suggesting that the stellar component and HII regions of LBGs are at rest with respect to one another (Shapley et al., 2003). Outside of this central region, observations suggest the presence of an outflowing envelope of hot gas, which is the source of the Lyα emission/absorption and ISM absorption lines evident in most LBG spectra. These outflows appear to be powered by the large number of Type II supernovae explosions, resulting from the high star-formation densities observed in LBGs.

1.4.3 Outflows and Feedback

The high-velocity turbulent flows of material that have been discussed above are considered to be a crucial component in galaxy formation and evolution, with far-reaching effects on the IGM as well as galaxies themselves. To begin with, it is evident that the IGM is significantly enriched with metals at the redshifts currently probed by QSO sight-lines (Songaila & Cowie, 1996; Pettini et al, 2003; Aguirre et al., 2004). Other than enrichment from galactic scale winds, it is difficult to see from where these metals originate. A similar story is found when we look at clusters, the ICM is highly enriched, such that there is a greater presence of metals in the ICM than in the cluster galaxies (Renzini, 1997).

Further to this, outflows form a crucial component in galaxy formation simulations. To begin with, the disruption of star formation by supernova explosions is the favored explanation for why so few baryons are found in stars today. Springel & Hernquist (2003) show with their cosmological SPH simulations that supernova feedback, leading to galactic outflows, is a crucial component of recreating the star formation history of the Universe. Importantly, by incorporating the strong feedback in the form of galactic winds, they find that 10% of all baryons have been turned into long-lived stars by the present in agreement with observational constraints. The powerful effects that these simulated galactic winds have on their environment is illustrated in figure 1.4, which is taken from Springel &

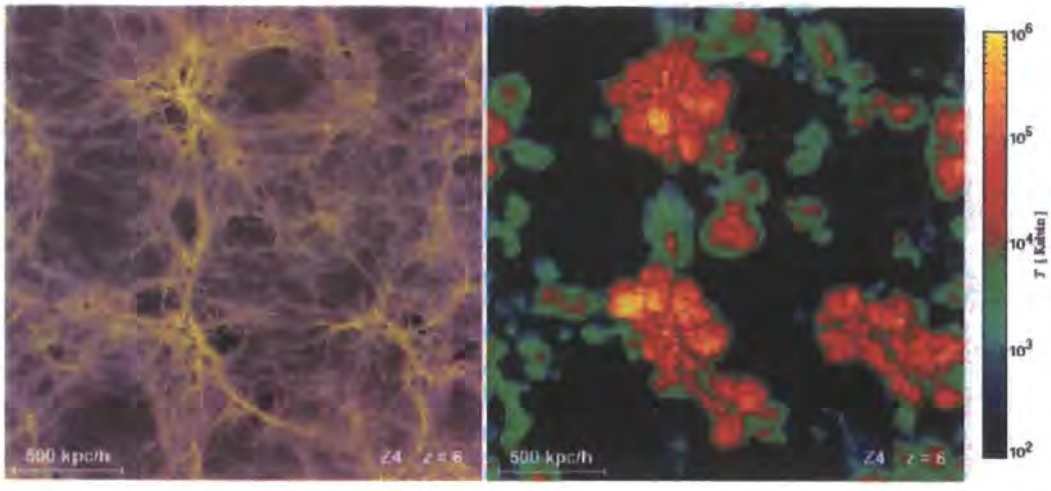

Figure 1.4: High spatial resolution baryonic density field (left panel) and projected temperature map (right panel) from the simulations of Springel & Hernquist (2003). Hot bubbles in the IGM caused by galactic winds are evident within which the gas temperature is up to 10^6K.

Hernquist (2003). This shows the baryon density distribution in a slice through their simulation (left-panel) and the associated mass-weighted temperature map (right-panel). Low-density (dark), high-temperature bubbles, caused by outflowing winds, can clearly be seen around high-density structures.

Similarly, without the presence of some sort of feedback, hierarchical galaxy formation models over-predict the numbers of very bright galaxies at early time (Benson et al., 2003). The low numbers of luminous galaxies is most easily explained if cooling in massive halos is strongly suppressed via the expulsion of cold disk gas by super-winds.

It is also found that without significant heat input from galactic winds, numerical simulations may not easily reproduce large disk galaxies. For example, Scannapieco et al. (2008) show through their simulations that supernova feedback plays a fundamental role in the evolution of galaxy disks. In their models, the supernova feedback efficiently regulates the star formation activity, pressurizes the gas and generates mass-loaded galactic winds. These processes affect several galactic properties including the final stellar mass, morphology, angular momentum, chemical properties, and final gas and baryon fractions. Their model reproduces the expected dependence on galaxy mass: while star formation is suppressed at most by a factor of a few in massive galaxies, in low-mass systems the effects can be much larger, giving star formation an episodic, bursty character.

A key observational method in constraining the effect of galactic winds on the IGM

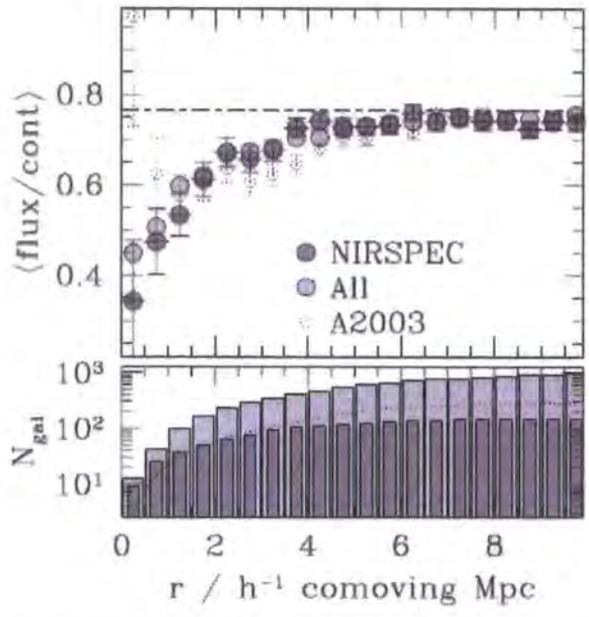

Figure 1.5: Adelberger et al. (2005) result from the cross-correlation of known LBGs with the Lyα absorption along the lines of sight to 23 QSOs.

around them was performed by Adelberger et al. (2003) and Adelberger et al. (2005). Adelberger et al. (2003) cross-correlated the positions of ≈ 400 of the Steidel et al. (2003) LBGs with the Lyα absorption profiles in the line of sight of 8 bright $z > 3$ QSOs, measuring the mean absorption as a function of distance from LBGs. Their result showed an increase in neutral hydrogen densities (i.e. decrease in line-of-sight flux) at separations of $r < 5h^{-1}Mpc$, but then showed a severe drop in neutral hydrogen densities at $r < 1h^{-1}Mpc$. They proposed that this drop in density was associated with the effect of galactic winds creating creating low-density bubbles around these high-redshift star-forming galaxies. However, their result at $r < 1h^{-1}Mpc$ was based on only a small number of confirmed LBGs and so had a low-significance. The measurement was therefore repeated by Adelberger et al. (2005) with an enlarged sample of LBGs around 23 bright QSOs. With the increased numbers of objects and with improved redshifts obtained from infrared spectroscopy, the $r < 1h^{-1}Mpc$ under-density disappeared (figure 1.5).

Based on the observations above, it is still unclear as to the extent of the influence of galaxy winds, whether they are localized to a few kpc around star-forming regions or they have significant impact across the entirety of a galaxy and its surroundings (as simulations would suggest). Further observational evidence can by supplied from direct

observations of individual high-redshift galaxies. Wilman et al. (2005) present 2-D IFU spectroscopy of a Lyα-emitting blob (LAB) associated with an LBG in the SSA22 proto-cluster. They observe significant structure in the observed galaxy, detecting double peaked Lyα emission throughout the galaxy, which they attribute to broad Lyα emission with line-widths of $\sim$ $1000 kms^{-1}$ FWHM, combined with absorption in the line of sight by cloud of neutral hydrogen. Further, the absorber is blue shifted from the Lyα emission by $\approx 250 kms^{-1}$. From the 2-D spatial data, they find that this absorbing medium covers a region of $\approx 100 kpc$. From this evidence, Wilman et al. (2005) thus conclude that they have a consistent picture in which the Lyα absorber is a highly ionized shell of gas outflowing from the central galaxy, with a spatial extent that demonstrates that super-winds are a galaxy-wide phenomenon.

In summary, supernovae driven winds in high redshift galaxies appear to be a key component in the history of galaxy and structure formation in the Universe. They provide a mechanism integral to recreating the properties of galaxies with computational simulations. Furthermore, outflowing material with high velocities is clearly observed in high-redshift star-forming galaxies and there is now some evidence to support their large-scale nature and hence an indication of their far-reaching effects.

CHAPTER 2

ANOMALOUS SZ CONTRIBUTION TO 3 YEAR WMAP DATA

Myers et al. (2004) made a cross-correlation analysis between galaxy cluster catalogues and the WMAP first year data (Hinshaw et al., 2003). They saw a statistical decrement near groups and clusters as detected by APM and also in more nearby groups and clusters as detected by 2MASS but the strongest signal was seen in the ACO rich cluster catalogue. There the decrement was approximately what was expected from predictions based on X-ray observations of the Coma cluster which is itself a richness class 2 cluster. However, the profile appeared to be more extended than expected from simple fits to these typical cluster X-ray data. The extent of the SZ effect, possibly to $\theta \approx 1$ degree, led Myers et al. (2004) to speculate whether the SZ effect could contaminate the measurement of the acoustic peaks, although the difference between the SZ and primordial CMB spectral indices may constrain such a possibility at least for the first peak (Huffenberger et al., 2004). We now return to this topic with the first aim to see if the extended SZ effect is reproduced in the 3-year WMAP data.

Meanwhile, Lieu et al. (2006) analysed the WMAP first year data now focusing only on 31 clusters with ROSAT X-ray data. They made basic predictions for the SZ decrement in each cluster and found that they over-predicted the SZ decrement. One possibility was that discrete radio sources in the clusters were diluting the decrements but this was argued against by Lieu et al. (2006). However, Lieu & Quenby (2006) suggested an alternative mechanism based on synchrotron radiation from cosmic ray electrons moving in the cluster magnetic field forming a diffuse cluster radio source which again may dilute the SZ effect. This model was also aimed at explaining the soft X-ray excesses detected in some clusters via inverse Compton scattering of the CMB by the same cosmic ray electrons in the cluster (e.g. Nevalainen et al. 2003 and references therein).

Here we shall check the result of Lieu et al. (2006) using our cross-correlation methodology and the full WMAP 3-year data. In the first instance, we shall take the X-ray models of Lieu et al. (2006) which follow the simple β model prescription described in Section 3 below. We shall also look at a new sample of clusters with excellent Chandra X-ray

Table 2.1: Properties of the WMAP frequency bands.

Band	Frequency	FWHM
W	94GHz	12.′6
V	61GHz	19.′8
Q	41GHz	29.′4
Ka	33GHz	37.′2
K	23GHz	49.′2

data (Bonamente et al., 2006). Again we shall simply take their models convolved for the WMAP PSF in the appropriate band and compare to the averaged SZ decrement seen in the WMAP3 data.

2.1 Data

2.1.1 WMAP Third Year Data

We use the raw CMB temperature maps provided in the WMAP 3 year data release (Hinshaw et al., 2006). These consist of temperature data from the five frequency bands and the internal linear combination (ILC) map (Table 2.1). In order to remove contamination from our own galaxy, we make use of the Kp0 foreground mask made available with the other WMAP data products and have applied this to all our maps prior to cross-correlation. The data is used here in the HEALPix format of equal area data elements, characterised by N_{side}=512, which gives an element width of $\approx 7'$.

2.1.2 Cluster Data

2.1.2.1 ACO

The ACO catalogue (Abell, Corwin & Olowin, 1989) lists clusters with 30 or more members, given the requirements that all members are within 2 magnitudes of the third brightest cluster member, whilst also lying within a 1.5 h^{-1} Mpc radius. A richness class, R, is applied to the individual clusters based on a scale of $0 \leq R \leq 5$. The catalogue covers both hemispheres and here we trim these samples such that we take clusters of only $R \geq 2$ and galactic latitudes of $|b| \geq 40°$.

2.1.2.2 APM

We shall also use galaxy group and cluster catalogues derived from the APM Galaxy Survey of Maddox et al. (1990) which covers the whole area with $\delta < -2.5\,\mathrm{deg}$ and $b < -40\,\mathrm{deg}$. These were identified using the same 'friends-of-friends' algorithm as Myers et al. (2003) and references therein. Circles around each APM galaxy with $B < 20.5$ are 'grown' until the over-density, σ, falls to $\sigma = 8$ and those galaxies whose circles overlap are called groups. The APM galaxy surface density is $N \approx 750\,\mathrm{deg}^{-2}$ at $B < 20.5$. Minimum memberships, m, of $m \geq 7$ and $m \geq 15$ were used. The sky density of groups and clusters is $3.5\,\mathrm{deg}^{-2}$ at $m \geq 7$ and $0.35\,\mathrm{deg}^{-2}$ at $m \geq 15$. We assume an average redshift of $z = 0.1$ for both APM samples.

2.1.2.3 2MASS

The third cluster catalogue is derived from the final data release of the 2MASS Extended Source Catalogue (XSC) (Jarrett et al., 2000) to a limit of $K_s \leq 13.7$. K-selected galaxy samples are dominated by early-type galaxies which are the most common galaxy-type found in rich galaxy clusters. Therefore the 2MASS survey provides an excellent tracer of the high density parts of the Universe out to $z < 0.15$ and so provides a further test for the existence of the SZ effect. Using the above 2-D friends-of-friends algorithm, Myers et al. (2004) detected 500 groups and clusters with $m \geq 35$ members at the density contrast $\sigma = 8$ in the $|b| \geq 10\,\mathrm{deg}$ area. The 2MASS groups have average redshift, $z \approx 0.06$.

2.1.2.4 ROSAT X-ray cluster sample

The 31 clusters published by Bonamente et al. (2002) were originally selected as a sample of X-ray bright clusters suitable for observing X-ray surface brightness profiles. These profiles were obtained with the ROSAT PSPC instrument and estimates of the gas temperature, density and distribution were made by fitting a β profile model to the data (see section 3 below). The X-ray data for these 31 clusters were previously used by Lieu et al. (2006) to construct predictive models of the SZ profile of each cluster. Redshifts for the clusters range from z$\sim$0.02 (Coma) up to z$\sim$0.3 (Abell 2744), whilst the sample lies in the galactic latitude range of $\mid b \mid \geq 25°$.

2.1.2.5 Chandra X-ray cluster sample

We further analyse the 38 clusters discussed by Bonamente et al. (2006). These clusters have been observed at 30GHz by OVRO and BIMA (see Bonamente et al. (2006) and references therein) to detect the SZ decrements and have also been observed by Chandra to provide the X-ray data needed to estimate the value of H_0. The interferometric radio observations have a resolution of $\approx 1'$ and the X-ray observations from the Chandra ACIS-I camera have a resolution of $\approx 1''$. Redshifts for these clusters are in the range $0.18 < z < 0.8$, a higher range than for the ROSAT sample. Bonamente et al. (2006) fitted both hydrostatic equilibrium and isothermal β models to the X-ray data and made predictions for the SZ decrements.

2.2 SZ X-ray modelling

The SZ effect is generally modelled using X-ray gas profiles, densities and temperatures. The X-ray data is most simply modelled by fitting a β model to the X-ray intensity profile:

$$S_X = S_{X0}\left(1+\frac{\theta^2}{\theta_c^2}\right)^{(1-6\beta)/2} \tag{2.1}$$

where S_{X0} is the central X-ray surface brightness and θ_c is the angular core radius. On the isothermal assumption, the temperature decrement, ΔT_{SZ}, as a function of the angular distance from the cluster-centre, θ, is then given by:

$$\Delta T_{SZ}(\theta) \;=\; \Delta T_{SZ}(0)\left[1+\left(\frac{\theta}{\theta_c}\right)^2\right]^{-\frac{3\beta}{2}+\frac{1}{2}} \tag{2.2}$$

Then the magnitude of the central temperature shift, $\Delta T_{SZ}(0)$, is given by:

$$\frac{\Delta T_{SZ}(0)}{T_{CMB}} \;=\; \frac{kT_e}{m_e c^2}\sigma_{Th}\int \mathrm{d}l \quad n_e\left[\frac{x(e^x+1)}{e^x-1}-4\right] \tag{2.3}$$

where $x = h\nu/kT_e$, σ_{Th} is the Thomson cross-section and n_e, T_e are the gas density and temperature derived from the X-ray data.

Lieu et al. (2006) use the cluster sample of Bonamente et al. (2002) and fit ROSAT PSPC cluster X-ray profiles. They assume isothermal gas distributions with T_e taken from Bonamente et al. (2002). Bonamente et al. (2006) use both a hydrostatic equilibrium model, allowing a double power-law β-model to allow for variations in the number density

with radius, and an isothermal β-model. With the hydrostatic model, they allow the gas temperature to vary with radius and a CDM component as well as gas to contribute to the cluster potential. We shall simply assume the isothermal models of Lieu et al. (2006) and Bonamente et al. (2006) and convolve the predicted SZ profile with the appropriate WMAP beam profile, modelled as a Gaussian with the FWHM beam-widths shown in table 2.1.

2.3 Cross-correlation analysis

We focus our analysis on the 94GHz W band from WMAP, looking for correlations characteristic of the SZ effect in this, the highest resolution band. We perform a cross-correlation analysis as described in Myers et al. (2004), calculating the mean temperature decrement/increment as a function of angular separation from galaxy clusters in the above datasets. Our cross-correlation takes the form:

$$\Delta T_c(\theta) = \sum_i \frac{\Delta T_i(\theta) - \overline{\Delta T}}{n_i(\theta)} \tag{2.4}$$

Where $\Delta T_i(\theta)$ is the WMAP temperature in an element i at an angular separation θ from a cluster centre and n_i is the number of elements at that separation. $\overline{\Delta T}$ is the mean WMAP temperature decrement across the entire region used in the analysis. For the 3-year W-band data, $\overline{\Delta T} \sim 10^{-3}$mK.

Errors on our results are estimated using repeated Monte Carlo realizations of the cluster data. Given that the cluster samples will each be highly clustered, it is important to incorporate the sample clustering into the realizations as randomly distributed sources are likely to under-estimate the errors. To do this, I follow the method used by Myers et al. (2004) and Frith (2005). Firstly mock cluster positions are produced using a random number generator, with 5$\times$ the number of mock galaxies as actual galaxies in the sample. Each mock galaxy cluster is assigned a weight, $(1 + w)$, derived from every other mock cluster, where w is the value of an input 2-point correlation power-law function with an input slope, γ, and amplitude, A. In order to avoid clusters at the edge of the survey area being assigned lower weightings due to having fewer numbers of close pairs, the initial mock cluster positions are generated to cover an area larger than the actual survey area. Each mock cluster is then rejected or accepted in turn with a probability given by the

calculated weighting. Any mock clusters remaining outside the survey field were then excluded and the overall mock sample size reduced to the number of survey clusters using a random sampling. In order to test the quality of the individual mock catalogues, the clustering of the each is measured using the angular correlation function and compared to the survey sample correlation function. Those that are a poor match to the actual sample are rejected. As discussed in Frith (2005), the weighting system requires a large input slope and normalization, but given this it is able to produce clustered mock catalogues comparable to the input data.

The calculation errors are then estimated by performing the cross-correlation with 100 mocks produced as described above and taking the standard deviation of the resulting distribution in each angular bin.

In addition to this we also perform a rotational analysis to provide an alternative estimate of the errors. In this case we perform the cross-correlation between the cluster positions and the WMAP data. We then shift the cluster positions by 20° in galactic longitude and recalculate the cross-correlation. We repeat this until we have rotated through a full 360°. A S/N is then calculated from the results of this rotational analysis.

2.4 Results

2.4.1 Optical/IR Cluster Samples

The results for the cross-correlation between the four large cluster datasets (APM $m \geq 7$, APM $m \geq 15$, ACO R$\geq$2 and 2MASS clusters) and the WMAP W-band data are shown in figure 2.1 (note that in this and other plots the points are plotted down to separations of less than the beam-width of each band - see table 2.1 - and these should not be regarded as being independent). A decrement is immediately evident on small scales within $\theta < 30'$ of cluster centres in all four data sets. As would be expected however, the APM datasets show a much smaller amplitude than the ACO and 2MASS results, due to their lower minimum membership requirement and hence lower masses (as discussed earlier the ACO and 2MASS clusters have minimum memberships of 30 and 35 respectively compared to minimum memberships of 7 and 15 for the APM samples). Looking in detail first at the ACO results, the WMAP3 cross-correlation strongly confirms the results of Myers et al. (2004) from WMAP 1st year data. Here, we find a decrement of $-0.021 \pm 0.007mK$ at

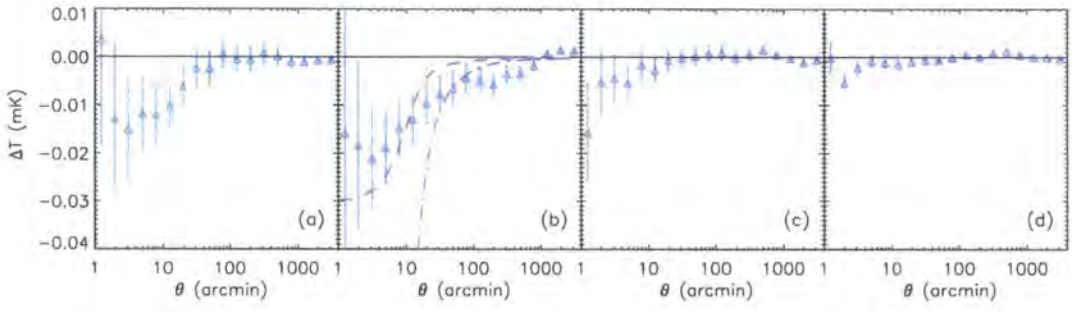

Figure 2.1: Cross-correlation results between the WMAP 3-year W-band temperature data and the four cluster datasets: (a) 2MASS, (b) ACO, (c) APM m≥15, and (d) APM m≥7. The dashed and dot-dashed lines in (b) show SZ models with $\Delta T = 0.083K$ and $\Delta T = 0.49K$ respectively, both with $\theta_c = 1.'5$ and $\beta = 0.75$ and convolved with the WMAP beam-width. The latter model is intended to be representative of the Coma cluster, scaled to redshift $z = 0.15$. The former is the ACO model fitted by Myers et al. (2004) in their analysis of the WMAP 1st year results. (Note that although points are plotted at $\theta < 6'.3$, these will not be independent as they are within the WMAP W-band beam width)

$\theta < 6'.3$ and $-0.010 \pm 0.004mK$ at $\theta < 60'$ for the W-band data (quoted accuracies are from the Monte-Carlo analysis). Basically, the ACO decrement has remained the same and the improved statistics at small angles has increased the S/N. In addition to the Monte-Carlo analysis, we also checked our ACO results using the rotational analysis described by Myers et al. (2004) and find the significance of the decrement at $6.'3$, $60'$ and $500'$ to be 3.2σ, 2.0σ and 1.2σ (see figure 2.2).

As in Myers et al. (2004), we see an extended signal out to angles of $\sim 100'$ in the ACO sample. The simplest explanation for this would be in the highly clustered nature of the clusters themselves, whereby each of our rich clusters is most likely surrounded by a number of other clusters that will contribute to the observed SZ signal at larger scales. We also produce the correlations with the four other WMAP bands, plus the ILC map, the results of which are shown in figure 2.3. Again, good agreement is seen between these updated results and the original first year data results. Despite the increasingly poor resolution of the bands, the decrement is observed in the V, Q and Ka bands, whilst even the ILC map and the Ka band map show a decrement.

Improvements in the small scale statistics are also observed in the 2MASS and APM results while the magnitudes of the decrements remain unchanged. However, the APM group ($m \geq 7$) SZ detections remain marginal even at small scales.

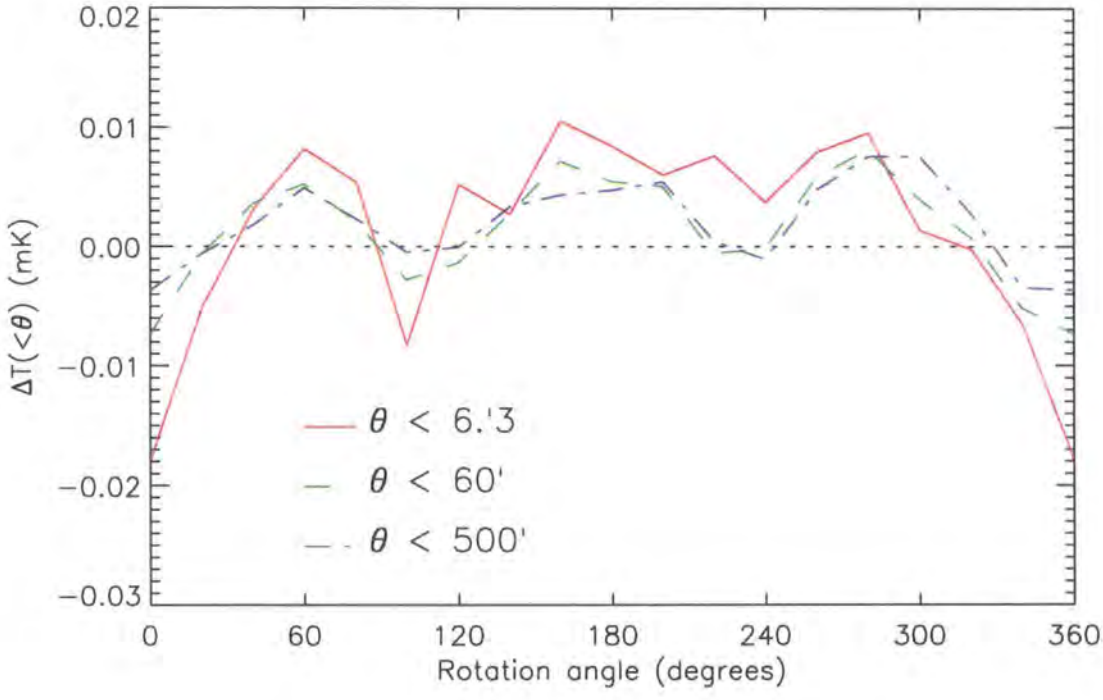

Figure 2.2: The cross-correlation of the ACO catalogue is shown after increments in galactic longitude of 20° in the Abell cluster positions. The mean ΔT is shown for WMAP pixels within 6.′3, 60′ and 500′ of cluster centres, where the significance at each angular limit is 3.2σ, 2.0σ and 1.2σ respectively.

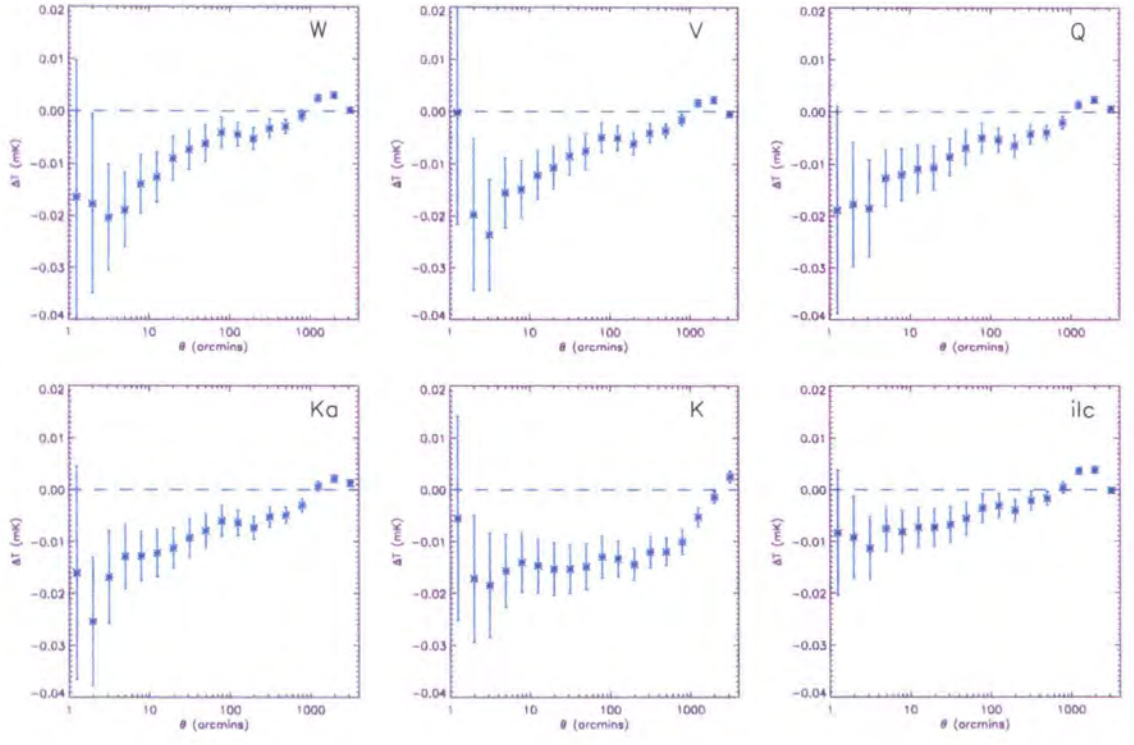

Figure 2.3: Cross-correlation results between 606 ACO rich galaxy clusters ($R \geq 2$, $|b| > 40$deg) and the WMAP 3-year maps in 5 band-passes (+ILC) as indicated.

2.4.2 ROSAT X-ray bright cluster sample

We next consider the X-ray bright clusters of Bonamente et al. (2002). Analysis of this data-set with respect to the first year WMAP results has already been performed by Lieu et al. (2006). Their main conclusion was that the SZ decrement in the WMAP1 data around the locations of these clusters has a lower magnitude than they would expect from their predictions based on the original X-ray observations of Bonamente et al. (2002). In figure 2.4 (left panel) we show our cross-correlation between the 31 clusters used by Lieu et al. (2006) and the WMAP year 3 data in the W-band (crosses). We also present the average model prediction based on the Bonamente et al. (2002) data (solid line). This has been convolved with a Gaussian beam profile of $\sigma = 6.'3$. We see the same general effect as seen by Lieu et al. (2006), that the SZ effect is somewhat smaller than predicted by the data. However, the significance of rejection is only $\approx 2\sigma$. Similar results are seen in the other WMAP bands.

We next split the Lieu et al. (2006) clusters by redshift as shown in figure 2.5. Again our results are given by the crosses, whilst the solid lines show the average model SZ profiles. The model for clusters at $z < 0.1$ is rejected by 4.2σ at $\theta < 6.'3$, whilst at $0.1 < z < 0.3$ the rejection drops to 1.6σ at $\theta < 6.'3$. We have also performed this analysis with a latitude split at $|b| = 40°$ and find some degeneracy between latitude and redshift as many of the low redshift clusters are also at low latitude. Supposing an increasing signal with redshift, this may be accounted for with the cluster sample at higher redshift being dominated by more massive clusters, however if this were the case the difference should also be seen in the models of Bonamente et al. (2002).

2.4.3 Chandra X-ray bright cluster sample

We next analysed the SZ decrements for the 38 clusters of Bonamente et al. (2006), using the WMAP3 W band results. In figure 2.4 (right panel) we compare the cross-correlation results with an average model constructed from the individual isothermal models given in table 5 of Bonamente et al. 2006 (solid line) and again find that the SZ effect is now quite severely over-predicted by the models, with a rejection significance of 5.5σ. We again looked for a dependence on redshift and found slight evidence for a greater SZ signal at $z < 0.3$ compared to to $z > 0.3$ (figure 2.6).

Given that Bonamente et al. (2006) only fit the Chandra data for $\theta < 2'$, there is

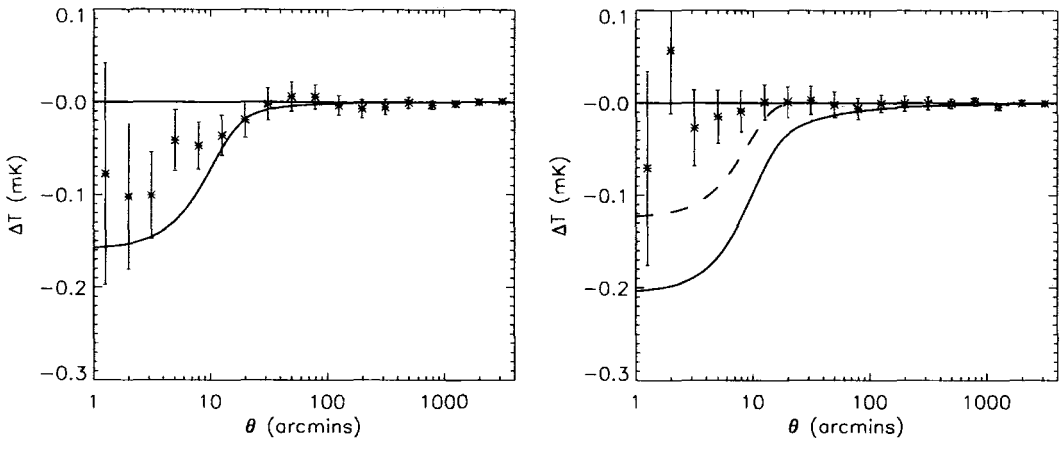

Figure 2.4: Average ΔT (from WMAP W-band data) plots for 30 clusters from the ROSAT sample (left) and 39 clusters from the Chandra sample (right). In both figures, the points show our cross-correlation results, whilst the curves show average SZ models (based on the parameters taken from Lieu et al. 2006 and Bonamente et al. 2006) convolved with a Gaussian representing the WMAP beam profile. For the Chandra sample, we plot the full isothermal model (solid line) and the same model limited to $\theta < 2'$ (dashed line).

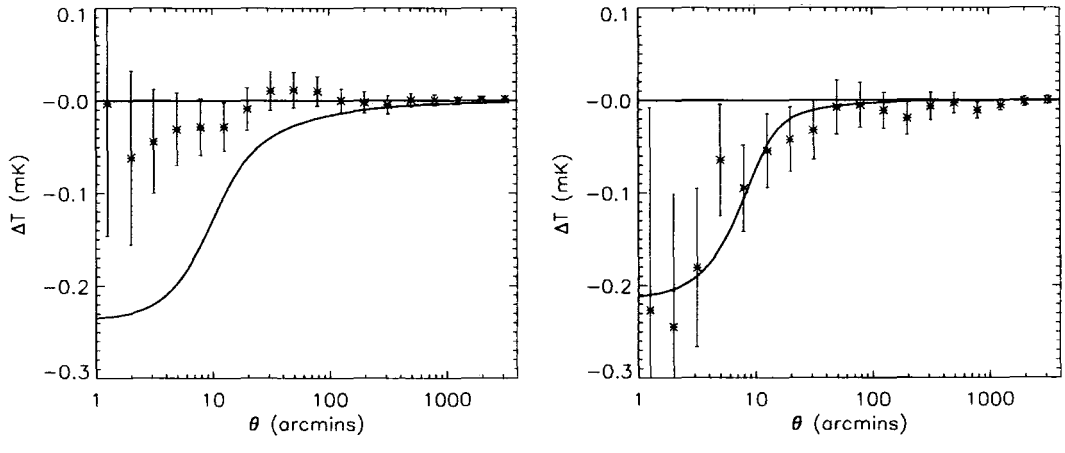

Figure 2.5: Average ΔT (from WMAP W-band data) correlations for the ROSAT X-ray clusters split by redshift: 21 clusters at $z < 0.1$ (left) and 9 at $z > 0.1$ (right). The solid lines show the predicted SZ models based on the parameters of Bonamente et al. (2002).

the possibility that this model may not apply at the large angles covered by the WMAP data. We therefore also show in figure 2.4 the SZ model truncated at $\theta = 2'$ before being convolved with the W-band beam (dashed line). The significance of rejection in this case is reduced to 2.5σ. We note that this is a strict lower limit to this significance limit as it assumes no SZ contribution beyond $2'$.

Although within the Chandra sample there is little evidence of redshift dependence, the fits of SZ models to the WMAP data do appear to deteriorate as we move from the average redshift, $z \approx 0.1$ of the ROSAT sample to $z \approx 0.3$ of the Chandra sample (figure 2.4). We have also noted that at the lowest redshift the WMAP SZ effect is clearly detected at about the predicted amplitude in the Coma cluster (figure 2.7). We therefore returned to the ACO data-set and identified 407 $R \geq 2$, $|b| > 40$deg clusters with measured redshifts. Splitting these at z=0.15 (figure 2.8), we see that there is some evidence confirming that clusters at higher redshift have observed SZ decrements that are significantly smaller than at lower redshift. Although the X-ray properties for the majority of these clusters are unknown, we have fitted the same average model, scaling θ_c to the appropriate average redshift before convolving with the WMAP beam. The fit appears significantly worse for the higher redshift clusters, with a rejection confidence at $\theta < 6.'3$ of $\approx 1\sigma$ for $z < 0.15$ and $\approx 4\sigma$ for $z > 0.15$. We note however that the loss of signal with increasing redshift may simply be the result of the smaller angular sizes of the clusters with increasing redshift and becoming significantly smaller than the instrument beam-size.

2.5 Discussion

The reduced SZ decrements in the WMAP3 data towards the ROSAT cluster sample and the almost lack of detection of the SZ effect in terms of the Bonamente et al. (2006) clusters is paradoxical. The most obvious explanation is that the WMAP data is contaminated by unresolved cluster radio sources within the WMAP beam. However, the contamination from synchrotron radio point sources varies with frequency as $T_\nu \propto \nu^{\alpha-2}$ (where $\alpha \approx 0.7$), whilst the discrepancy in the WMAP3 data for the Bonamente et al. (2006) cluster sample is as large at Ka (33GHz) as at W (94GHz) (see figure 2.6).

Further to this issue, we note that a survey of radio sources in the Chandra clusters has been performed by Coble et al. (2007). They see a population of radio sources with

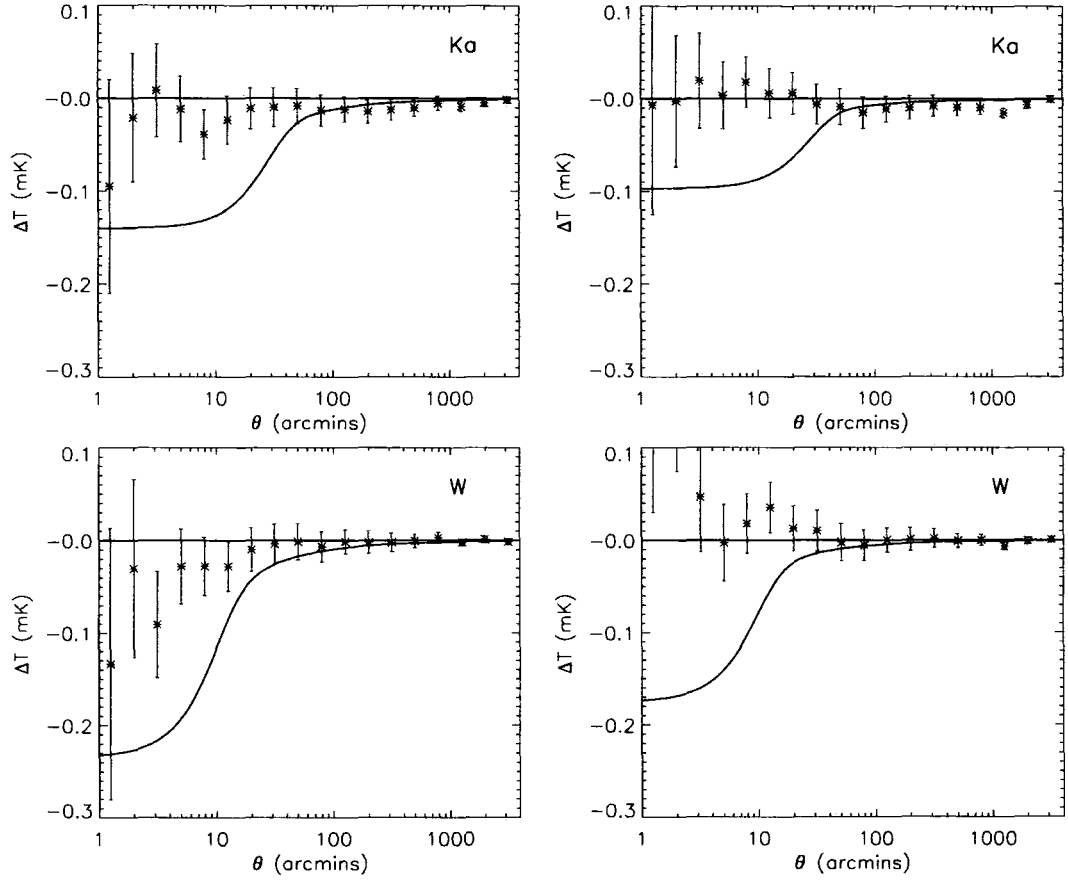

Figure 2.6: Top: Cross-correlations of WMAP Ka-band ΔT data with 20 clusters at $z < 0.3$ (left) and 19 at $z > 0.3$ (right) from the Chandra cluster sample. Bottom: The same for WMAP W-band data. The solid lines show the β models of Bonamente et al. (2006) convolved with the WMAP profiles.

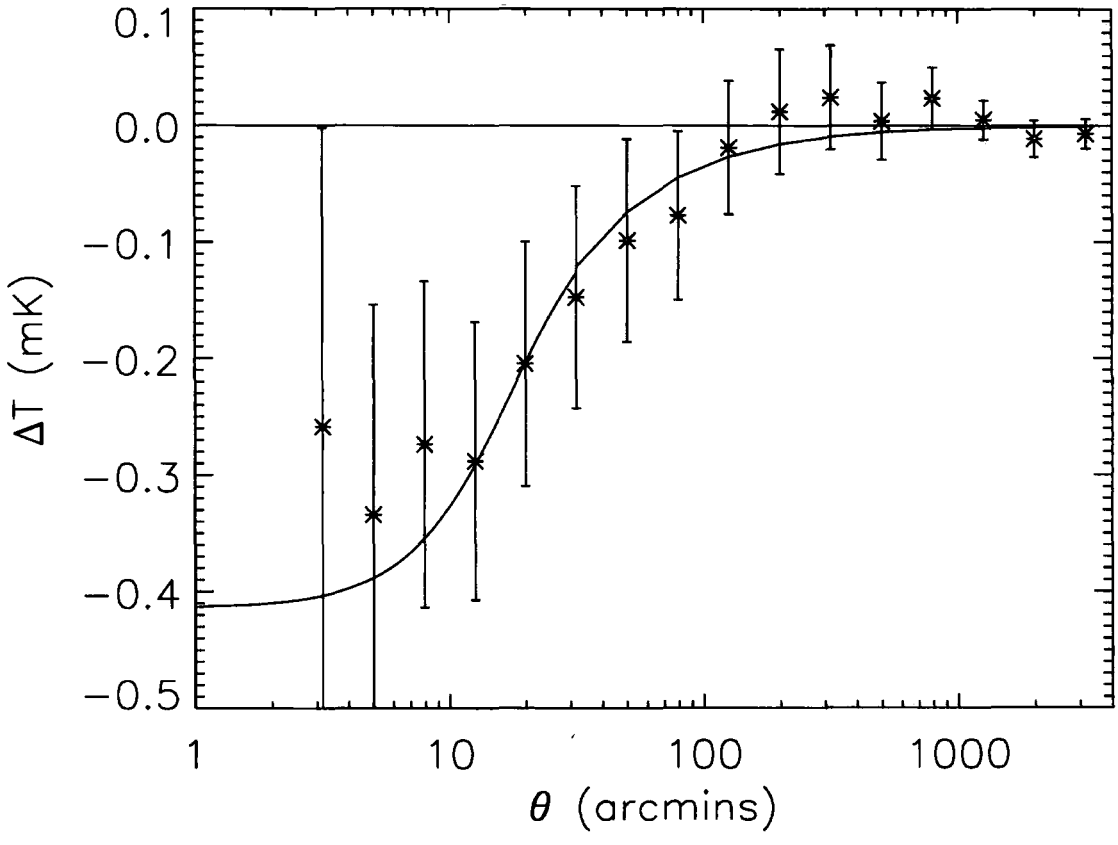

Figure 2.7: Binned ΔT data from the WMAP year-3 W-band data around the Coma cluster. The solid line shows the model predicted from X-ray data (taken from Lieu et al. 2006) convolved with the W-band beam profile.

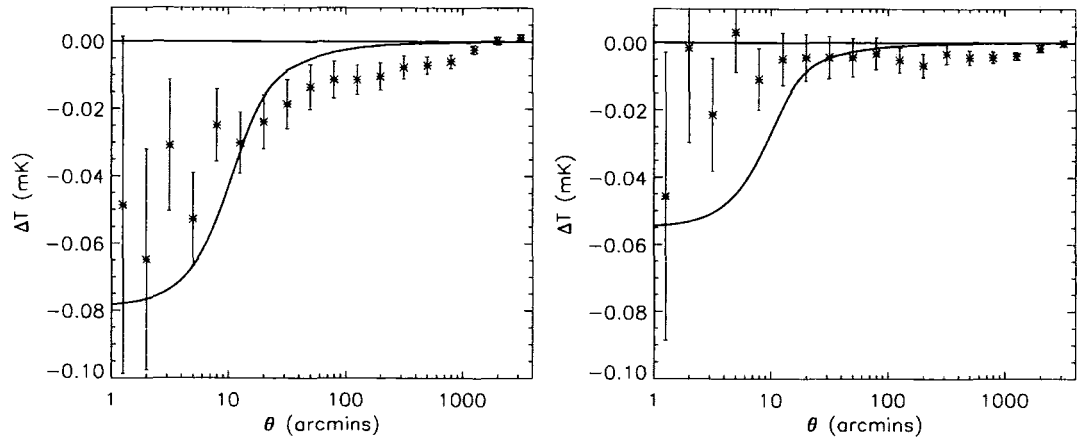

Figure 2.8: Average ΔT (from WMAP W-band data) plots for the data from the Abell cluster catalogue with 172 clusters at $z < 0.15$ (left) and 235 at $z > 0.15$ (right). Only clusters with $|b| \geq 40°$ are included here. Overlaid in both cases is a model with $\Delta T(0) = -0.16mK$, $\beta = 0.7$ and $\theta_c = 9.'8$ scaled to the mean redshift of the samples: $z = 0.1$ and $z = 0.2$. In both cases the model is convolved with the W-band beam profile. This model gives a reasonable fit to the data at $z < 0.15$, but significantly overestimates the $z > 0.15$ data.

a mean flux of $\approx$ 6.2mJy/cluster at 30GHz. Given $S_\nu \propto \nu^{-\alpha}$ with a spectral index of $\alpha \approx 0.7$ (taken from table 3 of Coble et al. 2007) this gives a flux of $\approx$ 3mJy/cluster at the W-band frequency of 90GHz. We note that were the contaminants GHz-peaked spectrum (GPS) radio sources, this value of the index would still be appropriate over this frequency range (Stanghellini et al., 1998). Following Lieu et al. (2006), the equivalent flux required to cause the lack of SZ effect observed in the Chandra clusters can be determined from the Rayleigh-Jeans flux multiplied by the solid angle:

$$S_{SZ} = \frac{2\pi k \Delta T \nu^2}{c^2} \frac{\theta^2}{4} \tag{2.5}$$

Taking $\Delta T = 0.1$mK, $\nu = 90$GHz and $\theta = 10'$, we obtain a flux of $S_{SZ} = 170$mJy. Even taking a value for the spectral index of $\alpha = 0$ for the radio sources (e.g. Bennett et al. 2003), the flux required is over an order of magnitude greater than the observed discrete radio source fluxes from Coble et al. (2007). In addition, Lin & Mohr (2007) make estimates of the contamination from radio point sources and for cluster masses typical of the Chandra sample ($M_{200} \sim 10^{15} M_\odot$, Reiprich & Böhringer 2002), they suggest that up to only 10% of these clusters may be lost due to point source radio contamination (see their figure 15). Although this assumes that there will be no increase in source contamination

with the WMAP beam area, we note that the counts of Coble et al. (2007) are usually lower than predicted by Lin & Mohr (2007, figure 13) and these effects may cancel.

Currently we have no explanation for the strong SZ decrements detected by the interferometric experiments as opposed to the lack of detections by WMAP. At higher resolution it may be more possible to detect the SZ against the noise caused by the primordial CMB fluctuations but our error analysis should take care of such statistical effects and the average model is rejected at the 5.5σ level by the WMAP data. A high value of $H_0 \approx 100\text{kms}^{-1}\text{Mpc}^{-1}$ for the SZ X-ray model might help explain the ROSAT cluster results but an even higher value would be required to explain the Chandra cluster results.

As noted above there may also be evidence that the SZ decrement is too low in the ACO-WMAP1 cross-correlation of Myers et al. (2004), as confirmed by the ACO-WMAP3 cross-correlation in figure 2.1. Myers et al. (2004) noted that the decrement that fitted the ACO $R \geq 2$ clusters with $\beta = 0.75$ was only $\Delta T(0) = 0.083\text{mK}$ compared to the 0.5mK predicted for the $R = 2$ Coma cluster. The WMAP3 data confirms that $\Delta T(0) = 0.5\text{mK}$ is needed to fit the observed Coma SZ decrement (see figure 2.7). In figure 2.1 the SZ models for these two values of the decrement are compared to the WMAP3 W band data for the $R \geq 2$ cluster sample. Both models assume $\beta = 0.75$. We see that while the data is well fitted at $\theta < 10'$ by the $\Delta T(0) = 0.083\text{mK}$ model, the $\Delta T(0) = 0.5\text{mK}$ at least begins to improve the fit at larger scales. One possibility is that, as well as detecting an extended SZ component to the ACO data, we may actually be detecting a lower central SZ amplitude than expected from the X-ray data.

Lieu et al. (2006) discussed other possible explanations for the unexpectedly small SZ decrements detected in the ROSAT sample. For example, Lieu & Quenby (2006) have discussed whether a diffuse cluster synchrotron source could explain the reduced SZ decrement. The main problem here is that non-thermal electrons would not give a good fit to the X-ray data which are usually well fitted by thermal bremsstrahlung, although Lieu & Quenby (2006) also noted that the soft X-ray excess seen in the central regions of some clusters may be indicative of a significant embedded non-thermal X-ray component there.

Fosalba et al. (2003) have discussed whether ISW effect could mask the SZ effect but the ISW effect is at $0.5\mu\text{K}$ and seems too small to mask the SZ effect which in the X-ray clusters can be $10\times$ higher.

There is also the possibility that the SZ decrement has been overestimated by the X-ray modelling. Certainly the Chandra predicted decrements for the 5 clusters in common with the ROSAT sample (A665, A1413, A1689, A1914, A2218) are on average $\approx 80\%$ larger than the predicted decrements from the ROSAT data. Most of this difference arises from A2218 where the ROSAT data imply $\Delta T(0) = -0.27$mK (corrected to 30GHz) and the Chandra data imply $\Delta T(0) = -0.87$mK, a factor 3.2 different. But since Chandra has higher spatial resolution, it is expected to probe the central core of a cluster more accurately and so the Chandra X-ray models might be expected to be more robust than those from the ROSAT data.

While this work was in preparation, Afshordi et al. (2006) used X-ray data of 193 Abell Clusters to search for the SZ decrement from WMAP3 data (see also Afshordi et al. 2005). These authors made a significant detection and also suggested that the size of SZ decrement implied that the cluster hot gas fraction was $32 \pm 10\%$ lower than the baryon fraction in the standard cosmological model. They also suggested that their WMAP results were consistent with the interferometric SZ results for the sample of 38 Chandra clusters analysed above. Note that the approach of Afshordi et al. (2006) is different from that used here in that the X-ray data is mainly used to define a template to detect SZ decrements and then the SZ data and the X-ray temperature data alone are used to establish the gas densities. This route therefore avoids comparing the SZ results with X-ray gas density models on the grounds that the latter depend on assumptions such as that of hydrostatic equilibrium. These authors also do not consider the possibility that the cluster SZ decrements may evolve with redshift.

Finally, if we assume that the WMAP SZ decrements are reliable, even in the case of the 38 Chandra clusters where the unexplained discrepancy persists with the OVRO/BIMA results of Bonamente et al. (2006), we might speculate whether a lower than expected SZ decrement in the higher redshift clusters could be caused by foreground lensing. The indication from WMAP that the higher redshift clusters may have reduced SZ decrements is consistent with the idea that gravitational lensing is having a significant effect on the detection of the SZ effect. Therefore it may be that the groups and clusters out to redshifts in the range $0.2 < z < 0.8$ in the foreground of the targeted Chandra clusters are lensing the cluster centres and smoothing the decrement away. Using CMBFAST we have constructed the lensing smoothing function for CMB scattering at $z = 0.3$ and find

that on the size of the $\approx$ 10 arcmin WMAP beam, the smoothing function is reduced by about a factor of $\approx$ 10 compared to the case where the surface of last scattering is at $z = 1100$. At $z = 0.7$, the factor is ≈ 5. Therefore for the standard model this would make the effect negligible because at z=0.3, $\epsilon = \sigma/\theta \approx 0.004$ and at $z = 0.7$, $\epsilon = \sigma/\theta \approx 0.008$. Only if the mass power spectrum is significantly higher than that for the standard model can this explanation apply. One such case is the high mass power spectrum advocated by Shanks (2006) as a route to modify the first acoustic peak in the CMB. Such a spectrum is motivated by the evidence from QSO lensing that the galaxy distribution is strongly anti-biased ($b \approx 0.1$) at least on $0.1 - 1\mathrm{h}^{-1}$Mpc scales with respect to the mass (Myers et al., 2003, 2005; Mountrichas & Shanks, 2007). However, the balance of other evidence may still argue against such a high amplitude for the mass power-spectrum.

Lensing would clearly also affect the X-ray cluster profiles as well as the SZ decrements. Although these are expected to be smoother than the SZ decrements, it might be expected that the profiles of lower redshift clusters are on average steeper than the profiles of higher redshift clusters. It remains to be seen whether this prediction of the lensing hypothesis can be decoupled from evolution of the cluster gas component. In any case, the flatness of the X-ray profiles towards the centres of many clusters may make this prediction more difficult to test.

2.6 Conclusions

We have confirmed the extended appearance of the SZ decrement in WMAP 3-year data around ACO $R \geq 2$ clusters out to $\theta \approx 30'$, first shown by Myers et al. (2004) using WMAP 1-year data. Further to this, we have confirmed the detection of the SZ decrement in the 3-year data around clusters identified in both the APM survey and 2MASS, showing an increase in detection significance compared to the 1-year data analysis.

We have also confirmed the result of Lieu et al. (2006) that the SZ decrement is somewhat lower than expected on standard model assumptions and ROSAT X-ray profiles for a sample of 31 clusters from Bonamente et al. (2002). We have further shown that even smaller X-ray decrements are seen in the higher-redshift sample of 38 clusters of Bonamente et al. (2006) that has Chandra X-ray data. The reason for the observational discrepancy between the WMAP data and the BIMA/OVRO data of Bonamente et al.

(2006) is not clear. We do not believe that discrete or diffuse cluster radio sources nor the ISW effect is likely to explain the discrepancy. Dividing the ACO clusters into high and low redshift samples also indicates that the deficit in the SZ decrement may increase at higher redshift.

In the light of the above results from our WMAP SZ analysis, we have discussed the possibility that the extended SZ signal detected for ACO and 2MASS clusters may actually be indicating a lack of SZ signal in the centres of clusters rather than an excess at the edges.

On the assumption that the WMAP SZ results are correct, one explanation we have considered is that lensing of the cluster centres by foreground groups and clusters could explain the over-prediction of the observed decrements by SZ models and in particular the apparent tendency for higher redshift clusters to have smaller SZ decrements. However, before considering such interpretations further, we need to clarify if this is a real observational discrepancy between the OVRO/BIMA data and WMAP.

It will clearly be interesting to see if these WMAP results are confirmed in the higher resolution SZ observations made using the Planck surveyor satellite.

CHAPTER 3

PHOTOMETRIC SELECTION OF EMISSION LINE GALAXIES, CLUSTERING ANALYSIS AND A SEARCH FOR THE ISW EFFECT

3.1 Introduction

Imaging surveys are in the process of mapping out a vast region of the Universe over a large range of the electromagnetic spectrum. The recent pace-setter in recent years is the Sloan Digital Sky Survey (SDSS), which now provides (as of DR6) photometric data for approximately 230 million distinct sources over an area of $8240 deg^2$. Current and future wide and deep field surveys such as VLT VISTA, VST ALTAS, SWIRE, CFHTLS and the SDSS itself will continue to add to the mapping of the Universe around us presenting a massive amount of data at a variety of wavelengths. Given this enormous effort in the collection of photometric data, and the expense of subsequent spectroscopic surveys, the filtering of galaxies by type and redshift via their photometric properties is a vital and powerful tool for the effective use of the large quantities of photometric data available to us. Selecting distinct galaxy populations in this way offers a relatively cheap route to large galaxy and QSO surveys, either through using the photometric redshifts themselves or by using photometric constraints to select specific galaxy populations for subsequent spectroscopic surveys.

In this Chapter, I discuss photometric constraints for selecting emission line galaxies in three redshift ranges at $z < 1$. COMBO-17 photometric redshift data is used in combination with SDSS data to perform a calibration of these photometric selections (section 3.2). Calibration of the highest redshift sample ($z \approx 0.7$) has been performed at the AAT and this is reviewed in section 3.3. In section 3.4 I evaluate the clustering properties of the galaxy populations contained in the photometric selections using SDSS data. The full samples of galaxies selected from the SDSS is then used to perform a search for the ISW effect in WMAP 5yr data (section 3.5).

3.2 Photometric Selection

3.2.1 Data & Selection

The aim of this work is to develop a set of photometric selection criteria using the SLOAN filter bands alone to isolate emission line galaxies in 3 separate redshift ranges. The target redshift ranges are approximately $z < 0.4$, $0.4 < z < 0.6$ and $z > 0.6$. At these redshifts, the 4000Å break is a key feature in the observed optical spectra of both red and blue galaxies as it moves through the g and r SLOAN filters with increasing redshift. In ELGs however, the break is somewhat weaker than in the spectra of LRGs, whilst the continuum at wavelengths greater than 4000Å remains lower compared to the LRG spectrum due to the dominance of young blue stars in the ELGs. These contrasts in the spectra of LRGs and ELGs inherently allow the separation of the two in colour space, whilst simultaneously facilitating photometric selection of galaxies at different redshifts.

With this in mind we have used the Bruzual and Charlot stellar population synthesis code (Bruzual & Charlot, 2003) to model the evolution of a typical emission line galaxy in the gri (AB) colour plane. We used a Salpeter IMF with a galaxy formed at $z = 6.2$ (i.e. with an age of 12.6Gyr at $z = 0$) and a $\tau = 9$Gyr exponential SFR. The resultant gri colour evolution track from $z = 1.2$ to $z = 0$ is shown in figure 3.1 (dashed black line). Here we see a clear evolution in the gri colour space around which we may build a selection regime for identifying candidates in our desired redshift ranges. We also plot a track (dot-dash line) for an elliptical galaxy using a $\tau = 1$Gyr exponential SFR and a redshift of formation of z=10 (with Solar metallicity and Salpeter IMF).

We note that the SSP models used do not account for thermally pulsing asymptotic giant branch (TP-AGB) stellar populations included in more recent models (for example Maraston 2005 and Bruzual 2007). However, given the age of galaxy we are modeling, the contribution from TP-AGB stars, which peaks in activity at ages of $t \lesssim 2Gyr$, is unlikely to be significant in our population.

We calibrate our selections using the photometric redshift data published by the COMBO-17 team (Wolf et al., 2003; Simon et al., 2008). The data we use is from the COMBO-17 S11 field, which covers an area of $0.5° \times 0.5°$ centred at 11h 42m 58s, -01 42′ 50″ (J2000) and the entirety of which is covered by SDSS imaging. This data provides accurate ($\delta z/(1+z) = 0.02$) photometric redshifts for a total of 7248 galaxies based on

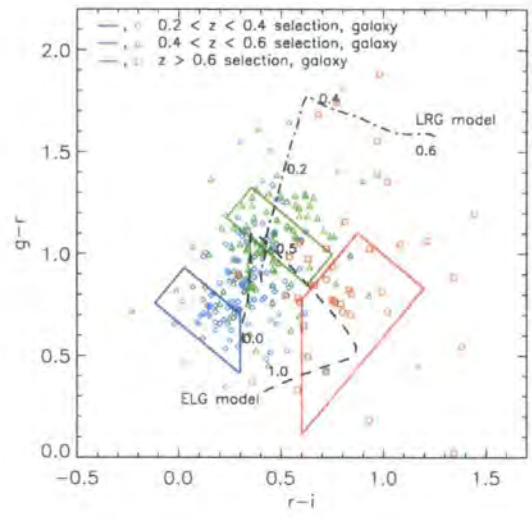

Figure 3.1: Galaxies in the COMBO-17 S11 field plotted in the gri (AB) colour plane using SDSS magnitudes. The cyan diamonds, green triangles and red squares show galaxies with photometric redshifts in the ranges $0.2 < z < 0.4$, $0.4 < z < 0.6$ and $z > 0.6$ respectively. The labelled black tracks show the evolution of an emission line and an elliptical galaxy based on a Salpeter model, from $z = 1.2$ to $z = 0$. Our photometric selections are marked by the solid blue, green and red lines for our low-, mid- and hi-redshift bins.

Table 3.1: Selection criteria chosen to identify galaxies in our three redshift ranges: $0.2 < z < 0.4$, $0.4 < z < 0.6$ and $0.6 < z < 1.0$. These are illustrated in the ugr colour plane in figure 3.1.

Low-z	Mid-z	Hi-z
$19.0 < i < 20.0$	$19.0 < i < 20.2$	$19.5 < i < 20.5$
$r - i < 0.3$	$g - r > 1.2(r - i) + 0.1$	$r - i > 0.5$
$g - r < 1.2(r - i) + 0.9$	$g - r < 1.2(r - i) + 0.9$	$g - r < 1.2(r - i) + 0.06$
$g - r > -1.2(r - i) + 0.75$	$g - r > -1.2(r - i) + 1.65$	$g - r > 1.2(r - i) - 0.6$
$g - r < -1.2(r - i) + 1.3$	$g - r < -1.2(r - i) + 1.95$	$g - r < -1.2(r - i) + 2.2$
	$r - i > -(i - z) + 0.5$	
	$-2.0 < u - g < 1.0$	
	$i - z > 0.55$	

broad and narrow band imaging using 17 different optical and near-infrared filters. We match the positions of COMBO-17 galaxies to the equivalent objects in the SDSS data, thus combining the SDSS ugriz magnitudes with the COMBO-17 photometric redshifts. The S11 objects are plotted in the (SDSS) gri colour plane in figure 3.1. For the purposes of clarity, we only plot those galaxies classed as blue spirals by the COMBO-17 team in this plot, however the presence of red-sequence galaxies is indicated by the LRG evolution track (dot-dash line). The COMBO-17 galaxies have been split into three populations for the purposes of this plot based on their assigned photometric redshift from COMBO-17: $0.2 < z < 0.4$ (blue diamonds), $0.4 < z < 0.6$ (green triangles) and $0.6 < z < 1.0$ (red squares).

Based on the distribution of the photometric redshifts and the ELG evolution track presented in the above plot, there is a clear progression in the gri colour plane based on ELG redshift. Further to this, areas of the plot can be isolated that should minimize the number of red-sequence galaxies, whilst maximizing the numbers of either z<0.4 or z>0.6 ELGs. The medium redshift range does however present significant problems. The ELG evolution track appears to pass through a region populated by both lower and higher redshift ELGs as well as low-redshift red-sequence galaxies in the 0.4<z<0.6 range.

From the above observations we construct three sets of colour cuts to preferentially select three redshift ranges. These are shown in figure 3.1 by the solid blue box (low redshift cut), green box (medium redshift cut) and red box (high redshift cut). As discussed above, the mid-z range is significantly exposed to contamination from both ELGs at unwanted redshifts and red-sequence galaxies. To minimize the numbers of these we have therefore added colour cuts to this sample based on the $r-i$, $i-z$ and $u-g$ colours of the selected galaxies. These additional cuts have also been calibrated using the COMBO-17 photometric redshifts. The forms of our three selections, including the additional mid-redshift colour cuts, are given explicitly in table 3.1. These cuts have been tailored to produce sky densities of candidates of $\approx 100 deg^{-2}$ in order to provide candidate numbers suitable for wide field spectroscopic surveys performed with instruments such as the 2dF/AAOmega spectrograph.

The photometric redshift distribution for our three samples are shown in figure 3.2. This plot includes all the selected galaxies from the S11 field, including those identified as being part of the red-sequence (these making up $\approx 4\%$ of the total selected across all

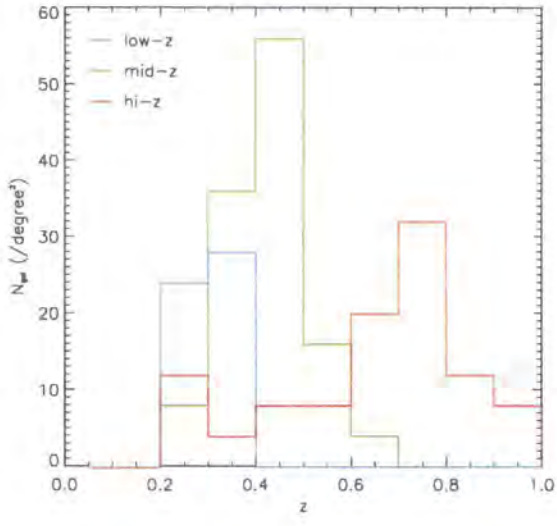

Figure 3.2: Redshift distributions of our three photometric selections based on photometric redshifts from the COMBO-17 data in the S11 field. The three samples give mean redshifts of $\bar{z}_{lo} = 0.29 \pm 0.05$ (blue histogram), $\bar{z}_{mid} = 0.44 \pm 0.08$ (green histogram) and $\bar{z}_{hi} = 0.65 \pm 0.21$. (red histogram)

three selections). The three selections are characterised by mean redshifts of $\bar{z}_{low} = 0.29$, $\bar{z}_{mid} = 0.44$ and $\bar{z}_{hi} = 0.65$, with standard deviations of $\sigma_{low} = 0.05$, $\sigma_{mid} = 0.08$ and $\sigma_{hi} = 0.21$.

For the purposes of this work we now use our three selections to create three datasets from the SDSS galaxy catalogue. We apply the selections to the SDSS DR6 data release taking our data from the PhotObjAll table. Aside from the colour-magnitude criteria given in table 3.1, we reject objects which do not meet the following criteria:

- $TYPE = 3$ (i.e. classed as a galaxy);
- $NCHILD = 0$;
- Flagged as BINNED1, BINNED2 and BINNED3;
- $90° < R.A. < 270°$.

We also limit our selection to the main SDSS region, rejecting stripes 40-43. Stripe 26 is also rejected as this appears to show some contamination and spurious density fluctuations. The photometric selections are performed using the SDSS model magnitudes with the appropriate extinction values subtracted. The total numbers of candidates given

by each selection are 892,528, 620,020 and 734,566 for the low-, mid- and hi-z selections respectively. These numbers give sky densities of $103deg^{-2}$, $71.9deg^{-2}$ and $85.1deg^{-2}$.

3.3 Spectroscopic Calibration

3.3.1 Overview

An important element of this work is the calibration of the photometric selection samples with spectroscopic observations to confirm the achievable redshift distribution of our selections. To this end, we have performed spectroscopic observations of our $z \approx 0.7$ sample using the AAOmega spectrograph at the AAT. AAOmega is a fibre-fed spectrograph, which allows the simultaneous observations of up to $\approx$ 360 objects in a circular field of view of diameter 2°.

3.3.2 Observations

Observations were taken during a 5-night run on the AAOmega instrument at the Anglo-Australian Observatory (AAO) in March 2006. The telescope was configured using the 5700Å dichroic, with the 580V grating mounted in the blue-arm and the 385R grating in the red-arm. The 580V grating gives a wavelength coverage of 370nm to 580nm, with a pixel size of 0.1nm/pixel and the 385R a coverage of 560nm to 880nm, with a pixel size of 0.16nm/pixel. Both provide a resolution of 1300. In total, the AAOmega offers 400 fibres per observation, however a significant number of these were at times used for other projects (e.g. Ross et al. 2008), were locked to guide-stars, sky-targets or simply malfunctioning and so our target numbers range from ~50-230 per observation. We targeted four 2° fields with multiple exposures of 1200s each. The observations are summarised in table 3.2.

Target objects were selected using our selection criteria applied to the SDSS data available for each of the fields. Over the course of the 5 nights, seeing ranged from $\sim 1.5'' - 3.0''$, with a mean of $\sim 2.0''$. All observations were flat fielded, arc calibrated and combined using the AAO's 2dFDR tool. Approximately 20% of fibres were affected by an early instrumentation problem known as fringing, which led to an almost sinusoidal signal in the output. In the S11 field this affected 27 of the fibres targeted on ELG candidates. A further problem, is encountered due to the strong sky emission lines above $\approx$ 8000Å. These limit the identification of Hβ and OIII above $z \approx 0.65 - 0.7$, however they do not

Table 3.2: Co-ordinates of the four fields targeted with the number of gri selected ELG candidates in each 2-degree field.

Field	COSMOS	δ05	ϵ04	S11
R.A.	150.118	200.399	221.899	175.741
Declination	+2.2052	-0.2124	-0.2141	-1.7159
Exposure time	3×1200s	3×1200s	4×1200s	3×1200s
Seeing	$\approx 3.0''$	$\approx 2.0''$	$\approx 2.5''$	$\approx 1.6''$
Candidates	378	329	343	391
Targeted	217	45	225	219
ELGs	44	10	84	142

interrupt identification of OII at $z < 1$ and so the impact of the sky lines is limited.

3.3.3 Galaxy redshifts

We use the AAT software AUTOZ and ZCODE to search for emission features with which to identify galaxies in our observed sample and determine redshifts. AUTOZ performs an initial identification of each spectrum, fitting absorption and emission features. Each fibre spectrum was then evaluated by eye to assign a redshift and quality rating, q_{op} (which ranges from 0 to 5 depending on the confidence of the identification). Only objects with $q_{op} \geq 3$ were accepted as positive identifications.

Examples of the spectra obtained with the AAOmega instrument are provided in figure 3.5. The spectra are all binned to a bin-width of $\approx$ 10Å and key emission and absorption features are marked. We also show the unbinned data for the OII feature (insets), where it is evident that the doublet nature of the feature is marginally detectable at the observed resolution. Although data were obtained on both the blue and red arms, only spectra from the red arm are plotted here as there are few features useful for identification in the blue wavelength range given the signal to noise of our data. The key emission features that facilitate the identification of these galaxies with short exposure times, i.e. OII, Hβ and the OIII doublet are all evident in these spectra.

A summary of the numbers of emission line galaxies identified in our four fields is provided in table 3.2. Our most successful field was the COMBO-17 S11 field in which we were able to target 219 ELG candidates in seeing conditions of $\approx 1.6''$. In this field

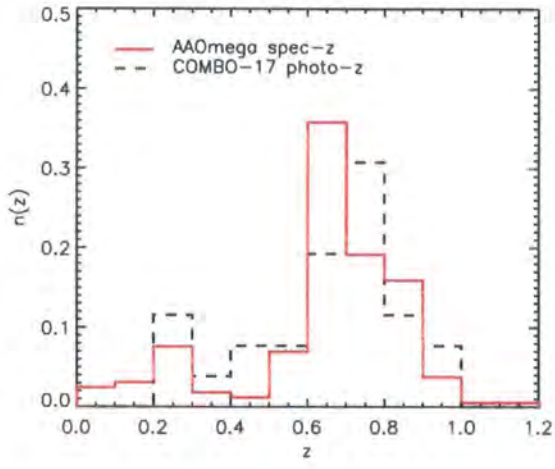

Figure 3.3: Redshift distributions of the spectroscopically identified emission line galaxies from the four fields targeted with AAOmega (red line) compared to the original photometric redshift distribution obtained with the COMBO-17 photo-z data in the S11 field. The spectroscopic sample contains 280 confirmed galaxies and the two distributions are normalised by the total numbers in each.

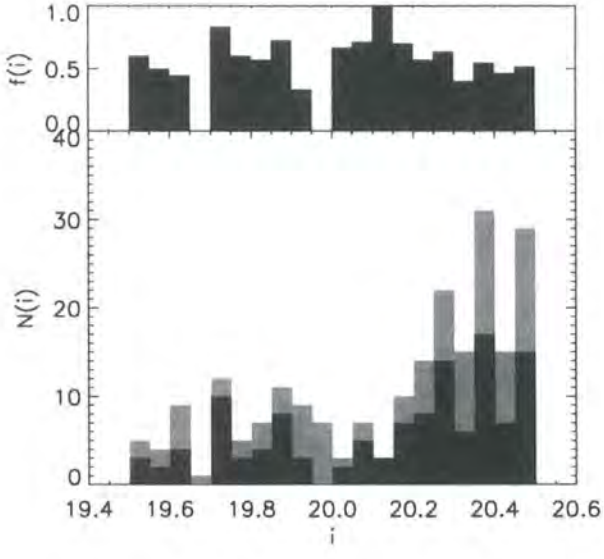

Figure 3.4: Number counts of objects observed as a function of SDSS i-band magnitude. The dark histogram shows counts of objects identified with emission lines (N_{em}), whilst the pale histogram shows the total number of objects (N_T) observed in each magnitude bin. The top panel shows the fraction N_{em}/N_T as a function of i-band magnitude. Data are only shown from the S11 field as all other fields were limited by adverse seeing.

we identified 121 of the 219 candidates as being emission line galaxies from their emission lines with a confidence of $q_{op} \geq 3$. In total we were able to identify 311 emission line galaxies over a combined area of 12.4 deg^2, giving an average sky density of 25 deg^{-2}. However, three of the observed fields suffered poor seeing conditions of $\geq 2.0''$, limiting our ability to successfully identify objects in these fields. At worst, completeness was reduced to $< 25\%$ in the COSMOS field due to the seeing of $\approx 3.0''$. However, in the more reasonable observing conditions encountered with the observations in the S11 field (where the seeing was $1.6''$) we find that the identification rate is a more promising $\sim 65\%$, with a sky density of $\approx 40 deg^{-2}$.

Figure 3.3 gives the redshift distribution of the spectroscopically confirmed galaxies in the S11 field. The plot incorporates all galaxies identified in the S11 field and the original photometric redshift distribution from COMBO-17 data (black dashed line) also from the S11 field. Our spectroscopic sample follows the expected distribution closely, with $\bar{z}_{spec} = 0.66 \pm 0.23$ (compared to $\bar{z}_{phot} = 0.65 \pm 0.21$). There is some contamination from lower redshift (i.e. z< 0.5) galaxies and in the spectroscopic sample this is at a level of $\approx 18\%$ (compared to a level of $\approx 23\%$ obtained with the COMBO-17 photometric redshift sample).

Figure 3.4 shows identifications as a function of source magnitude in the S11 field. The lower panel shows number counts of spectroscopically confirmed galaxies exhibiting emission lines (N_{em}, dark bars) and of all objects targeted with AAOmega fibres (N_T, pale bars), whilst the upper panel shows the fraction, N_{em}/N_T. The consistency of the 65% identification rate across our magnitude range is evident and we are clearly reaching the $r = 20.5$ magnitude limit successfully. A small fall-off in the fraction of ELGs identified is observed in the fainter magnitude bins, however numbers still remain high.

In figure 3.6, we compare our spectroscopically determined redshifts against the COMBO-17 photometric redshifts for those galaxies lying in the central $0.5° \times 0.5°$ region covered by the COMBO-17 data. The vertical error bars represent the $\sigma_z \sim 0.03$ error quoted by the COMBO-17 team for the photometric redshifts. We find a total of 24 objects that have both COMBO-17 photometric redshifts and spectroscopic redshifts from this work. Overall there appears to be good agreement between the data with just 4 outliers (taken here as a difference between the photometric and spectroscopic results of $3\sigma_z$) having significantly different redshifts. The spectra for all four of these objects are given in figure 3.5

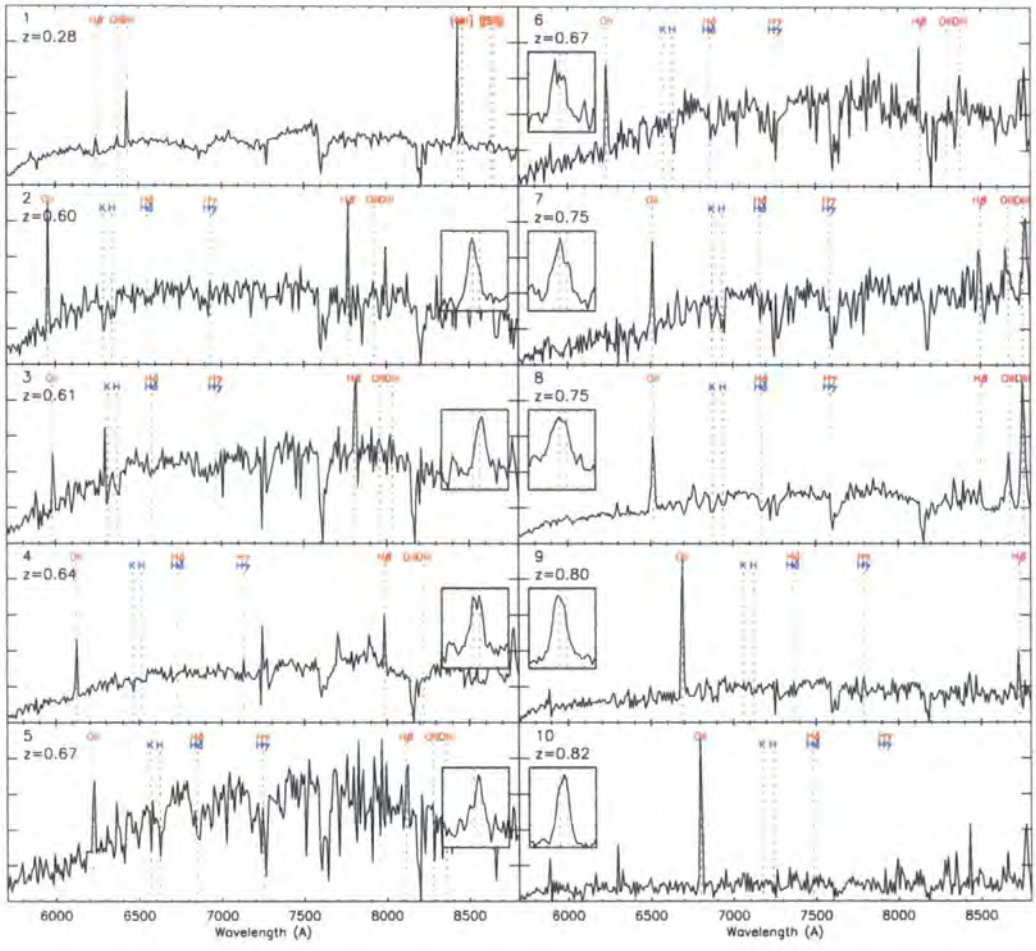

Figure 3.5: Example spectra taken on the AAOmega spectrograph with the 385R grism, binned to 10Å bins. Wavelengths of galaxy emission and absorption features are marked, however the features of key use in identification were the OII, Hβ and OIII doublet emission lines. The insets each show the OII feature in close-up and unbinned, showing the doublet nature of the OII feature to be marginally discernible given the resolution of the spectrograph. The red dashed-lines show the expected positions of the doublet peaks at rest-wavelengths of 3726Å and 3729Å.

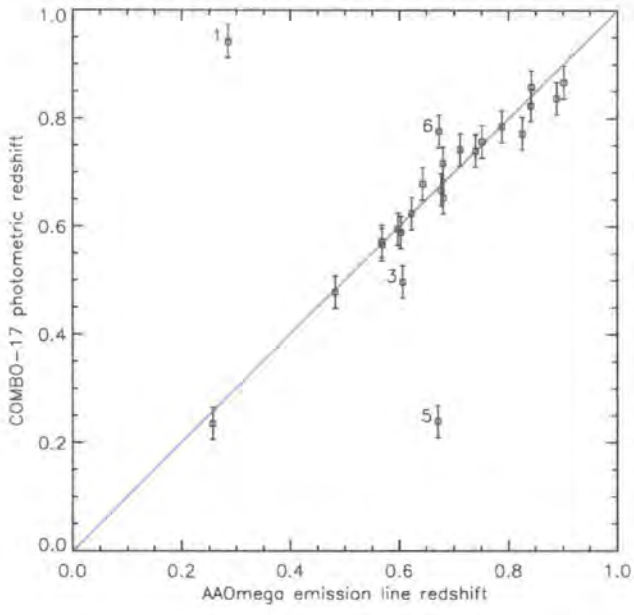

Figure 3.6: Comparison of the spectroscopic redshifts of 24 galaxies in the central $0.5° \times 0.5°$ of the S11 field with photometric redshifts from the COMBO-17 survey. The error bars show the $\sigma_z \sim 0.03$ error quoted by the COMBO-17 team for their photometric redshifts. The four numbered points (1, 3, 5 and 6) are objects in which the photometric and spectroscopic redshifts disagree by more than $3\sigma_z$ (the numbers refer to the spectrum numbers from figure 3.5).

and each of the outliers are marked in figure 3.6 by the spectrum number (1, 3, 5 and 6) from figure 3.5. We find a mean offset between the spectroscopic and photometric redshifts of $\Delta z = 0.01 \pm 0.04$ (after excluding points 1 and 5).

Now looking at the properties of the galaxy spectra, we measure the equivalent widths of the nebular emission lines by fitting Gaussian curves to the OII 3727Å, Hβ and OIII 5007Å lines. We were able to measure equivalent widths with confidence for OII 3727Å, Hβ and OIII 5007Å in 109, 53 and 51 of the galaxies in our sample respectively. From these we determined mean widths of 23.0Å, 8.12Å and 8.98Å for OII 3727Å, Hβ and OIII 5007Å respectively. These mean equivalent widths are broadly consistent with other measurements of emission lines in late-type galaxies (e.g. Kennicutt 1992; Shi et al. 2006). In 27 of these galaxies we were able to measure all three of the above nebular emission lines with confidence and have attempted to evaluate the presence of AGN in our sample using the "blue diagnostic" constraints of Lamareille et al. (2004), which are based on

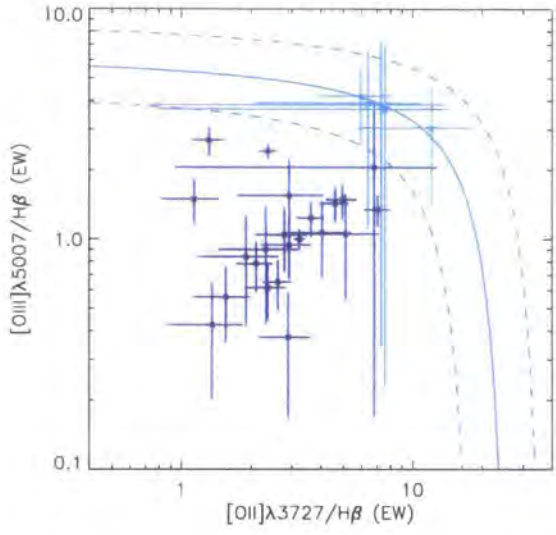

Figure 3.7: "Blue diagnostic" diagram based on Lamareille et al. (2004). Line ratios are plotted for the sub-sample of our spectroscopically observed sample for which we have equivalent widths for the [OII]λ3727, Hβ and [OIII]λ5007 nebular emission lines. The solid line marks the limit estimated by Lamareille et al. (2004) between star-forming galaxies and AGN and the dashed lines show the region of uncertainty. In total 22 objects lie within the star-forming region of the diagnostic plot and are marked by filled blue circles. A further 5 lie within the overlap region (cyan stars) and none of the objects lie within the AGN region.

the [OII]λ3727/Hβ and [OIII]λ5007/Hβ line ratios. This is shown in figure 3.7, where the solid line marks the estimated division between AGN (above) and star-forming galaxies (below). The dashed lines mark the region of uncertainty between the two populations. In all, 22 of this sub-sample fall within the star-forming galaxy region, whilst the remaining 5 (2 of which have large uncertainties) fall within the uncertain region and none lie in the AGN region. Within the reliability of the blue diagnostic diagram, we can say that our sample is dominated by star-forming galaxies and this method shows no positive evidence for any AGN contamination of our sample although there are a small number of borderline cases.

Figure 3.8 shows a composite spectrum of all of the confirmed emission line galaxies over all redshifts, with significant emission and absorption features labelled. The key emission lines used in our spectral identification (i.e. OII, Hβ and OIII) are clearly evident. We also see the Balmer absorption features red-wards of the OII emission, whilst the weak

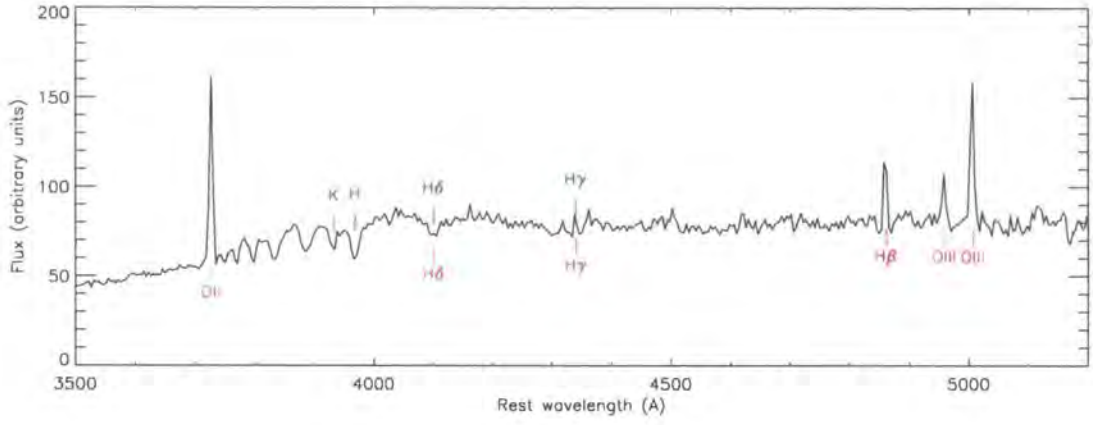

Figure 3.8: Composite spectrum of the 280 successfully identified emission line galaxies. The key emission line features used for identification are clearly visible: OII, Hβ and OIII, whilst absorption features which are difficult to observe in individual spectra are now evident.

ELG 4000Åbreak is also apparent in this composite.

Looking at our selection in detail, we show in figure 3.9 the distribution of spectroscopically confirmed $z > 0.5$ ELGs (blue squares), $z < 0.5$ ELGs (red triangles) and objects with no emission lines (red crosses) in the g-r vs r-i colour plane. It is evident that the $z > 0.5$ emission line galaxies are reasonably evenly spread in the g-r vs r-i colour plane as are the objects without any discernible emission. Finally, the $z < 0.5$ emission line galaxies appear to be biased towards the upper left limits of the selection region, towards the low-redshift main sequence. These may be further reduced by shifting the limit slightly, however this would also remove several $z > 0.5$ objects at the same time. The model evolution track from figure 3.1 is again plotted for reference.

3.4 Clustering

3.4.1 Angular Correlation Function

We now evaluate the angular correlation function for a sample of galaxies selected based on our three photometric selections. The datasets taken from SDSS DR6, as described in the previous section, are used for this purpose. We calculate the angular-correlation function of the samples using the estimator:

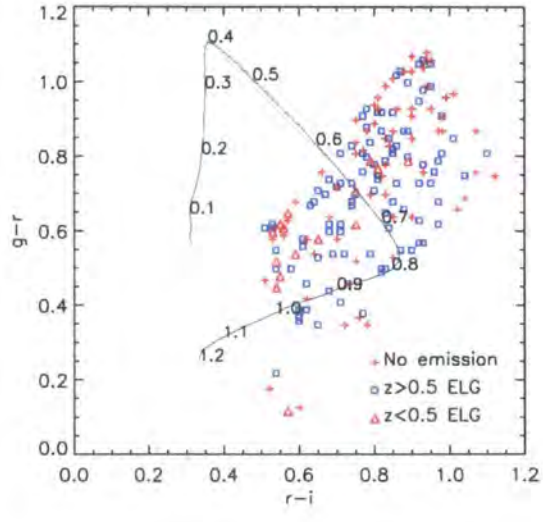

Figure 3.9: Spectroscopic results from the S11 and ϵ04 fields. We show objects identified as $z \geq 0.5$ emission line galaxies (blue squares), $z \leq 0.5$ emission line galaxies (red triangles) and objects with no detectable emission lines (red crosses). The same evolution track as plotted in figure 3.1 is also plotted. We find little variation in numbers of contaminants across our selection range, except for a slight increase in the numbers of $z \leq 0.5$ galaxies in the region given by $g - r > 0.55$ and $r - i < 0.6$ (i.e. closest to the low-redshift segment of the model evolution track).

$$w(\theta) = \frac{n_R}{n_D}\frac{DD}{DR} - 1 \tag{3.1}$$

where DD and n_D are the numbers of galaxy-galaxy pairs and the total number of galaxies respectively. For these calculations we use a random catalogue which exactly matches the coverage of our SDSS galaxy samples and with a factor of 20 more random points than galaxies in each of our galaxy samples. The total number of random points is given by n_R and DR is simply the number of galaxy-random pairs. Statistical errors are estimated using field-to-field errors, using 16 separate fields within our complete field. Our results for the three photometric samples are shown in figure 3.10 where the blue triangles, green squares and red crosses show the low, mid and high redshift samples respectively. For comparison we also plot $w(\theta)$ for a photometrically selected LRG sample from SDSS data at $z \approx 0.7$ (Sawangwit et al., 2009). The clustering amplitude of all three of our samples is significantly lower than the LRG amplitude.

Given that these samples are broad photometric samples (and based on the photometric analysis discussed earlier), we would expect some level of contamination from other galaxy populations such as red sequence galaxies or other galaxies outside of our targeted redshift ranges. The effect of either the highly clustered LRGs or lower redshift galaxies would act to increase the measured clustering signal. Conversely, the inclusion of higher redshift galaxies may cause a reduction in the measured clustering strength. This ultimately makes spectroscopic confirmation of subsets of the complete samples an important aspect of confirming these clustering measurements.

From these measurements of the angular correlation function, we now estimate the 2-point correlation function (2PCF, $\xi(r)$) using Limber's formula. We make an estimate of $\xi(r)$ for each of the samples using a double power-law with a central break, i.e. $\xi(< r_b) = (\frac{r}{r_{0,1}})^{-\gamma_1}$ and $\xi(> r_b) = (\frac{r}{r_{0,2}})^{-\gamma_2}$. This is then combined with our best estimate of the redshift distribution based on the COMBO-17 photometric redshift data (figure 3.2) to calculate the resultant $w(\theta)$ with Limber's formula. A full treatment of this calculation is given by Phillipps et al. (1978). We then perform a χ^2 fitting, in the range $2' < \theta < 20'$ to our data. The best fitting models are plotted with the data in figure 3.10, whilst the associated parameters are listed in table 3.3. We find reasonable fits to both the low- and mid-redshift samples, the low-redshift sample being well fitted by a double power law with a break at $0.5h^{-1}Mpc$ and the mid-redshift sample by just a single power-law. We note

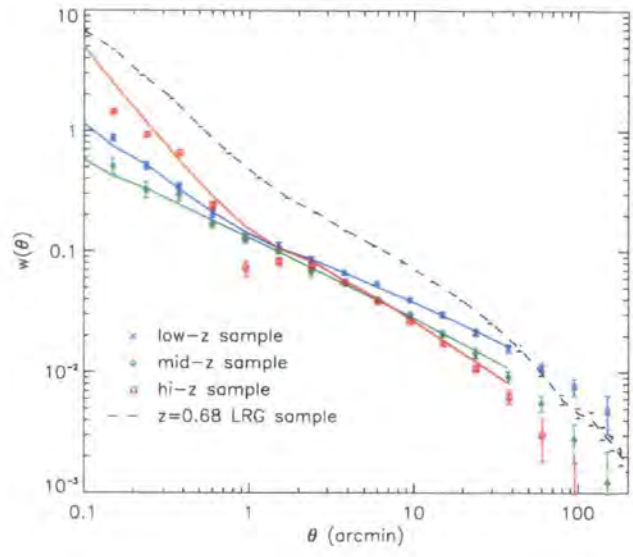

Figure 3.10: The angular correlation functions, $w(\theta)$ for our three photometric redshift selections. Blue crosses, green diamonds and red squares represent the low- ($z < 0.4$), mid- ($0.4 < z < 0.6$) and high-redshift ($z > 0.6$) samples respectively. The best fitting single or double power law models are plotted through each set of data. The dashed black line shows the $w(\theta)$ of Sawangwit et al. (2009) for their sample of photometrically selected Luminous Red Galaxies at $z = 0.68 \pm 0.1$.

Table 3.3: Comoving correlation lengths, r_0 and power-law slopes, γ, for the double power-law model used to provide fits to the angular correlation functions for each redshift selection.

z	r_b (h^{-1}Mpc)	$r_0(< r_b)$ (h^{-1}Mpc)	$\gamma(< r_b)$	$r_0(> r_b)$ (h^{-1}Mpc)	$\gamma(> r_b)$	b
0.29 ± 0.05	0.5	$1.30^{+0.02}_{-0.03}$	$2.21^{+0.02}_{-0.01}$	$2.65^{+0.05}_{-0.08}$	$1.54^{+0.02}_{-0.02}$	0.70
0.44 ± 0.08	n/a	n/a	n/a	$3.62^{+0.06}_{-0.06}$	$1.65^{+0.01}_{-0.01}$	0.92
0.65 ± 0.21	0.5	$2.30^{+0.05}_{-0.05}$	$2.72^{+0.01}_{-0.01}$	$5.88^{+0.12}_{-0.12}$	$1.83^{+0.03}_{-0.01}$	1.46

however, that we struggle to fit to the high-redshift sample with either a double or single power law. This is largely due to strong deviations from a simple power law trend at separations of $< 2'$. This results in large χ^2 values for our attempts to fit the correlation function at in this range. The angular correlation function does however return to a simple power law at separations of $2' < \theta < 20'$ where we are able to provide a reasonable power-law fit using the Limber method.

From our estimates of $\xi(r)$, we now go on to estimate the bias of each sample. The biasing parameter, b, quantifies the relative clustering of a given galaxy population compared to the underlying dark matter distribution (Tegmark & Peebles, 1998). This can be

expressed as the following:

$$\xi_{gal}(r) = b^2 \xi_{DM}(r) \tag{3.2}$$

Here, $\xi_{gal}(r)$ is the 2PCF of the galaxy sample and $\xi_{DM}(r)$ is the 2PCF of dark matter at the same epoch. We determine the dark matter correlation function by first using the CAMB (Code for Anisotropies in the Microwave Background, Lewis et al. 2000) software to estimate the DM power spectrum at the mean redshifts of each of our galaxy samples. The power spectrum is calculated using the HALOFIT model (Smith et al., 2003) to fit non-linear features, at each of the mean redshifts of our samples. With the DM power spectra calculated at each redshift we then simply calculate the corresponding 2PCFs via the Fourier transform:

$$\xi_{DM}(r) = 4\pi \int_0^\infty k^2 P(k) \frac{sin(kr)}{kr} dk \tag{3.3}$$

We estimate the bias parameter using the volume averaged correlation function $\bar{\xi}(x)$ evaluated to a limit of $x = 20h^{-1}Mpc$. This scale limit and the use of the volume averaged form as opposed to the correlation functions themselves is aimed at minimizing the contribution of non-linear effects on our estimate of the bias of the galaxy populations (following the examples of da Ângela et al. 2005b and Ross et al. 2007). Thus the biasing parameter can be estimated using:

$$b^2 = \frac{\bar{\xi}_{gal}(20)}{\bar{\xi}_{DM}(20)} \tag{3.4}$$

Where $\bar{\xi}(x)$ is given by:

$$\bar{\xi}(x) = \int_0^x r^2 \xi(r) dr \tag{3.5}$$

We show $\bar{\xi}(20)$ for each of our three redshift samples in figure 3.11 (denoted by the stars). Based on the redshift and apparent magnitude distributions of our three samples, we estimate absolute magnitude ranges of $M_{b_j} - 5log_{10}(h) = -19.9 \pm 0.3$, -20.0 ± 0.3 and -20.9 ± 0.4 for the low, mid and high redshift samples respectively. These estimates include K+e corrections based on the $\tau = 9$Gyr SFR model.

For comparison we also plot $\bar{\xi}(20)$ for the 2dFGRS late type galaxy samples of Norberg et al. (2002). These are split into absolute magnitude bins of $-18 < M_{bj} - 5log_{10}(h) < -19$,

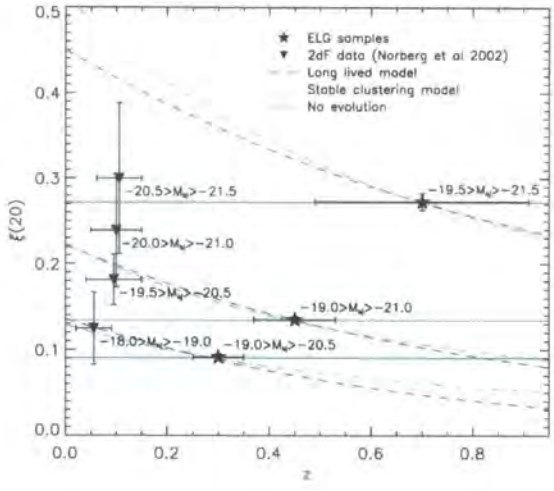

Figure 3.11: $\bar{\xi}(20)$ plotted versus redshift for each of our three photometric samples (stars). Also plotted is the $\bar{\xi}(20)$ for late type galaxies from the 2dFGRS from Norberg et al. (2002), split by absolute magnitude (triangles). The dashed cyan lines show the long-lived model normalised to the ELG data-points, whilst the blue dash-dot lines show the stable clustering model also normalized to the ELG data. The solid green lines project the clustering of each population with no evolution.

$-19 < M_{bj} - 5log_{10}(h) < -20$, $-20 < M_{bj} - 5log_{10}(h) < -21$ and $-20.5 < M_{bj} - 5log_{10}(h) < -21.5$ and are calculated based on the correlation parameters given in their table 3.3. Overall we find the clustering of our three samples is comparable to that of the 2dF late-type galaxy datasets at equivalent magnitude ranges.

As an illustration of how we may expect the clustering of the samples to evolve with time, I also plot in figure 3.11 three simple clustering evolution models: the long-lived model (dashed blue lines), stable clustering (dot-dashed cyan lines) and no evolution of the comoving-space clustering (solid green lines). All three models have been normalised to each of the ELG clustering amplitudes.

The long-lived model is equivalent to assuming that the galaxies have ages of order the Hubble time. The clustering evolution is then governed by their motion within the gravitational potential (Fry, 1996; Croom et al., 2005). The bias evolution is thus governed by:

$$b(z) = 1 + \frac{b(0) - 1}{D(z)} \tag{3.6}$$

where $D(z)$ is the linear growth rate and is determined using the fitting formulae of Carroll,

Press & Turner (1992). For the bias, b, we use the values given in table 3.3: 0.70, 0.92 and 1.46 for the low, mid and high redshift samples respectively. The stable clustering model represents the evolution of virialised structures and is characterised by (Peacock, 1999):

$$\bar{\xi}(r,z) \propto r^{-\gamma} \propto (1+z)^{\gamma-3} \tag{3.7}$$

where r is the comoving distance. Finally, the no evolution model simply assumes that there is no evolution of the clustering in comoving coordinates.

3.4.2 Redshift-space Correlation Function

We now estimate the z-space correlation function, $\xi(s)$, using $z \geq 0.5$ galaxies identified with $q_{op} \geq 3$. The redshift distribution from figure 3.3 is used to create random catalogues for the two fields with 20× the number of randoms as galaxies in our redshift catalogues. As in the previous section, we use the correlation estimator given in equation 3.1 and calculate errors using Poisson estimates. We use all four fields observed using AAOmega, giving a total of 276 galaxies across $12.6 deg^2$. The result is shown in figure 3.12. We fit the result with a single power-law (noting that the break used in the double-power laws previously lies below the range of our $\xi(s)$ result) and find a best-fit (using a fixed slope of $\gamma = 1.8$) given by a clustering length of $s_o = 5.5 \pm 0.8 h^{-1} Mpc$. Despite the small numbers involved, the result appears to be in reasonable agreement with the estimate of $\xi(r)$ from the angular correlation function ($r_0 = 5.88 \pm 0.12 h^{-1} Mpc$ and $\gamma = 1.83^{+0.03}_{-0.01}$).

If we now compare to the LRG sample of Ross et al. (2008) at this redshift, we find that the blue population clustering length given here is approximately a factor of 2 less than the LRG clustering length, $s_{o,LRG} = 9.9 \pm 0.3 h^{-1}$Mpc, at this redshift. For a more comparable sample, Blake et al. (2009) give a clustering length of $r_0 = 5.3 h^{-1} Mpc$ for their sample of $0.5 < z < 0.75$ galaxies which are selected using similar magnitude ad colour cuts.

3.5 Integrated Sachs-Wolfe Effect

3.5.1 Overview

As described in the introduction the ISW effect is characterised by the energy boost that CMB photons experience as they cross temporally evolving gravitational potential wells in

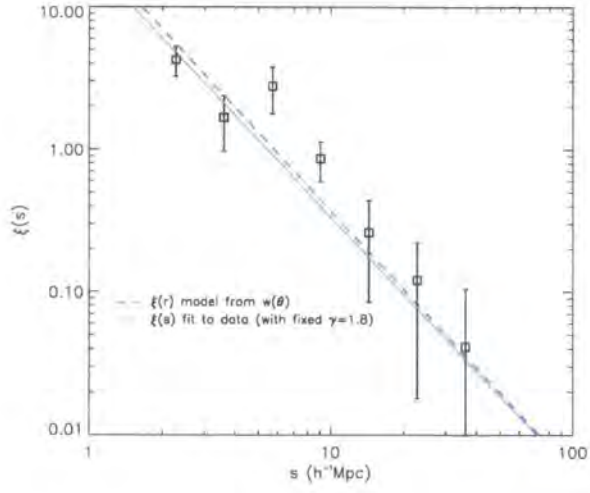

Figure 3.12: The redshift-space correlation function ($\xi(s)$) for the full sample of spectroscopically identified objects. The data-points show the correlation function of the spectroscopic sample of galaxies incorporating the S11, COSMOS, $\epsilon 04$ and $\delta 05$ fields. The solid line shows a best fit to the data points (with a fixed slope of $\gamma = 1.8$), which is characterised by a correlation length of $s_o = 5.5 \pm 0.8 h^{-1} Mpc$. The dashed line is the correlation function determined using Limber's formula and the angular correlation function ($r_o = 5.88 h^{-1} Mpc$, $\gamma = 1.83$ at $r > 1 h^{-1} Mpc$).

an accelerating Universe. The effect is therefore a potential tool for placing constraints on the acceleration of the Universe as characterised by the cosmological constant, Λ. Given the effect's large scale, the production of all-sky CMB maps from the WMAP experiment has made it possible to attempt measures of the effect through the cross-correlation of galaxies (as tracers of the large gravitational potentials) with the CMB. Further to this, the large scale nature of the effect lends itself well to the use of photometrically selected galaxy populations as detailed redshift information is unnecessary. In this vein, several authors (Fosalba et al., 2003; Scranton et al., 2003; Cabré et al., 2006; Rassat et al., 2007) have used a number of galaxy samples to attempt measurements of the ISW signal in the WMAP 1st and 3rd year data. The samples used have mostly been photometrically selected LRGs at redshifts of $z < 0.6$ and simple magnitude selected samples.

We now use our ELG sample to attempt to measure the ISW effect in WMAP 5-year data at our sample redshifts of $z \approx 0.3$, $z \approx 0.5$ and $z \approx 0.7$. As stated much of the ISW work done thus far has been with LRGs and magnitude cut samples at $z < 0.6$. Our use of the ELG samples provides the benefit of extending to greater redshifts, whilst also using an alternative galaxy population. This in itself has benefits and draw-backs.

Firstly, the measured signal will be heavily dependant on the bias of the sample (i.e. how well the sample traces the dark matter structure and hence the gravitational potential). Given that the ELGs are less clustered than the LRG samples used thus far, we therefore expect to measure a weaker signal, making the measurement potentially more difficult. The potential gain in the low clustering strengths of the ELG samples however, is that they are less likely to reside in rich clusters and so we may expect the ISW signal to be less affected by the SZ effect produced as CMB photons pass through hot intra-cluster gas. This potentially provides an interesting alternative to the highly clustered LRG samples used in a number of the previous studies.

3.5.2 Data

For this cross-correlation, we have used the W, V, Q and K band temperature maps from the WMAP 5-year data release (Hinshaw et al., 2008). We use the full-resolution maps with $NSIDE = 512$ in all cases. Before performing the cross-correlation we apply two masks to the data. The first is the WMAP KP0 mask (Bennett et al., 2003) which removes the majority of the galactic (Milky Way) foreground and is the most rigorous mask provided by the WMAP team. Secondly we mask the data to match the coverage of our SDSS DR6 galaxy samples, which is described further below.

Pixelised sky-density maps are constructed from each of the three galaxy samples using the HEALPIX software. These are constructed with a resolution identical to the WMAP temperature maps characterised by the parameter $NSIDE = 512$ (pixel width$\approx 7'$). We then limit our galaxy sample to incorporate only the contiguous north galactic pole region of the SDSS. Thus our sample is limited to $100° < R.A. < 270°$.

3.5.3 Estimating the ISW Effect

Following the work of Fosalba et al. (2003); Cabré et al. (2006), we use the estimate the cross-correlation of the galaxy and WMAP data as the expectation value of the product of the galaxy over-density, $\delta_g = \frac{\rho_g - \bar{\rho}_g}{\bar{\rho}_g}$ and the normalised CMB anisotropy temperature, $\Delta T = T - \bar{T}$ as a function of the angular separation, θ. This is given by:

$$w_{Tg}(\theta) = \frac{\sum_{i,j} \Delta T(\theta_i)\delta_g(\theta_j)}{n_{\Delta T} n_{\delta_g}} \tag{3.8}$$

Again following Fosalba et al. (2003); Cabré et al. (2006), the form of the ISW as probed by a given galaxy population can be expressed by the following Legendre polynomial expansion:

$$w_{TG}^{ISW}(\theta) = \sum_{l} \frac{2l+1}{4\pi} p_l(\cos\theta) C_{GT}^{ISW}(l) \tag{3.9}$$

$C_{GT}^{ISW}(l)$ is simply the ISW/galaxy population power spectrum as given by:

$$C_{GT}^{ISW}(l) = \frac{4}{(2l+1)^2} \int W_{ISW}(z) W_G(z) \frac{H(z)}{c} P(k) dz \tag{3.10}$$

Where P(k) is the mass power spectrum and $W_{ISW}(z)$ and $W_G(z)$ are given by:

$$W_{ISW}(z) = 3\Omega_m \left(\frac{H_0}{c}\right)^2 \frac{d[D(z)/a]}{dz} \tag{3.11}$$

$$W_G(z) = b(z)\phi(z)D(z) \tag{3.12}$$

Where $D(z)$ is the linear growth rate and $b(z)$ is the bias of the galaxy population (see section 3.4). $\phi(z)$ is the galaxy selection function, set from the $n(z)$ distribution of each of the galaxy samples.

3.5.4 Results & Error Analysis

We perform the cross correlation using the NPT (N-point spatial statistic) software (Gray et al., 2004) with the weighting for each pixel given by the galaxy density, δ_g and the CMB anisotropy temperature, ΔT. The results are shown in figures 3.13 to 3.15 for four WMAP bands: W, V, Q and K. We also plot the predicted result using predictions based on equation 6 of Cabré et al. (2006). Our errors are calculated using field-to-field estimates from the 16 subfields within our data. The overall error on each bin was calculated as the sample variance in each data bin scaled to the overall sample size (i.e. scaled by $\sqrt{16}$). Summing over all bins at $\theta < 100'$ we find amplitudes for $w_{Tg}(< 100')$ in the WMAP W-band of $(0.25 \pm 0.27)\mu K$, $(0.17 \pm 0.20)\mu K$ and $(0.17 \pm 0.16)\mu K$ for the low, mid and high redshift samples respectively. Similar results are obtained with the V and Q bands, whilst the K-band (which has a greater level of galactic contamination and a lower resolution) is less consistent, giving signals of $w_{Tg}(< 100') = (0.13 \pm 0.36)\mu K$, $(-0.16 \pm 0.29)\mu K$ and $(0.38 \pm 0.18)\mu K$ for the low, mid and high redshift samples respectively.

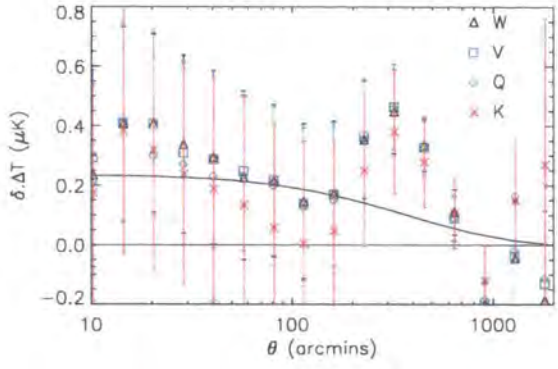

Figure 3.13: Cross correlation between the low-redshift galaxy sample and the WMAP 5 year data. Results obtained with the WMAP W, V, Q and K bands are all shown and, except for the K-band which is most susceptible to galactic contamination, little variation is seen between each (consistent with an ISW effect). The solid line shows the predicted model. Errors are field-to-field based on splitting the data sample into 16 distinct segments.

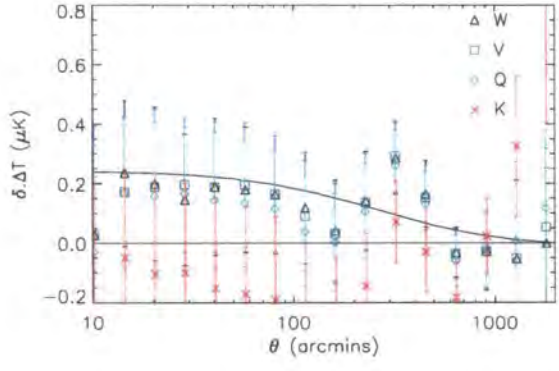

Figure 3.14: As in figure 3.13 but with our mid-redshift sample of emission line galaxies.

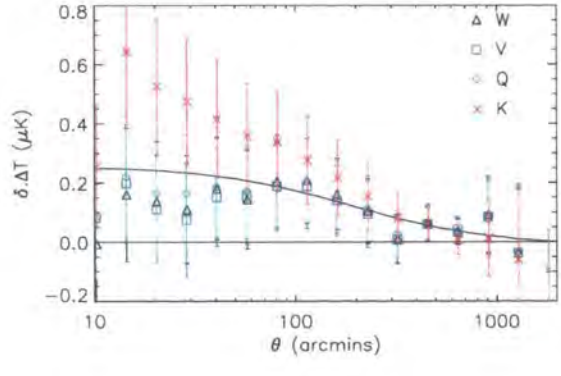

Figure 3.15: As in figure 3.13 but with our high-redshift sample of emission line galaxies.

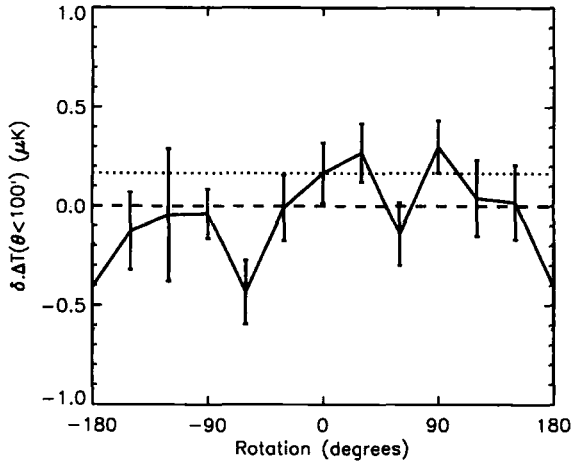

Figure 3.16: Cross-correlation signal, $w_{Tg}(< 100')$, for the high redshift galaxy sample as a function of rotation of the WMAP 5yr data in galactic longitude. The plotted errors are field-to-field errors based on the segmentation of the data into 16 distinct regions.

We also evaluate the significance of the observed correlation by repeating the cross-correlation with rotated realisations of the WMAP data. This method uses the data itself in place of random realisations by rotating the masked WMAP data in 30° steps in galactic longitude. We note at this point that rotating in R.A. would lead to the galactic plane entering the field of view and although the galactic plane region is masked, it would reduce the number of pixels in the analysis significantly. For consistency, we also rotate the WMAP Kp0 mask before applying it to the galaxy density map. The result of this treatment, using the hi-z sample, is given in figure 3.16. Here the $w_{Tg}(< 100')$ signal is plotted as a function of rotation of the WMAP data through a full 360° in galactic longitude. The dotted line shows the non-rotated signal. Again we see that the positive signal that we see in the data does not appear statistically significant, with the rotated results showing a large amount of scatter around $w_{Tg}(< 100') = 0\mu K$ and two of the results (at 30° and 90°) showing more significant positive correlation than the non-rotated result.

We now attempt to improve our statistics by combining the low-, mid- and hi-redshift results. Figure 3.17 shows the mean of the 3 × 16 separate cross-correlation results. The errors are again given by the field-to-field errors, this time across the whole 48 sample set. Again we see a positive signal that appears to show some agreement with the model. In the W, V, Q and K WMAP bands we derive signals of $w_{Tg}(< 100') = (0.20 \pm 0.12)\mu K$,

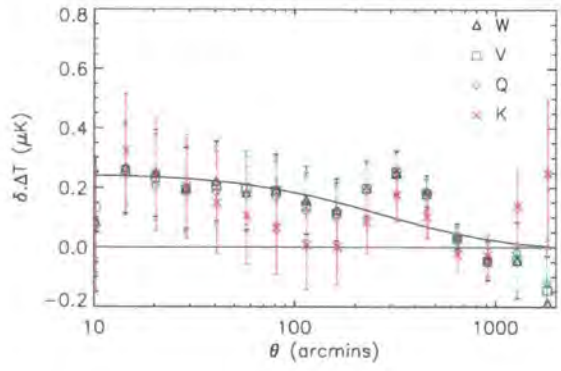

Figure 3.17: Cross correlation result averaged across the 3×16 redshift/segment samples. Again we show the W, V, Q and K band results and as in the previous results, little variation i seen between the results for the W, V and Q bands. The solid line again shows the predicted ISW effect based on a ΛCDM cosmology.

$(0.20 \pm 0.12)\mu K$, $(0.18 \pm 0.12)\mu K$ and $(0.11 \pm 0.16)\mu K$ respectively. Repeating the rotation analysis (figure 3.18), but with the combined sample, we again find significant scatter about $w_{Tg}(< 100') = 0$. Indeed, a stronger signal is again found at some rotation angles than at the zero position.

Comparing this analysis to previous results, Cabré et al. (2006) obtained a signal at $100'$ of $w_{Tg} = 0.6 \pm 0.3\mu K$ using a sample of $\bar{z} \approx 0.5$ LRGs and a signal of $w_{Tg} = \approx 0.65 \pm 0.2\mu K$ with a $20 < r < 21$ magnitude selected sample with a median redshift of $\bar{z} = 0.28$. In addition, Fosalba & Gaztañaga (2004) claimed a detection of $0.35 \pm 0.14\mu K$ at angular scales of $\theta = 4^\circ - 10^\circ$ using APM galaxies, but found their signal was dominated by the SZ component at scales of $\theta < 4^\circ$. Our observed signal is consistent with the weaker signal expected of the ELG samples, based on both the model predictions and comparison with correlations based on more strongly clustered populations. However, the estimated errors on the measurement prohibit us from claiming a significant detection of the ISW effect at this point.

3.6 Summary

In this chapter I have discussed the development of a number of photometric constraints to select emission line galaxies at redshifts of $z < 1$. Based on COMBO-17 photometric redshifts, the three final photometric selections are predicted to have redshift distributions of

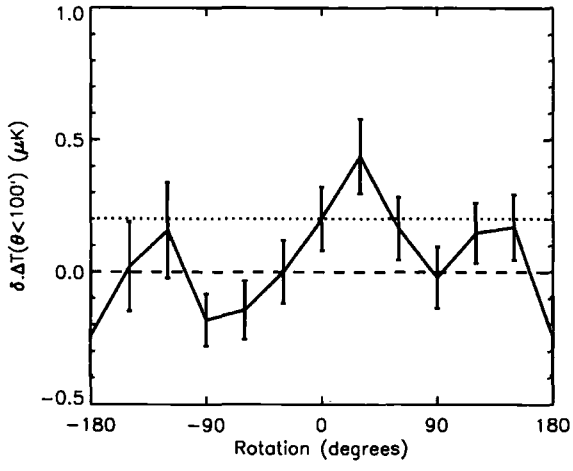

Figure 3.18: Cross-correlation signal, $w_{Tg}(< 100')$, for the combined low-, mid- and high-redshift galaxy sample as a function of rotation of the WMAP 5yr data in galactic longitude. The plotted errors are field-to-field errors based on the segmentation of the data into 3×16 distinct regions.

$z = 0.29 \pm 0.05$, $z = 0.44 \pm 0.08$ and $z = 0.65 \pm 0.21$. Following this, I have described spectroscopic observations of the high-redshift sample using the AAT AAOmega instrument and find good agreement between the photometric and spectroscopic redshift distributions for this sample. Further to this the spectroscopic redshifts show good agreement with the photometric redshifts of individual galaxies taken from the COMBO-17 data. Looking at the clustering of the galaxy samples, the low, mid and high redshift samples are each estimated to have clustering lengths (at $r > 0.5h^{-1}Mpc$) of $r_0 = 2.65^{+0.05}_{-0.08}h^{-1}Mpc$, $r_0 = 3.62^{+0.06}_{-0.06}h^{-1}Mpc$ and $r_0 = 5.88^{+0.12}_{-0.12}h^{-1}Mpc$ respectively based on measurements of their angular clustering correlation functions and redshift distributions. The increasing clustering strength with the redshift of the three samples broadly follows an increase in the brightness/absolute magnitude ranges of the three samples, whilst the relatively low clustering amplitudes of the $z \lesssim 0.4$ and $0.4 \lesssim z \lesssim 0.6$ samples suggest they reside in low-density regions. The higher redshift ($z > 0.6$) sample has a somewhat higher clustering strength, comparable to the clustering amplitude of low-redshift late-type galaxies, but is still relatively weakly clustered compared to LRGs/early-type galaxies.

Finally, I have used the three samples to search for the ISW effect in the WMAP 5 year data release. Given the comparably weak clustering of the ELGs, it is a potentially difficult aim to measure the ISW effect using these galaxy samples. However, the low clustering and hence the lower likelihood of these galaxies lying in clusters should reduce

the contamination of the result by the SZ effect. However, our cross-correlation analysis does not produce a significant signal with any of the three galaxy samples. We note that in all three samples and with a combined sample we find an overall positive trend consistent with the predicted ISW effect, however at most this trend has a significance of 1.67σ and we are unable to claim a positive detection from the analysis.

CHAPTER 4

A SURVEY OF LBGS AT REDSHIFT 3

4.1 Introduction

In the following chapters I review a survey of $z \approx 3$ galaxies using the VLT VIMOS spectrograph. The survey is aimed at building on the work of Steidel et al. (2003) and Adelberger et al. (2003) and studying the clustering properties of galaxies at $z \approx 3$ and the relationship between galaxies and the IGM at these redshifts. The total survey will ultimately produce a catalogue of ≈ 3000 galaxies, however at the point of writing, the survey consists of $\approx \frac{1}{3}$ of this total. This work therefore reviews the data acquired thus far and the initial analysis performed so far.

This chapter presents a review of the data acquisition, incorporating the initial survey imaging, photometric selection of candidates and follow-up spectroscopy. The following chapter reviews the clustering properties of the spectroscopic LBG catalogue and chapter 6 reviews the initial work towards using the LBG sample to study the relationship between galaxies and the IGM at $z \approx 3$.

4.2 Imaging

4.2.1 Target fields

A primary aim of this work is to investigate the relationship between galaxies and gas at high redshift. With this in mind, the survey is centred on a number of fields around known bright $z > 3$ QSOs. Each of these QSOs have existing high-resolution optical spectra and are at declinations appropriate for observations from the VLT at Cerro Paranal. The selected quasars are Q0042-2627 (z=3.29), SDSS J0124+0044 (z=3.84), HE0940-1050 (z=3.05), SDSS J1201+0116 (z=3.23) and PKS2126-158 (z=3.28). Q0042-2627 has been observed by Williger et al. (1996) using the Argus multifibre spectrograph on the Blanco 4m telescope at Cerro Tololo Inter-American Observatory (CTIO) and as part of the Large Bright QSO Survey (LBQS) using Keck/HIRES (Hewett et al., 1995). Pichon

et al. (2003) observed HE0940-1050 and PKS2126-158 using the Ultraviolet and Visual Echelle Spectrograph (UVES) on the VLT and SDSS J0124+0044 has been observed by Péroux et al. (2005) also using UVES. Finally, SDSS J1201+0116 has been observed by the SDSS team using the SLOAN spectrograph and by O'Meara et al. (2007) using the Magellan Inamori Kyocera Echelle (MIKE) high resolution spectrograph on the Magellan 6.5m telescope at Las Campanas Observatory.

4.2.2 Observations

The imaging for our 5 selected fields was obtained using a combination of the MOSAIC Imager on the Mayall 4-m telescope at KPNO, the MOSAIC-II Imager on the Blanco 4-m at CTIO and VLT VIMOS in imaging mode. Q0042-2627, HE0940-1050 and PKS2126-158 were all observed at CTIO between January 2004 and April 2005. J0124+0044 and J1201+0044 were observed at KPNO in September 2001 and April 2006 respectively. All of these fields were observed with the broadband Stromgen U filter and the Harris B and R filters, except for J0124+0044, which was observed with the Harris B, V and I broadband filters but not the Harris R. A full description of the observations is given in table 4.1.

We note that during the observations of the HE0940-1050 field, there was a malfunction of one of the CCDs leaving a gap of $\approx 8' \times 18'$ in the field of view. The remaining CCDs provided unaffected data however, which we use here.

Table 4.1: Details of the imaging data acquired in each of our five target fields. Coordinates are given for the imaging centre, which is not necessarily the same as the position of the bright corresponding QSO.

Field	α (J2000)	δ (J2000)	Facility	Band (Vega)	Exp time (s)	Seeing	Depth 3σ	Depth 50% comp.
Q0042-2627	00:46:45	-25:42:35	CTIO/MOSAIC2	U	12,600	1.8″	26.22	24.03
				B	3,300	1.8″	26.93	25.07
			VLT/VIMOS	R	235	1.1″	25.79	24.33
J0124+0044	01:24:03	+00:44:32	CTIO/MOSAIC2	U	13,400	1.5″	25.60	...
				B	2,800	1.5″	26.44	...
				V	3,100	1.4″	26.14	...
				I	7,500	1.1″	25.75	24.48
HE0940-1050	09:42:53	-11:04:25	CTIO/MOSAIC2	U	29,000	1.3″	26.75	24.82
				B	4,800	1.3″	26.66	24.68
				R	2,250	1.0″	26.24	25.01
J1201+0116	12:01:43	+01:16:05	KPNO/MOSAIC	U	9,900	1.6″	26.12	23.73
				B	6,000	2.4″	27.01	24.29
			VLT/VIMOS	R	235	0.7″	26.24	24.99
PKS2126-158	21:29:12	-15:38:42	CTIO/MOSAIC2	U	26,400	1.3″	26.97	24.63
				B	7,800	1.6″	27.49	24.79
				R	6,400	1.5″	26.79	24.55

The MOSAIC Imagers each have a field of view of $35' \times 35'$, covered by 8 2048×4092 CCDs. Adjacent chips are separated by a gap of up to $12''$ and we have therefore performed a dithered observing strategy for the acquisition of all our imaging data. For all observations we took bias frames, sky flats (during twilight periods), dome flats and also observed Landolt (1992) standard-star fields with each filter on each night of observation for the calibration process.

In the Q0042-2627 and J1201+0116 fields, we also use imaging from the VLT VIMOS instrument with the broadband R filter. VIMOS consists of 4 CCDs each covering an area of $7' \times 8'$, with gaps of $2'$ between adjacent chips. The fields were observed with 4 separate pointings, with $< 1'$ overlap between adjacent pointings giving a total field of view of $\approx 32' \times 36'$.

4.2.3 Data Reduction

All data taken using the MOSAIC Imagers were reduced using the MSCRED package within IRAF, in accordance with the NOAO Deep Wide-Field Survey guidelines of Januzzi et al (2000). Firstly the calibration data was processed using ZEROCOMBINE to create the bias images for each separate night. Dome and Sky-flat frames were then processed for each night's observing using CCDPROC to trim the images, subtract the overscan level and subtract the bias-frame. Before flat-fielding the science images, the "pupil-ghost" artifact was removed from the U-band flat frames. This artifact is an additive signal due to reflections in the optics of the MOSAIC camera and is removed using the MSCPUPIL task.

The science images were then processed using CCDPROC again to trim the images, subtract the overscan level, remove cross-talk effects between CCDs and then subtract the bias-frame and perform the flat-fielding using both the dome and sky-flat combined frames. Again for the U-band images the pupil-ghost artifact was removed from the science images using MSCPUPIL and RMPUPIL tasks. With the individual images having undergone initial processing, bad-pixels and cosmic rays were then removed. The CRREJECT task (in the IMRED package) was used to identify cosmic-rays and create a cosmic-ray mask. This was then combined with the standard bad-pixel masks using the CRPLUSBPMASK task provided by NOAO, before the FIXPIX task (also in IMRED) was used to remove the marked bad-pixels and cosmic-rays from the images, using the interpolation setting.

The processed science images were then deprojected using the MSCIMAGE task after having optimised the astrometry solutions using MSCCMATCH. Sky-variations were then removed using MSCSKYSUB and the images were combined using MSCIMATCH and MSCSTACK to produce the final images in each band.

The data reduction for the R-band imaging from VLT VIMOS was reduced using the VIMOS pipeline. Again bias frames were subtracted and the images were flat fielded using dome flats acquired on the night of observation. Individual exposures were then deprojected and stacked using the SWARP software (Bertin et al., 2002).

4.2.4 Photometry

We performed object extraction using SEXTRACTOR, with a detection threshold of 1.2σ and a minimum object size of 5 pixels. Object detection was performed on the R-band images and fluxes were calculated in all bands using Kron, fixed-width (with a diameter of twice the image seeing FWHM) and isophotal width apertures. Zeropoints for each of the observations were calculated from the Landolt standard-star field observations made during the observing runs. Each of the standard-star field images were processed using the same method as for the science frames. The depths reached in the U, B and R bands for each field are given in table 4.1. We quote the 3σ depths, which give the limit for detecting an object 5 pixels in size with a signal of $3\times$ the background RMS detection, and the 50% completeness level.

The U, B and R number counts from the 4 fields are plotted in figures 4.1 to 4.3. We plot for comparison the number counts of Metcalfe et al (2001) for comparison. All counts are from our MOSAIC data except for the R band counts of Q0042-2627 and SDSS1201+0116, which are from the VLT VIMOS. Stars have been removed for the purpose of these plots using a limit of $s-g < 0.8$ on the SEXTRACTOR star-galaxy separation measure.

4.2.5 Selection Criteria

We perform a photometric selection based on that of Steidel et al. (1996, 2003), but applied to the U, B and R band imaging available from our imaging survey. As in Steidel et al. (2003) our selection takes advantage of the Lyman-Break at 912Å and the Lyα-forest passing through the U-band and into the B-band in the redshift range $2.0 < z < 3.5$.

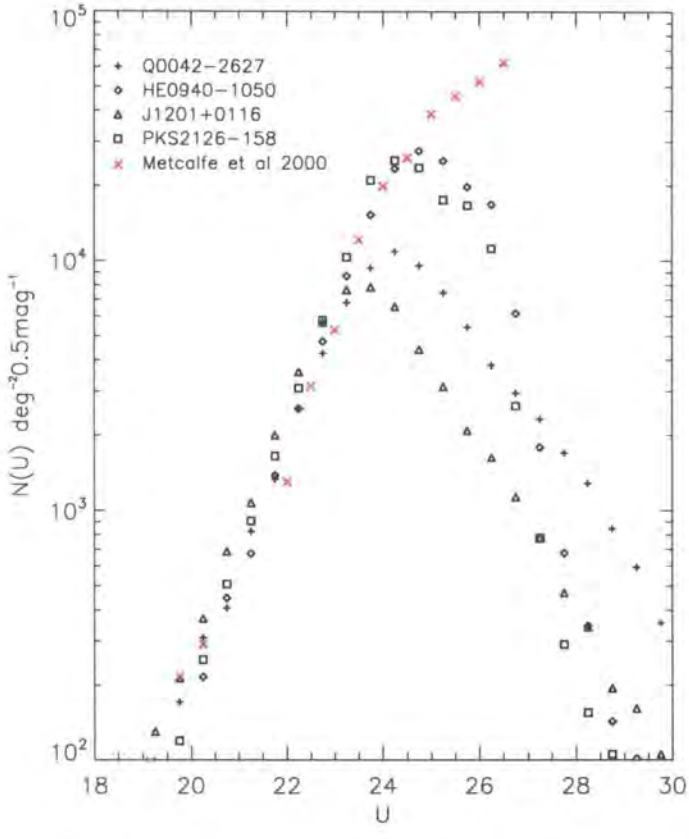

Figure 4.1: U-band number counts from the four fields Q0042-2627 (black crosses), HE0940-1050 (diamonds), J1201+0116 (triangles) and PKS2126-158 (squares). The counts of Metcalfe et al (2001) from the William Herschel Deep Field are shown for comparison (red crosses).

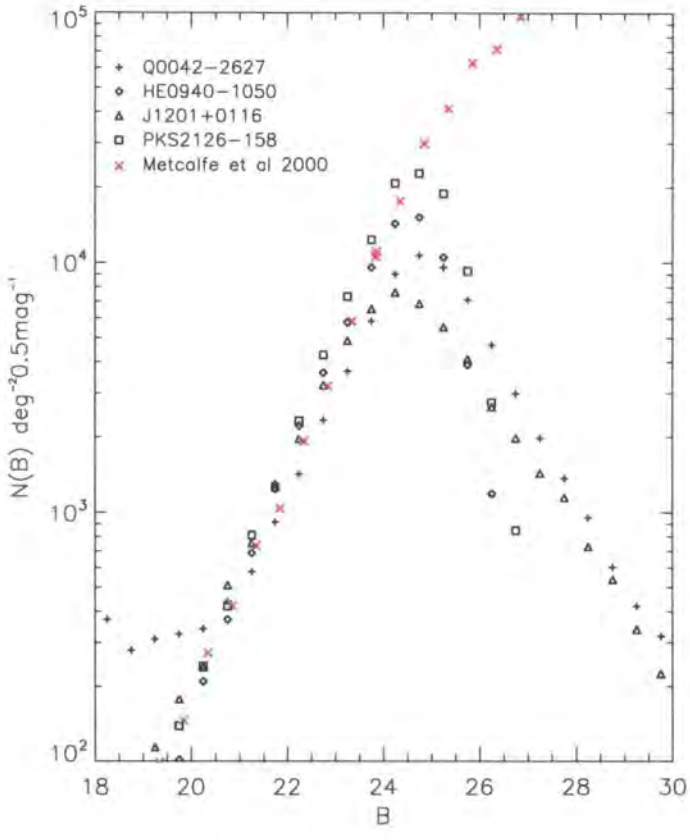

Figure 4.2: B-band number counts from the four fields Q0042-2627 (black crosses), HE0940-1050 (diamonds), J1201+0116 (triangles) and PKS2126-158 (squares). The counts of Metcalfe et al (2001) from the William Herschel Deep Field are shown for comparison (red crosses).

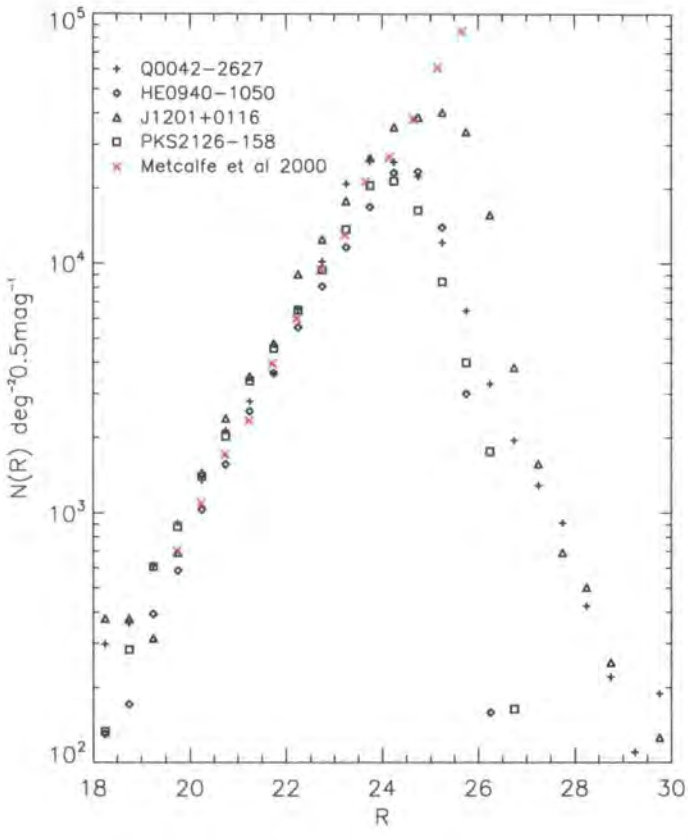

Figure 4.3: R-band number counts from the four fields Q0042-2627 (black crosses), HE0940-1050 (diamonds), J1201+0116 (triangles) and PKS2126-158 (squares). The counts of Metcalfe et al (2001) from the William Herschel Deep Field are shown for comparison (red crosses).

The selection consists of four groups labelled LBG_PRI1, LBG_PRI2, LBG_PRI3 and LBG_DROP, which are defined as follows:

- LBG_PRI1
  1. $23 < R < 25.5$
  2. $U - B > 0.5$
  3. $B - R > 0.8(U - B) + 0.6$
  4. $B - R < 2.2$
- LBG_PRI2
  1. $23 < R < 25.5$
  2. $U - B > 0.0$
  3. $B - R > 0.8(U - B) + 0.8$
  4. $B - R < 2.8$
- LBG_PRI3
  1. $23 < R < 25.5$
  2. $-0.5 < U - B < 0.0$
  3. $B - R > 0.8(U - B) + 0.6$
- LBG_DROP
  1. $23 < R < 25.5$
  2. $NoU detection$
  3. $B - R < 2.2$

LBG_PRI1 is our primary sample and selects candidates that are expected to be the most likely $2.5 < z < 3.0$ galaxies. The LBG_PRI2 sample provides a further level of candidate selection, targeting objects with colours closer to the main sequence of low-redshift galaxies than the LBG_PRI1 objects. This sample is therefore expected to include a greater level of contamination from low redshift galaxies. In addition, based on the path of the evolution tracks in figures 4.4 and 4.5, we also expect the $z > 2.5$ population that this selection samples to have, on average, a lower redshift than the LBG_PRI1 sample. The next selection sample, LBG_PRI3, takes this further and is intended to target a $2.0 < z < 3.0$ galaxy redshift based on the evolution tracks. Finally, we select a sample of U-dropout objects (LBG_DROP) with detections in only our B and R band data.

Table 4.2: Number of candidate high redshift objects in each of the selected fields. Note that candidates in the J0124+0044 were selected as described in Bouché & Lowenthal (2004) and not using the four selection criteria sets described in this paper.

Field	LBG_PRI1	LBG_PRI2	LBG_PRI3	LBG_DROP	Total
Q0042-2627	1,366	1,381	650	1,390	4,787
J0124+0044					3,679
HE0940-1050	1,646	2,249	741	1,042	5,678
J1201+0116	477	487	469	606	2,029
PKS2126-158	1,380	2,119	713	667	4,879
Total	4,869	6,236	2,573	3,705	21,062

In none of the above samples do we attempt to remove stellar-like objects. The half-light radius of $z \approx 3$ LBGs has been shown to be on average $0.4''$ and so will not be resolved in our data, which is mostly taken under conditions of $> 0.8''$ seeing. We also plot the model colour tracks for a star-forming galaxy (solid black line) in each of the UBR plots in figures 4.4 and 4.5. The model is derived using the GALAXEV stellar population synthesis code of Bruzual & Charlot (2003) and uses a Salpeter initial mass-function, assuming solar metallicity, with a galaxy formed at $z = 6.2$ (i.e. with an age of 12.6Gyr at $z = 0$) and a $\tau = 9$Gyr exponential SFR. The model is shown from $z = 0$ up to $z = 4$.

We apply these selection criteria to four of our QSO fields: Q0042-2627, HE0940-1050, J1201+0116 and PKS2126-158. The candidate selection for the J0124+0044 field was performed separately and is discussed in Bouché & Lowenthal (2004). Figures 4.4 and 4.5 shows the four selection criteria applied to these four fields. The selection boundaries are shown by the red, green and blue lines for the LBG_PRI1, LBG_PRI2 and LBG_PRI3 selections respectively. Objects selected as candidates by each criteria set are shown by red, green, blue and cyan points for the LBG_PRI1, LBG_PRI2 and LBG_PRI3 selections respectively. The grey contours in each plot show the extent of the complete galaxy population in each of the fields.

The numbers of objects selected by each selection for each field are given in table 4.2. These candidate selections were used as the basis for the spectroscopic work which is now described in the following sections.

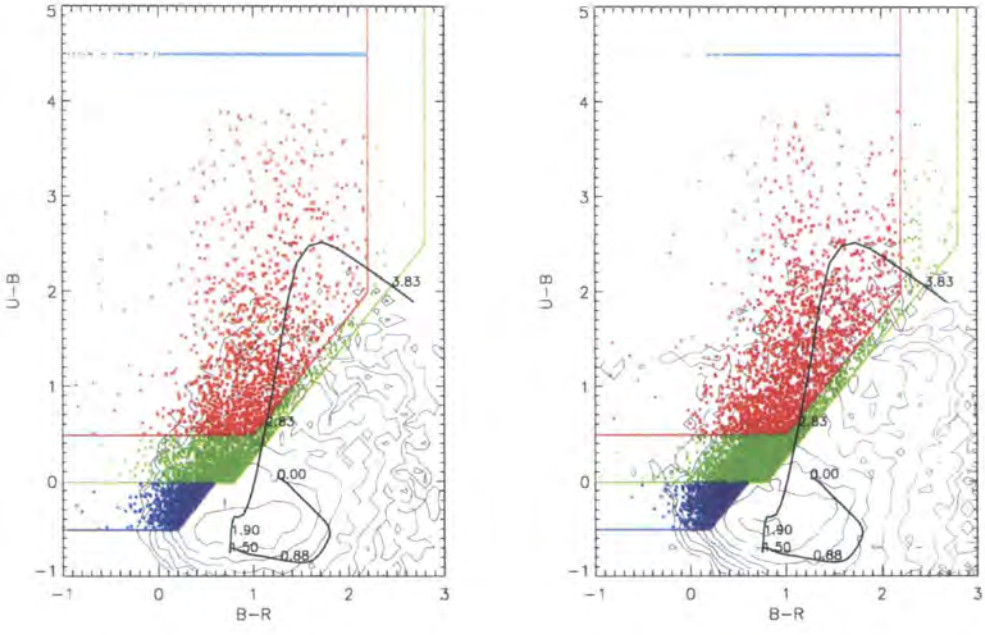

Figure 4.4: Our selection criteria in UBR colour space shown for the Q0042-2627 (left) and HE0940-1050 (right). The red line and points show the LBG_PRI1 selection, the green line and points show the LBG_PRI1 selection, the blue line and points show the LBG_PRI3 selection and the cyan line at $U - B = 4.5$ shows the LBG_DROP selection. The grey contours show the entire galaxy population in the field and the black lines show the galaxy evolution model for a galaxy with a $\tau = 9$Gyr exponential SFR formed at $z = 6.2$.

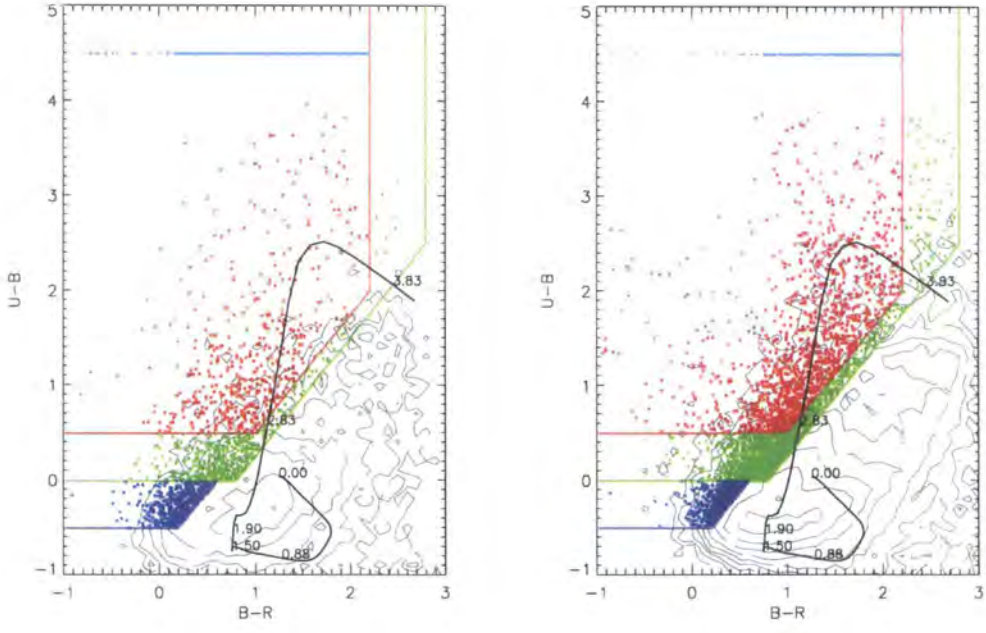

Figure 4.5: Our selection criteria in UBR colour space shown for the J1201+0116 and PKS2126-158 fields (left to right). The red line and points show the LBG_PRI1 selection, the green line and points show the LBG_PRI1 selection, the blue line and points show the LBG_PRI3 selection and the cyan line at $U - B = 4.5$ shows the LBG_DROP selection. The grey contours show the entire galaxy population in the field and the black lines show the galaxy evolution model for a galaxy with a $\tau = 9$Gyr exponential SFR formed at $z = 6.2$.

4.2.6 QSO Candidate Selection

At redshifts of $z \approx 3$, the optical region of QSO and galaxy spectra exhibit similar shapes, both essentially being heavily influenced by the Lyman break feature. We therefore add to our targets, a number of QSO candidates in each field using the following selection (which is closely based on our high priority $z \approx 3$ LBG selection):

- QSO
    1. $class\_star > 0.8$
    2. $20 < R < 23$
    3. $U - B > 0.5$
    4. $B - R < 0.8(U - B) + 0.8$
    5. $0.0 < B - R < 2.2$

This selection gives 71, 39, 15 and 38 QSO candidates in the Q0042-2627, HE0940-1050, J1201+0116 and PKS2126-158 fields respectively. Note that only a small number of these have actually been observed as the LBG candidates remained the higher priority.

4.3 Spectroscopy

4.3.1 Observations

We observed our LBG candidates using the VIMOS instrument on the VLT UT3 (Melipal) between September 2005 and March 2007. As described earlier, the VIMOS camera consists of four CCDs, each with a field of view of $7' \times 8'$, arranged in a square configuration, with $2'$ gaps between the field-of-views of adjacent chips. Each observation therefore covers a field of view of $16' \times 18'$ with $224 arcmin^2$ being covered by the CCDs. The instrument was set up with the low-resolution blue grating (LR_Blue) in conjunction with the OS_Blue filter, giving a wavelength coverage of 3700Å to 6700Å and a resolution of 180 with $1''$ slits, corresponding to 28Å FWHM at 5000Å. The dispersion with this setting is $5.3\mathring{A}$ per pixel. We note that this configuration also projects the zero diffraction order onto the CCDs.

Given the size of our imaging fields ($36' \times 36'$) it is possible to target 4 distinct sub-fields with the VIMOS field of view. We have therefore observed a total of 19 sub-fields across our 5 fields, i.e. 4 sub-fields in each field except for HE0940-1050 in which only 3

sub-fields were achievable due to the CCD malfunction during the imaging observations. Each sub-field was observed with $10 \times 1,000s$ exposures, apart from sub-field three of the PKS2126-158, which was observed with only $4 \times 1,000s$ due to time constraints in the VIMOS schedule. All observations were performed during dark time, with $< 0.8''$ seeing and < 1.3 air-mass.

Slit-masks for each quadrant of each sub-field were designed using the standard VIMOS mask software, VMMPS. We used minimum slit-lengths of $8''$, which equates to 40 pixels given the pixel scale of $0.205''/pixel$. With the effectively point-like nature of our sources and our maximum seeing constraint of $0.8''$ this allows us a minimum of $\approx 7''$ for sky spectra per slit (with which to perform the sky-subtraction when extracting the spectra). Using the VMMPS software with the LR_Blue grism we were able to target up to $\approx 60-70$ objects per quadrant (i.e. ≈ 250 objects per sub-field), depending on the sky density of the candidate objects.

Table 4.3: Details of the spectroscopic data acquired in each of our five target fields. Coordinates are given for the targeting centre of each sub-field.

Field	Sub-field	α (J2000)	δ (J2000)	Dates	Exp time (s)	Seeing
Q0042-2627	f1	00:45:11.14	-26:04:22.0	8-10,15/08/2007	10,000	$0.6 - 1.0''$
Q0042-2627	f2	00:43:57.30	-26:04:22.0	18-19/08/2007 & 5-6/09/2007	10,000	$0.9 - 1.0''$
Q0042-2627	f3	00:45:10.35	-26:19:06.9	11-12/09/2007	10,000	$0.9 - 1.0''$
Q0042-2627	f4	00:43:55.97	-26:19:16.1	7,10/09/2007	10,000	$0.9 - 1.0''$
J0124+0044	f1	01:24:41.82	+00:52:18.8	1-2,4/11/2005	10,000	$0.8 - 0.9''$
J0124+0044	f2	01:23:32.06	+00:52:13.1	5,29,31/10/2005	10,000	$0.6 - 1.0''$
J0124+0044	f3	01:23:31.29	+00:37:02.0	19-20/09/2007	10,000	$0.8 - 1.0''$
J0124+0044	f4	01:24:41.86	+00:36:51.4	4/12/2005 & 22/08/2006	10,000	$0.8 - 0.9''$
HE0940-1050	f1	09:42:08.02	-11:08:14.2	26-27,29/01/2006	10,000	$0.5 - 0.8''$
HE0940-1050	f2	09:43:21.53	-11:08:35.0	30-31/01/2006, 1,25/02/2006 & 1/03/2006	10,000	$0.5 - 1.0''$
HE0940-1050	f3	09:43:21.58	-10:54:31.8	14,19/12/2007 & 31/01/2008	10,000	$0.6 - 1.0''$
J1201+0116	f1	12:02:14.01	+01:09:09.9	13-15/04/2007 & 17/04/2007	10,000	$0.6 - 1.0''$
J1201+0116	f2	12:01:10.01	+01:09:09.9	23/04/2007 & 8,11,14/05/2007	10,000	$0.4 - 0.9''$
J1201+0116	f3	12:01:10.04	+01:24:09.8	16-17/05/2007	10,000	$0.5 - 0.9''$
J1201+0116	f4	12:02:14.07	+01:24:08.0	18/05/2007 & 6,8,10/02/2008	10,000	$0.6 - 0.7''$
PKS2126-158	f1	21:29:59.57	-15:31:30.2	17/08/2006 & 1,21-26/09/2006	10,000	$0.7 - 1.0''$
PKS2126-158	f2	21:28:46.20	-15:31:29.9	5-6/08/2005	10,000	$0.6 - 1.0''$
PKS2126-158	f3	21:30:00.41	-15:47:18.3	27/09/2006	4,000	$0.8 - 1.0''$
PKS2126-158	f4	21:28:46.27	-15:47:11.9	9-11,25,29/08/2005	10,000	$0.7 - 0.9''$

4.3.2 Data reduction

Bias frames were obtained by the VLT service observers at the beginning of each night of observations. Lamp-flats were also taken with each of the masks with the observation setup in place (i.e. the OS_Blue filter and LR_Blue grism). These were also taken by the service observers at the beginning of each night's observation. Arc frames were taken during the night with each of the masks with the LR_Blue grism and OS_Blue filter.

Data reduction was performed using the VIMOS pipeline software, ESOREX. Firstly the bias frames were combined to form a master bias using VMBIAS. The flat frames were then processed and combined using the VMSPFLAT recipe. VMSPCALDISP was then used to process (bias subtract and flat-field) the arc lamp exposure and to determine the spectral distortions of the instrument. With the bias, flat and arc exposures all processed, the object frames were then reduced and combined using the VMMOSOBSSTARE recipe to produce the reduced 2-D spectra.

We extract the 1-D spectra using purpose written IDL routines. For each spectrum, we first fit the shape of the spectrum across the slit. This is implemented by binning the 2-D aperture along the dispersion axis and then fitting a Gaussian profile to each bin to find the centre of the object signal in each bin. We then fit the resultant spread in the central pixel with a 4th order polynomial function. We then lay an object aperture with a width of n_{ap} pixels over the object and a sky aperture covering all of the usable sky region in the slit. The object and sky spectra are then taken as being the mean over the widths of their respective apertures. Finally, we subtract the sky spectrum from the object spectrum to produce the final object spectrum. The dominant remaining sky-contamination after sky-subtraction were the strong sky emission lines [OI]5577Å [NaI]5990Å and [OI]6300Å.

We estimate the signal-to-noise using by taking the RMS of the sky aperture in each wavelength bin and dividing by $\sqrt{n_{ap}}$, where n_{ap} is the width of the aperture used to extract the 1-D spectrum of a given object. Figure 4.6 shows the mean signal-to-noise per resolution element (i.e. 28Å) in the wavelength range 4100Å$< \lambda <$5300Å in our sky-subtracted spectra as a function of source R-band magnitude. The selected range covers much of the key emission and absorption lines exhibited in LBGs in the redshift range $2.5 < z < 3.5$, whilst excluding the strong sky lines. The points in figure 4.6 show the mean spectrum SNR per resolution element, whilst the error bars show the standard deviation within each bin. In the faintest bin ($25.25 < R < 25.5$), we achieve a mean continuum

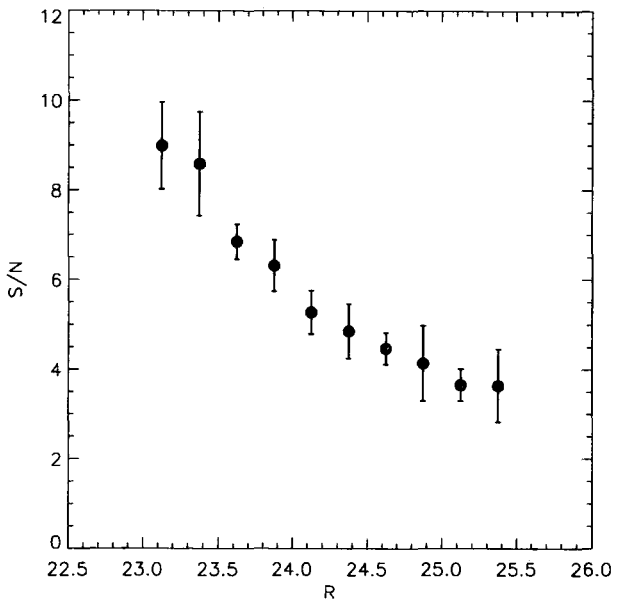

Figure 4.6: Mean signal-to-noise per resolution element (28Å) in the wavelength range 4100Å< λ <5300Å as a function of R-band magnitude in our VLT VIMOS spectra with integration times of 10,000s.

signal-to-noise of ≈ 3.5 on the continuum signal of our objects. This rises to a continuum signal-to-noise ≈ 9 for our brightest objects ($23 < R < 23.25$).

4.3.3 Object Identification

We perform the object identification for each slit individually by eye. Given the wavelength range covered by the LR_Blue grism combined with the redshift range of our targets, $2 < z < 3.5$, there are several key spectral features that facilitate the identification of those targets. These primarily take the form of the following:

- Lyman limit, 912Å;
- Lyβ emission/absorption, 1026Å
- OVI emission, 1035Å;
- Lyα forest, <1215Å;
- Lyα emission/absorption, 1215Å;
- Inter-stellar medium (ISM) absorption lines:

- SiII 1260.4Å;
- OI 1302.Å;
- CII 1336Å;
- SiIV doublet 1393Å& 1403Å;

- CIV doublet absorption/emission, 1554Å.

The most prominent of these features is most frequently the Lyα emission/absorption feature at 1215Å. We measure the individual galaxy redshifts from the above spectral features. However, as discussed by Shapley et al. (2003), the observed optical (rest-frame UV) absorption and emission features are thought to originate from an outflowing shell of material surrounding the core nebular region of the galaxy. These features do not therefore represent the redshift of the rest-frame of the galaxy but in fact of these outflows.

For each confirmed LBG we therefore measure the redshift of the Lyα emission/absorption feature and the redshift of the ISM absorption features. In order to measure the Lyα redshift, we fit the feature with a Gaussian function allowing the amplitude, central wavelength and width to be free parameters. From these we determine the redshift and linewidth of the feature. Unfortunately the use of a Gaussian profile will not provide an ideal measurement of the redshift of the Lyα emission due to absorption blue-wards of the emission wavelength which produces an asymmetry in the observed emission line. However, accounting for this asymmetry with an asymmetric fit as opposed to a Gaussian fit is far from simple given the variability in the extent of the absorption between sources and the low-resolution of our spectroscopy. The asymmetry will hence produce a systematic in our measurement of the Lyα emission redshift. This is to some degree characterized and accounted for however by the relations between the measured Lyα and ISM redshifts and the intrinsic redshift outlined by Adelberger et al. (2003) who also fit the spectral features with Gaussian profiles. These relations are discussed in more detail later in this section.

We have performed an estimate of the accuracy of our redshift results by repeating the spectral line fitting method with mock spectra. Each mock spectrum consists of a single Gaussian emission line (i.e. $f = Ae^{-(\lambda-\lambda_o)^2/2\sigma^2}$) at a random redshift in the range $2.5 < z < 3.5$ and a FWHM of $\sigma = 850 kms^{-1}$ (equivalent to the resolution of the instrument). Gaussian random noise was then added onto the basic emission line shape to give the required signal-to-noise. For each mock spectrum, we then performed

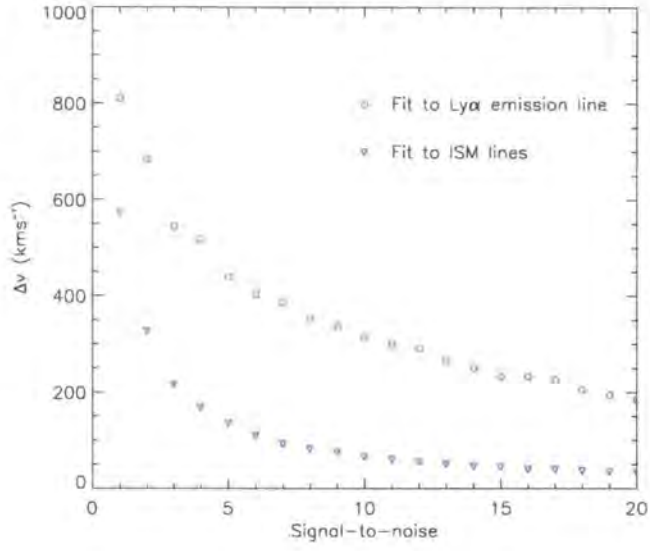

Figure 4.7: Estimate of the accuracy of the Gaussian line-fitting based on iteratively fitting mock spectra with Gaussian random noise. The open circles show the results of applying the fitting method to a single emission line spectrum with a range of signal-to-noise (where the signal-to-noise is defined as the ratio between the peak signal and the width of the Gaussian noise). The blue triangles show the result of the same method applied to a simple absorption line spectrum including the ISM lines: SiII (1260Å), OII (1302Å), CII (1336Å) and SiIV (1393Å, 1402Å).

the Gaussian fitting, iteratively performing the process for a total of 10^4 mock spectra at a given signal-to-noise. The difference between the input redshift and the Gaussian line fitting redshift was then measured for each of the iterations and the error estimated from the distribution of this difference in input and measurement. The process was then repeated with the emission line peak being increased from 1 to 20× the Gaussian noise width.

The results are given in figure 4.7, where the measured accuracy is plotted as a function of the calculated signal-to-noise (red circles). Further to this, we measure the distribution of Lyα emission peak signal-to-noise in our galaxy sample, which is shown in figure 4.8 as a percentage of the total number of LBGs exhibiting Lyα emission. If we now compare these two plots, we see that $\approx 90\%$ of our emission line LBGs have an emission line signal-to-noise of > 3, which suggests that 90% of the Lyα emission line redshifts have velocity errors of less than $\approx 550 kms^{-1}$. Further, the median Lyα emission line signal-to-noise is ≈ 5.5 which gives a velocity error of $\approx 400 kms^{-1}$. Our higher quality spectra (i.e. the top

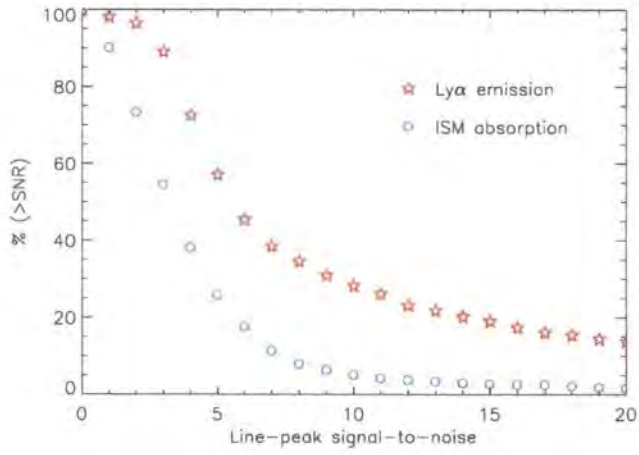

Figure 4.8: The distribution of Lyα emission line (red stars) and ISM absorption line (blue circles) signal-to-noise measurements in our LBG sample. The calculated signal-to-noise is the ratio between the emission/absorption line peak (after subtracting the continuum) and the measured noise. The final ISM signal-to-noise value is taken as the median of the calculated values for the ISM lines used. See figure 4.7 for the estimated velocity errors based on the feature signal-to-noise.

20%) however, are estimated to achieve velocity errors on the Lyα emission line redshifts as small as $\approx 200 kms^{-1}$.

Where feasible, we also attempt to measure the redshift of the ISM absorption lines based on the SiII, OI, CII and SiIV doublet. Measuring the individual absorption lines in most of our spectra is difficult given the SNR of the absorption features in our spectra, however our ability to estimate the redshift of the ISM lines can be greatly improved by attempting to determine the mean ISM redshift by fitting the five lines simultaneously.

To evaluate this method we repeat the iterative error analysis performed for the Lyα emission line fitting, but fitting five absorption lines (with $\sigma_{ISM} = 850 kms^{-1}$) simultaneously. Again we measure the offset between the input redshift and the output redshift measured from the Gaussian line fitting. The result is again plotted in figure 4.7 (blue triangles), whilst the distribution of ISM signal-to-noise measurements in the data is again given in figure 4.8. This suggests that we may reasonably expect a significant improvement in the estimated redshift compared to measuring just a single line. We now predict an accuracy of $\approx 200 kms^{-1}$ at a signal-to-noise of ≈ 3, which based on figure 4.8 accounts for 55% of our sample.

With the Lyα and ISM redshifts determined, we estimated the intrinsic redshifts, z_{int}, of our LBG sample using the relations of Adelberger et al. (2005). These relations were derived from a sample of 138 LBGs observed spectroscopically in both the optical and the near infrared and are based on the offsets found between the Lyα plus ISM lines and the nebular emission lines, [OII]3727Å, Hβ, [OIII]5007Å and Hα. These lines are all associated with the central star-forming regions of LBGs as opposed to the outflowing material and are thus expected to be more representative of the intrinsic redshift of a given LBG. The relations of Adelberger et al. (2005) that we use here are as follows:

For LBGs with only a redshift from the Lyα emission line we used:

$$z_{int} = z_{Ly\alpha} - 0.0033 - 0.0050(z_{Ly\alpha} - 2.7) \tag{4.1}$$

For objects with Lyα absorption and a measurement of z_{ISM} we used:

$$z_{int} = z_{ISM} + 0.0022 + 0.0015(z_{ISM} - 2.7) \tag{4.2}$$

And for objects with redshifts measured from both the Lyα emission line and the ISM absorption lines we used:

$$z_{int} = \bar{z} + 0.070\Delta z - 0.0017 - 0.0010(\bar{z} - 2.7) \tag{4.3}$$

where $\bar{z}$ is the mean of the Lyα redshift ($z_{Ly\alpha}$) and the ISM absorption line redshift (z_{ISM}) and $\Delta z \equiv z_{Ly\alpha} - z_{ISM}$. Adelberger et al. (2005) quote rms scatters of $\sigma_z = 0.0027, 0.0033, 0.0024$ respectively for each of the above relations based on their application to their optical and IR spectroscopic sample of LBGs.

As well as $z \approx 3$ galaxies, our selection also samples a small number of contaminating objects. These consist of low-redshift emission line galaxies (identified by [OII]3727Å, Hβ, [OIII]5007Å and Hα emission), low-redshift Luminous Red Galaxies (LRGs - identified by [OII]3727Å emission, Ca H, K absorption and the 4000Å break) and faint red stars (mostly M and K-type stars). We show examples of the spectra of several LBGs and contaminant low-redshift galaxies taken with the VLT VIMOS in this survey in figure 4.9.

All identified objects, including stars and low-redshift galaxies, were assigned a quality rating, q, based on the confidence of the identification. The value of q was assigned on a scale of 0 to 1, with 1 being the most confident and 0 being unidentified. All objects with $q < 0.5$ were rejected as spurious identifications and are not included in the spectroscopic catalogue used in the remainder of this work. LBGs were generally classified as follows:

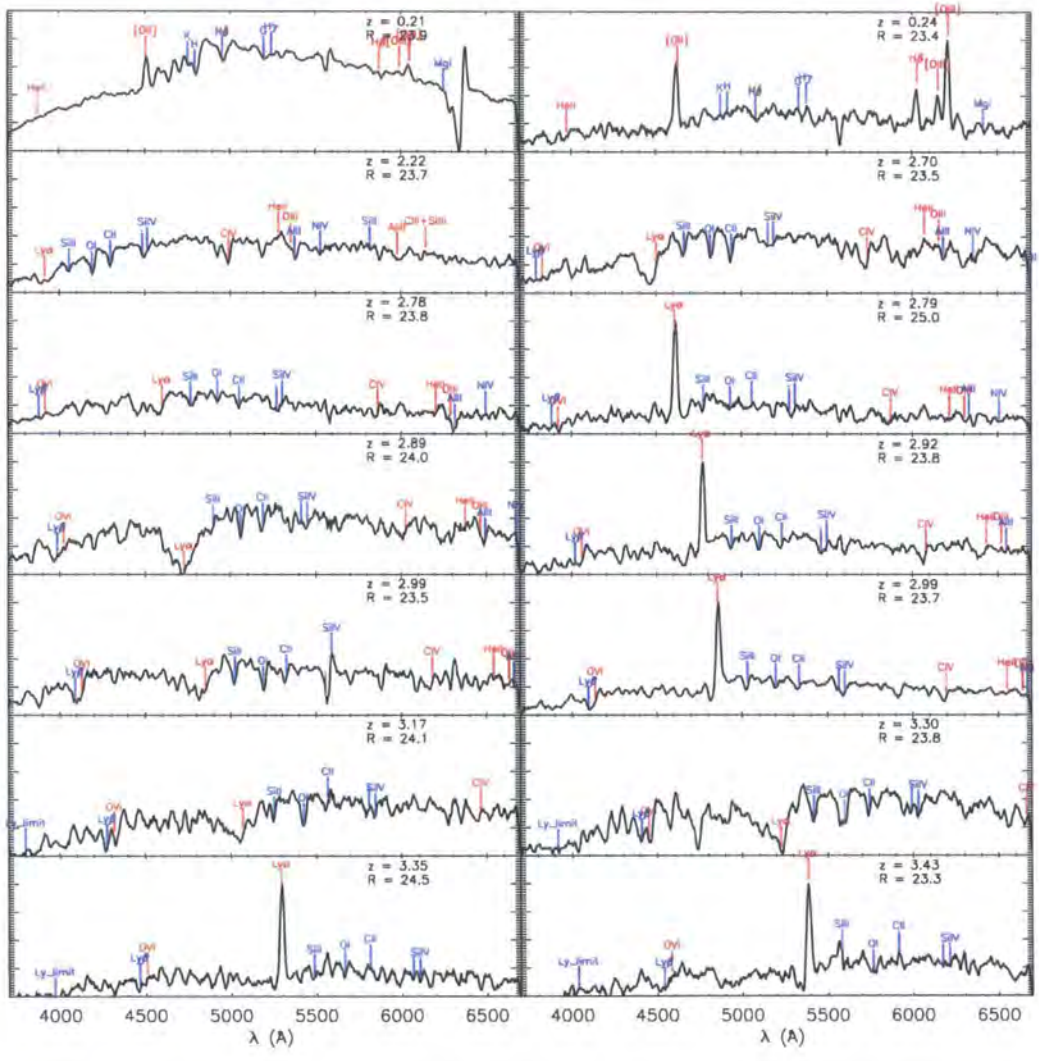

Figure 4.9: Example spectra taken using 10,000s integration time with the LR_Blue grism on the VLT VIMOS instrument. The top two spectra are examples of contaminating low-redshift galaxies. The remaining 12 panels show LBG spectra exhibiting both Lyα emission and absorption over the redshift range $2 < z < 3.5$. ISM lines are also clearly identifiable in the individual LBG spectra as is the Lyman limit. Both galaxy redshift and apparent R-band magnitude (Vega) are quoted for each object. Note that all the above spectra have been binned to ≈ 16Å.

- 0.5 - Lyα emission or absorption line evident plus some 'noisy' ISM absorption features.
- 0.6 - Lyα emission or absorption plus some ISM absorption features.
- 0.7 - Lyα emission or absorption plus most ISM absorption features.
- 0.8 - Clear Lyα emission or absorption plus all ISM absorption features.
- 0.9 - Clear Lyα emission or absorption plus high signal-to-noise ISM features.

With this classification scheme, we have obtained 512, 263, 172, 110 and 92 $z > 2$ galaxies with q =0.5, 0.6, 0.7, 0.8 and 0.9 respectively.

4.3.4 Sky Density, Completeness & Distribution

We summarize the numbers of objects observed in table 4.4. Our mean sky-density for successfully identified LBGs is $0.27 arcmin^{-2}$, whilst the percentage of $z > 2$ galaxies in the entire observed sample (the completeness given in table 4.4.) is 32.2%. The remaining observed objects are a mix of low-redshift galaxies, stars and unidentifiable objects (generally very low-signal to noise spectra). In the worst case field (J1201+0116), we have almost as many low-redshift galaxies as high redshift detections. We attribute this to the relatively poor depth of the imaging observation in this field. The result is a success rate of only $\approx \frac{1}{5}$. Further to this we also note that the PKS2126-158 field is at a relatively low galactic latitude and thus as a higher proportion of contamination by galactic stars. However, the field still shows a high proportion of $z > 2$ galaxies.

In figure 4.10 and table 4.5 we summarize the redshift distributions of each of our sample selections in our observed fields. The overall redshift distribution across all fields is shown in the bottom panel of figure 4.10, with the black histogram showing the redshift distribution from UBVI selected objects from J0124+0044 and the red, green, light blue and dark blue histograms showing the LBG_DROP, LBG_PRI1, LBG_PRI2 and LBG_PRI3 respectively. The overall mean redshift for our confirmed LBG sample is $\bar{z} = 2.87 \pm 0.34$. Looking at the redshift distributions for the different selection criteria, it is evident from both the plots and the tabulated data that the separate selection sets give slightly differing (but overlapping) segments of the redshift distribution. As may be expected, the

Table 4.4: Summary of objects identified in the VLT VIMOS observations. Example spectra of the high-redshift and low-redshift galaxies are shown in figure 4.9. All nine identified $z > 2$ QSO spectra are provided in figure 4.16.

Field	Subfields	Galaxies $z > 2$	QSOs $z > 2.0$	Galaxies $z < 2.0$	Stars	Completeness
Q0042-2627	4	343 ($0.38 arcmin^{-2}$)	1	83	3	39.0%
J0124+0044	4	255 ($0.28 arcmin^{-2}$)	0	51	16	30.6%
HE0940-1050	3	180 ($0.27 arcmin^{-2}$)	0	26	33	35.9%
J1201+0116	4	133 ($0.15 arcmin^{-2}$)	5	122	63	19.0%
PKS2126-158	4	238 ($0.27 arcmin^{-2}$)	3	24	115	36.4%
Total	19	1149 ($0.27 arcmin^{-2}$)	9	306	227	32.2%

Table 4.5: Redshift ranges of $z > 2$ galaxies identified from each of our photometric selections.

Field	LBG_PRI1	LBG_PRI2	LBG_PRI3	LBG_DROP
Q0042-2627	2.75 ± 0.28	2.67 ± 0.27	2.65 ± 0.29	3.01 ± 0.30
J0124+0044		2.86 ± 0.34		
HE0940-1050	3.01 ± 0.33	2.73 ± 0.29	2.93 ± 0.39	3.11 ± 0.22
J1201+0116	2.71 ± 0.29	2.64 ± 0.41	2.62 ± 0.31	2.75 ± 0.31
PKS2126-158	2.98 ± 0.29	2.73 ± 0.27	n/a	3.24 ± 0.29
All fields	2.90 ± 0.32	2.72 ± 0.28	2.66 ± 0.30	2.99 ± 0.35

LBG_DROP selection is the most biased towards the higher end of our redshift distribution, with an overall mean redshift across all our samples of $\bar{z} = 2.99$. The mean LBG redshift for the three remaining selection sets appears to increase with increasing U-B colour, with $\bar{z}$ =2.66, 2.77 and 2.90 for the LBG_PRI3, LBG_PRI2 and LBG_PRI1 respectively. We also show the redshift distributions for each individual field in the top five panels of figure 4.10, with the LBG_DROP, LBG_PRI1, LBG_PRI2 and LBG_PRI3 plotted as red, green, light blue and dark blue respectively as in the 'all fields' plot. In each field we again see that the LBG_PRI3 selection preferentially selects the lowest redshift range, followed by LBG_PRI2, LBG_PRI1 and LBG_DROP showing the highest redshift range (although this is less pronounced in the J1201+0116 field in which the imaging depths were least faint).

We illustrate the distribution of our LBG sample in each of our 5 fields in figure 4.11. The fields are ordered by R.A. top to bottom and all identified $z > 2$ galaxies (filled

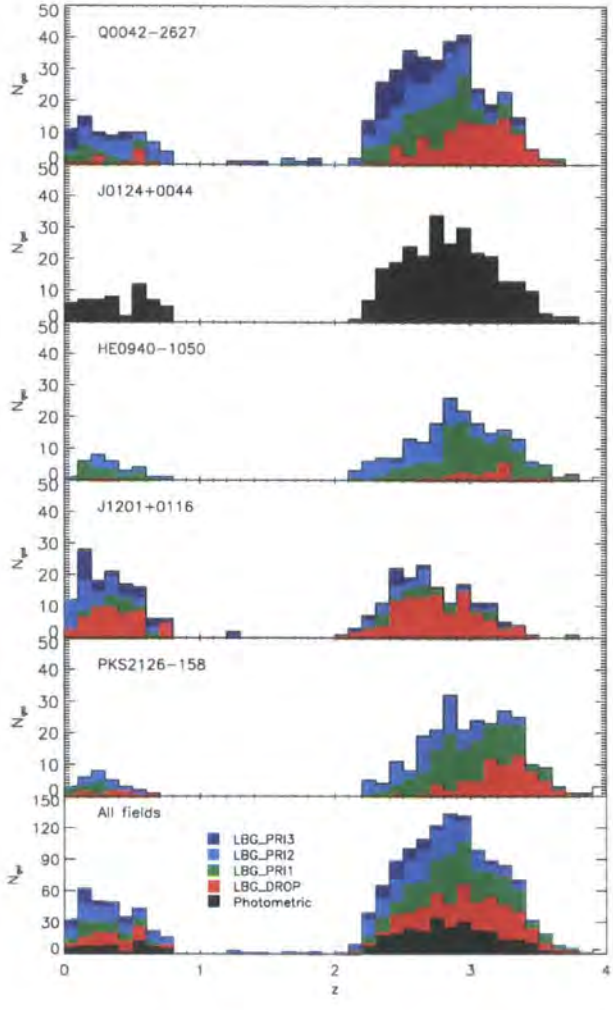

Figure 4.10: Differential redshift distribution in each of our fields and summed over all fields. We show the number counts split by selection criteria: LBG_DROP (red histograms), LBG_PRI1 (green histograms), LBG_PRI2 (pale blue histograms) and LBG_PRI3 (dark blue histograms). Although the selections overlap significantly, the difference in redshift coverage between the four selections is clearly evident with LBG_DROP biased towards the highest redshift range down to LBG_PRI3, which is biased towards the lowest. The mean redshifts for each selection are given in table 4.5.

blue circles) are shown along with all known $z > 2$ QSOs identified from the NASA Extragalactic Database. We also plot QSOs identified in our own QSO survey which is described further in chapter 6.

In figure 4.12 we plot the number of identified LBGs in magnitude bins for each of our fields. The filled histograms show the cumulative numbers of successfully identified objects (including interlopers as well as $z > 2$ galaxies) split by their selection criteria. LBG_DROP selected objects are shown by the red histogram, LBG_PRI1 by the green histogram, LBG_PRI2 by the cyan histogram and LBG_PRI3 by the blue histogram. The distribution of all spectroscopically observed objects is given by the solid line histogram in each case. As the J0124+0044 objects were not selected using the same selection criteria, these are simply left as a single group shown by the filled black histogram. In all fields, we see that we are successfully identifying objects down to the magnitude limit of R= 25.5 (I= 25 in the case of J0124+0044), although a significant number of objects remain unidentified in each field at the fainter magnitudes as spectral features become more difficult to discern in the spectra. We note also that the shapes of the overall magnitude distributions are biased more towards brighter objects in the Q0042-2627 and J1201+0116 fields in which a greater number of LBG_PRI3 objects are included (and also the imaging depths achieved in these fields are shallower than in the other fields).

We now compare our overall predicted number densities to those of Steidel et al. (1999, 2003). Taking the data plotted in figure 4.12, we estimate the number densities we might expect from our whole LBG candidate sample. To do this, we multiply the number of candidates selected in each field by the fraction of spectroscopically observed candidates that were successfully identified as $z > 3$ galaxies. The result for the data from the four fields with R_{Vega} data is shown in figure 4.13 (black triangles). The filled orange circles show the number counts of Steidel et al. (2003), whilst the open red circles show the number counts of Steidel et al. (1999). Both of these datasets have been converted from the AB magnitude system to the Vega magnitude system with a shift of $R_{Vega} = R_{AB} - 0.18$. Based on these estimates, we find that the numbers of $z \approx 3$ galaxies are consistent with those of Steidel et al. (2003) at magnitudes of $R < 24.5$. However, we find our numbers are significantly ($\approx 2\times$) lower than those of Steidel et al. (2003) at magnitudes of $R > 24.5$. This is not a physical phenomenon, but rather a consequence of the relatively low number counts in the U and B-band imaging observations from a number of our imaging fields (in

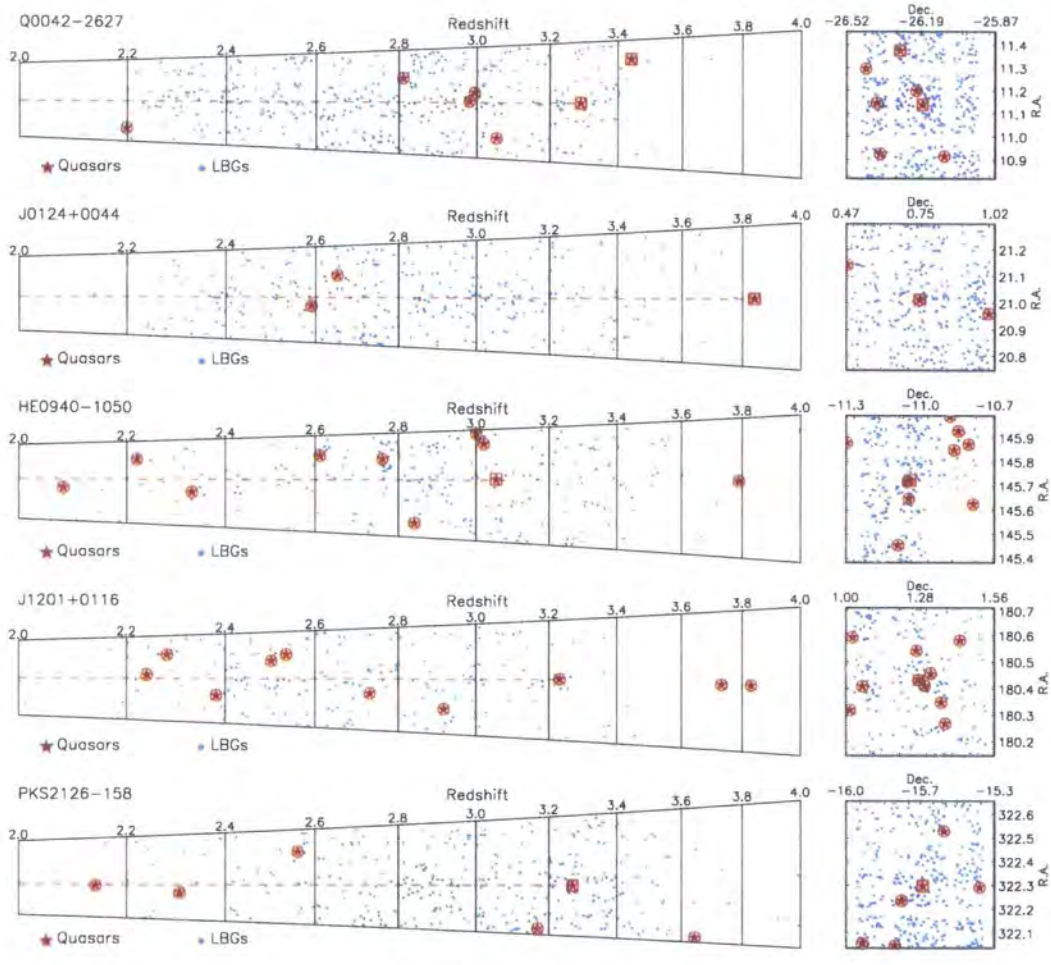

Figure 4.11: Distribution in R.A., Declination and redshift for each of our five fields. From the top panel, the fields are: Q0042-2627, J0124+0044, HE0940-1050, J1201+0116 and PKS2126-158. Spectroscopically confirmed LBGs are marked by blue filled circles and known QSOs by dark red stars. We also identify those QSOs with low-resolution spectra available (red circles, i.e. VLT VIMOS and AAT AAOmega), medium-resolution spectra (red crosses, i.e. SDSS - SDSS J1201+0116 only) and high-resolution spectra (red squares, i.e. VLT UVES, Keck HIRES).

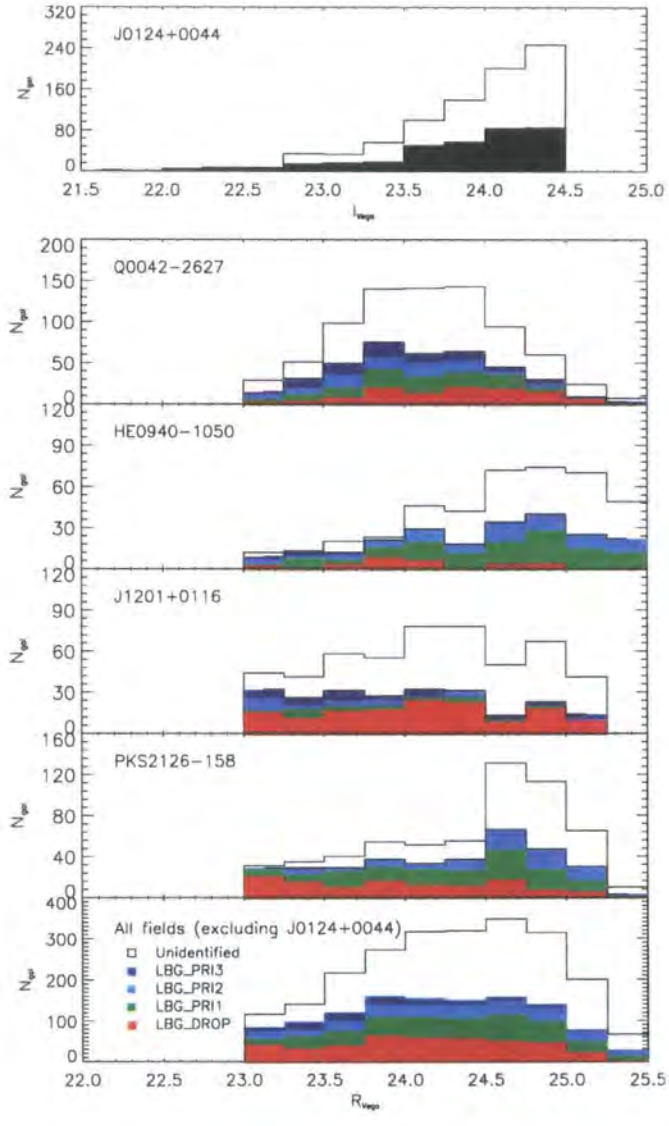

Figure 4.12: Number counts as a function of R_{Vega} (I_{Vega}) magnitude for all fields (J0124+0044). The shaded histograms show the numbers of successfully identified objects with the colour coding the same as in figure 4.10: the red histogram shows counts of LBG_DROP objects, the green shows LBG_PRI1 objects, the pale blue shows LBG_PRI2 objects and the dark blue shows LBG_PRI1 objects. The unshaded histogram shows the total number of candidates observed with VLT-VIMOS in each field (i.e. the gap between the shaded regions and solid line shows the number of unidentified objects as a function of magnitude).

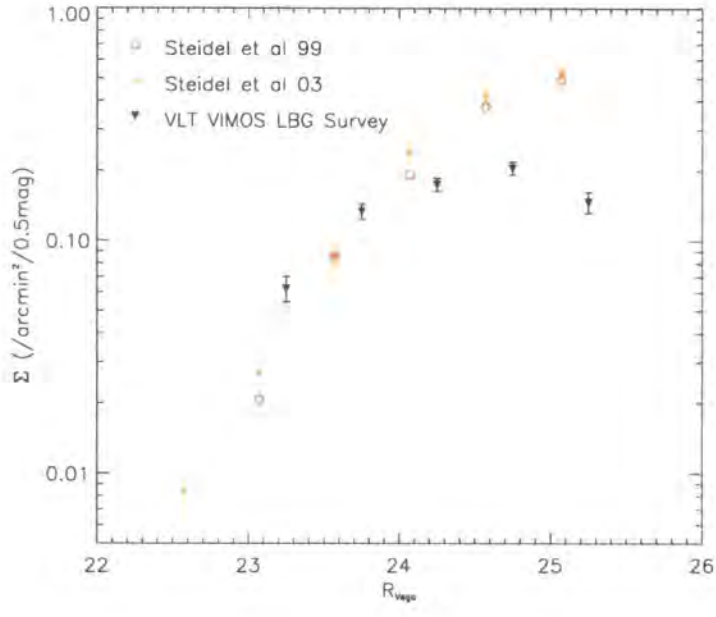

Figure 4.13: Predicted sky densities of the LBG sample as a function of R_{Vega} magnitude. The overall sky density is estimated as the fraction of successfully identified LBGs to the number of candidates observed spectroscopically, multiplied by the total number of candidates (black triangles). We also plot the sky densities of Steidel et al. 1999 (open red circles) and Steidel et al. 2003 (closed orange circles). Note that we shift the Steidel et al. (1999, 2003) R_{AB} magnitude bins by -0.18 to convert to R_{Vega}.

particular Q0042-2627 and J1201+0116).

4.3.5 Velocity Offsets and Composite spectra

The galaxy spectra contain a wealth of information as illustrated by the work of Shapley et al. (2003). We now look at how our spectra compare to previous work in terms of the well documented velocity offsets between the different spectral features. For the galaxies that exhibit both measurable Lyα emission and ISM absorption lines, we calculate the velocity offsets between these lines, $\Delta v = v_{em} - v_{abs}$. The distribution of Δv for our galaxy sample is shown in figure 4.14. The distribution of velocity offsets exhibits a strong peak with a mean of $\langle \Delta v \rangle = 570 \pm 310 kms^{-1}$. This compares to a value measured by Shapley et al. (2003) of $650 kms^{-1}$.

Following this, we have produced composite spectra in several equivalent width bins in order to produce spectra with increased signal-to-noise. The composite spectra are shown

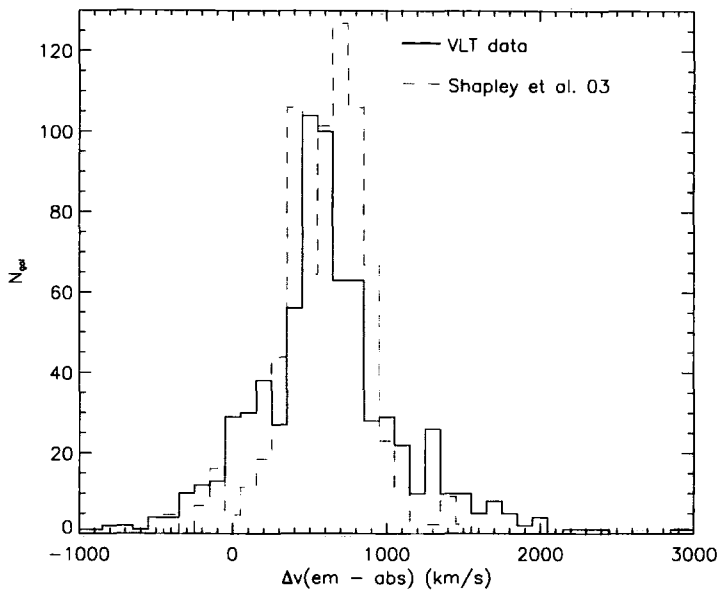

Figure 4.14: Distribution of the velocity offsets between ISM absorption lines and the Lyα emission line in individual galaxies from our redshift survey (solid histogram). We measure a mean velocity offset between Lyα emission and the ISM lines of $\Delta\bar{V} = 570 \pm 310 kms^{-1}$. The dashed histogram shows the result of Shapley et al. (2003).

in figure 4.15 and are split into (from bottom to top) equivalent width ranges of W< -20Å (50 galaxies), -20Å<W<0Å (134 galaxies), 0Å<W<5Å (166 galaxies), 5Å<W<10Å (218 galaxies), 10Å<W<20Å (181 galaxies), 20Å<W<50Å (112 galaxies) and W>50Å (60 galaxies). Between them, the composites incorporate a total of 921 of the galaxy sample, excluding any objects with $q < 0.5$ or with significant contamination, for example from zeroth order overlap. The key emission and absorption features are marked and we can immediately identify both absorption and weak emission for the ISM lines: SiII, OI, CII, SiIV and CIV. All the features have been marked at $z = 0$. The presence of an offset between the apparent line centres of the Lyα emission and the ISM absorption lines is evident in these composite spectra, a result of the asymmetry of the Lyα, potentially combined with an intrinsic difference between the velocities of the sources of the Lyα emission and the ISM absorption features.

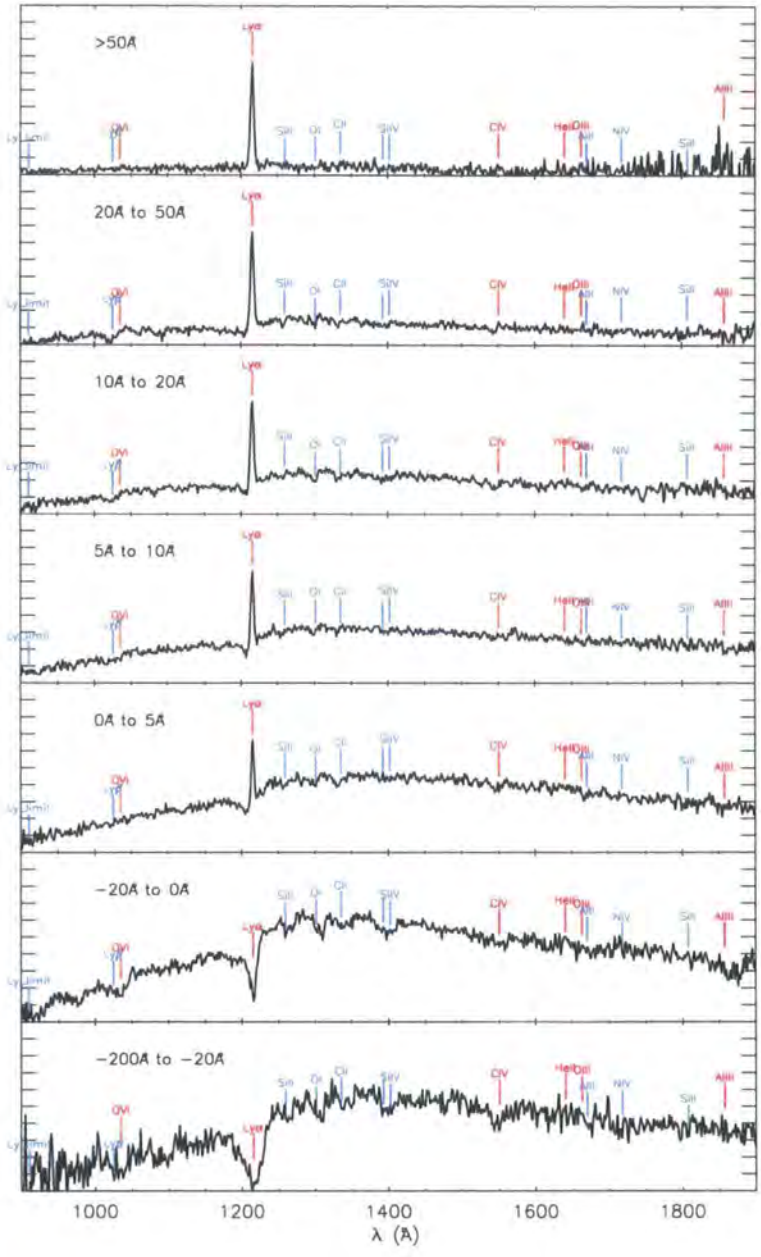

Figure 4.15: Composite spectra collated from our VLT VIMOS sample. Each spectrum shows the composite of a sub-sample of the LBGs, grouped by Lyα equivalent width measurements. The key UV spectral features discussed in the text (i.e. Lyα and Lyβ emission/absorption, ISM absorption lines) are all evident in these composite spectra.

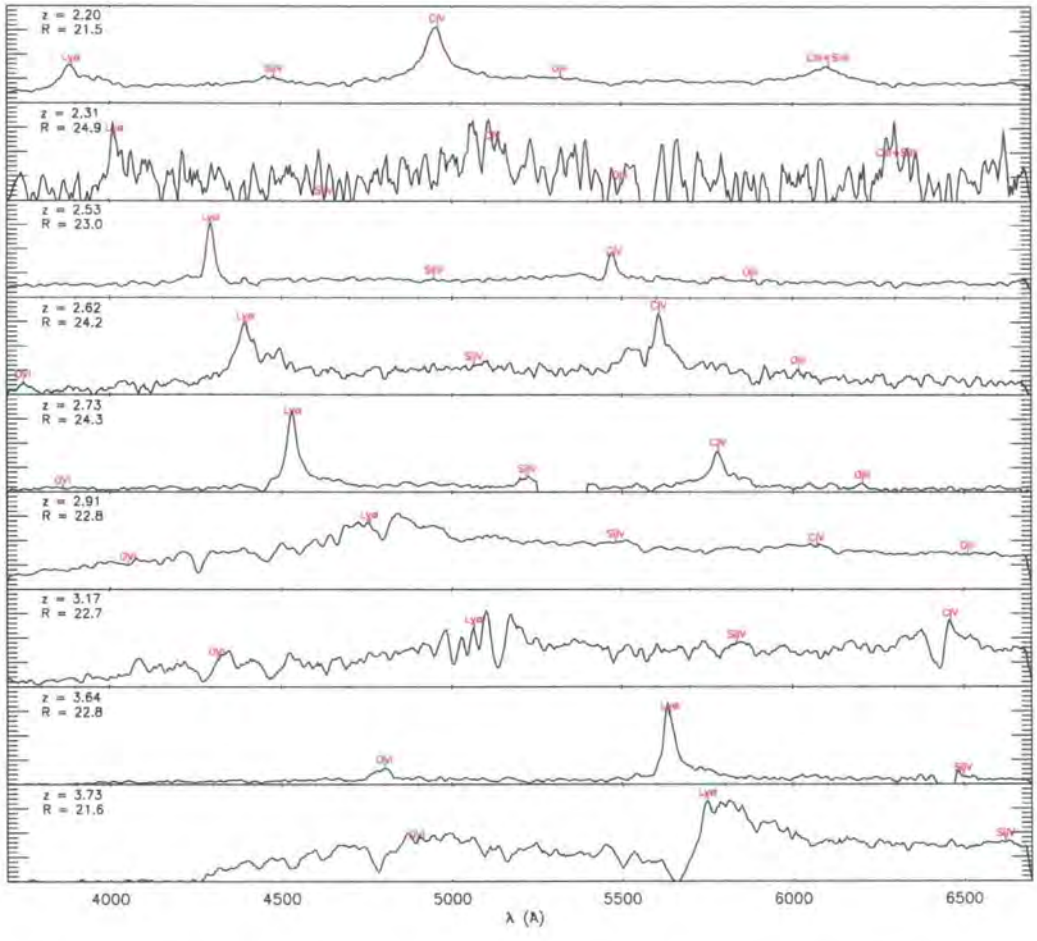

Figure 4.16: The $z > 2$ QSOs observed as part of the VLT VIMOS LBG survey. Redshifts and R-band magnitudes are given for each QSO and significant broad emission features are marked.

4.3.6 VLT AGN and QSO observations

As discussed earlier, we also targeted a small number of $z \approx 3$ QSO candidates also selected from our UBR photometry. In combination with this, due to the similarity in the shape of the spectra of LBGs and QSOs, the LBG selections also produced a handful of faint QSOs and AGN. We present the spectra of these in figure 4.16, whilst the numbers of QSOs in each field are given in table 4.4. The positions of the observed QSOs are also shown in figure 4.11.

4.4 Summary

In this chapter I have reviewed the VLT VIMOS survey of $z \approx 3$ galaxies in a number of fields around bright $z > 3$ QSOs. In total this survey has so far produced a total of 1149 LBGs at redshifts of $2 < z < 3.5$ over a total area of $1.18 deg^2$. Based on the fraction of objects observed, we find that our estimated number densities are consistent with previous studies of LBGs in this redshift range. Overall we obtain a mean redshift of $\tilde{z} = 2.87 \pm 0.34$. From the data obtained we have shown evidence for the existence of galactic outflows with comparable offsets between emission and absorption lines as in previous studies (e.g. Pettini et al 1998, 2002 and Shapley et al. 2003)

This concludes the data acquisition for the initial phase of the VLT VIMOS LBG Survey. At the time of writing, these are the most up to date observations, however the survey has a number of observations yet to be acquired. It is expected that over the coming 12-24 months, the survey will be increased by another 25 VIMOS pointings. Upon completion therefore, the survey will comprise a total of 34 VLT pointings, building significantly on this initial data-set providing a catalogue of $\approx 3,000$ $z > 2$ galaxies over a sky area of $2.11 deg^2$.

CHAPTER 5

CLUSTERING OF LBGS AT REDSHIFT 3

5.1 Introduction

In this chapter I describe the clustering analysis of the $z \approx 3$ galaxy sample, incorporating estimates of the angular auto-correlation function for our complete LBG candidates catalogue and the redshift space auto-correlation function of our spectroscopically confirmed sample. Developing from these estimates, I use a combined sample of the VLT VIMOS LBG data-set and the Steidel et al. (2003) data-set to evaluate the 2-D correlation function and place constraints on the infall parameter, β. Finally, I relate the clustering properties of the $z \approx 3$ sample to those of lower-redshift samples.

5.2 Angular Auto-correlation Function

We now evaluate the clustering properties of our candidate and spectroscopically confirmed LBGs. Using all five of our imaging fields, we begin by calculating the angular correlation function of the LBG candidates. We use all LBG candidates selected using the LBG_PRI1, LBG_PRI2, LBG_PRI3 and LBG_DROP selections plus the candidates from the J0124+0044 field. The total number of objects is thus 18,489 across an area of 1.8deg^2. We calculate the angular auto-correlation function using the Landy-Szalay estimator:

$$w(\theta) = \frac{< DD > -2 < DR > + < RR >}{< RR >} \tag{5.1}$$

Where DD is the number of galaxy-galaxy pairs at a given separation, θ, DR is the number of galaxy-random pairs and RR is the number of random-random pairs. The random catalogue were produced for each field, with random sky coordinates within identical fields of view to the data and sky densities of 20$\times$ the real object sky densities. The numbers of DD, DR and RR pairs were calculated using the NPT tree code software (Gray et al., 2004) and the results are shown in the top panel of figure 5.1. Both field to field and

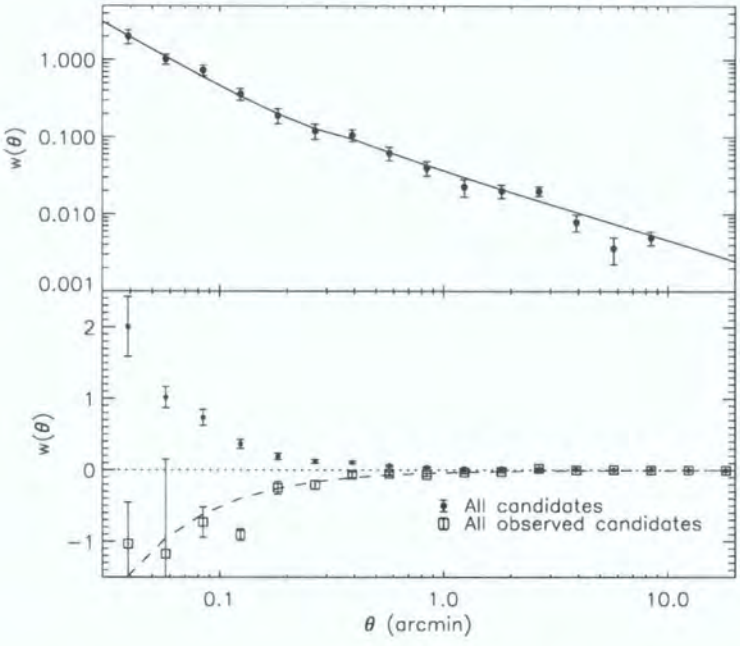

Figure 5.1: Top panel: The angular correlation function, $w(\theta)$, from our imaging fields. The circular points show the correlation function for the photometrically selected sample around our 5 V≈17 z≈3 QSOs. Lower panel: Filled circles are as in the top panel. Open squares show the correlation function calculated from only the sub-sample of objects that were observed using the VLT VIMOS. A significant loss of clustering is evident at scales of $\theta < 2'$, which corresponds to the dispersion length along the VIMOS CCD for a single object.

Poisson error estimates were calculated and found to be comparable, whilst in figure 5.1 we plot the Poisson error estimate, which is given by:

$$\sigma_w = \sqrt{\frac{1 + w(\theta)}{DD}} \tag{5.2}$$

We now estimate the real-space correlation function from our measurement of $w(\theta)$ using the same method as performed in section 3.4 for the low-redshift emission line galaxy samples. As before we use Limber's formula (Phillipps et al., 1978) with our measured redshift distribution (figure 4.10) to find the form of the real-space correlation function, $\xi(r)$ that best fits the measured LBG $w(\theta)$. Again we use a double power-law form of $\xi(r)$ given by:

$$\xi(r < r_b) = \left(\frac{r_{0,1}}{r}\right)^{-\gamma_1}, \xi(r > r_b) = \left(\frac{r_{0,2}}{r}\right)^{-\gamma_2} \tag{5.3}$$

Where r_b is the break at which the power-law is split between the two power-laws, $r_{0,1}$

and $r_{0,2}$ are the clustering lengths above and below the break, γ_1 and γ_2 are the slopes below and above the break and all distances are in comoving coordinates. Firstly, we find that $w(\theta)$ is best fit with a break at $r_b = 0.4h^{-1}Mpc$. Performing a χ^2 fit to the data, we then determine best fitting values for the power-law parameters of $r_{0,1} = 1.70^{+0.09}_{-0.14}\mathrm{h}^{-1}\mathrm{Mpc}$, $\gamma_1 = 2.65^{+0.09}_{-0.14}$, $r_{0,2} = 4.32^{+0.13}_{-0.12}\mathrm{h}^{-1}\mathrm{Mpc}$ and $\gamma_2 = 1.90^{+0.09}_{-0.14}$. The resultant $w(\theta)$ calculated from these values is also plotted in the top panel of figure 5.1 (solid black line).

We note now that based on our spectroscopic observations, the data from which $w(\theta)$ is measured will contain a number of stars and low redshift galaxies. Considering the stars, these should have a predominantly unclustered distribution and act to reduce the amplitude of the measured angular correlation function. In contrast the presence of low redshift galaxies will act to increase the amplitude. This will especially be the case in the J1201+0116 field in which we have shown that our sample contains almost as many low redshift galaxies as $z > 2$ galaxies.

Comparing this to previous results, da Ângela et al. (2005b) obtained a clustering length of $r_0 = 4.48^{+0.09}_{-0.14}\mathrm{h}^{-1}\mathrm{Mpc}$ with a slope of $\gamma = 1.76^{+0.08}_{-0.09}$ and Adelberger et al. (2003) obtained $r_0 = 3.96 \pm 0.15\mathrm{h}^{-1}\mathrm{Mpc}$ and $\gamma = 1.55 \pm 0.29$, both using a single power-law function fit ($\xi(r) = (r/r_0)^{-\gamma}$) to the same $z \approx 3$ LBG data (Steidel et al., 2003). Based on the angular auto-correlation measurement from our sample, these results would suggest that our sample has a comparable clustering strength to that of (Steidel et al., 2003) with both samples exhibiting a clustering strength of $r_0 \approx 4\mathrm{h}^{-1}\mathrm{Mpc}$. We note however that our sample has a slightly broader redshift range, which would be expected to lead to a lower measurement of the clustering amplitude. A further comparison can be made with the work of Foucaud et al. (2003), who measured an amplitude of $r_0 = 5.9 \pm 0.5h^{-1}Mpc$ from the $w(\theta)$ of a sample of 1294 LBG candidates, slightly higher than the above measurements.

5.2.1 Slit Collisions

From calculating the angular-correlation function, the next step is to use the redshift information from our spectroscopic survey in order to confirm the clustering properties of the LBGs. However, before we do this we need to evaluate the extent to which we are limited in observing close-pairs by the VIMOS instrument set up. Using the LR_Blue grism, each dispersed spectrum covers a length of 570 pixels on the CCD. Further to this each slit has a length (perpendicular to the dispersion axis) in the range of 40-120 pixels.

Given the VIMOS camera pixel scale of $0.205''/pixel$, each observed object therefore covers a minimum region of $\approx 120'' \times 8.2''$, in which no other object can be targeted.

In order to evaluate this effect, we calculate the angular auto-correlation function for only those candidate objects that were targeted in our spectroscopic survey, $w_{slits}(\theta)$. To do so we require a tailored random catalogue that accounts for the geometry of the VIMOS CCD layout. We therefore create random catalogues for each sub-field using a mask based on the layout of the four VIMOS quadrants, excluding any objects that fall within the $2'$ gaps between adjacent CCDs. The sky-density of randoms in each sub-field is set to be $20\times$ the sky-density of data points in the corresponding parent field. From this data, which consists of ≈ 3400 targeted objects, we calculate $w_{slits}(\theta)$ using the Landy-Szalay estimator (equation 5.1). The result is shown in the lower panel of figure 5.1 (again pair counts are computed using the NPT tree code software of Gray et al. 2004). The original angular auto-correlation function calculated from all LBG candidates in our five fields is given by the filled circles, whilst $w_{slits}(\theta)$ is given by the open squares. At $\theta > 2'$ the two correlation functions follow each other closely, however at separations of $\theta < 2'$ we see a significant loss of clustering showing the effect of the instrument setup. At redshifts of $z \approx 3$, this corresponds to a comoving separation of $r \approx 2.6\mathrm{h}^{-1}\mathrm{Mpc}$.

We now use this result to estimate a weighting factor with which to attempt to correct for this effect following the method used by Croom et al. (2001). To determine the appropriate weighting function we fit a power-law to $w_w = w_0 - w_{slit}$, where w_0 is the original angular auto-correlation function including all candidate objects and w_{slit} is the corresponding function for the sub-sample consisting only of those objects that were observed with the VLT VIMOS. The resultant power-law is then $w_{pl} = 0.0738\theta^{-1.052}$, giving a weighting function for close pairs of:

$$W = \frac{1}{1 - 0.0738\theta^{-1.052}} \tag{5.4}$$

Applying this weighting function to DD pairs at separations of $\theta < 2'$ then allows the recovery of the original correlation function from the VIMOS sub-sample correlation function down to separations of $\theta \approx 0.1'$. Below $\theta \approx 0.1'$ however we are unable to recreate the original candidate correlation function as no close pairs can be observed below this scale due to the slit lengths ($8'' < \theta < 24''$) used in the VIMOS masks.

5.3 Redshift Space Correlation Function

The redshift-space correlation function, $\xi(s)$, is an estimator of the clustering of a galaxy population as a function of the redshift-space distance, s, which is given by $s = \sqrt{\sigma^2 + \pi^2}$. In this instance, σ is the transverse separation given by the separation on the sky, whilst π is the line of sight separation given by the comoving distance calculated from the difference in the redshifts of two objects. Now, using the sample of 1,149 $q \geq 0.5$ spectroscopically confirmed $z > 2$ galaxies, we estimate $\xi(s)$ using the estimator:

$$\xi(s) = \frac{\langle DD(s) \rangle}{\langle DR(s) \rangle} - 1 \tag{5.5}$$

Where $\langle DD(s) \rangle$ and $\langle DR(s) \rangle$ are the numbers of data-data pairs and data-random pairs at a given separation s. Again the random catalogues were produced individually for each field to match the VIMOS geometry and with 20× the number of objects as in the associated data catalogues. The DD pairs were then calculated using the angular weighting function (equation 5.4) applied to pairs with separations of $\theta < 2'$. The result is shown in figure 5.2 (filled circles) with Poisson error estimates. Plotted for comparison is the result of da Ângela et al. (2005b) (open squares), whilst the dashed line gives their single power-law (real-space) correlation function, with $r_0 = 4.48h^{-1}Mpc$.

The two samples show good agreement at separations of $s > 8\mathrm{h}^{-1}\mathrm{Mpc}$, however the VLT sample shows a significant drop in clustering strength at $s < 8\mathrm{h}^{-1}\mathrm{Mpc}$ compared to the da Ângela et al. (2005b) measurement. This seems at odds with the $w(\theta)$ result, which points to the two samples having similar clustering strengths. However, we note that the estimate of the line-of-sight distances are sensitive to any errors on the redshift estimate, which will have a subsequent effect on the measured redshift space correlation function. We therefore now estimate the effect of our redshift errors on this result. The error on a given LBG redshift is a combination of the error on the spectral feature measurements (taken as the mean of the Lyα emission line error and the ISM absorption lines, i.e. $\approx 300kms^{-1}$) combined with the error on the estimation of the intrinsic redshift from that measured from the outflow features ($\approx 200kms^{-1}$). Combining these uncertainties gives an overall combined error of $\sigma_z = \sqrt{(300kms^{-1})^2 + (200kms^{-1})^2} \approx 360kms^{-1}$. The overall error on the separation between two galaxies is therefore $\sqrt{2} * 360kms^{-1} \approx 510kms^{-1}$.

In addition to the observational uncertainties, the redshift of each galaxy also incorpo-

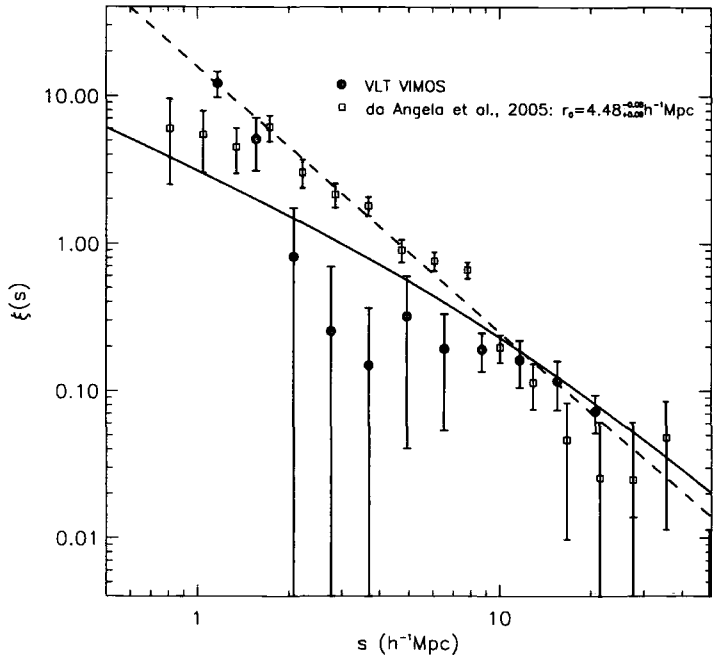

Figure 5.2: Redshift-space clustering function, $\xi(s)$, calculated from the spectroscopically identified Lyman Break galaxies. The filled circles give the measured clustering from the five fields observed using the VLT VIMOS, whilst the open squares show the measurement of the clustering of the Steidel et al. (2003) LBG sample by da Ângela et al. (2005b). The single-power law fit to the clustering result from da Ângela et al. (2005b) is shown by the dashed line. A reduction in clustering strength is observed in the VLT sample at $s < 8\mathrm{h}^{-1}\mathrm{Mpc}$, which is consistent with a clustering strength of $r_0 = 4.32h^{-1}Mpc$ (as measured from the LBG angular correlation function) when redshift distortions are taken into account (solid black line - $\xi(r) = (r/4.32h^{-1}Mpc)^{-1.9}$ modelled with $a = 650kms^{-1}$ and $\beta = 0.25$).

rates the peculiar velocity of that galaxy. This itself consists of two elements: on the small scale random pair-wise velocities lead to the well known "finger of god" effect, whilst on larger scales bulk infall motion towards over-dense regions becomes a significant factor.

We now model these effects in conjunction with our estimated redshift errors and determine how they would affect the correlation function measured from the LBG auto-angular correlation function, $w(\theta)$, and if this is consistent with the measured LBG redshift-space correlation function, $\xi(s)$. Following Hawkins et al. (2003), we use the real-space prescription for the large scale infall effects given by Hamilton (1992) whereby the 2-D infall affected correlation function is given by:

$$\xi'(\sigma,\pi) = \xi_0(s)P_0(\mu) + \xi_2(s)P_2(\mu) + \xi_4(s)P_4(\mu) \tag{5.6}$$

Where $P_l(\mu)$ are Legendre polynomials, $\mu = cos(\theta)$ and θ is the angle between r and π. For a simple power-law form of $\xi(r)$ the forms of $\xi_l(s)$ are:

$$\xi_0(s) = \left(1 + \frac{2\beta}{3} + \frac{\beta^2}{5}\right)\xi(r) \tag{5.7}$$

$$\xi_2(s) = \left(\frac{4\beta}{3} + \frac{4\beta^2}{7}\right)\left(\frac{\gamma}{\gamma-3}\right)\xi(r) \tag{5.8}$$

$$\xi_4(s) = \frac{8\beta^2}{35}\left(\frac{\gamma(2+\gamma)}{(3-\gamma)(5-\gamma)}\right)\xi(r) \tag{5.9}$$

Where γ is the slope of the power-law form of the real-space correlation function: $\xi(r) = (r/r_0)^{-\gamma}$. As in Hawkins et al. (2003), the infall affected clustering, $\xi'(\sigma,\pi)$ is then convolved with the random motion (in this case the pair-wise motion combined with the measurement uncertainties):

$$\xi(\sigma,\pi) = \int_{-\infty}^{\infty} \xi'(\sigma,\pi - \nu/H_0)f(\nu)d\nu \tag{5.10}$$

Where $f(\nu)$ is the profile of the random motions for which we use:

$$f(\nu) = \frac{1}{a\sqrt{2}}e^{-(\sqrt{2}|\nu|/a)} \tag{5.11}$$

With this form of $f(\nu)$, the effective velocity dispersion, a, is the combination of the random pair-wise peculiar motion and the observational uncertainty. For the purposes of

this estimate we combine the estimated galaxy-pair velocity error of $510 kms^{-1}$ with the pair-wise velocity given by da Ângela et al. (2005b) of $400 kms^{-1}$, giving a total pair-wise velocity of $\approx 650 kms^{-1}$. Now taking an estimate of $\beta = 0.25$ from da Ângela et al. (2005b), we may model the effect of these velocity components on the LBG sample $\xi(\sigma, \pi)$ using a single power-law with $r_0 = 4.32 h^{-1} Mpc$ and $\gamma = 1.90$ (assumed from the $w(\theta)$ result). The form of $\xi(s)$ estimated from the resultant $\xi(\sigma, \pi)$ is plotted in figure 5.2 (solid black line).

With the given parameters, this model of the redshift-space correlation function from the estimated real-space correlation function appears relatively consistent with the measured result. Convolving the velocity dispersion into the correlation function effectively reduces the measured clustering at scales of $r_0 < 8 h^{-1} Mpc$.

5.4 Estimating β

We now use the modeling methods described above to place constraints on the infall parameter, β, using the combination of our VLT LBG data and the LBG data of Steidel et al. (2003). β quantifies the extent of large scale coherent infall towards overdense regions via the imprint of the infall motion on the observed redshift space distortions. Given its dependence on the distribution of matter, measuring β can provide a useful dynamical constraint on $\Omega_m(z)$ (Hamilton, 1992; Heavens & Taylor, 1995; Hawkins et al., 2003; da Ângela et al., 2008; Cabré et al., 2009). It relates the real-space clustering and redshift-space clustering as outlined in the previous section (see equations 5.6 to 5.9).

As discussed in section 5.3, the two samples possess comparable real-space clustering strengths, with measured clustering lengths of $r_0 = 4.32^{+0.13}_{-0.12} h^{-1} Mpc$ and $r_0 = 4.48^{+0.09}_{-0.14} h^{-1} Mpc$ for the VLT and Steidel et al. (2003) samples respectively. We therefore combine the two samples and calculate the 2-point correlation function, $\xi(\sigma, \pi)$ of the whole sample.

The Steidel et al. (2003) sample consists of 831 $z > 2$ LBGs in the redshift range $2.67 < z < 3.25$, contained within 17 individually observed fields. Most of the fields are $\approx 8' \times 8'$ with a few exceptions (the largest field being $\approx 15' \times 15'$). These fields cover a total area of $0.38 deg^2$, with just a small number of the fields being adjacent. An overview of the data is given in table 5.1.

Table 5.1: Overview of the LBG survey fields of Steidel et al. (2003).

Field	Dimensions (arcmin^2)	Number of LBGs
Q0000-263	3.69×5.13	15
CDFa	8.80×8.91	34
CDFb	9.05×9.10	20
Q0201+1120	8.69×8.72	21
Q0256-000	8.54×8.46	42
Q0302-003	6.50×6.90	40
B20902+34	6.36×6.57	30
Q0933+2854	8.93×9.28	58
HDF-N	8.62×8.73	53
Westphal	15.0×15.1	176
Q1422+2309	7.28×15.5	109
3C 324	6.65×6.63	11
SSA22a	8.74×8.89	50
SSA22b	8.64×8.98	35
DSF2237a	9.08×9.08	39
DSF2237b	8.99×9.08	42
Q2233+1341	9.25×9.25	38
Total	$0.38 deg^2$	831

Combining the two datasets, we therefore have a total of 1,980 LBGs over a total area of $1.56 deg^{-2}$. We first estimate the clustering length of the combined sample by measuring the projected correlation function, $w_p(\sigma)$ (Davis & Peebles, 1983), which is given by:

$$w_p(\sigma) = 2\int_0^\infty \xi(\sigma,\pi)d\pi \tag{5.12}$$

We perform the integration over the line of sight range from $\pi = 0$ to $20h^{-1}Mpc$. This encompasses much of the bulk of the significant signal in the correlation function and performing the calculation with limits of $\pi = 0$ to $30h^{-1}Mpc$ gives little change to the results. The result is shown in figure 5.3 with the best fit clustering model determined by a χ^2 fit to the data. For the projected correlation function the simple power law form of $\xi(r)$ becomes:

$$w_p(\sigma)/\sigma = \left(\frac{\sigma}{r_0}\right)^{-\gamma}\left[\frac{\Gamma(0.5)\Gamma(0.5(\gamma-1))}{\Gamma(0.5\gamma)}\right] \tag{5.13}$$

Where $\Gamma(x)$ is the Gamma function. We perform the fit to the data using a fixed value for the slope of the function of $\gamma = 1.8$. With this value, we obtain $r_0 = 3.63\pm0.19h^{-1}Mpc$, which compares to an r_0 computed in a similar way for the Steidel et al. (2003) sample of $r_0 = 3.96 \pm 0.29h^{-1}Mpc$ (Adelberger et al., 2003).

Using the clustering length derived from our measurement of the combined sample projected correlation function, we now calculate the 2-point correlation function with which we may place constraints on the infall parameter, β. As with our determination of $\xi(s)$, we use the estimator given in equation 5.5 taking randoms tailored to each individual field, whilst errors are again calculated using the Poisson estimate (equation 5.2). The resultant $\xi(\sigma,\pi)$ is plotted in figure 5.4. To more clearly show the redshift distortions, we mirror the result (which is obtained purely in the positive σ and π directions) into the negative directions for the purpose of this plot. Having done this, the elongation in the π dimension, due to the pair-wise velocity dispersion and redshift errors, is clearly evident at small scales.

Now using this measurement of $\xi(\sigma,\pi)$, we may make an estimate of the infall parameter, β. For this we use the single power-law model of $\xi(r)$ based on the combined data with $r_0 = 3.63h^{-1}Mpc$ and $\gamma = 1.80$ with a fixed velocity dispersion of $a = 650kms^{-1}$. With these parameters set, we iteratively calculate the model outlined in equations 5.6 to 5.11 over a range of values of β. We then perform a simple χ^2 fitting analysis and estimate

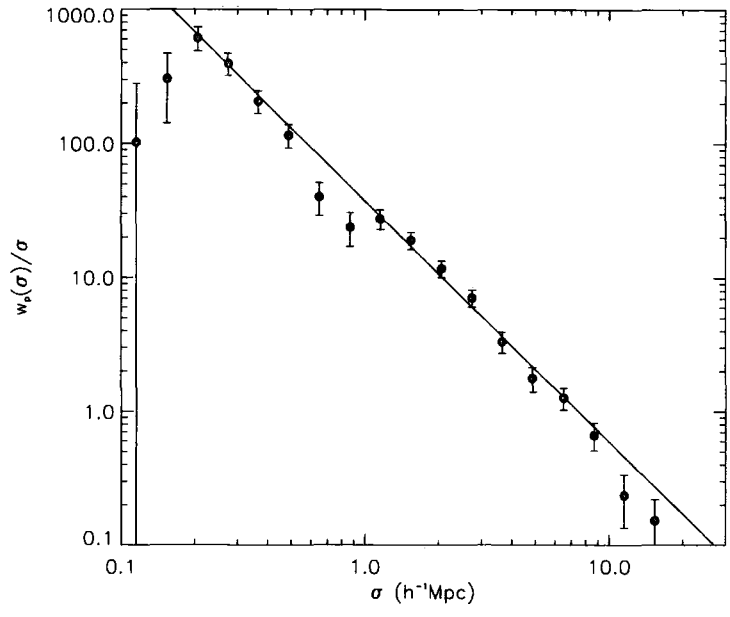

Figure 5.3: Projected correlation function, $w_p(\sigma)$ of the combined Steidel et al. (2003) and VLT LBG samples. The solid line shows the best fitting function characterised by $r_0 = 3.63 \pm 0.19 h^{-1} Mpc$ and a fixed slope of $\gamma = 1.8$.

a bias of $\beta_{LBG}(z \approx 3) = 0.23 \pm 0.09$ for our combined LBG sample. Comparing this to previous estimates of $\beta(z \sim 3)$, we find a somewhat lower figure than the work of da Ângela et al. (2005b) who estimate a value of $\beta = 0.25^{+0.05}_{-0.06}$ (though not inconsistent). As discussed by the same authors, the measurement of the bias of a sample of LBGs from the Canada-France Deep Survey by Foucaud et al. (2003) measured a value of $b = 3.5 \pm 0.3$, which given the WMAP ΛCDM cosmology gives $\beta = 0.27$.

These measurements provide a useful check of the impact of large scale dynamics on our measurement of the clustering of our $z \approx 3$ galaxies. The agreement with the result of da Ângela et al. (2005b) validates our use of their value of β in our earlier analysis of the clustering of our sample via $\xi(s)$.

5.5 Clustering Evolution

We now qualitatively compare the clustering strength of the LBG samples to that of lower redshift galaxies, using the same methods as in section 3.4. Thus, we first determine the volume-averaged correlation function at $20 h^{-1} Mpc$ using the single power-law form of the

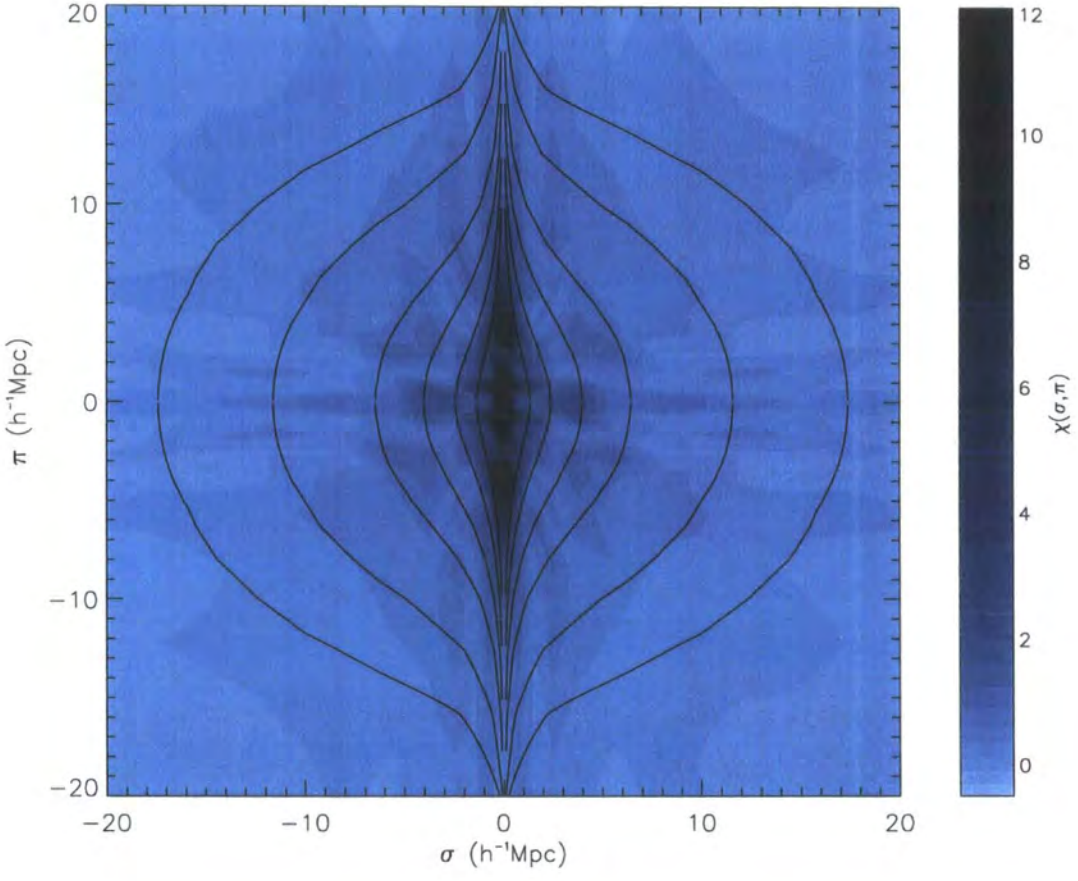

Figure 5.4: $\xi(\sigma, \pi)$ projected correlation function calculated from the spectroscopically confirmed LBGs from the combined Steidel et al. (2003) and VLT VIMOS LBG samples. The colour scale shows the measured signal, whilst the contour lines show the model calculated using the best-fitting infall parameter of $\beta = 0.23 \pm 0.09$, with a single power-law given by $r_0 = 3.63h^{-1}Mpc$ and $\gamma = 1.8$ combined with the estimated uncertainty in the LBG pair-wise positions of $a = 650kms^{-1}$.

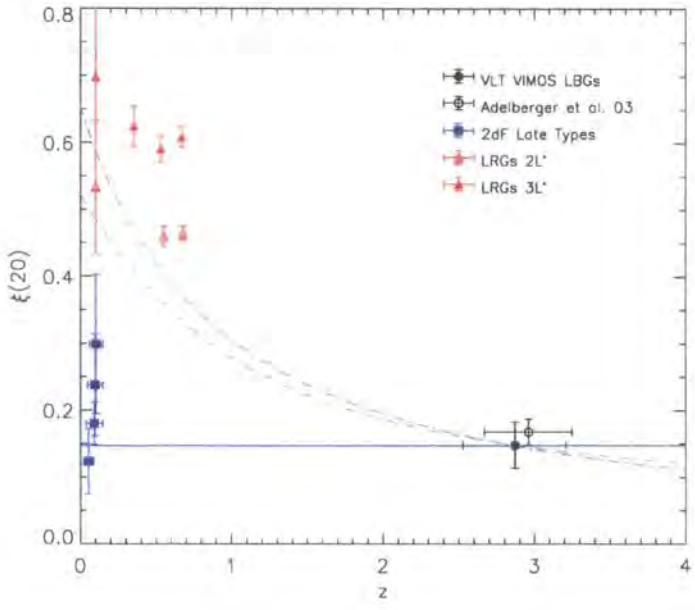

Figure 5.5: The volume-averaged correlation function, $\bar{\xi}(20)$, is plotted for our LBG sample alongside $\bar{\xi}_{20}$ measurements for several other galaxy populations. We also show the long-lived (dashed line) and stable (dot-dash line) clustering evolution models. The solid horizontal lines simply show the path of no clustering evolution in comoving space.

clustering of both our own and the Steidel LBG sample as prescribed in equation 3.5.

The result is shown in figure 5.5 with our own sample given by the filled circle and the Steidel et al. (2003) data given by the open circle. In addition, we also plot a number of low-redshift samples: $2L^*$ and $3L^*$ LRGs from Sawangwit et al. (2009) and the 2dF late type galaxies from Norberg et al. (2002). In order to perform a cursory analysis of the clustering evolution we use the three simple evolution models used in section 3.4: the long-lived model (dashed line); stable clustering (dot-dash line); and no evolution of the comoving-space clustering (solid line). These are all calculated identically to the methods laid out in section 3.4 and subsequently normalised to the VLT LBG sample clustering strength.

The apparent B-band magnitude range of our sample is $B = 25.69 \pm 0.76$. Using the overall redshift range of our sample ($z = 2.87 \pm 0.34$) and K+e corrections determined using the Bruzual & Charlot (2003) stellar population evolution, this equates to an absolute B-band magnitude of $M_B \approx -21.5 \pm 1.1$. First considering the LRG samples of Sawangwit et al. (2009), these have absolute i-band magnitudes of $M_{i(AB)} = -22.4 \pm 0.5$ and $M_{i(AB)} =$

-22.6 ± 0.4 for the $2L^*$ and $3L^*$ samples respectively, which based on typical elliptical galaxy colours would suggest absolute B-band magnitude ranges of $M_{B(Vega)} = -20.8 \pm 0.4$ and $M_{B(Vega)} = -21.0 \pm 0.4$. Now looking at the 2dF data, these are estimated to have absolute B-magnitude ranges of $-18 > M_{bj} > -19$, $-19 > M_{bj} > -20$, $-20 > M_{bj} > -21$ and $-20.5 > M_{bj} > -21.5$ (in order of lowest to highest clustering data-points).

Comparing the clustering of the LBG samples with the lower-redshift data, the $z \approx 3$ galaxies show clustering strengths comparable to the low-magnitude late types of Norberg et al. (2002). Given the large differences in the estimated absolute magnitudes however, it would seem unlikely that the LBG samples could be linked in evolutionary terms to these comparatively faint spirals. Taking the long-lived and stable clustering models on the other hand hint at a potential evolutionary link between the LBG populations and the low-redshift LRG populations, which are at least of comparable brightness. However, as evidenced by the range of low redshift clustering amplitudes, the clustering is heavily influenced by the sample brightness and population type and it is difficult to draw more solid conclusions from this exercise. It does seem clear however, that an increase in clustering (in the comoving frame) from redshifts of $z \sim 3$ to the low redshift Universe must have occurred in order for the LBG populations probed by this work and others to evolve into populations of comparable brightness at low redshift.

5.6 Summary

In this chapter I have reviewed the clustering properties of the VLT VIMOS LBG sample. Based on the angular auto-correlation function of the photometric LBG candidates, the redshift-space correlation function is estimated to take the form of a double power-law, with a break at $r_b = 0.4h^{-1}Mpc$. This is parametrised by a clustering length and slope below the break of $r_{0,1} = 1.70^{+0.09}_{-0.14}\mathrm{h}^{-1}\mathrm{Mpc}$ and $\gamma_1 = 2.65^{+0.09}_{-0.14}$ and above the break of $r_{0,2} = 4.32^{+0.13}_{-0.12}\mathrm{h}^{-1}\mathrm{Mpc}$ and $\gamma_2 = 1.90^{+0.09}_{-0.14}$. This measurement of the clustering at $r > 0.4h^{-1}Mpc$ is consistent with previous measurements of the clustering of LBGs at $z \approx 3$ made by Adelberger et al. (2003) and da Ângela et al. (2005b).

Following this I have measured the redshift-space LBG auto-correlation function. However, this appears to be significantly affected by the redshift estimate errors at scales of $r < 8h^{-1}Mpc$ and is well fit by the convolution of the power-law form of $\xi(r)$, estimated

from $w(\theta)$, with the estimated redshift errors of $360kms^{-1}$. Following this I go on to combine our LBG sample with that of Steidel et al. (2003) with the aim of measuring the infall parameter, $\beta(z = 3)$. I first estimate the combined clustering strength from the measurement of the projected correlation of the combined sample and find the data is best fit by a power-law with $r_0 = 3.63 \pm 0.19h^{-1}Mpc$. Fitting this power-law form of the correlation function to the measurement of $\xi(\sigma, \pi)$ from the combined data-set produces a best fitting infall parameter of $\beta = 0.23 \pm 0.09$.

CHAPTER 6

INTERACTIONS BETWEEN GALAXIES AND THE IGM AT z≈3

6.1 Introduction

We now use the VLT LBG data to investigate the relationship between gas and galaxies at $z > 2$. As discussed in the introduction the impact of galaxies on their surroundings is suspected to be a key factor in galaxy formation and evolution. Galactic scale winds powered by star-forming regions may heat the IGM, whilst also seeding it with metals.

Following on from Adelberger et al. (2003, 2005), we now look at performing a cross-correlation between our $z > 2$ galaxy sample and the IGM gas density as traced by the Lyα forest in QSO spectra. Both Adelberger et al. (2003) and Adelberger et al. (2005) used the LBG-Lyα cross-correlations to investigate the interactions between galaxies and the surrounding IGM and showed a decrease in quasar spectral flux close ($s < 5h^{-1}Mpc$) to LBGs corresponding to an increase in the gas density within these distances. Further to this, the results of Adelberger et al. (2003) exhibited an average upturn in the QSO spectral flux at separations of $s < 0.5h^{-1}Mpc$ from nearby LBGs, suggesting a local envelope of low density space surrounding the high-redshift galaxies, potentially the result of galactic winds pushing material out of the regions immediately around the galaxies. However, this result was based on a relatively small number of galaxies and was subsequently contradicted by the results of Adelberger et al. (2005) which showed a continued reduction in the QSO spectral flux and no sign of an upturn as in the previous result.

The VLT LBG data described thus far provides the foundation for further work in the vein of Adelberger et al. (2003, 2005), with a number of large samples of LBG within $s < 20h^{-1}Mpc$ of bright QSOs. In addition, we have surveyed the LBG fields for further $z > 2$ QSOs with which to perform the LBG-Lyα cross-correlation technique using the AAOmega instrument at the AAT.

In this penultimate chapter, I therefore describe the use of the VLT LBG data with a range of QSO data to investigate the relationship between galaxies and the IGM at

Table 6.1: QSOs used in the cross-correlation calculation.

Name	R.A.	Dec	z	Mag.	Facility
Q0042-2627	00:42:06.42	-26:27:45.3	3.289	$B_j = 18.47$	Keck
[WH091]0043-265	00:45:30.48	-26:17:09.8	3.45	$B_j = 19.37$	Keck
SDSS J0124+0044	01:24:03.77	+00:44:32.8	3.83	$g = 19.2$	UVES
HE0940-1050	09:42:53.40	-11:04:25.0	3.06	$B = 17.2$	UVES
SDSS J1201+0116	12:01:44.37	+01:16:11.6	3.233	$g = 17.7$	SDSS
PKS2126-158	21:29:12.17	-15:38:41.0	3.268	$V = 17.3$	UVES

$z \approx 3$. I first describe the QSO data available in these fields, both from archive resources (section 6.2) and from our own AAT observing (section 6.3), and describe the methods used to process these in preparation for the cross-correlation analysis (section 6.4). The cross-correlation and results are presented in sections 6.5 and 6.6.

6.2 High Resolution QSO Spectra

6.2.1 Data

For the cross-correlation we use high resolution UVES and Keck HIRES spectra of the bright QSOs Q0042-2627, Q0043-265, SDSS J0124+0044, HE0940-1050 and PKS2126-158 and a medium resolution spectrum of SDSS J1201+0116 from the SDSS archive. As discussed in section 4.2.1, UVES archive high resolution spectra are available for SDSS J0124+0044, HE0940-1050 and PKS2126-158, whilst a Keck/HIRES (Vogt et al, 1994) archive spectrum is available for Q0042-2627 and a SDSS 1Å spectrum is available for SDSS J1201+0116. Added to this we also have a Keck/HIRES spectrum for a second bright QSO in the Q0042-2627 field. This is Q0043-265, which is at a redshift of $z = 3.45$. A summary of the bright QSOs is provided in table 6.1. The associated reduced spectra are shown in figure 6.1.

The observations of Q0043-265 were taken on the night of 22nd of August 2007 using Keck/HIRES with the Red cross-disperser and C1 dekker, giving a slit width of 0.861 arcsec and resolution of 6.7 km/s (FWHM). Three 3,600 second exposures and one 1,800 second exposure were taken. These were extracted and wavelength calibrated using the Makee package (http://spider.ipac.caltech.edu/staff/tab/makee/). The individual exposures were combined to form a single spectrum using the UVES-popler software

(http://astronomy.swin.edu.au/~mmurphy/UVES_popler). The wavelength coverage is 4000-8535Å, whilst there are gaps at 5425-5498Å (see figure 6.1) and 7016-7094Å due to the gaps between the three HIRES detectors. There are also smaller gaps between Echelle orders at wavelengths longer than 6400Å, where orders are too wide to be completely recorded by the detector.

The SDSS J1201+0116 spectrum was obtained directly from the SDSS Data Archive Server (DAS) and as such had been sky subtracted, corrected for telluric absorption and spectrophotometrically calibrated using the SPECTRO2D pipeline. It has a wavelength coverage of 3800Å to 9250Å and a resolution of R=2000.

6.3 Low-Resolution QSO Sample

6.3.1 Data & Selections

In each of the above fields any known z≈3 QSOs within the magnitude limits were also observed. These mainly originated from private communications and a search of the NASA Extragalactic Database (NED). All such objects and their sources are listed in Appendix B.

6.3.1.1 VLT VIMOS LBG Survey Imaging Data

The primary selections in Q0042-2627, J0124+0044, J1201+0116 and PKS2126-158 were performed using the imaging data from the MOSAIC Imagers at KPNO and CTIO described in section 4.2.2. Candidate selection was performed based on the results of Richards et al. (2004), adapted to the U, B and R (or U, B and V in the case of J0124+0044) photometry available from the MOSAIC imaging. From this, two selection methods are used to select objects likely to be $z > 2$ QSOs. The first is the UV-excess selection, which targets stellar-like objects with large U-B colours and is relies on the separation of QSOs from stars via their non-thermal spectra. The second is the UV-Dropout selection, which selects objects with detections in both B and R (or V) but no detection in the U-band photometry and is based on the Lyman-Break feature in QSO spectra passing through the U band (as discussed for LBGs in the previous chapter).

With our Vega U, B and R band photometry, the selections take the following form:

- UVX

  $18 < R_{Vega} < 22$

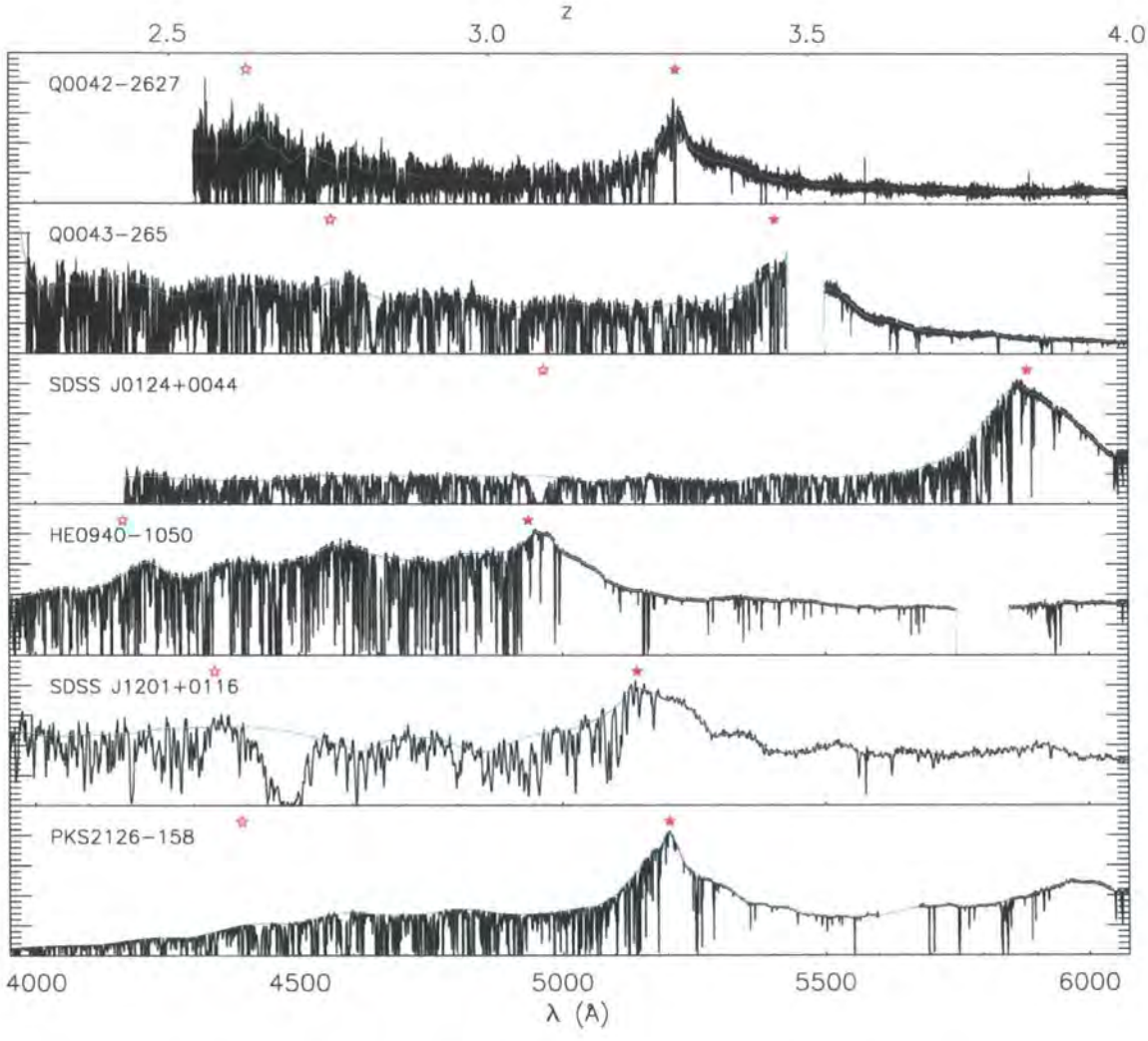

Figure 6.1: High resolution QSO spectra from the VLT UVES, the Keck and the SDSS spectrograph. The lower axis gives the observed wavelength, whilst the upper axis gives the Lyα redshift. The black lines show the observed spectra, whilst the blue line shows the continuum level determined as outlined in the text. Wavelengths of the intrinsic QSO Lyα are shown by the filled stars and intrinsic Lyβ are shown by the open stars. Note the DLA in the spectrum of SDSS J1201+0116, which is removed prior to our estimate of the cross-correlation.

$B_{Vega} - R_{Vega} < 1.1$

$B_{Vega} - R_{Vega} < 0.54(U_{Vega} - B_{Vega}) - 0.35$ **OR** $B_{Vega} - R_{Vega} < 0.1$

$(U_{Vega} - B_{Vega}) > 0.6$

- UV Drop

  $18 < R_{Vega} < 22$

  $B_{Vega} - R_{Vega} < 1.1$

  no U_{Vega} detection

The UVX and UV Dropout selections are shown for the four fields in figures 6.2 to 6.5. The solid blue line shows the boundary of the QSO selection, whilst selected QSO candidates are shown by blue stars (UVX) and green triangles (UV Dropouts). The contours and black points show the objects classed as stellar like (based on the Sextractor star-galaxy separation) in each field in the magnitude range $16 < R_{Vega} < 23$ ($15 < V_{Vega} < 23$ for the J0124+0044 field), which illustrates how the selection is designed to select outliers from the main stellar locus with high U-B colours.

6.3.1.2 MegaCAM Data

In the HE0940-1050 field, the primary selections were performed using imaging data from the MegaCAM instrument at the Canada-France-Hawaii Telescope (CFHT). MegaCAM offers a significant advantage over the CTIO data available for this field due to its $1° \times 1°$ field of view, whilst providing comparable magnitude depths. The data was taken from 14th to the 27th April 2004 (PI: P. Petitjean) and has been released via the CFHT Legacy Survey (CFHTLS) archive. In this work we use MegaPipe stacked images and sextracted catalogues providing u, g and r (AB) band magnitudes (as provided by P. Petitjean). The total integration times are 6800s, 3100s and 3720s in the u, g and r bands respectively, whilst the mean seeing in each stack was $1.13''$, $0.96''$ and $0.94''$.

Using this data candidates were selected using the UVX and UV drop-out methods described above, tailored to the u, g and r band MegaCAM data. These took the form of the following constraints:

- UVX

  $18 < r_{AB} < 22$

  $g_{AB} - r_{AB} < 1.1$

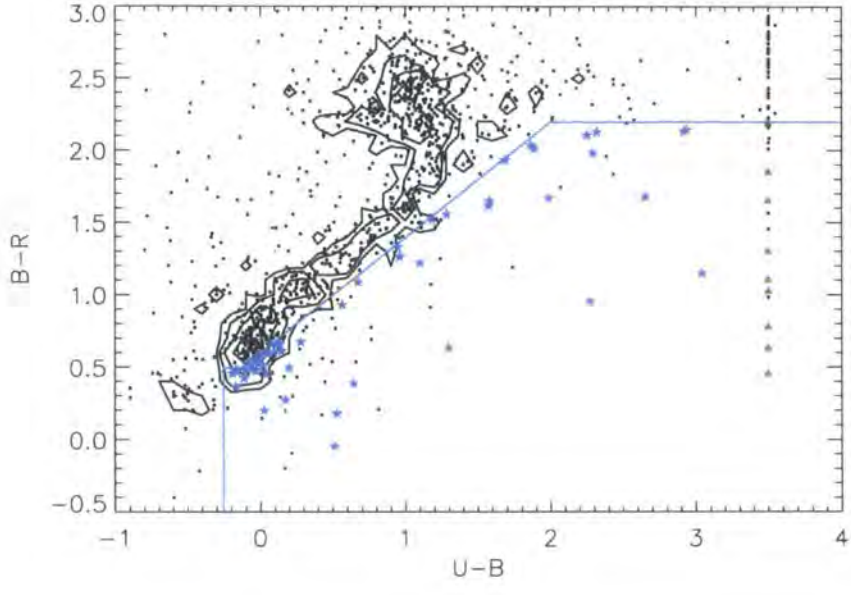

Figure 6.2: QSO selections for the $0.5° \times 0.5°$ Q0042-2627 field with U, B and R band photometry. The contours show the distribution of stellar-like objects (based on the Sextractor star-galaxy separator), whilst the black points show all objects classed as stellar like with $16 < R_{Vega} < 23$. The blue stars show those objects selected using the UVX selection and the green stars show objects selected using the UVDrop selection (all given a U-B=3.5 for plotting purposes). The blue line shows the boundary of the UVX selection.

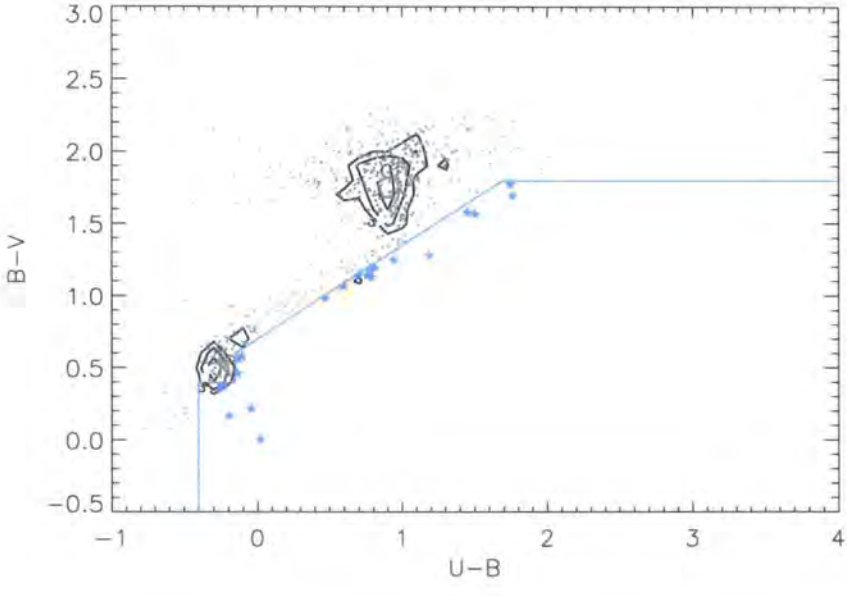

Figure 6.3: QSO selections for the $0.5° \times 0.5°$ J0124+0044 field with U, B and V band photometry. The contours show the distribution of stellar-like objects (based on the Sextractor star-galaxy separator), whilst the black points show all objects classed as stellar like with $15 < V_{Vega} < 23$. The blue stars show those objects selected using the UVX selection and the green stars show objects selected using the UVDrop selection (all given a U-B=3.5 for plotting purposes). The blue line shows the boundary of the UVX selection.

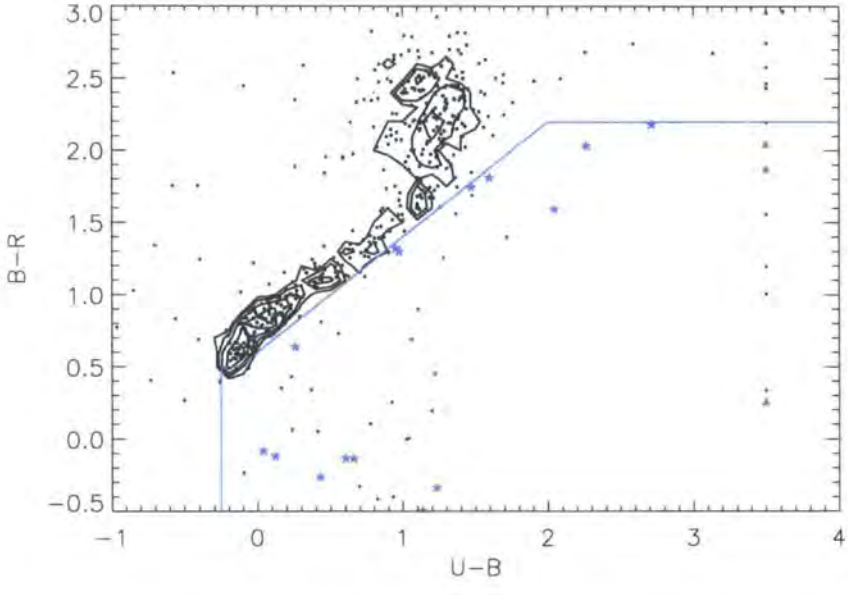

Figure 6.4: QSO selections for the $0.5° \times 0.5°$ J1201+0116 field with U, B and R band photometry. The contours show the distribution of stellar-like objects (based on the Sextractor star-galaxy separator), whilst the black points show all objects classed as stellar like with $16 < R_{Vega} < 23$. The blue stars show those objects selected using the UVX selection and the green stars show objects selected using the UVDrop selection (all given a U-B=3.5 for plotting purposes). The blue line shows the boundary of the UVX selection.

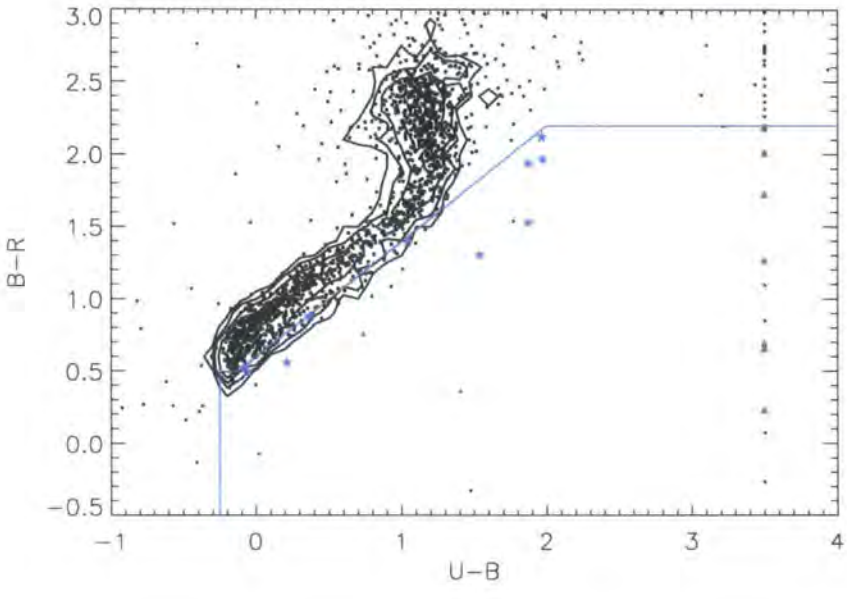

Figure 6.5: QSO selections for the $0.5° \times 0.5°$ PKS2126-158 field with U, B and R band photometry. The contours show the distribution of stellar-like objects (based on the Sextractor star-galaxy separator), whilst the black points show all objects classed as stellar like with $16 < R_{Vega} < 23$. The blue stars show those objects selected using the UVX selection and the green stars show objects selected using the UVDrop selection (all given a U-B=3.5 for plotting purposes). The blue line shows the boundary of the UVX selection.

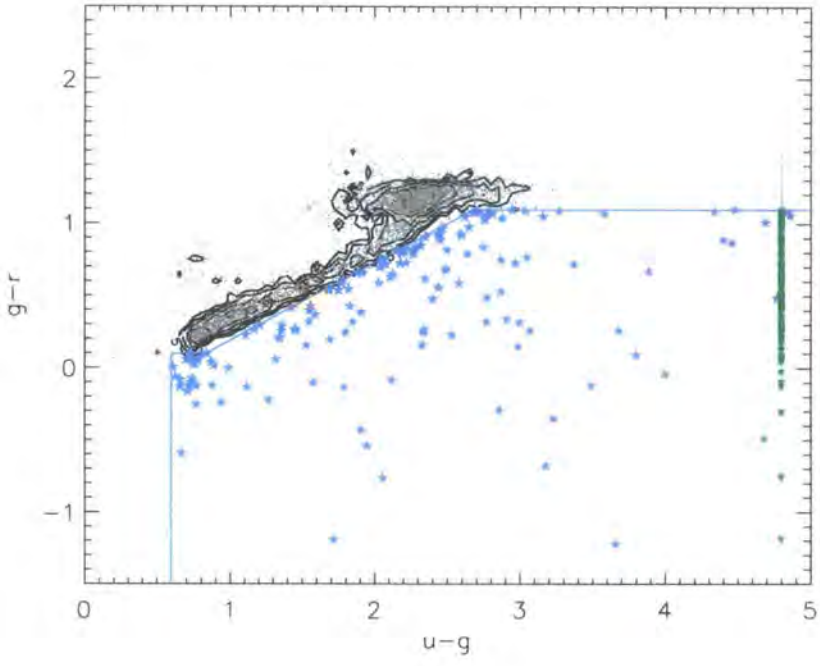

Figure 6.6: Photometric selection of QSOs in the HE0940-1050 field using ugr AB magnitudes from MegaCAM data. The contours show the stellar locus in the field and grey points show all stellar-like objects with magnitudes $r_{AB} < 22$. The filled stars and triangles show the UVX (145 candidates) and UVdrop (130 candidates) selected objects respectively (note: objects with no u detection are given a value of (u-g)=4.8).

$g_{AB} - r_{AB} < 0.54(u_{AB} - g_{AB}) - 0.35$ **OR** $g_{AB} - r_{AB} < 0.1$

$(u_{AB} - g_{AB}) > 0.6$

- UV Drop

  $18 < r_{AB} < 22$

  $g_{AB} - r_{AB} < 1.1$

  no u_{AB} detection

Only objects with a sextracted stellar classification of $CLASS\_STAR > 0.8$ were included in the candidate selection. This gave a selection of 145 UVX objects and 130 UV drop-out galaxies in the $1° \times 1°$ MegaCAM field around HE0940-1050. The selection is shown in figure 6.6, where UVX selected candidates are shown by filled stars and UVdrop selected candidates are shown by filled triangles.

Table 6.2: Details of observations from AAT AAOmega.

Field	R.A.	Dec	Obs. date	Exp. time	Grisms	Seeing
Q0042-2627	11.141646	-26.19251	10/07/07	7,200s	1500V, 1000R	2.0″
J0124+0044	21.019300	+0.340858	24-25/10/08	21,600s	570V, 385R	1.5 – 2.0″
HE0940-1050	145.722577	-11.07437	5-6/02/08	14,600s	570V, 385R	1.2 – 1.6″
J1201+0116	180.435059	+1.268840	5-6/02/08	9,000s	570V, 385R	1.2 – 1.6″
PKS2126-158	322.299364	-15.64416	29/06/08	9,000s	570V, 385R	1.5 – 2.0″

6.3.1.3 SDSS NBC QSO Candidate Catalogue

In order to add further QSO candidates and to maximise the use of the whole 2dF field of view, the SDSS photometric QSO candidate selections of Richards et al. (2004) have been included in our target lists for the J0124+0044 and J1201+0116 fields.

6.3.1.4 APM Data

In the remaining three fields, further photometric data was acquired from the APM catalogues. Although not as deep as our central imaging or the SDSS data, the APM supplies coverage over the whole 2dF area in each of the three fields, allowing the maximal use of the observing area. U, B_j and R band imaging data was obtained for all three fields and the UVX and UV Dropout selections applied to supply further $z > 2$ QSOs.

6.3.2 AAT QSO Observations

Observations took place on the AAOmega instrument on the AAT, over a period from March 2007 to October 2008 (see table 6.2). All five QSO fields were observed during this period. The first field, Q0042-2627, was observed using the 1500V and 1300R grisms providing a wavelength coverage of 4250Å to 6850Å. The remaining fields were all observed with the lower resolution grisms, 570V and 385R, providing higher signal-to-noise and wavelength coverage (3800Å to 8900Å).

For each observation, dome-flats, sky-flats and arcs were taken for each configuration and reductions were performed using the 2dFDR software. The final spectra for the successfully confirmed QSOs in the central $0.5° \times 0.5°$ observed regions (i.e. those with LBGs from the LBG survey) are shown in figures 6.7 to 6.12.The solid grey line gives the QSO signal, whilst the variance is shown by the solid red line in each case. The full list

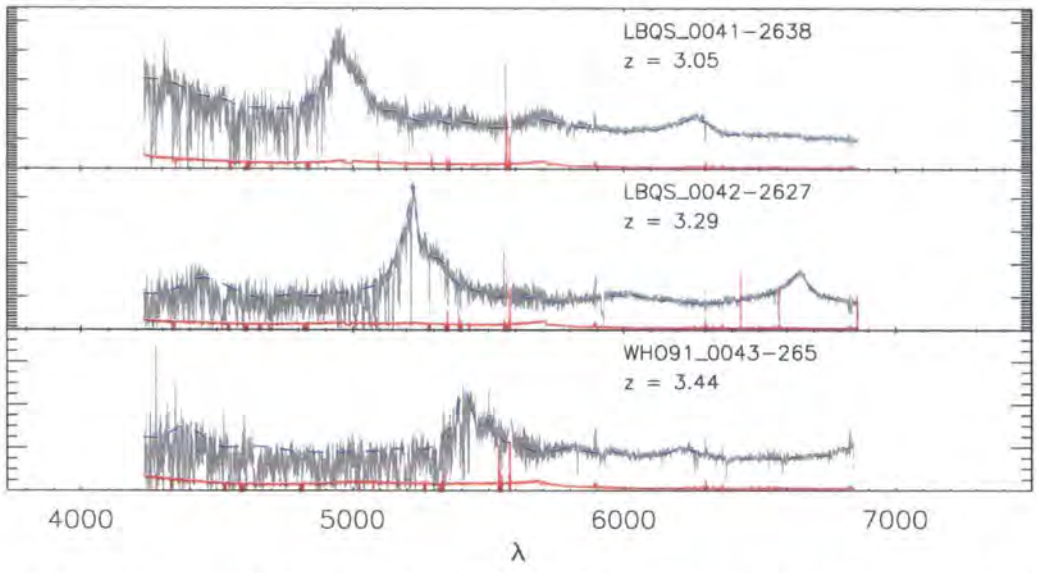

Figure 6.7: QSO spectra obtained with the AAT AAOmega spectrograph using the 1500V and 1000R grisms in the Q0042-2627 field. Only QSOs from the central $0.5° \times 0.5°$ region (i.e. those that overlap with the LBG data) are shown. The grey line shows the spectrum, whilst the blue dashed line shows the estimated continuum level and the red line shows the estimated noise level. A full list of the Q0042-2627 QSOs is given in table B.1. (Note that the shorter spectral coverage in these spectra compared to the other fields is due to these being observed with the medium resolution filters as opposed to the low resolution filters.)

of confirmed QSOs in each field is provided in Appendix B.

We show our observed sky density of $z > 2.2$ QSOs as a function of R_{Vega} band magnitude in figure 6.13 (circles). The data includes all spectroscopically confirmed $z > 2.2$ QSOs in each of the observed fields, covering a combined area of $15.7 deg^2$. As a comparison, we show the COMBO-17 completeness corrected sky densities of Wolf et al. (2003). At magnitudes of $R_{Vega} < 22$ Wolf et al. (2003) quote a sky density of $41.8 deg^{-2}$ for $z > 2.2$ QSOs, whilst our observations sample an average quasar sky-density of $7.6 deg^{-2}$, again for $z > 2.2$, across all five fields. In addition we show the redshift distribution of the AAOmega high-redshift QSO sample in figure 6.14.

6.3.3 Final Low-Resolution QSO Sample

For the purposes of the cross-correlation we limit our QSO sample to only those QSOs from the AAT AAOmega observations that lie within $5'$ of the QSO fields. Added to this, we also include a number of QSOs from the "Quasars near Quasars" (QNQ) survey

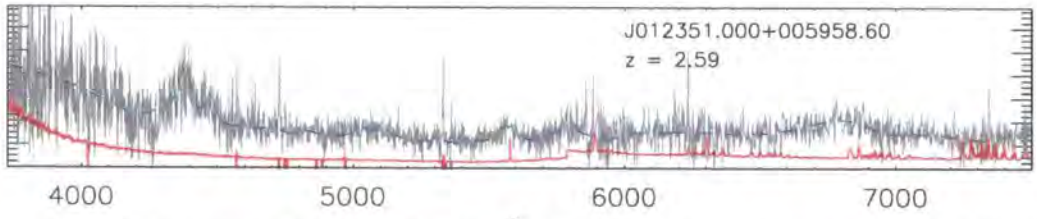

Figure 6.8: QSO spectrum obtained with the AAT AAOmega spectrograph using the 1500V and 1000R grisms in the J0124+0044 field. The grey line shows the spectrum, whilst the blue dashed line shows the estimated continuum level and the red line shows the estimated noise level. This is the only QSO confirmed within the central $0.5° \times 0.5°$ region (aside from the central bright QSO itself). A full list of the J0124+0044 QSOs is given in table B.2.

observed with FORS2 on the VLT. Full details of this data can be obtained from Worseck & Wisotzki (2008). Further to this we also add the spectra of the central bright QSOs from table 6.1. To do so, we re-sample the high resolution spectra to the pixel-scale obtained with the low-resolution AAT grisms.

The full list of QSOs used for the cross-correlation of Lyα with LBGs is given in table 6.3.

6.4 Continuum Fitting of QSO Spectra

In order to perform the cross-correlation analysis, we require the transmissivity in the Lyα forest for each of the bright and faint quasars. This is defined as:

$$T = \frac{f}{f_{cont}} \tag{6.1}$$

Where f is the measured flux and f_{cont} is the flux level of the continuum (i.e. the intrinsic unabsorbed QSO spectrum) in the Lyα forest. We therefore require an estimate of f_{cont} from the forest profile. To do this, we perform a continuum fitting method based on those of Young et al. (1979), Carswell et al. (1982) and Dall'Aglio et al. (2008).

First the QSO spectrum is split into uniform intervals and the mean and standard deviation are calculated within each interval. Pixels that lie $> 3\sigma$ below the mean are then rejected and the mean re-calculated. The process is then repeated iteratively until the remaining pixel fluxes show an approximately Gaussian distribution. With the continuum level determined in these discrete intervals, a cubic spline was then used to interpolate across the whole of the spectrum. The results of this fitting process for each of the primary

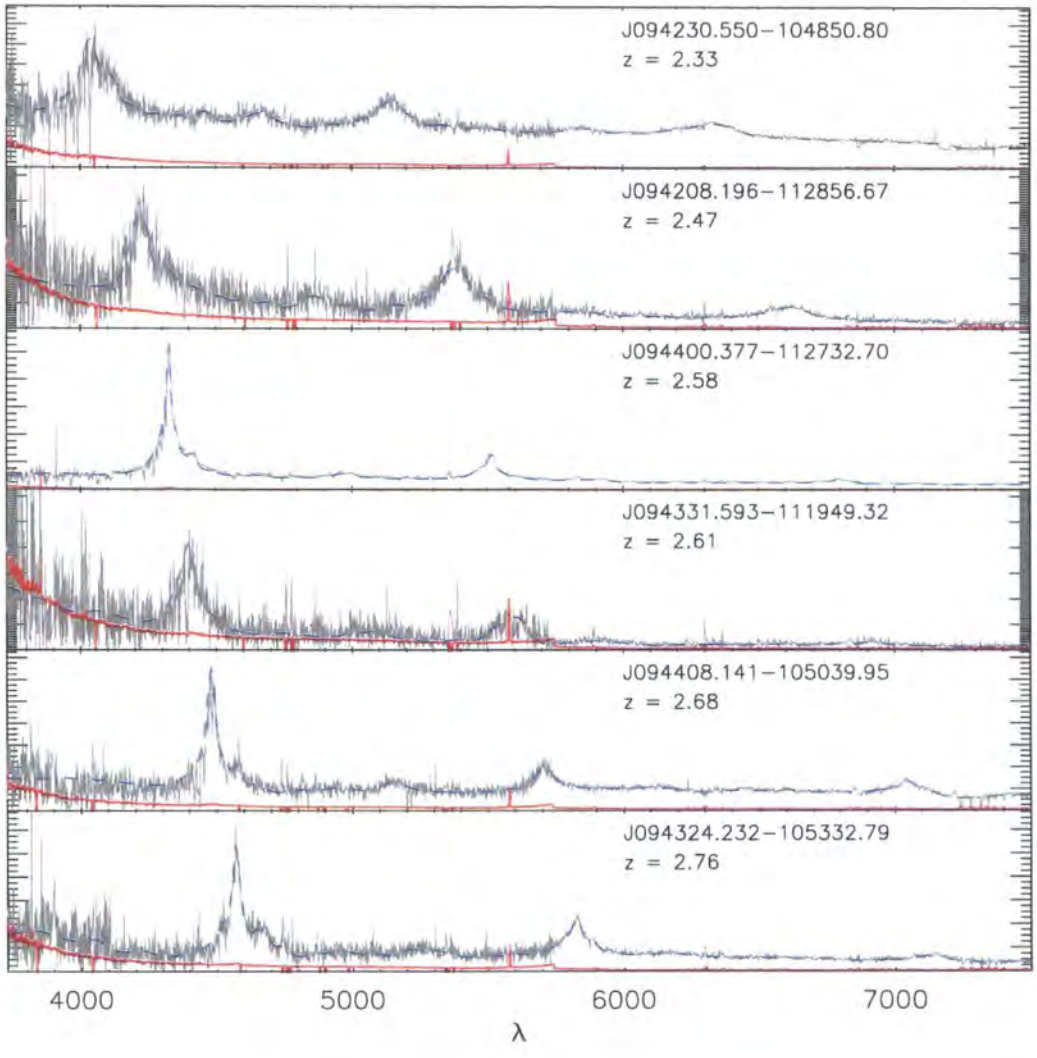

Figure 6.9: First six QSO spectra obtained with the AAT AAOmega spectrograph in the He0940-1050 field. Only QSOs from the central $0.5° \times 0.5°$ region (i.e. those that overlap with the LBG data) are shown. The grey line shows the spectrum, whilst the blue dashed line shows the estimated continuum level and the red line shows the estimated noise level. A full list of the HE0940-1050 QSOs is given in table B.3.

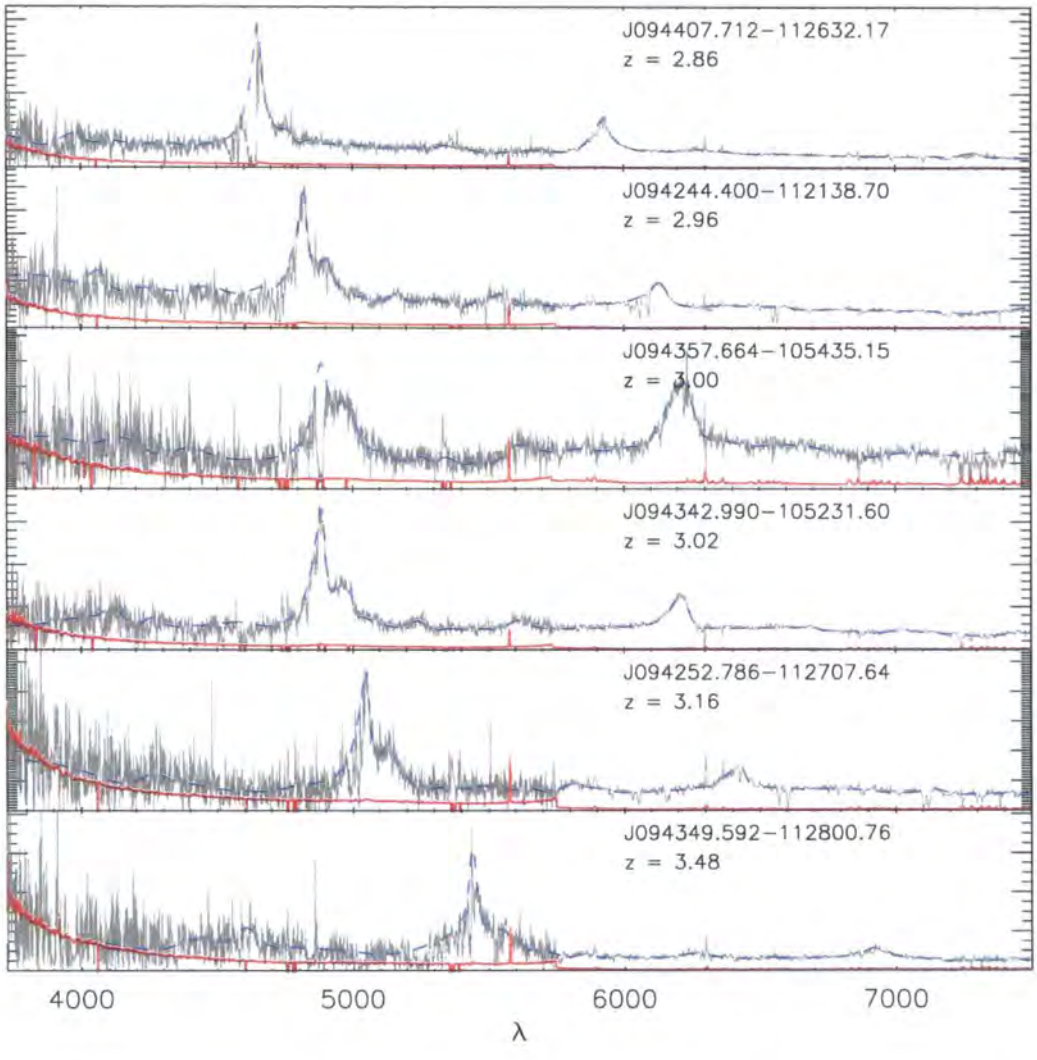

Figure 6.10: Second set of QSO spectra obtained with the AAT AAOmega spectrograph using the 1500V and 1000R grisms in the He0940-1050 field. The grey line shows the spectrum, whilst the blue dashed line shows the estimated continuum level and the red line shows the estimated noise level. Only QSOs from the central $0.5° \times 0.5°$ region (i.e. those that overlap with the LBG data) are shown. A full list of the HE0940-1050 QSOs is given in table B.3.

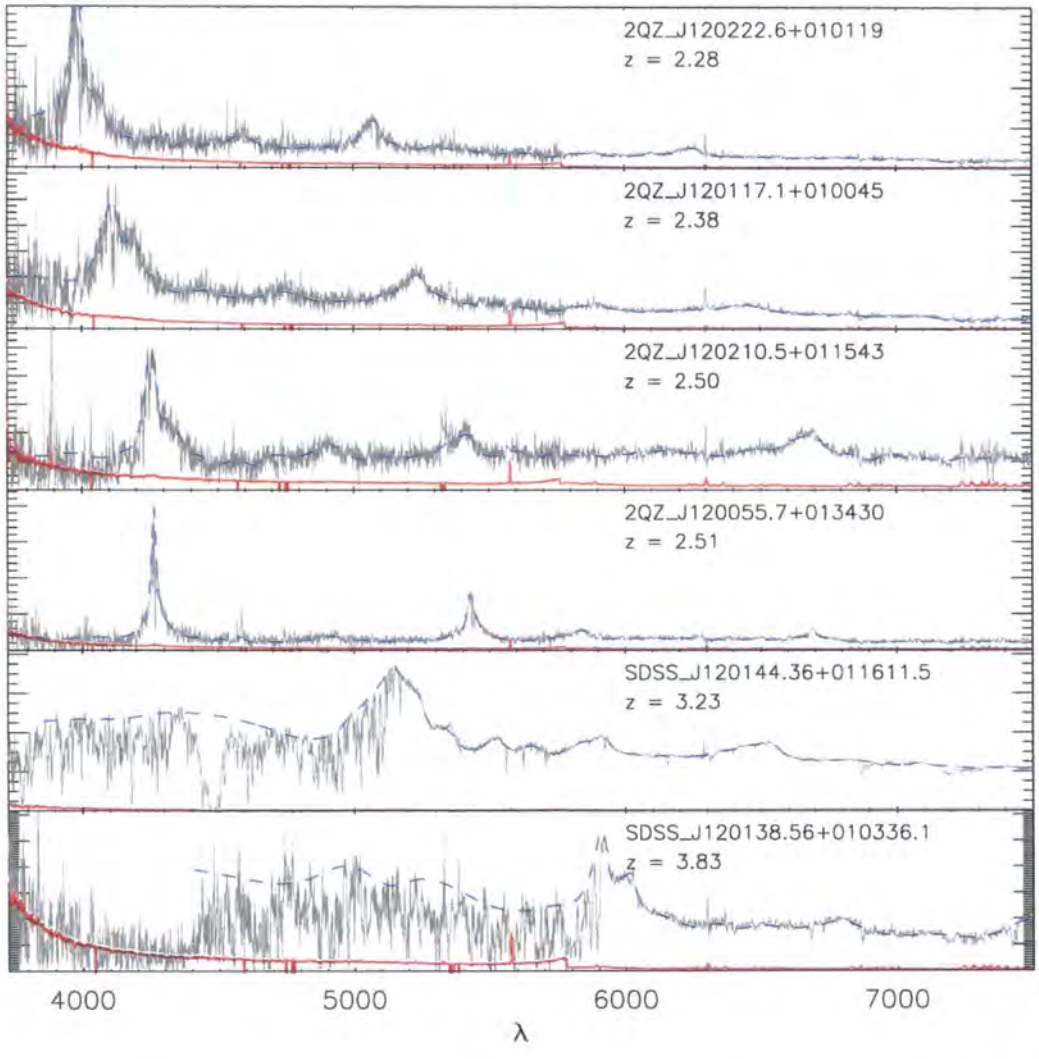

Figure 6.11: QSO spectra obtained with the AAT AAOmega spectrograph in the J1201+0116 field. Only QSOs from the central $0.5° \times 0.5°$ region (i.e. those that overlap with the LBG data) are shown. The grey line shows the spectrum, whilst the blue dashed line shows the estimated continuum level and the red line shows the estimated noise level. A full list of the J1201+0116 QSOs is given in table B.4.

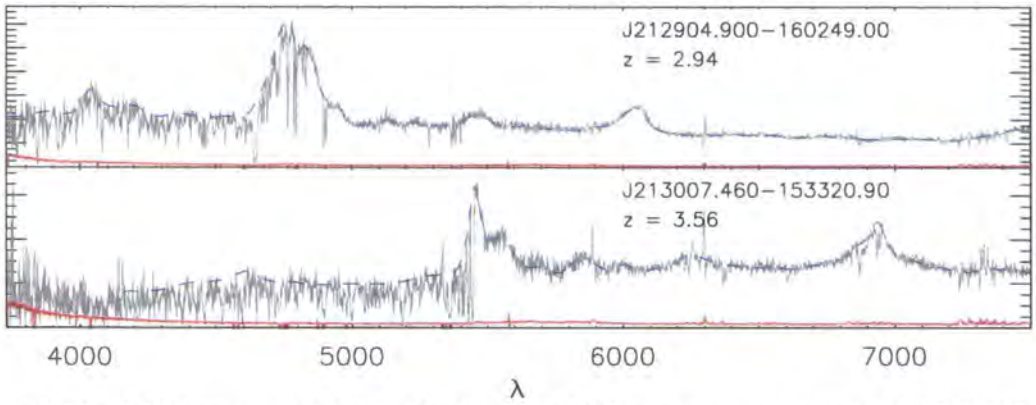

Figure 6.12: QSO spectra obtained with the AAT AAOmega spectrograph in the PKS2126-158 field. Only QSOs from the central $0.5° \times 0.5°$ region (i.e. those that overlap with the LBG data) are shown. The grey line shows the spectrum, whilst the blue dashed line shows the estimated continuum level and the red line shows the estimated noise level. A full list of the PKS2126-158 QSOs is given in table B.5.

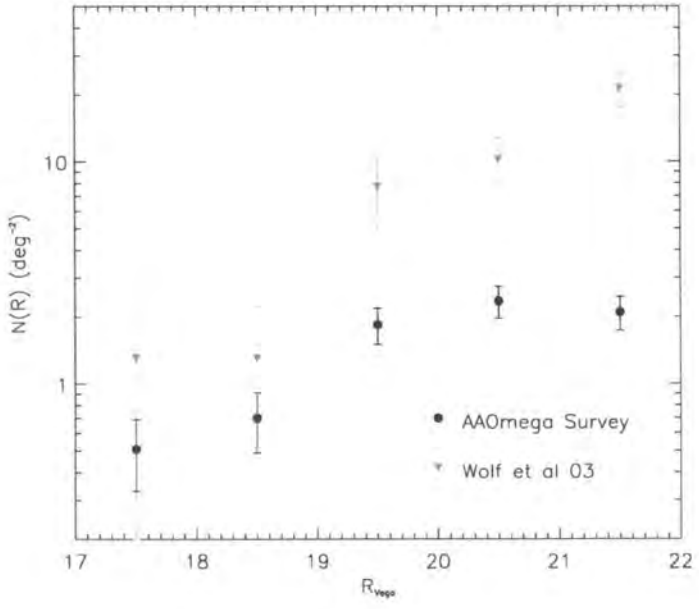

Figure 6.13: Number densities of confirmed quasars in the LBG survey fields.

Table 6.3: Full list of QSOs used in the low resolution cross-correlation calculation.

Name	R.A.	Dec	z	Mag.	Facility
Q0042-2627	00:42:06.42	-26:27:45.3	3.29	$B_j = 18.47$	Keck
[WH091]0043-265	00:45:30.48	-26:17:09.8	3.45	$B_j = 19.37$	Keck
LBQS 0041-2638	00:43:42.81	-26:22:10.7	3.05	$R = 18.62$	AAT
SDSS J0124+0044	01:24:03.77	+00:44:32.8	3.83	$g = 19.2$	UVES
J012351+005958	01:23:51.00	+00:59:58.6	2.59	$R = 21.49$	AAT
HE0940-1050	09:42:53.40	-11:04:25.0	3.05	$B = 17.2$	UVES
J094208-112856	09:42:08.19	-11:28:56.6	2.47	$r = 20.98$	AAT
J094220-112215	09:42:20.07	-11:22:15.8	2.81	$r = 21.49$	AAT
J094252-112707	09:42:52.78	-11:27:07.6	3.16	$r = 20.82$	AAT
J094331-111949	09:43:31.59	-11:19:49.3	2.61	$r = 21.33$	AAT
J094342-105231	09:43:42.99	-10:52:31.6	3.02	$R = 19.58$	AAT
J094349-112800	09:43:49.59	-11:28:00.7	3.48	$r = 20.70$	AAT
J094357-105435	09:43:57.66	-10:54:35.1	3.02	$r = 20.82$	AAT
J094400-112732	09:44:00.37	-11:27:32.7	2.56	$r = 18.66$	AAT
J094407-112632	09:44:07.71	-11:26:32.1	2.83	$r = 19.92$	AAT
J094408-105039	09:44:08.14	-10:50:39.9	2.68	$r = 20.75$	AAT
J09425-1048	09:42:30.59	-10:48:50.9	2.32	$B = 20.70$	FORS2
J09427-1121	09:42:44.43	-11:21:38.9	2.96	$B = 20.99$	FORS2
J09434-1053	09:43:24.22	-10:53:33.0	2.76	$B = 21.16$	FORS2
J09435-1049	09:43:30.05	-10:49:59.0	2.22	$B = 20.79$	FORS2
J09437-1052	09:43:43.00	-10:52:31.7	3.02	$B = 20.78$	FORS2
SDSS J1201+0116	12:01:44.37	+01:16:11.6	3.23	$g = 17.7$	SDSS
SDSS J120055.77+013430.7	12:00:55.77	+01:34:30.7	2.51	$R = 20.59$	AAT
2QZ J120117.1+010045	12:01:17.10	+01:00:45.4	2.38	$R = 20.06$	AAT
SDSS J120210.55+011544.2	12:02:10.55	+01:15:44.2	2.50	$R = 19.85$	AAT
SDSS J120222.68+010120.1	12:02:22.68	+01:01:20.1	2.28	$R = 20.16$	AAT
SDSS J120138.56+010336.1	12:01:38.56	+01:03:36.1	3.86	$r = 20.07$	AAT
PKS2126-158	21:29:12.17	-15:38:41.0	3.27	$V = 17.3$	UVES
J212904-160249	21:29:04.90	-16:02:49.0	2.92	$R = 19.23$	AAT
J21291-1524B	21:29:10.85	-15:24:23.7	2.48	$B = 20.3$	FORS2
J21301-1533	21:30:07.46	-15:33:20.9	3.49	$B = 21.9$	FORS2

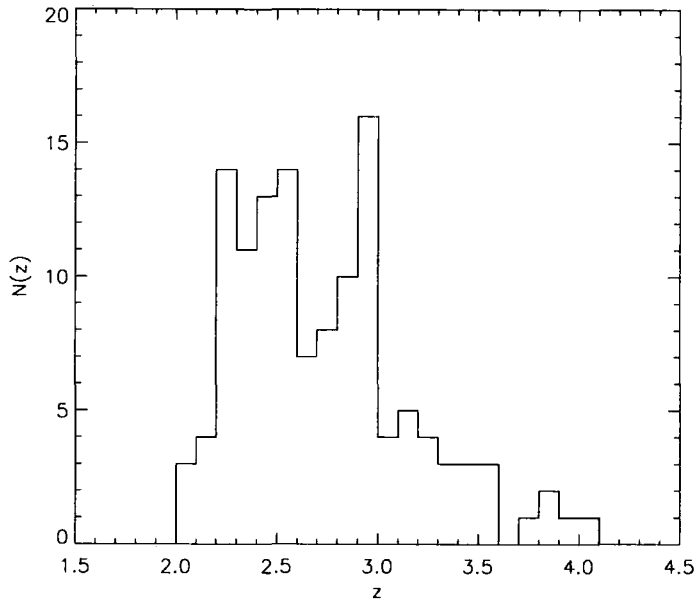

Figure 6.14: N(z) of confirmed quasars in the AAOmega survey fields.

(bright) QSOs are shown in figures 6.1 (solid cyan line) and the resulting continua for the fainter AAOmega survey QSOs are shown in 6.7 to 6.12 (dashed blue line).

Before performing the cross-correlation, the QSO transmissivities were normalized to compensate for the evolution of the spectral profiles with redshift. We performed two different methods to perform this normalization. The first used the relationship:

$$\bar{T} = 0.676 - 0.220(z - 3) \tag{6.2}$$

Used by Adelberger et al. (2003), this is based on the mean transmissivities of a number of QSO sight-lines and is taken from McDonald et al. (2000). As an alternative approach, we also determine $\bar{T}$ from our own individual QSO sight-lines, by binning the spectra into discrete ranges and finding the mean within those bins.

6.5 Cross-correlation

We now perform the cross-correlation using the normalised QSO transmissivity profiles, $U = \frac{T}{\bar{T}}$. Firstly, we take only the QSO spectral range between Lyβ and Lyα. By removing anything below the intrinsic QSO Lyβ emission, we prevent the possibility of contamination by Lyβ absorption lines, whilst the spectrum above the intrinsic QSO Lyα

is also excluded. Further to this, we also exclude the range within 20Å of the intrinsic Lyα emission to avoid proximity effects from the QSOs themselves. Additionally, we remove any damped Lyα systems present in the spectra from the analysis, in particular the large system at $z = 2.69$ evident in the spectrum of J1201+0116 is completely excluded. Finally, we also exclude any regions in either the high or low-resolution spectra where $f_{cont}/\sqrt{variance} < 3$.

The Lyα-LBG cross correlation function was evaluated using the Landy-Szalay estimator (as used in Adelberger et al. 2003):

$$\xi_U(s) = \frac{D_g U_{Ly\alpha} - D_g U_R - R_g U_{Ly\alpha} - R_g U_R}{R_g U_R} \tag{6.3}$$

Where $D_g U_{Ly\alpha}$ is the number of galaxy-Lyα pairs weighted by the transmissivity, U, for each pair. $D_g U_R$ is the number of galaxy-random Lyα pairs weighted by the transmissivity of the random QSO spectra, U_R. $R_g U_{Ly\alpha}$ is the number of random galaxy-Lyα pairs, weighted by $U_{Ly\alpha}$. $R_g U_R$ is the number of random galaxy-random Lyα pairs weighted by U_R. The separation, s, is the distance between an individual QSO spectral element such that $s = \sqrt{\sigma^2 + \pi^2}$, where σ is the tangential distance and π is the line of sight distance between a given galaxy and spectral element. This cross-correlation encompasses each QSO spectral element point (within the specified range) for every galaxy point. The weighted pair counting was performed using the NPT software (Gray et al., 2004).

The random galaxy catalogue with which pairs involving R_g were calculated was constructed as described in section 5.3 again with 20× as many random galaxies as data points. The random transmissivity profiles were simply taken by re-sampling the normalised transmissivity data randomly.

From $\xi_U(s)$, the transmissivity profile is calculated as a function of the galaxy-Lyα pair separation as:

$$T(s) = (1 + \xi_U(s))\bar{T} \tag{6.4}$$

Where $\bar{T}$ is the mean global transmissivity at z=3 and is set to $\bar{T} = 0.676$ as in Adelberger et al. (2005).

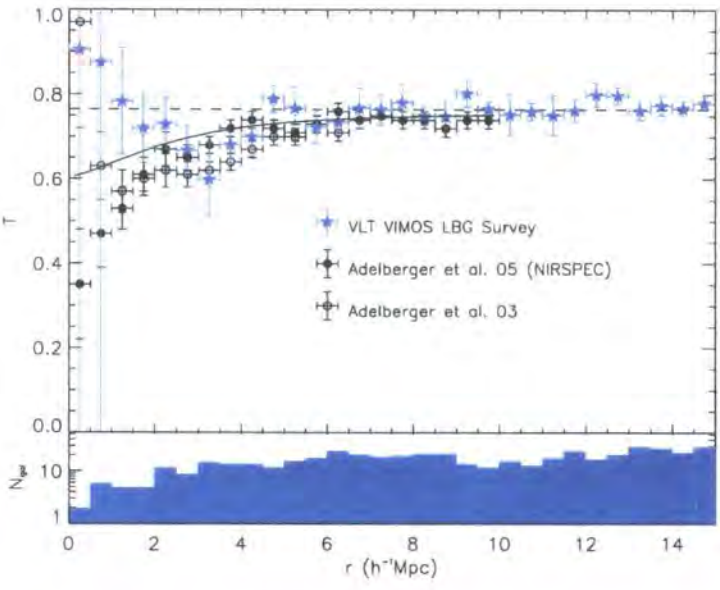

Figure 6.15: Lyα absorption along QSO sight-lines as a function of galaxy-Lyα separation, s. The result is obtained using the 6 QSO sight-lines with high resolution spectroscopy, as described in the text, combined with the VLT LBG sample (blue stars). The open circles and filled circles show the results of Adelberger et al. (2003) and Adelberger et al. (2005) respectively. The solid line shows the Adelberger et al. (2005) data convolved with velocity errors of $\sigma_v = 360 kms^{-1}$.

6.6 Results

The result of the cross-correlation between our LBG data and the Lyα transmissivity in the bright QSO sight-lines is shown in figure 6.15 (blue stars). We also show the original results from Adelberger et al. 2003 (open circles) and from Adelberger et al. 2005 (filled circles). As in Adelberger et al. (2005) we use a bin-size of $0.5h^{-1}Mpc$. We estimate our errors using both a field-to-field estimate based on the variation between the result for each of our six QSOs and a jackknife estimate. The results of the two error estimates are comparable and in the figure we plot field-to-field errors (note that the error bars in the s direction simply show the bin-size). The number of galaxies at a given transverse distance from the quasar line of sight is shown by the lower panel of the figure.

We find from our analysis that we are in reasonable agreement with both the Adelberger et al. (2003) and Adelberger et al. (2005) results at separations of $s > 2h^{-1}$Mpc. However, at separations below $s = 2h^{-1}$Mpc, our result diverges from the Adelberger et al. (2005) result, showing an increase in the transmissivity. One caution is the effect of the velocity

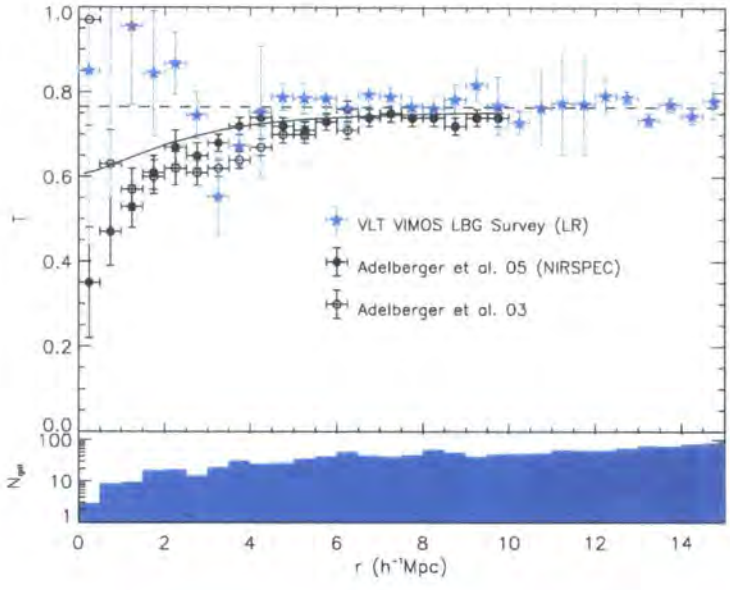

Figure 6.16: Lyα absorption along QSO sight-lines as a function of galaxy-Lyα separation, s. The result is obtained using the 31 QSO sight-lines with low resolution spectroscopy, as described in the text, combined with the VLT LBG sample (blue stars). The open circles and filled circles show the results of Adelberger et al. (2003) and Adelberger et al. (2005) respectively. The solid line shows the Adelberger et al. (2005) data convolved with velocity errors of $\sigma_v = 360 kms^{-1}$.

errors on the measurement of $T(s)$. We therefore estimate the effect of the velocity errors using a similar method as applied to our measurement of the LBG auto-correlation, $\xi(s)$. To do this we take the Adelberger et al. (2005) result and fit a power law to $\xi_T(s)$ calculated from the Adelberger et al. (2005) $T(s)$ profile. We then convolve this with our estimated velocity errors and transform the result back into $T(s)$. As the Adelberger et al. (2005) result will already include velocity effects, this method will overestimate the effect of our velocity errors and so should be considered an upper limit on the effect. The Adelberger et al. (2005) data convolved with our $\sigma_v = 360 kms^{-1}$ combined velocity errors is shown by the solid black line in figure 6.15. Based on this estimate, the increase at $s < 2h^{-1}Mpc$ does not appear statistically significant given the estimated errors on the $T(s)$ data-points. We note also that the $s < 0.5h^{-1}Mpc$ result is based on just a single LBG, whilst the $0.5h^{-1}Mpc > s > 1.0h^{-1}Mpc$ and $1.0h^{-1}Mpc > s > 1.5h^{-1}Mpc$ points are based on just 5 and 4 LBGs respectively.

Continuing with this analysis, we now look at the result achieved with the additional sight-lines from the low-resolution spectroscopy. The transmissivity profile is calculated

using the same method as with the high resolution spectra. We show the result, calculated from a total of 26 QSO spectra, in figure 6.16. Again the errors are field-to-field errors, whilst the numbers of LBGs at a given transverse separation from a QSO sight-line is shown by the histogram in the lower-panel.

Again we see a similar result with an increase in the transmissivity at $s < 2h^{-1}Mpc$. Although the $s < 0.5h^{-1}Mpc$ result is based on only 2 LBGs, the overall numbers of LBGs at $s < 2h^{-1}Mpc$ is increased somewhat and appears to add to the upturn in correlation function in this range. Again we plot the Adelberger et al. (2005) data convolved with our estimated velocity errors and see that the effect is only at the $1 - 2\sigma$ level based on the field-to-field errors.

Clarifying the results of this analysis with further data remains important, especially given that these initial results appear to show some agreement with the original Adelberger et al. (2003) result and not the Adelberger et al. (2005) result at separations of $< 5h^{-1}Mpc$. We note that a potentially important difference between the Adelberger et al. (2005) data and ours (and that of citealtadelberger03) is the differing redshift ranges of the galaxy populations. Our data and the Adelberger et al. (2003) both possess mean redshifts of $z \approx 3$, whilst the Adelberger et al. (2005) sample samples a somewhat lower redshift range with a mean redshift of $z \approx 2.5$ and extends to a minimum redshift of $z \approx 1.5$. It may be that this difference contributes to the differing results and further observations are required to clarify this discrepency.

6.7 Conclusions

Our cross-correlation of LBG positions with the transmissivity in the Lyα forest of a number of high and low resolution QSO spectra has produced some interesting results. The data appears to show some fall in the transmissivity in the Lyα forest at scales of $\sim 5h^{-1}Mpc$ away from LBGs. This shows some agreement with previous results from Adelberger et al. (2003) and Adelberger et al. (2005) and indicates an increase in gas densities at these scales. However we find no significant change from the mean transmissivity at scales of $< 3h^{-1}Mpc$, potentially at odds with the Adelberger et al. (2005) result. Conversely, our result potentially hints at some agreement with the Adelberger et al. (2003) result, which showed a peak in the transmissivity at scales of $s < 1h^{-1}Mpc$, potentially

signifying the presence of low density holes in the IGM close to LBGs. Combined with the evidence from this and previous work for galactic winds in these star-forming galaxies, the potential remains for the existence of galactic 'super-winds' which may cause such low-density regions in the IGM close to the source galaxies. However, it is premature to draw strong conclusions from this data as the numbers of LBGs close to QSO sight-lines remains significantly lower than in the Adelberger et al. (2005) sample at the present time, whilst although we may increase the numbers of Lyα-LBG pairs through the addition of the low-resolution spectra, these spectra are at present relatively noisy. This work does however present the foundation for such analyses given the additional data that is to be added to both the LBG and QSO samples. The present LBG data covers $\approx$ 4200arcmin^2, incorporating 6 QSOs with high resolution spectra. We are in the process of adding to this a further $\approx$ 5000arcmin^2, more than doubling our LBG dataset. Further to this, we aim to acquire high-resolution spectroscopy for the high redshift QSOs in our fields through the continuation of our QSO survey using AAOmega and subsequent use of the X-Shooter instrument on the VLT to provide the high-resolution data. Based on the $\approx$ 20deg^2 $z > 2.5$ in our present fields, we may expect a total of 50 high redshift QSOs across our survey area, with which we may perform the LBG-Lyα cross-correlations. This is approximately an order of magnitude improvement in numbers on our present high-resolution QSO sample, whilst we expect to more than double the numbers in our LBG sample. Given these improvements, we would expect an increase in the numbers of close pairs by a factor of $\approx$ 20, suggesting an improvement in the accuracy of any result of $\approx$ 4, suggesting the analysis performed here will then provide results with an accuracy comparable to, or better than, the Adelberger et al. (2003, 2005) work at scales of $r > 1h^{-1}Mpc$.

CHAPTER 7 | SUMMARY

7.1 Overview

In this thesis I have reported on studies of clustering and related phenomenon in a number of distinct environments and epochs. Using the SZ effect, I have discussed the tracing of the cluster distribution through the imprint of clusters in the CMB. From this I have moved onto the clustering properties of a number of photometric samples of $z > 0.5$ emission line galaxies, ultimately using these to search for the presence of another secondary CMB anisotropy: the ISW effect. Moving on from the lower redshift Universe, I report on the survey of a number of samples of $z \approx 3$ galaxies, selected through the UV dropout/Lyman Break technique. I measure their clustering properties and conclude with an introduction to the cross-correlation of galaxies with the IGM using the Lyα forest in QSO sight-lines.

I now provide an overview of the key findings and results from this broad range of work in the following pages.

7.2 Anomalous SZ Contribution to 3 Year WMAP Data

Through the cross-correlation of clusters found in the APM, ACO and 2MASS catalogues, I have confirmed the presence of the SZ effect in the WMAP 3rd year data, showing an increase in detection significance compared to the 1-year data analysis. The extended appearance of the SZ decrement out to $\theta \approx 30'$, first shown by Myers et al. (2004) using WMAP 1-year data, is also evident in the WMAP 3-year data around ACO $R \geq 2$ clusters. Additionally, I have also confirmed the result of Lieu et al. (2006) that the SZ decrement is somewhat lower than expected on standard model assumptions and ROSAT X-ray profiles for a sample of 31 clusters from Bonamente et al. (2002). Complementing this analysis, I have also shown that the discrepancy appears more pronounced in a higher redshift sample of 38 clusters with Chandra X-ray profiles (Bonamente et al., 2006). The reason for the observational discrepancy between the WMAP data and the BIMA/OVRO data of

Bonamente et al. (2006) is not clear. Discrete or diffuse cluster radio sources are expected to make some contribution to the reduction in the observed SZ effect, however these are not expected to be a large enough factor to explain the observed discrepancy. In the light of these results from the WMAP SZ analysis, the possibility is discussed that the extended SZ signal detected for ACO and 2MASS clusters may actually be indicating a lack of SZ signal in the centres of clusters rather than an excess at the edges.

On the assumption that the WMAP SZ results are correct, one explanation we have considered is that lensing of the cluster centres by foreground groups and clusters could explain the over-prediction of the observed decrements by SZ models and in particular the apparent tendency for higher redshift clusters to have smaller SZ decrements. This solution seems impractical however, as any lensing of the SZ profile would also affect the X-ray profiles. A further possibility is that the use of the X-ray data to estimate the magnitude of the SZ profiles is not perfectly valid. However, before considering such interpretations further, clarification of whether this is a real observational discrepancy between the OVRO/BIMA data and WMAP is required.

7.3 Photometric Selection of Galaxies for Baryonic Oscillation Surveys

Following from the analysis of the SZ signature of $z < 0.3$ clusters of galaxies in the WMAP 3rd year data, I have gone on to study emission line galaxies at redshifts of $z < 1$. Whereas clusters of galaxies trace heavily clustered dense environments, emission line galaxies are more sparsely clustered and present a contrasting view of the Universe.

To begin I have developed a number of photometric constraints to select emission line galaxies in three broad redshift ranges characterised by $z = 0.29 \pm 0.05$, $z = 0.44 \pm 0.08$ and $z = 0.65 \pm 0.21$ based on galaxies with photometric redshifts from the COMBO-17 survey. Each sample is constrained using simple colour cuts based on SDSS photometry, facilitating the isolation of galaxies in these redshift ranges across the entirety of the SDSS coverage. I have presented a calibration of the highest redshift sample using spectroscopic observations AAT AAOmega spectrograph. Through this calibration I find good agreement between the spectroscopic redshift coverage and the corresponding photometric redshift profile estimated from the COMBO-17 data. Additionally, the spectroscopic redshifts show good

agreement with the photometric redshifts of individual galaxies taken from the COMBO-17 data.

Taking the full catalogues selected from the available SDSS imaging, I have analysed the clustering of the galaxy samples. Based on the angular auto-correlation functions of the three samples, I find that the low and high redshift samples are each best fit by a double power-law form of the real-space correlation function, with clustering lengths of $r_0 = 2.65^{+0.05}_{-0.08}h^{-1}Mpc$ and $r_0 = 5.88^{+0.12}_{-0.12}h^{-1}Mpc$ at $r > 0.5h^{-1}Mpc$. The mid-redshift sample is in contrast easily fitted with a single power-law form, which is in turn characterised by a clustering length of $r_0 = 3.62^{+0.06}_{-0.06}h^{-1}Mpc$. The clustering of the $z \sim 0.7$ sample is comparable to the clustering of late-type galaxies at low-redshift from the 2dF Galaxy Redshift Survey data. In conjunction, the result is comparable to the clustering lengths obtained for the ELG samples identified in the early data release of the WiggleZ survey over the redshift range of $z = 0.2 - 1.0$. Given the clustering lengths obtained, our selected samples are relatively weakly clustered and present a potentially closer tracer of the underlying dark matter than samples such as LRGs which are highly clustered and form in the peaks of the density distribution.

Finally, to conclude this portion of the work, I have used the three samples to search for the ISW effect in the WMAP 5 year data release. The ISW effect provides the presently most attainable possibility for a measurement of any acceleration in the expansion of the Universe, without relying on geometrical effects (such as is the case for the SN1a and BAO measurements). Based on a cross-correlation analysis, I find a positive trend in the results comparable in magnitude to the predicted of the ISW effect. However, the signal does not appear statistically significant based on the error estimates from field-to-field errors. This remains the case, even when all three galaxy samples are joined, resulting in a final measurement of $w_{Tg} = 0.20 \pm 0.12\mu K$ in the WMAP W-band. Ultimately, the result is consistent with the magnitude and scale of the ISW effect based on both ΛCDM and cosmologies where the ISW effect is expected to be weaker, such as a flat CDM cosmology. Previous results using magnitude limited galaxy samples, LRG samples and QSOs have provided marginally more significant results than the one presented here, but given further data incorporating the Southern hemisphere (potentially from future surveys such as VISTA) using such data samples as used here may provide the route to a complimentary measurement of the ISW effect, which remains a key tool in understanding

the nature of the Universe.

7.4 Initial Results from the VLT VIMOS LBG Survey

In the bulk of this thesis, I have presented the initial data and analysis from a study of star-forming galaxies in the high-redshift $z \approx 3$ Universe. The overall aims of this work consist of:

- investigating the clustering properties of galaxies at $z \approx 3$ and the use of galaxy dynamics to constrain Ω_m at these redshifts.
- providing an independent measurement of the Lyα distribution around galaxies at $z \approx 3$ via cross-correlation with the Lyα forest of bright QSOs, building on the work of Adelberger et al. (2003, 2005). Through this we may constrain the extent to which the IGM may be seeded with metals via superwinds from star-forming galaxies in the $z \approx 3$ Universe.

Using relatively wide field deep imaging of sky regions around a number of bright $z > 3$ QSOs, we are conducting a survey of Lyman Break Galaxies using spectroscopic observations with the VLT VIMOS instrument, the initial data and results of which I review here. To this end I present a detailed analysis of the imaging data upon which the survey is based. The data was obtained during several visits to the CTIO and KPNO sites and was acquired using the MOSAIC Imagers. From this imaging data I have performed a photometric selection of LBGs down to a magnitude of $R_{Vega} = 25.5$, producing a total of $\approx 21,000$ LBG candidates across a total area of $\approx 1.25 deg^2$.

I go on to review the spectroscopic observations using VLT VIMOS. A total of 19 VIMOS pointings have been observed across the 5 QSO fields, encompassing a total observed sky area of $1.18 deg^2$. A total of $1,149$ $z > 2$ LBGs are successfully identified over the entire survey area, with the remaining objects largely being composed of low-redshift interlopers and galactic stars. Redshifts for the LBG sample have been estimated based on identification of the Lyα emission/absorption line and the ISM absorption lines, with estimated errors on our redshifts of $\approx 360 kms^{-1}$. With these measurements we estimate a mean redshift for our entire LBG sample of $\tilde{z} = 2.87 \pm 0.34$. As in previous work, we have

verified the presence of offsets between ISM absorption features and the Lyα emission in these high redshift galaxies, indicating the presence of high velocity winds.

Using the photometric and spectroscopic samples, I continue by analysing the clustering properties of the LBGs. Firstly, I have estimated the angular auto-correlation function of the photometric LBG candidates. Based on this estimate and the measured redshift distribution of the spectroscopic sample, I have estimated the redshift-space correlation function using Limber's formula. From this I find that the $w(\theta)$ is best fit by a double power law form of the real-space correlation function, $\xi(r)$, with a break at $r_b = 0.4h^{-1}Mpc$. This is parametrised by a clustering length and slope below the break of $r_{0,1} = 1.70^{+0.09}_{-0.14}$h^{-1}Mpc and $\gamma_1 = 2.65^{+0.09}_{-0.14}$ and above the break of $r_{0,2} = 4.32^{+0.13}_{-0.12}$h^{-1}Mpc and $\gamma_2 = 1.90^{+0.09}_{-0.14}$.

Continuing from the $w(\theta)$ analysis, I have used the spectroscopic catalogue to estimate the redshift-space LBG auto-correlation function. At separations of $s > 8h^{-1}Mpc$, we find a strong clustering signal comparable to previous data, however at $s < 8h^{-1}Mpc$ I find a significant loss of signal in the clustering of the LBGs. The most likely cause of this loss of signal appears to be the combined errors on the LBG redshift estimates. By modelling the effect of our $\approx 360kms^{-1}$ redshift determination error on the $\xi(r)$ determined from the measurement of the angular correlation function, I find that the results are reconciled with the resulting $\xi(s)$ model proving consistent with the measurement of $\xi(s)$. Our measurement of the clustering length of the VIMOS LBG sample is similar to that of the Adelberger et al. (2005) data ($3.96 \pm 0.29h^{-1}Mpc$) and the Foucaud et al. (2003) data ($5.0 \pm 0.6h^{-1}Mpc$). Ultimately, all of these estimates of the clustering of LBG samples are comparable to the clustering of star-forming galaxies (e.g. Norberg et al. 2002; Blake et al. 2009) at low-redshift.

Following the work of da Ângela et al. (2005b), we investigate the large scale bulk flow dynamics of the galaxy population at $z \approx 3$, estimating the infall parameter, β, that quantifies these dynamics. By estimating β, we may better understand the clustering results obtained from the LBG redshifts, which inherently contain the imprint of the galaxy dynamics (note that any measurement of the clustering from the redshift-space clustering without taking into account the bulk flow motions is likely to overestimate the level of clustering). With this aim, we have taken the VLT VIMOS spectroscopic LBG sample and combined it with the LBG data of Steidel et al. (2003) to form a complete data-set of 1,980 LBGs across an area of $1.56deg^2$. The two datasets provide a complementary view of

the LBG population, with the VLT VIMOS data sampling the population comparatively sparsely, but over wide fields of view ($\sim 0.5°$) and the Steidel et al. (2003) data providing a greater sampling of the population at small scales. I first determine the $w_p(\sigma)$ clustering profile of the complete sample and estimate a clustering length of $r_0 = 3.63 \pm 0.19 h^{-1} Mpc$. We have then calculated the 2-D redshift space correlation function, $\xi(\sigma, \pi)$, from the combined data-set. As in previous analyses (e.g. da Ângela et al. 2005b), the result is somewhat noisy, however I go on to make an estimate of the infall parameter based on a model of the redshift space distortions in a ΛCDM, finding a value of $\beta = 0.23 \pm 0.09$. This measurement is consistent with the da Ângela et al. (2005b) result, validating our use of this value in our analysis of the clustering of the LBGs. Comparing this to low-redshift measurements, we find a lower value than found for low-redshift samples, such as the 2dFGRS result of $\beta = 0.47^{0.19}_{-0.16}$ of Hawkins et al. (2003) and the WiggleZ survey estimate of $\beta \approx 0.5$ for low-redshift star-forming galaxies Blake et al. (2009), suggesting bulk motions provide a weaker contribution to the dynamics of $z \approx 3$ galaxies compared to the lower redshift Universe.

Finally, I have concluded this work with an initial analysis of the relationship between galaxies and the IGM at $z \approx 3$. As discussed, the LBG observations have been acquired in regions of sky centred on bright high redshift ($z > 3$) QSOs. Spectroscopy is available from the UVES, Keck and SDSS archives on each of these QSOs, whilst we have additional high-resolution spectroscopy on a further QSO in one of our fields acquired using the HiRES instrument at the Keck Observatory. In addition to this we have conducted a survey to identify fainter $z > 2$ QSOs in each of our five fields using the AAT AAOmega spectrograph in low-resolution mode. These observations have produced an additional 32 $z > 2$ QSOs close to the LBG samples and numerous others in the surrounding regions of sky. Using the six primary QSO spectra, I have performed a cross-correlation analysis between the Lyα lines in the QSO spectra and the LBG positions in the five observed fields. This shows a comparable result to that of Adelberger et al. (2005) at separations of $r > 3h^{-1} Mpc$, with the Lyα flux showing a reduction in strength around identified galaxies, indicative of increases in the gas density correlating with LBG positions. However, at separations of $r < 3h^{-1} Mpc$ we find the Lyα flux profile (and hence the IGM gas density) returns to the mean value, suggesting a reduction in the gas density at such separations compared to the $3h^{-1} Mpc < r < 5h^{-1} Mpc$ range. This is a potential indication of the presence of galaxy

'super-winds', supernovae driven winds capable of producing pockets of low-density ionised gas around star-forming galaxies. Developing on this work, I repeat the analysis with the inclusion of the low-resolution (and low signal-to-noise) AAOmega spectra of faint QSOs in the fields. In addition I also include the spectra of a number of QSOs observed by Worseck & Wisotzki (2008) in two of the QSO fields. This also produces a similar result to the smaller (but higher signal-to-noise) group. As discussed, the extent of super-winds from $z \approx 3$ galaxies is an important element of the understanding of the galaxy formation history of the Universe. As such the potential disagreement between the Adelberger et al. (2003) and Adelberger et al. (2005) results at small separations is something that clearly requires further investigation. This work lays the foundation for an independent result which may clarify the impact of super-winds on the IGM at high-redshift.

The above results present the initial work on the ongoing VLT VIMOS LBG Survey. At present, a further 3 QSO fields are to be observed with additional observations also due on an extended field of $1° \times 1°$ around the bright QSO HE0940-1050. These observations will increase the quantity of data in this work significantly over the next 2 years, providing a greater depth of data with which to more accurately investigate the ideas discussed in this thesis and extend the work to further analyses. Ultimately we expect to more than double the present number of LBGs in our survey and provide ≈ 50 QSO spectra at high-resolution with which to perform a firm analysis of the interactions between LBGs and the IGM. Through this, I aim to be involved in using the complete dataset to refine the analyses presented here including the clustering and dynamical properties of the galaxy population and the effect of the galaxy population on their surroundings.

Bibliography

Abell G.O., Corwin H. & Olowin R., 1989, ApJS, 70, 1

Adelberger, K. L., Steidel, C. C., Shapley, A. E. & Pettini, M., 2003, ApJ, 584, 45

Adelberger, K. L., Shapley, A. E., Steidel, C. C., Pettini, M., Erb, D. K. & Reddy, N. A., 2005, ApJ, 629, 636

Afshordi N., Loh Y.-T. & Strauss M.A., 2004, Phys.Rev.D, 69, 8, 083525

Afshordi N., Lin, Y.-T. & Sanderson, A.J.R. 2005, ApJ, 629, 1

Afshordi N., Lin, Y.-T., Nagai, D. & Sanderson, A.J.R., 2007, MNRAS, 378, 293

Aguirre, A., Schaye, J., Kim, T.-S., Theuns, T., Rauch, M. & Sargent, W. L. W., 2004, ApJ, 602, 38

Alpher R. A., Follin J. W. & Herman R. C., 1953, Phys. Rev., 92, 1347

Bartlett, J. G., Chamballu, A., Melin, J.-B., Arnaud, M. & Members of the Planck Working, 2008, Astron. Nacht., 329, 147

Baum, W.A., 1962, Problems of Extragactic Research, IAU Symposium 15, 390

Bennett C. L., Smoot G. F., Janssen M., Gulkis S., Kogut A., Hinshaw G., Backus, C., Hauser M. G., Mather J. C., Rokke L., Tenorio L., Weiss R., Wilkinson D. T., Wright E. L., de Amici G., Boggess N. W., Cheng E. S., Jackson P. D., Keegstra P., Kelsall T., Kummerer R., Lineweaver C., Moseley S. H., Murdock T. L., Santana J., Shafer R. A. & Silverberg R. F., 1992, ApJ, 391, 466

Bennett C. L., Smoot G. F., Hinshaw G., Wright E. L., Kogut A., de Amici G., Meyer S. S., Weiss R., Wilkinson D. T., Gulkis S., Janssen M., Boggess N. W., Cheng E. S.,

Hauser M. G., Kelsall T., Mather J. C., Moseley S. H., Murdock T. L., Silverberg R. F., 1992, ApJ, 396, 7

Bennett, C. L.; Hill, R. S.; Hinshaw, G.; Nolta, M. R.; Odegard, N.; Page, L.; Spergel, D. N.; Weiland, J. L.; Wright, E. L.; Halpern, M.; Jarosik, N.; Kogut, A.; Limon, M.; Meyer, S. S.; Tucker, G. S.; Wollack, E. 2003, ApJS, 148, 97

Benson A. J., Bower R. G., Frenk, C. S., Lacey, C. G., Baugh, C. M. & Cole, S., 2003, ApJ, 599, 38

Bertin, E., Mellier, Y., Radovich, M., Missonnier, G., Didelon, P., Morin, B., 2002, ASPC, 281, 228

Birkinshaw, M., Gull, S. F. & Northover, K. J. E., 1978, MNRAS, 185, 245

Birkinshaw, M., 1979, MNRAS, 187, 847

Birkinshaw, M.; Hughes, J. P.; Arnaud, K. A. 1991, ApJ, 379, 466

Blake C., Collister A., Bridle S. & Lahav O., 2007, MNRAS, 374, 527

Blake C. et al., 2009, arXiv:0901.2587

Bonamente M., Lieu R., Joy M. K. & Nevalainen J.H., 2002, ApJ, 576, 688

Bonamente M., Joy M. K., LaRoque S. J., Carlstrom J. E., Reese E. D. & Dawson K. S., 2006, ApJ, 647, 25, 2006, ApJ, 647, 25

Bouché N., Lowenthal J.D., 2004, ApJ, 609, 513

Bruzual G. & Charlot S., 2003, MNRAS, 344, 1000

Bruzual G., 2007, ASPC, 374, 303

Cabré A., Gastanãga E., Manera M., Fosalba P. & Castander F., 2006, MNRAS, 372, 23

Cabré A. & Gastanãga E., 2009, MNRAS, tmp, 122

Cannon, R., Drinkwater, M., Edge, A., Eisenstein, D., Nichol, R., Outram, P., Pimbblet, K., de Propris, R., Roseboom, I., Wake, D., Allen, P., Bland-Hawthorn, J., Bridges, T., Carson, D., Chiu, K., Colless, M., Couch, W., Croom, S., Driver, S., Fine, S., Hewett,

P., Loveday, J., Ross, N., Sadler, E. M., Shanks, T., Sharp, R., Smith, J. A., Stoughton, C., Weilbacher, P., Brunner, R. J., Meiksin, A., Schneider, D. P., 2006, MNRAS, 372, 425

Carlstrom, J. E., Joy, M. & Grego, L., 1996, ApJ, 456, 75

Carlstrom, J. E., Holder, G. P. & Reese, E. D., 2002, ARA&A, 40, 643

Carroll S. M., Press W. H. & Turner E. L., 1992, ARA&A, 30, 499

Carswell, R. F., Whelan, J. A. J., Smith, M. G., Boksenberg, A. & Tytler, D., 1982, MNRAS, 198, 91

Coble, K., Carlstrom, J.E., Bonamente, M., Dawson, K., Holzapfel, W., Joy, M., LaRoque, S. & Reese, E.D., 2007, AJ, 134, 897

Cole S., Percival W. J., Peacock J. A., Norberg P., Baugh C. M., Frenk C. S., Baldry I., Bland-Hawthorn J., Bridges T., Cannon R., Colless M., Collins C., Couch W., Cross N. J. G., Dalton G., Eke V. R., De Propris R., Driver S. P., Efstathiou G., Ellis R. S., Glazebrook K., Jackson C., Jenkins A., Lahav O., Lewis I., Lumsden S., Maddox S., Madgwick D., Peterson B. A., Sutherland W. & Taylor K., 2005, MNRAS, 362, 505

Collister A., Lahav O., Blake C., Cannon R., Croom S., Drinkwater M., Edge A., Eisenstein D., Loveday J., Nichol R., Pimbblet K., de Propris R., Roseboom I., Ross N., Schneider D. P., Shanks T. & Wake D., 2007, MNRAS, 375, 68

Condon J., Cotton W., Greisen E., Yin W. F., Perley R., Taylor G. & Broderick J., 1998, AJ, 115, 1693

Conklin E. K., 1969, Nature, 222, 971

Connolly, A.J., Csabai, I., Szalay, A.S., Koo, D.C., Kron, R.G., & Munn, J A., 1995 AJ, 110, 2655

Coppin, K. E. K., Swinbank, A. M., Neri, R., Cox, P., Smail, I., Ellis, R. S., Geach, J. E., Siana, B., Teplitz, H., Dye, S., Kneib, J.-P., Edge, A. C. & Richard, J., 2007, ApJ, 665, 936

Corey B. & Wilkinson D., 1976, BAAS, 8, 351

Croom, S., Shanks, T., Boyle, B. J., Smith, R. J., Miller, L., Loaring, N. S. & Hoyle, F., 2001, MNRAS, 325, 483

Croom S., Boyle B.J., Shanks T., Smith R.J., Miller L., Outran P.J., Loaring N.S., Hoyle F. & da Ângela J., 2005, MNRAS, 356, 415

Cunha, J. V., Marassi, L. & Lima, J. A. S., 2007, MNRAS, 379, 1

da Ângela, J., Outram, P. J.; Shanks, T.; Boyle, B. J.; Croom, S. M.; Loaring, N. S.; Miller, L.; Smith, R. J, 2005, MNRAS, 360, 1040

da Ângela, J., Outram, P. J. & Shanks, T., 2005, MNRAS, 361, 879

da Ângela, J.; Shanks, T.; Croom, S. M.; Weilbacher, P.; Brunner, R. J.; Couch, W. J.; Miller, L.; Myers, A. D.; Nichol, R. C.; Pimbblet, K. A.; de Propris, R.; Richards, G. T.; Ross, N. P.; Schneider, D. P.; Wake, D 2008, MNRAS, 383, 565

Dall'Aglio, A., Wisotzki, L. & Gábor Worseck, 2008, A&A, 480, 359

Davis, M. & Peebles, P. J. E., 1983, ApJ, 267, 465

Dicke R. H., Peebles P. J. E., Roll P. G. & Wilkinson D. T., 1965, ApJ, 142, 414

Diego J.M., Silk J. & Sliwa W., 2003, MNRAS, 346, 940

Douspis, M., Castro, P. G., Caprini, C. & Aghanim, N., 2008, A&A, 485, 395

Eisenstein D. J., Annis J., Gunn J. E., Szalay A. S., Connolly A. J., Nichol R. C.; Bahcall N. A., Bernardi M., Burles S., Castander F. J., Fukugita M., Hogg D. W., Ivezić Ž., Knapp G. R., Lupton R. H., Narayanan V., Postman M., Reichart D. E., Richmond M., Schneider D. P., Schlegel D. J., Strauss M. A., SubbaRao M., Tucker D. L., Vanden Berk D., Vogeley M. S., Weinberg D. H. & Yanny B., 2001, AJ, 122, 2267

Eisenstein D. J., Zehavi I., Hogg D. W., Scoccimarro R., Blanton M. R., Nichol R. C., Scranton R., Seo H-J., Tegmark M., Zheng Z., Anderson . F., Annis J., Bahcall N., Brinkmann J., Burles S., Castander F. J., Connolly A., F I., Doi M., Fukugita M., Frieman J. A., Glazebrook K., Gunn J. E., Hendry J. S., Hennessy G., Ivezi? Z., Kent S., Knapp G. R., Lin H., Loh Y-S., Lupton R. H., Margon B., McKay T. A., Meiksin A., Munn J. A., Pope A., Richmond M. W., Schlegel D., Schneider D. P., Shimasaku

K., Stoughton C., Strauss M. A., SubbaRao M., Szalay A. S., Szapudi I., Tucker D. L., Yanny B. & York D. G., 2005, ApJ, 633, 560

Fosalba P., Gaztañaga E. & Castander F.J., 2003, ApJ, 597, L89

Fosalba P. & Gaztañaga E., 2004, MNRAS, 350, L37

Foucaud S., McCracken H. J., Le Fèvre O., Arnauts s., Brodwin M., Lilly S. J., Crampton D. & Mellier Y., 2003, A&A, 409, 835

Frith W. J., 2005, PhD Thesis

Fry N., 1996, ApJ, 461, L65

Gamow G., 1946, Phys. Rev., 70, 572

Giavalisco M., Steidel C. & Macchetto F. D., 1996, ApJ, 470, 189

Glazebrook K., Blake C., Couch W., Forbes D., Drinkwater M., Jurek R., Pimbblet K., Madore B., Martin C., Small T., Forster K., Colless M., Sharp R., Croom S., Woods D., Pracy M., Gilbank D., Yee H., Gladders M., 2007, ASPC, 379, 72

Gray A.G., Moore A.W., Nichol R.C., Connolly A.J., Genovese C. & Wasserman L., 2004, ASPC, 314, 249

Guhathakurta P., Tyson J. A. & Majewski S. R., 1990, ApJ, 357, 9

Gull, S. F. & Northover, K. J. E., 1976, Nature, 263, 572

Hamilton A. J. S., 1992, ApJ, 385, L5

Harrison E. R., 1970, PhRevD, 1, 2726

Hawkins, E., Maddox, S., Cole, S., Lahav, O., Madgwick, D. S., Norberg, P., Peacock, J. A., Baldry, I. K., Baugh, C. M., Bland-Hawthorn, J., Bridges, T., Cannon, R., Colless, M., Collins, C., Couch, W., Dalton, G., De Propris, R., Driver, S. P., Efstathiou, G., Ellis, R. S., Frenk, C. S., Glazebrook, K., Jackson, C., Jones, B., Lewis, I., Lumsden, S., Percival, W., Peterson, B. A., Sutherland, W. & Taylor, K., 2003, MNRAS, 346, 78

Heavens A. & Taylor A. N., 1995, MNRAS, 275, 483

Henry P., 1971, Nature, 231, 516

Hernández-Monteagudo, C. & Rubiño-Martn, J. A., 2004, MNRAS, 347, 403

Hewett, P. C., Foltz, C. B., Chaffee, F. H., 1995, AJ, 109, 1498

Hewitt A. & Burbidge G., 1989, ApJ, 69, 1

Hinshaw, G., Spergel, D.N., Verde, L., Hill, R.S., Meyer, S.S., Barnes, C., Bennett, C.L., Halpern, M., Jarosik, N., Kogut, A., Komatsu, E., Limon, M., Page, L., Tucker, G.S., Weiland, J.L., Wollack, E. & Wright, E.L., 2003, ApJS, 148, 63

Hinshaw G., Nolta M.R., Bennet C.L., Bean R., Dore O., Greason M.R., Halpern M., Hill R.S., Jarosik N., Kogut A., Komatsu E., Limon M., Odegard N., Meyer S.S., Page L., Peiris h.P., Spergel D.N., Tucker G.S., Verde L., Weiland J.L., Wollack E. & Wright E.L., 2007, ApJS, 170, 288

Hinshaw G., Weiland J. L., Hill R. S., Odegard N., Larson D., Bennett C. L., Dunkley J., Gold B., Greason M. R., Jarosik N., Komatsu E., Nolta M. R., Page L., Spergel D. N., Wollack E., Halpern M., Kogut A., Limon M., Meyer S. S., Tucker G. S. & Wright E. L., 2008, arXiv, 0803.0732

Huffenberger K.M., Seljak U. & Makarov A, 2004, Phys.Rev.D, 70, 6, 063002

Jarrett, T.H., Chester, T., Cutri, R., Schneider, S., Skrutskie, M. & Huchra, J.P., 2000, AJ, 119, 2498

Jakobsen P., Jansen R.A., Wagner S. & Reimers D., 2003, A&A, 397, 891

Januzzi, B. T., Claver, J. & Valdes F., 2005, The NAOA Deep Wide-Field Survey MOSAIC Data Reductions

Jones, M. E., Edge, A. C., Grainge, K., Grainger, W. F., Kneissl, R., Pooley, G. G., Saunders, R., Miyoshi, S. J., Tsuruta, T., Yamashita, K., Tawara, Y., Furuzawa, A., Harada, A. & Hatsukade, I., 2005, MNRAS, 357, 518

Kennicutt, R. C., 1992, ApJ, 388, 310

Komatsu, E. & Kitayama, T., 1999, ApJ, 526, 1

Koo, D.C., 1985, AJ, 90, 418

Lamareille F., Mouhcine M., Contini T., Lewis I. & Maddox S., 2004, MNRAS, 350, 396

Landolt, A. 1992, AJ, 104, 340

Landsman, W. B, 1993, Astronomical Data Analysis Software and Systems II, ASPC, 52, 246

Le Fèvre, O., Paltani, S., Arnouts, S., Charlot, S., Foucaud, S., Ilbert, O., McCracken, H. J., Zamorani, G. & the VIMOS VLT Deep Survey team, 2005, Nature, 437, 519

Lemaître G., 1931, MNRAS, 91, 483

Lewis A., Challinor, A. & Lasenby, A., 2000, ApJ, 538, 473

Lieu R., Mittaz J.P.D. & Zhang S.-N., 2006, ApJ, 648, L176

Lieu R. & Quenby J., 2006, ApJ submitted, astro-ph/0607304

Lin Y.-T. & Mohr J.J., 2007, ApJS, 170, 71

Loh, E.D., & Spillar, E.J., 1986, ApJ, 303, 154

Lowenthal, J. D., Koo, D. C., Guzman, R., Gallego, J., Phillips, A. C., Faber, S. M., Vogt, N. P., Illingworth, G. D. & Gronwall, C., 1997, ApJ, 481, 673

Maddox, S. J., Efstathiou, G., Sutherland, W. J., Loveday, J., 1990, MNRAS, 243, 692

Madau, P., Ferguson, H. C., Dickinson, M. E., Giavalisco, M., Steidel, C. C. & Fruchter, A., 1996, MNRAS, 283, 1388

Maraston, C., 2005, MNRAS, 362, 799

McDonald, P., Miralda-Escudé, J., Rauch, M., Sargent, W. L. W., Barlow, T. A., Cen, R. & Ostriker, J. P., 2000, ApJ, 543, 1

Metcalfe N., Fong R., Shanks T., 1995, MNRAS, 274, 769

Metcalfe, N., Shanks, T., Campos, A., McCracken, H.J. & Fong, R., 2001, MNRAS, 323, 795

Mountrichas, G. & Shanks, T. 2007, MNRAS, submitted, astro-ph/0701870

Myers, A.D., Outram, P.J., Shanks, T., Boyle, B.J., Croom, S.M., Loaring, N.S, Miller, L. & Smith, R.J., 2003, MNRAS, 342, 467

Myers A.D., Shanks T., Outram P.J., Frith W.J. & Wolfendale A.W., 2004, MNRAS, 347, L67

Myers A.D., Outram P.J., Shanks T., Boyle, B.J., Croom, S.M., Loaring, N.S., Miller, L., Smith & R.J., 2005, MNRAS, 359, 741

Nevalainen, J., Lieu, R., Bonamente, M., and Lumb, D., 2003, ApJ, 584, 716

Norberg P., Baugh C., Hawkins E., Maddox S., Madgwick D., Lahav O., Cole S., Frenk C., Baldry I., Bland-Hawthorn J., Bridges T., Cannon R., Colless M., Collins C., Couch W., Dalton G., De Propis R., Driver S.P., Efstathiou G., Ellis R.S., Glazebrook K., Jackson C., Lewis I., Lumsden S., Peacock J., Peterson B.A., Sutherland W. & Taylor K., 2002, MNRAS, 332, 827

O'Meara J.M., Prochaska J.X., Burles S., Prochter G., Bernstein R.A. & Burgess K.M., 2007, ApJ, 656, 666

Padmanabhan N., Budavari T., Schlegel D. J., Bridges T., Brinkmann J., Cannon R., Connolly A. J., Croom S. M., Csabai I., Drinkwater M., Eisenstein D. J., Hewett P.C., Loveday J., Nichol R. C., Pimbblet K. A., De Propris R., Schneider D. P., Scranton R., Seljak U., Shanks T., Szapudi I., Szalay A. S. & Wake D., 2005, MNRAS, 359, 237

Padmanabhan, N., Hirata, C. M., Seljak, U., Schlegel, D. J., Brinkmann, J., Schneider, Donald P., 2005, PhRvD, 72, 3525

Peacock J. A., 1999, "Cosmological Physics", Cambridge University Press

Peebles P. J. E. & Yu J. T., 1970, ApJ, 162, 815

Peebles P. J. E., 1980, "The Large-Scale Structure of the Universe", Princeton University Press

Penzias A. A. & Wilson R. W., 1965, ApJ, 142, 419

Perlmutter, S., Aldering, G., Goldhaber, G., Knop, R. A., Nugent, P., Castro, P. G., Deustua, S., Fabbro, S., Goobar, A., Groom, D. E., Hook, I. M., Kim, A. G., Kim, M.

Y., Lee, J. C., Nunes, N. J., Pain, R., Pennypacker, C. R., Quimby, R., Lidman, C., Ellis, R. S., Irwin, M., McMahon, R. G., Ruiz-Lapuente, P., Walton, N., Schaefer, B., Boyle, B. J., Filippenko, A. V., Matheson, T., Fruchter, A. S., Panagia, N., Newberg, H. J. M., Couch, W. J. & The Supernova Cosmology Project, 1999, ApJ, 517, 565

Péroux C., Dessauges-Zavadsky M., D'Odorico S., Sun Kim T. & McMahon R. G., 2005, MNRAS, 363, 479

Pettini, M., Kellogg, M., Steidel, C. C., Dickinson, M., Adelberger, K. L., Giavalisco, M., 1998, ApJ, 508, 539

Pettini,M., Steidel, C. C., Adelberger, K. L., Dickinson, M. & Giavalisco, M., 2000, ApJ, 528, 96

Pettini,M., Shapley, A. E., Steidel, C. C., Cuby, J.-G., Dickinson, M., Morwood, A. F. M., Adelberger, K. L. & Giavalisco, M., 2001, ApJ, 554, 981

Pettini,M., Rix, S. A., Steidel, C. C., Adelberger, K. L., Hunt, M. & Shapley, S., 2002, ApJ, 569, 742

Pettini, M., Madau, P., Bolte, M., Prochaska, J. X., Ellison, S. L. & Fan, X., 2003, ApJ, 594, 695

Phillipps S., Fong R., Fall R.S., Ellis S.M. & MacGillivray, H.T., 1978, MNRAS, 182, 673

Pichon C., Scannapieco E., Aracil B., Petitjean P., Aubert D., Bergeron J. & Colombi S., 2003, ApJ, 397, 97

Phleps S., Peacock J.A., Meisenheimer K. & Wolf C., 2006, A&A, 457, 145

Rassat, A., Land, K., Lahav, O. & Abdalla, F. B., 2007, MNRAS, 377, 1085

Reiprich, T.H. & Böhringer, H., 2002, ApJ, 567, 716

Refregier A., Spergel D.N. & Herbig T., 2000, ApJ, 531, 31

Renzini, A., 1997, ApJ, 488, 35

Richards, G. T., Nichol, R. C., Gray, A. G., Brunner, R. J., Lupton, R. H., Vanden Berk, D. E., Chong, S. S., Weinstein, M. A., Schneider, D. P., Anderson, S. F., Munn, J. A.,

Harris, H. C., Strauss, M. A., Fan, X., Gunn, J. E., Ivezić, Ž, York, D. G., Brinkmann, J. & Moore, A. W., 2004, ApJS, 155, 257

Ross N. P., da ngela J., Shanks T., Wake D. A., Cannon R. D., Edge A. C., Nichol R. C., Outram P. J., Colless M., Couch W. J., Croom S. M., de Propris R., Drinkwater M. J., Eisenstein D. J., Loveday J., Pimbblet K. A., Roseboom I. G., Schneider D. P., Sharp R. G. & Weilbacher P. M., 2007, MNRAS, 381, 573

Ross N. P., Shanks T., Cannon R. D., Wake D. A., Sharp R. G., Croom S. M. & Peacock J.A., 2008, MNRAS, 387, 1323

Riess A. G., Filippenko A. V., Challis P., Clocchiatti A., Diercks A., Garnavich P. M., Gilliland R. L., Hogan C. J., Jha S., Kirshner R. P., Leibundgut B., Phillips M. M., Reiss D., Schmidt B. P., Schommer R. A., Smith R. C., Spyromilio J., Stubbs C., Suntzeff N. B. & Tonry J., 1998, AJ, 116, 1009

Sawangwit U., Shanks T., 2009, In Prep.

Sachs R. K. & Wolfe A. M., 1967, ApJ, 147, 73

Scannapieco, C., Tissera, P. B., White, S. D. M. & Springel, V., 2008, MNRAS, 389, 1137

Schäfer, B. M., Pfrommer, C., Bartelmann, M., Springel, V. & Hernquist, L., 2006, MNRAS, 370, 1309

Scranton, R., Connolly, A. J., Nichol, R. C., Stebbins, A., Szapudi, I., Eisenstein, D. J., Afshordi, N., Budavari, T., Csabai, I., Frieman, J. A., Gunn, J. E., Johnson, D., Loh, Y., Lupton, R. H., Miller, C. J., Sheldon, E. S., Sheth, R. S., Szalay, A. S., Tegmark, M. % Xu, Y., 2003, astro.ph, 7335

Seitz, S., Saglia, R. P., Bender, R., Hopp, U., Belloni, P. & Ziegler, B., 1998, MNRAS, 298, 945

Shanks T., 2007, MNRAS, 376, 173

Shen Y., Strauss M. A., Oguri M., Hennawi J. F., Fan X., Richards G. T., Hall P., Gunn J. E., Schneider D. P., Szalay A., Thakar A., Vanden-Berk D., Anderson S., Bahcall N. A., Connolly A. J., and Knapp G. R., 2007, AJ, 133, 2222

Shi L., Gu Q. S. & Peng Z. X., 2006, A&A, 450, 15

Shmaonov T., 1957, Pribory i Teknika Eksperimenta

Simon P., Hetterscheidt M., Wolf C., Meisenheimer K., Hildebrandt H., Schneider P., Schirmer M. & Erben T., 2008, astro-ph/0805.3459

Shapley, A. E., Steidel, C. C., Adelberger, K. L., Dickinson, M., Giavalisco, M. & Pettini, M., 2001, ApJ, 562, 95

Shapley, A. E., Steidel, C. C., Pettini, M. & Adelberger, K. L., 2003, ApJ, 588, 65

Smail, I., Swinbank, A. M., Richard, J., Ebeling, H., Kneib, J.-P., Edge, A. C., Stark, D., Ellis, R. S., Dye, S., Smith, G. P. & Mullis, C., 2007, ApJ, 654, 33

Smith R. E., Peacock J. A., Jenkins A., White S. D. M., Frenk C. S., Pearce F. R., Thomas P. A., Efstathiou G. & Couchman H. M. P., 2003, MNRAS, 341, 1311

Smoot G. F., Bennett C. L., Weber R., Maruschak J., Ratliff R., Janssen M., Chitwood J., Hilliard L., Lecha M., Mills R., Patschke R., Richards C., Backus C., Mather J., Hauser M., Weiss R., Wilkinson D., Gulkis S., Boggess N., Cheng E., Kelsall T., Lubin P., Meyer S., Moseley H., Murdock T., Shafer R., Silverberg R. & Wright E., 1990, ApJ, 360, 685

Smoot G. F., Bennett C. L., Kogut A., Wright E. L., Aymon J., Boggess N. W., Cheng E. S., de Amici G., Gulkis S., Hauser M. G., Hinshaw G., Jackson P. D., Janssen M., Kaita E., Kelsall T., Keegstra P., Lineweaver C., Loewenstein K., Lubin P., Mather J., Meyer S. S., Moseley S. H., Murdock T., Rokke L., Silverberg R. F., Tenorio L., Weiss R., Wilkinson D. T., 1992, ApJ, 366, 1

Songaila, V. & Cowie, L., 1996, AJ, 112, 335

Springel, V. & Hernquist, L., 2003, MNRAS, 339, 312

Stanghellini, C., O'Dea C. P., Dallacasa D., Baum S. A., Fanti R. & Fanti C., 1998, A&AS, 131, 303

Stark, D., Swinbank, A. M., Ellis, R. S., Dye, S., Smail, I. R. & Richard J., 2008, Nature, 455, 775

Steidel C. & Hamilton D., 1992, AJ, 104, 941

Steidel C. & Hamilton D., 1993, AJ, 105, 2017

Steidel C., Pettini M. & Hamilton D., 1995, AJ, 110, 2519

Steidel C., Giavalisco M., Pettini M., Dickinson M. & Adelberger K. L., 1996, ApJ, 462, L17

Steidel C., Adelberger K. L., Giavalisco M., Dickinson M. & Pettini M., 1999, ApJ, 519, 1

Steidel C., Adelberger K. L., Shapley A. E., Pettini M., Dickinson M. & Giavalisco M., 2003, ApJ, 592, 728

Stern D., Spinrad H, Eisenhardt A., Bunker A. J., Dawson S., Stanford S. A., & Elston R., 2007, ApJ, 533, 75

Strukov I. A., Brukhanov A. A., Skulachev D. P. & Sazhin M. V., 1992, MNRAS, 258, 37

Sunyaev R. A. & Zel'dovich Y. B., 1972, Comm. Astrophys. Sp. Phys., 4, 173

Sunyaev R. A. & Zel'dovich Y. B., 1980, ARA&A, 18, 537

Tegmark M. & Peebles J., 1998, ApJ, 500, L79

Teplitz, H. I., McLean, I. S., Becklin, E. E., Figer, D. F., Gilbert, A. M., Graham, J. R., Larkin, J. E., Levenson, N. A. & Wilcox, M. K., 2000, AJ, 533, L65

Veron-Cetty, M.-P. & Veron P., 1996, ESO Scientific Report, Garching: European Southern Observatory (ESO), 7th ed.

Vogt, S.S. et al., 1994, Proc. SPIE, 2198, 362

Wake, D. A., Sheth, R. K., Nichol, R. C., Baugh, C. M., Bland-Hawthorn, J., Colless, M., Couch, W. J., Croom, S. M., de Propris, R., Drinkwater, M. J., Edge, A. C., Loveday, J., Lam, T. Y., Pimbblet, K. A., Roseboom, I. G., Ross, N. P., Schneider, D. P., Shanks, T. & Sharp, R. G., 2008, MNRAS, 387, 1045

Williger G. M.; Hazard C.; Baldwin J. A. & McMahon R. G., 1996, ApJS, 104, 145

Wilman, R. J., Gerssen, J., Bower, R. G., Morris, S. L., Bacon, R., de Zeeuw, P. T. & Davies, R. L., 2005, Nature, 436, 227

Windhorst R. A., Burstein D., Mathis D. F., Neuschaefer L. W., Bertola F., Buson L. M., Koo D. C., Matthews K., Barthel P. D. & Chambers K. C., 1991, ApJ, 380, 362

Wolf C., Meisenheimer K., Roeser H.-J., Beckwith S.V.W., Fockenbrock R., Hippelein H., Von Kuhlmann B., Phleps S. & Thommes E., 1999, A&A, 343, 399

Wolf C., Meisenheimer K., Rix H.-W., Borch A., Dye S. & Kleinheinrich M., 2003, A&A, 401, 73

Worseck, G. & Wisotzki, L., 2006, A&A, 450, 495

Worseck, G., Wisotzki, L. & Selman, F., 2008, A&A, 487, 539

Yee, H. K. C., Ellingson, E., Bechtold, J., Carlberg, R. G., & Cuillandre, J.-C., 1996, AJ, 111, 1783

Young, P. J., Sargent, W. L. W., Boksenberg, A., Carswell, R. F. & Whelan, J. A. J., 1979, ApJ, 229, 891

Zel'Dovich Y. B., 1970, A&A, 5, 84

APPENDIX A

VLT LBG & QSO SPECTROSCOPIC DATA

Table A.1: Spectroscopically confirmed LBGs in the Q0042-2627 field.

ID	R.A.	Dec.	U	B	R	$z_{Ly\alpha}$	z_{ISM}	$W_{Ly\alpha}$	q
52317	11.36044	-26.09418	99.00	25.41	24.96	3.043	3.033	6.27	0.7
50010	11.32632	-26.09983	99.00	25.60	23.75	3.410	3.403	9.22	0.6
53786	11.38119	-26.09961	26.07	25.31	24.62	3.281	3.273	22.70	0.8
52441	11.36135	-26.10434	99.00	26.33	23.83	2.663	2.651	-0.50	0.5
58214	11.44962	-26.10336	24.49	24.43	23.87	2.266	0.000	0.00	0.5
51154	11.34320	-26.11006	99.00	25.05	23.96	3.020	3.012	5.70	0.5
57420	11.43475	-26.10988	99.00	26.05	23.71	3.077	3.069	4.45	0.5
52899	11.36731	-26.11397	25.83	24.53	23.58	3.038	3.065	-11.05	0.8
58139	11.44717	-26.11389	99.00	26.20	23.99	3.378	3.440	-22.39	0.7
57870	11.44250	-26.12039	24.91	25.14	24.22	3.091	3.077	-2.71	0.5
51436	11.34775	-26.12468	99.00	26.22	24.74	2.911	2.365	10.20	0.6
58084	11.44736	-26.12419	25.93	25.70	24.99	2.879	2.864	12.07	0.5
52352	11.36119	-26.13094	99.00	25.21	24.19	3.166	3.158	84.55	0.7
56062	11.41375	-26.13610	25.48	24.82	23.77	2.568	2.601	-34.53	0.7
56410	11.41949	-26.14035	26.20	25.52	24.99	3.275	3.266	-24.30	0.5
54627	11.39373	-26.14287	99.00	25.83	24.26	3.065	3.082	10.34	0.5
49976	11.32719	-26.14790	99.00	26.53	24.51	3.344	3.336	0.30	0.5
54014	11.38443	-26.15287	99.00	25.44	23.72	2.893	2.886	-2.39	0.5
57103	11.42996	-26.15161	24.82	24.67	23.83	2.849	2.837	7.70	0.6
53681	11.38045	-26.15673	26.24	25.72	24.95	2.306	2.298	55.36	0.6
55498	11.40570	-26.16275	99.00	25.90	24.19	2.677	2.714	-23.36	0.7
56789	11.42661	-26.17525	99.00	26.39	24.95	2.348	2.340	12.33	0.5
52368	11.36120	-26.18172	99.00	25.80	24.16	3.693	3.685	4.50	0.5
50357	11.33194	-26.18739	99.00	25.01	23.43	2.848	2.840	3.42	0.6
57881	11.44380	-26.18554	25.58	25.35	24.72	2.532	2.529	14.83	0.5
50170	11.33004	-26.19670	24.73	25.19	24.19	3.065	3.061	11.51	0.5
50012	11.32668	-25.94995	99.00	26.34	24.97	2.888	2.886	5.87	0.5
50237	11.32822	-25.95347	25.22	24.34	23.20	2.823	2.814	3.86	0.9
53340	11.37352	-25.95252	24.79	24.44	23.77	2.219	2.220	-75.63	0.7

Table A.1 – continued from previous page

ID	R.A.	Dec.	U	B	R	$z_{Ly\alpha}$	z_{ISM}	$W_{Ly\alpha}$	q
58576	11.45578	-25.95296	99.00	25.23	24.68	2.898	2.881	11.16	0.7
52490	11.35779	-25.95747	24.75	24.45	21.53	3.049	3.057	6.36	0.5
57160	11.42959	-25.96631	99.00	24.85	23.60	2.866	2.858	67.43	0.7
55333	11.40128	-25.97015	24.33	24.38	23.50	2.409	2.402	2.83	0.5
49989	11.32596	-25.97297	99.00	26.26	24.50	2.878	2.891	-14.48	0.6
54189	11.38569	-25.97315	99.00	25.52	24.24	3.138	3.130	-15.69	0.5
52361	11.35960	-25.97561	99.00	25.42	23.86	3.492	3.481	13.61	0.7
50243	11.32643	-25.98054	23.13	23.33	21.43	2.398	2.399	9.05	0.5
53929	11.38271	-25.98320	99.00	25.97	24.41	2.837	2.823	10.38	0.5
52662	11.36223	-25.98786	99.00	25.17	23.08	3.188	3.179	2.17	0.5
57086	11.42958	-25.99710	99.00	26.17	24.68	3.286	3.285	7.03	0.5
52858	11.36717	-26.01341	25.44	24.70	24.15	2.276	2.270	18.46	0.6
58270	11.44991	-26.01407	99.00	25.73	24.11	3.356	3.310	-3.14	0.6
51005	11.34125	-26.02566	99.00	26.74	24.98	2.910	2.904	6.62	0.5
55926	11.40971	-26.03113	24.75	24.65	22.98	3.196	3.184	5.64	0.6
55336	11.40268	-26.03737	99.00	25.85	24.59	2.973	2.966	6.00	0.5
55365	11.40294	-26.03974	99.00	25.77	24.58	2.900	2.888	15.60	0.6
49982	11.32612	-26.04301	25.34	25.09	24.26	2.763	2.754	4.30	0.5
51040	11.34164	-26.04777	25.79	25.09	24.89	3.026	3.019	21.53	0.7
39655	11.17038	-25.95004	99.00	25.09	23.58	2.975	2.956	-8.83	0.5
42990	11.22148	-25.96475	26.17	25.08	23.58	3.366	3.355	12.14	0.8
46410	11.26959	-25.96203	99.00	26.19	24.27	3.309	3.300	39.07	0.7
42100	11.20835	-25.97116	25.17	25.05	24.14	2.333	2.328	-10.64	0.5
45833	11.26332	-25.97051	99.00	25.80	24.33	2.829	2.821	6.63	0.5
38497	11.15409	-25.98135	25.72	24.83	23.84	3.221	3.213	35.20	0.8
42517	11.21502	-25.97953	25.17	24.61	24.04	2.941	2.929	5.08	0.6
39790	11.17310	-25.98404	26.07	25.12	24.25	2.986	2.978	9.01	0.5
46220	11.26850	-25.98530	25.39	24.52	23.36	2.553	2.545	-1.43	0.5
39009	11.16136	-25.99330	24.90	24.35	24.22	2.677	2.669	3.39	0.5
45561	11.25881	-25.99356	99.00	25.65	23.89	3.277	3.261	18.09	0.8
40991	11.18954	-26.00104	25.70	24.87	23.85	2.644	2.636	2.98	0.6
45238	11.25457	-26.00036	25.09	24.65	23.88	2.554	2.538	36.69	0.7
39923	11.17433	-26.01108	24.78	24.22	23.69	2.321	2.313	4.49	0.5
45011	11.25198	-26.01508	99.00	25.51	24.39	3.023	3.015	9.49	0.7
36527	11.13299	-26.01792	99.00	25.34	23.96	2.434	2.426	5.19	0.5
40092	11.17678	-26.01942	25.73	25.04	23.93	2.503	2.495	71.68	0.6
42926	11.22110	-26.02407	99.00	25.67	24.28	3.251	3.244	18.43	0.5

Table A.1 – continued from previous page

ID	R.A.	Dec.	U	B	R	$z_{Ly\alpha}$	z_{ISM}	$W_{Ly\alpha}$	q
44756	11.24679	-26.03119	25.61	25.00	24.10	3.017	3.009	5.01	0.5
46169	11.26869	-26.03502	99.00	25.55	24.82	3.428	3.421	170.96	0.8
39182	11.16166	-26.03883	26.00	24.54	21.49	3.380	3.368	121.53	0.5
42221	11.20962	-26.03892	25.72	24.38	23.28	2.394	2.386	6.87	0.6
42426	11.21438	-26.11025	99.00	26.11	24.32	2.406	2.399	10.46	0.5
39069	11.16275	-26.11247	24.34	24.15	23.72	2.298	2.296	56.19	0.7
42151	11.21002	-26.11339	25.14	24.97	24.52	3.215	3.207	13.57	0.5
40256	11.18038	-26.11608	25.48	25.43	24.65	2.795	2.777	6.05	0.5
44943	11.25119	-26.11946	99.00	25.60	23.99	2.932	2.929	8.23	0.5
40194	11.17953	-26.12470	99.00	25.79	24.17	2.522	2.512	11.24	0.6
39860	11.17455	-26.12815	99.00	24.46	24.12	2.283	2.264	-64.85	0.7
39277	11.16587	-26.13522	26.09	24.79	24.05	2.650	2.637	8.09	0.5
39267	11.16617	-26.13783	25.77	24.83	24.66	2.392	2.381	9.46	0.5
42591	11.21764	-26.13833	99.00	25.84	24.31	3.388	3.380	38.96	0.5
44390	11.24285	-26.14153	99.00	26.32	24.81	2.422	2.417	8.95	0.5
39978	11.17666	-26.14409	26.21	25.01	24.38	2.272	2.261	-36.74	0.5
42931	11.22212	-26.15629	24.24	24.29	24.10	2.285	2.277	3.09	0.7
41916	11.20580	-26.15898	99.00	25.68	23.67	2.735	2.733	7.62	0.5
39287	11.16697	-26.16535	99.00	26.13	24.61	2.788	2.778	21.91	0.5
42287	11.21291	-26.16791	24.68	24.93	24.51	2.692	2.684	37.37	0.6
39901	11.17419	-26.17357	25.39	24.30	23.13	3.039	3.061	-4.34	0.7
36524	11.13451	-26.17903	26.29	24.80	24.58	2.491	2.472	6.89	0.5
40626	11.18611	-26.17812	99.00	26.41	24.43	2.987	2.978	10.50	0.5
36785	11.13617	-26.18979	25.02	25.10	23.43	2.628	2.633	16.21	0.6
41236	11.19517	-26.19042	25.22	25.39	24.34	3.323	3.310	4.93	0.5
45845	11.26510	-26.18838	26.02	24.99	24.22	2.564	2.548	3.62	0.5
41826	11.20529	-26.19892	24.88	24.73	24.05	2.619	2.583	5.25	0.6
41169	11.19376	-26.20137	99.00	25.30	23.88	3.404	3.387	36.01	0.7
30237	11.05472	-26.09487	24.81	24.57	23.60	2.861	2.852	9.98	0.6
30130	11.05457	-26.10023	25.64	24.75	24.69	2.307	2.299	6.22	0.5
27194	11.01867	-26.10287	24.77	24.65	23.95	2.423	2.434	-58.89	0.8
30694	11.05995	-26.10567	25.73	24.95	23.61	2.543	2.540	1.86	0.5
36577	11.13468	-26.10696	99.00	25.89	25.50	2.531	2.523	4.02	0.6
29930	11.05187	-26.11035	26.04	25.16	23.98	2.757	2.753	8.01	0.7
34192	11.10089	-26.10938	99.00	25.92	24.64	2.999	2.990	22.34	0.6
34192	11.10089	-26.10938	99.00	25.92	24.64	3.235	3.227	14.92	0.5
31761	11.07217	-26.11348	25.17	24.67	23.67	2.793	2.785	11.22	0.8

Table A.1 – continued from previous page

ID	R.A.	Dec.	U	B	R	$z_{Ly\alpha}$	z_{ISM}	$W_{Ly\alpha}$	q
29915	11.05198	-26.11983	24.88	24.70	24.36	2.409	2.401	8.45	0.6
32466	11.08039	-26.12165	24.91	24.78	24.07	2.667	2.655	-8.87	0.7
27227	11.02024	-26.13477	99.00	25.42	25.08	2.498	2.490	6.11	0.7
31655	11.07213	-26.13497	99.00	25.43	24.80	2.682	2.693	-16.61	0.5
36599	11.13490	-26.13359	23.74	23.95	23.97	2.410	2.386	-1.50	0.6
37623	11.14495	-26.13859	25.18	25.01	23.76	2.978	2.973	9.20	0.6
27611	11.02495	-26.14230	99.00	26.11	24.42	2.556	2.547	5.76	0.5
35094	11.11239	-26.14479	23.88	23.92	22.10	2.897	2.890	3.58	0.5
28383	11.03327	-26.14899	24.57	24.43	23.66	2.339	2.336	1.76	0.6
35386	11.11977	-26.14787	25.18	24.63	24.52	2.232	2.230	7.56	0.8
32064	11.07677	-26.15244	25.91	25.10	24.64	2.479	2.471	6.13	0.5
34306	11.10204	-26.15920	99.00	25.01	24.08	3.301	3.288	23.88	0.8
33567	11.09238	-26.16185	23.55	23.68	23.36	2.265	2.250	5.00	0.6
33826	11.09664	-26.16807	25.99	25.09	24.48	2.257	2.258	2.74	0.6
26853	11.01304	-26.17423	25.78	24.28	21.66	2.855	2.858	6.68	0.5
32691	11.08355	-26.17521	26.25	25.63	24.64	2.784	2.785	8.09	0.5
34525	11.10132	-26.17751	24.97	24.74	22.53	2.927	2.920	13.60	0.5
29581	11.04721	-26.18296	25.42	24.62	23.82	2.600	2.605	-17.32	0.8
38156	11.15251	-26.18042	26.18	25.58	24.04	2.343	2.343	4.66	0.5
29035	11.03861	-26.18534	25.39	23.89	21.51	3.299	3.291	18.97	0.8
34584	11.10594	-26.18957	24.31	24.32	23.62	2.695	2.691	6.33	0.6
29974	11.05238	-26.19224	25.85	24.96	23.78	2.805	2.798	4.83	0.5
36271	11.12949	-25.95489	99.00	25.86	24.06	3.177	3.205	-11.77	0.5
30119	11.05375	-25.96168	25.64	25.01	24.30	2.505	2.487	7.16	0.6
36262	11.13002	-25.95996	99.00	26.03	24.64	3.168	3.159	8.80	0.5
27367	11.02087	-25.96491	24.66	24.65	24.25	2.628	2.622	3.93	0.5
35843	11.12305	-25.96457	26.02	24.72	23.24	3.224	3.218	1.45	0.5
27910	11.02704	-25.97148	24.96	24.68	24.05	2.611	2.626	-23.77	0.7
32906	11.08485	-25.97185	26.16	25.47	24.72	2.618	2.603	6.29	0.5
37501	11.14291	-25.97160	99.00	26.25	24.00	3.241	3.233	4.89	0.5
34990	11.11221	-25.98407	25.32	24.83	23.89	2.733	2.721	9.19	0.9
35739	11.12378	-25.98954	26.04	25.27	24.84	3.044	3.035	7.60	0.5
35604	11.12180	-25.99564	26.15	24.87	24.64	2.428	2.404	6.37	0.5
29690	11.04834	-26.00688	24.70	24.49	23.83	2.665	2.680	-11.61	0.8
34873	11.10566	-26.00655	24.93	23.71	20.98	3.231	3.226	2.46	0.7
33633	11.09280	-26.00996	99.00	25.32	23.53	2.964	2.962	13.94	0.7
29700	11.04559	-26.02339	24.30	24.41	22.67	2.788	2.772	10.99	0.5

Table A.1 – continued from previous page

ID	R.A.	Dec.	U	B	R	$z_{Ly\alpha}$	z_{ISM}	$W_{Ly\alpha}$	q
27692	11.02338	-26.02976	24.33	24.49	22.82	2.875	2.862	17.42	0.5
32575	11.07968	-26.03167	24.83	24.26	23.13	2.909	2.901	3.49	0.5
36401	11.13090	-26.03923	24.28	24.49	23.99	2.389	2.386	-1.09	0.5
28404	11.03435	-26.05667	24.63	24.79	24.85	2.630	2.632	82.26	0.5
19418	10.90369	-25.94191	99.00	25.53	23.85	2.407	2.373	2.86	0.6
20529	10.92085	-25.94408	99.00	25.73	24.59	3.505	3.497	12.38	0.5
14941	10.82662	-25.96262	24.23	23.11	23.13	3.108	3.109	2.92	0.5
18461	10.88869	-25.96419	99.00	26.01	24.31	3.518	3.502	14.92	0.6
21823	10.94053	-25.96622	24.58	24.46	23.77	2.276	2.298	-2.84	0.6
17911	10.87979	-25.97200	25.90	24.89	23.85	2.974	2.966	13.24	0.5
20677	10.92178	-25.97205	99.00	26.45	24.35	2.476	2.468	17.85	0.5
16106	10.84875	-25.97499	99.00	25.78	24.46	2.637	2.641	-20.32	0.5
18938	10.89607	-25.98278	23.52	23.82	23.16	2.387	2.415	-9.19	0.9
16810	10.86100	-25.99040	25.71	25.13	24.19	3.267	3.266	12.22	0.8
15935	10.84626	-26.00318	25.65	25.50	24.27	3.085	3.075	26.12	0.8
19996	10.91164	-26.00281	23.68	24.12	23.66	2.350	2.337	-10.88	0.5
15723	10.84195	-26.00849	99.00	25.29	23.90	2.794	2.786	29.04	0.8
20407	10.91873	-26.00961	24.43	24.52	23.89	2.429	2.421	24.67	0.9
18537	10.89071	-26.01225	99.00	26.16	25.11	3.144	3.135	8.20	0.6
17580	10.87324	-26.02220	99.00	25.12	23.80	3.182	3.176	74.63	0.7
21556	10.93485	-26.02401	25.91	24.61	23.37	2.627	2.611	35.96	0.8
15532	10.83896	-26.03046	24.79	25.05	24.61	2.558	2.550	5.33	0.5
20388	10.91821	-26.02900	23.73	24.19	23.84	2.334	2.334	3.67	0.5
20474	10.92079	-26.03510	99.00	26.10	24.69	2.615	2.634	-11.75	0.7
14708	10.82457	-26.04274	24.28	22.04	24.19	2.806	2.792	23.81	0.8
18780	10.89207	-26.04103	25.86	25.17	22.15	2.928	2.920	21.12	0.5
23331	10.96080	-26.04388	24.75	25.05	22.71	2.940	2.959	-4.76	0.5
14694	10.82430	-26.04722	24.19	21.97	24.27	2.939	2.931	5.44	0.5
21049	10.92885	-26.04650	26.24	24.77	23.99	2.922	2.913	53.05	0.8
15968	10.84695	-26.09343	25.66	24.94	24.35	2.731	2.723	8.60	0.5
14897	10.82722	-26.10015	23.76	23.20	23.78	2.622	2.632	12.65	0.5
15284	10.83436	-26.10326	25.39	24.52	24.15	2.899	2.891	4.21	0.5
23109	10.95953	-26.10344	24.50	24.37	22.55	3.152	3.133	-7.51	0.5
14710	10.82360	-26.10949	24.44	22.12	23.64	2.604	2.602	4.67	0.6
20233	10.91451	-26.11913	24.23	24.10	23.05	2.755	2.747	8.58	0.7
16867	10.86167	-26.12171	99.00	25.49	23.73	3.056	3.050	3.81	0.5
20105	10.91204	-26.13473	26.03	24.37	21.88	2.956	2.958	5.59	0.5

Table A.1 – continued from previous page

ID	R.A.	Dec.	U	B	R	$z_{Ly\alpha}$	z_{ISM}	$W_{Ly\alpha}$	q
22858	10.95713	-26.13199	24.04	24.27	23.73	2.524	2.514	12.38	0.5
16006	10.84729	-26.13984	99.00	25.68	23.80	2.655	2.649	-4.14	0.7
17708	10.87601	-26.15058	25.05	24.54	23.25	2.786	2.777	12.84	0.8
22863	10.95776	-26.15129	25.03	24.84	24.37	3.019	3.008	6.73	0.6
16813	10.86154	-26.17201	23.90	24.35	24.15	2.352	2.339	2.33	0.7
18181	10.88251	-26.17508	24.52	24.13	21.59	2.716	2.713	14.48	0.5
50117	11.33053	-26.34037	25.19	25.21	24.57	2.807	2.799	6.28	0.5
57502	11.43789	-26.34723	23.93	24.38	23.94	2.661	2.690	-5.63	0.6
53184	11.37515	-26.35092	25.95	25.24	24.58	2.761	2.754	14.62	0.7
49788	11.32663	-26.35363	99.00	26.14	24.94	3.002	2.987	-13.28	0.6
52691	11.36678	-26.35703	25.26	25.30	23.89	2.856	2.840	7.76	0.5
55941	11.41414	-26.35678	24.63	24.32	24.42	2.553	2.540	126.79	0.6
58232	11.45118	-26.35927	24.57	24.59	23.86	2.549	2.565	-1.33	0.5
56907	11.42864	-26.36855	25.49	24.71	23.49	2.907	2.913	-20.31	0.9
52151	11.35919	-26.37226	99.00	25.16	23.62	2.947	2.932	5.45	0.6
54742	11.39685	-26.37849	24.52	24.81	24.19	2.641	2.635	5.08	0.5
57757	11.44290	-26.37723	25.56	25.01	24.43	2.968	2.959	4.46	0.6
58182	11.45134	-26.38505	26.21	25.20	24.06	2.542	2.555	-22.78	0.5
58387	11.45410	-26.39939	23.97	24.33	23.62	2.576	2.590	-0.01	0.5
51102	11.34477	-26.40415	25.08	24.83	24.26	2.462	2.466	7.36	0.6
55339	11.40426	-26.40452	24.71	24.43	23.54	2.331	2.322	0.05	0.6
52971	11.37201	-26.40923	24.10	24.42	24.43	2.966	2.944	13.09	0.5
52971	11.37201	-26.40923	24.10	24.42	24.43	2.559	2.552	15.69	0.5
49809	11.32689	-26.41207	25.27	25.29	24.82	3.105	3.094	14.67	0.7
50561	11.33771	-26.41942	24.65	24.91	24.99	2.427	2.415	6.39	0.6
54585	11.39489	-26.43174	24.99	24.92	24.06	2.855	2.846	21.32	0.5
57878	11.44575	-26.43252	24.46	24.41	24.39	2.425	2.417	132.50	0.6
57807	11.44378	-26.43493	23.88	24.36	23.85	2.746	2.731	9.54	0.6
52005	11.35536	-26.21651	23.82	24.08	23.34	2.322	2.324	19.21	0.5
56309	11.41846	-26.21929	25.16	24.85	23.96	2.679	2.668	-6.82	0.6
51380	11.34607	-26.22130	23.68	24.12	23.56	2.301	2.294	9.12	0.8
51556	11.34908	-26.22929	23.83	24.07	23.67	2.329	2.325	29.12	0.7
58434	11.45423	-26.22858	24.24	24.48	23.90	3.139	3.135	3.41	0.6
58646	11.45816	-26.23414	25.09	24.99	23.48	2.886	2.878	22.66	0.5
53597	11.37973	-26.24443	24.69	25.12	24.36	2.506	2.502	4.83	0.5
57314	11.43410	-26.24450	23.63	23.96	23.34	2.430	2.422	3.45	0.9
55643	11.40798	-26.25232	26.06	24.97	23.60	2.837	2.837	-22.95	0.7

Table A.1 – continued from previous page

ID	R.A.	Dec.	U	B	R	$z_{Ly\alpha}$	z_{ISM}	$W_{Ly\alpha}$	q
53688	11.38123	-26.25969	24.64	24.67	24.60	2.293	2.285	11.96	0.5
55676	11.40872	-26.26391	99.00	26.14	23.81	3.294	3.285	6.33	0.5
56798	11.42682	-26.26745	26.28	25.63	24.53	2.589	2.585	-40.90	0.6
57237	11.43408	-26.27794	25.31	24.99	24.37	2.574	2.564	14.53	0.6
50621	11.33771	-26.28004	25.68	25.27	24.48	2.352	2.353	7.24	0.5
51015	11.34169	-26.28276	25.49	24.61	23.63	2.837	2.873	-16.12	0.9
55381	11.40522	-26.28459	26.21	25.64	24.56	2.918	2.900	13.35	0.6
50959	11.34204	-26.28746	99.00	25.43	25.01	2.963	2.944	32.57	0.5
57924	11.44474	-26.28766	99.00	26.27	23.83	2.842	2.843	-0.10	0.5
54293	11.38902	-26.29636	25.04	24.69	23.99	2.411	2.420	3.69	0.5
53590	11.37932	-26.29942	26.03	24.87	23.81	2.727	2.720	1.76	0.6
42948	11.22232	-26.19871	25.08	24.73	24.21	2.895	2.280	8.39	0.6
42246	11.21269	-26.20142	99.00	25.57	24.64	2.944	2.936	7.81	0.6
43170	11.22662	-26.22198	25.89	25.00	25.27	2.466	2.452	14.21	0.5
43729	11.23387	-26.22851	25.77	25.01	23.99	2.415	2.414	4.19	0.7
39518	11.17027	-26.23623	25.14	24.86	24.07	2.969	2.961	10.12	0.5
44300	11.24169	-26.23915	24.39	24.55	23.92	2.560	2.552	14.67	0.5
36849	11.13811	-26.24487	26.29	25.39	24.59	2.596	2.589	9.94	0.5
41865	11.20502	-26.25251	23.78	24.24	23.41	2.321	2.312	9.09	0.5
45005	11.25280	-26.25302	99.00	26.31	24.23	3.118	3.106	7.39	0.6
38511	11.15409	-26.25996	26.19	25.00	23.51	3.332	3.323	15.34	0.5
40060	11.17780	-26.26540	25.80	24.92	23.90	2.907	2.900	12.82	0.9
45896	11.26611	-26.26641	25.64	24.94	24.28	2.514	2.507	2.55	0.5
36341	11.13130	-26.27307	26.33	24.83	23.71	2.839	2.860	-11.07	0.6
40677	11.18786	-26.27443	99.00	26.29	24.96	3.236	3.228	26.82	0.7
44059	11.23903	-26.27303	24.97	25.24	24.29	3.396	3.388	14.27	0.7
37010	11.13883	-26.28142	24.82	24.59	23.68	2.546	2.535	12.61	0.9
45346	11.25832	-26.28174	25.88	25.12	24.09	2.749	2.737	5.97	0.7
38464	11.15609	-26.28685	25.57	25.06	24.25	2.919	2.911	13.63	0.5
41861	11.20669	-26.28506	25.87	25.21	24.39	2.508	2.500	7.61	0.5
38613	11.15764	-26.28937	24.74	24.87	23.92	2.425	2.406	10.71	0.8
39214	11.16629	-26.29185	24.74	25.01	25.26	2.864	2.872	-8.52	0.5
38966	11.16281	-26.29435	26.13	25.62	24.33	2.881	2.915	-20.84	0.6
36422	11.13282	-26.35176	23.77	23.89	23.30	2.404	2.431	-5.59	0.8
37688	11.14774	-26.35476	99.00	26.20	24.27	3.232	3.224	3.10	0.5
43582	11.23278	-26.35545	25.47	24.70	24.03	2.717	2.714	1.71	0.5
45107	11.25460	-26.35825	99.00	25.35	23.32	3.349	3.342	3.43	0.5

Table A.1 – continued from previous page

ID	R.A.	Dec.	U	B	R	$z_{Ly\alpha}$	z_{ISM}	$W_{Ly\alpha}$	q
36178	11.12925	-26.36088	23.58	22.98	23.44	2.772	2.768	28.69	0.7
38448	11.15700	-26.36948	99.00	26.64	25.50	2.940	2.917	7.77	0.6
43520	11.23218	-26.36955	99.00	26.47	24.32	3.087	3.079	21.26	0.5
43822	11.23584	-26.37244	25.30	24.81	24.06	2.638	2.636	12.09	0.5
43113	11.22629	-26.37898	25.43	24.90	24.82	2.347	2.341	9.51	0.5
40248	11.18212	-26.38212	26.10	25.15	25.09	2.753	2.745	10.15	0.5
44064	11.23938	-26.38439	24.49	24.94	24.36	2.632	2.625	5.74	0.5
44889	11.25237	-26.38921	99.00	26.25	24.78	2.660	2.654	9.68	0.5
44761	11.25003	-26.39457	24.48	24.77	24.08	2.955	2.947	19.10	0.5
44910	11.25258	-26.41051	26.32	25.67	24.15	2.934	2.928	7.60	0.6
37921	11.15032	-26.41840	25.63	25.13	23.98	2.984	2.976	15.73	0.7
42050	11.21015	-26.41953	99.00	25.57	24.20	3.115	3.111	15.97	0.6
43837	11.23729	-26.42871	99.00	25.28	24.58	2.842	2.848	37.19	0.5
44981	11.25370	-26.43613	26.06	24.82	24.16	2.841	2.845	101.01	0.6
39603	11.17256	-26.44024	99.00	25.02	23.89	3.008	3.000	-0.62	0.7
29529	11.04802	-26.34197	25.66	24.92	24.44	2.856	2.853	126.14	0.7
36504	11.13365	-26.34167	24.56	24.39	23.18	2.916	2.910	2.58	0.6
37688	11.14774	-26.35476	99.00	26.20	24.27	3.154	3.152	-22.07	0.5
28221	11.03306	-26.36738	23.92	24.24	23.61	2.496	2.487	6.84	0.5
36755	11.13640	-26.36758	24.08	24.36	23.67	2.367	2.359	6.12	0.6
30389	11.05784	-26.37083	25.14	25.01	23.84	2.572	2.552	6.35	0.5
31757	11.06819	-26.37708	24.83	24.26	21.62	2.400	2.394	21.68	0.5
35184	11.11698	-26.37759	24.07	24.44	23.55	2.570	2.572	5.15	0.6
35545	11.12232	-26.38431	25.24	24.50	23.84	2.534	2.531	4.51	0.6
29707	11.05028	-26.38895	26.28	25.27	24.33	2.763	2.756	27.30	0.7
36653	11.13693	-26.38795	99.00	25.55	24.57	3.241	3.219	4.20	0.5
29544	11.04827	-26.39123	99.00	26.36	24.44	2.766	2.763	13.28	0.6
26675	11.01396	-26.40882	25.68	25.08	23.69	3.027	3.025	-0.31	0.6
26366	11.01123	-26.42517	99.00	25.91	24.30	3.313	3.305	5.38	0.5
30429	11.05894	-26.42549	24.58	24.46	24.19	2.392	2.392	3.74	0.7
35216	11.11732	-26.42309	25.63	25.03	23.60	2.972	3.018	-41.40	0.7
27059	11.01752	-26.44611	24.38	24.26	22.93	2.554	2.546	0.46	0.6
35046	11.11496	-26.20087	99.00	26.64	25.17	3.013	3.039	-9.92	0.5
0	11.06874	-26.21792	99.00	0.00	0.00	2.588	2.580	138.55	0.7
26760	11.01523	-26.22063	99.00	26.56	24.71	3.201	3.173	16.96	0.5
32808	11.08367	-26.22328	24.03	24.48	23.71	2.290	2.291	3.67	0.6
36464	11.13391	-26.22852	99.00	26.51	24.75	3.064	3.057	8.18	0.5

Table A.1 – continued from previous page

ID	R.A.	Dec.	U	B	R	$z_{Ly\alpha}$	z_{ISM}	$W_{Ly\alpha}$	q
29661	11.04943	-26.24067	99.00	25.50	24.75	3.352	3.337	30.44	0.6
31897	11.07427	-26.24554	99.00	25.28	23.81	3.048	3.039	12.47	0.8
35030	11.11403	-26.24940	99.00	25.69	23.79	2.945	2.941	8.67	0.5
29309	11.04428	-26.27122	99.00	26.68	23.49	2.641	2.632	7.96	0.5
29155	11.04332	-26.27714	24.17	24.27	23.46	2.477	2.473	12.94	0.9
37393	11.14429	-26.27765	99.00	25.17	24.37	2.776	2.756	8.31	0.8
30004	11.05420	-26.28788	99.00	26.70	24.83	3.250	3.243	14.28	0.6
35455	11.12134	-26.29152	24.96	24.78	23.81	2.559	2.576	-11.82	0.5
30104	11.05468	-26.29646	24.14	24.34	23.91	2.480	2.472	11.20	0.6
36518	11.13335	-26.29612	24.99	24.55	23.20	2.826	2.807	5.02	0.6
26812	11.01499	-26.29992	24.85	25.01	23.71	2.805	2.799	7.92	0.7
31492	11.07134	-26.30026	99.00	25.56	25.04	2.832	2.824	93.07	0.6
26772	11.01411	-26.23337	25.18	24.52	23.67	2.638	2.631	-5.63	0.5
21796	10.94016	-26.19428	99.00	25.67	23.52	2.691	2.689	-0.00	0.6
16921	10.86352	-26.20063	99.00	25.94	24.40	3.248	3.242	6.17	0.6
21763	10.94085	-26.20296	25.08	24.94	24.61	2.421	2.413	5.46	0.7
17606	10.87473	-26.20806	25.26	24.31	23.87	2.756	2.749	6.71	0.8
16440	10.85548	-26.21198	25.94	24.92	24.22	2.640	2.632	15.05	0.9
18158	10.88279	-26.21454	99.00	25.60	23.38	3.221	3.211	5.60	0.5
21438	10.93539	-26.21392	99.00	25.88	24.60	3.197	3.182	5.53	0.5
20415	10.92049	-26.22541	99.00	26.25	25.32	3.174	3.163	19.26	0.7
15636	10.83961	-26.22862	25.01	25.21	22.85	2.115	2.120	4.19	0.5
22793	10.95538	-26.22916	23.59	23.88	23.01	2.344	2.336	5.92	0.5
17428	10.87290	-26.23171	25.26	25.32	24.35	2.750	2.754	37.56	0.7
14598	10.82273	-26.24241	25.43	24.89	23.96	2.739	2.722	25.88	0.8
18955	10.89791	-26.24347	24.92	24.39	23.44	2.712	2.754	-27.59	0.9
18275	10.88690	-26.24932	25.77	24.98	24.45	2.775	2.766	10.71	0.9
14866	10.82854	-26.25793	24.92	25.12	25.14	2.803	2.839	-23.07	0.7
17127	10.86784	-26.26082	99.00	25.19	24.47	3.179	3.170	60.53	0.7
20900	10.92644	-26.27696	25.36	24.89	23.68	3.106	3.105	6.26	0.5
15698	10.84075	-26.27991	24.58	24.22	22.82	2.837	2.828	3.28	0.5
19626	10.90849	-26.28002	25.18	24.86	24.79	2.527	2.532	-7.51	0.5
17534	10.87456	-26.30362	99.00	25.88	24.92	3.457	3.452	7.25	0.5
15305	10.83446	-26.18976	99.00	24.70	23.47	3.348	3.342	5.83	0.5
17915	10.87980	-26.19055	24.39	24.40	23.84	2.588	2.574	0.65	0.6
21508	10.93531	-26.34054	24.36	23.93	23.64	2.714	2.705	-12.54	0.8
17609	10.87566	-26.34315	99.00	25.80	24.02	3.013	3.005	17.83	0.5

Table A.1 – continued from previous page

ID	R.A.	Dec.	U	B	R	$z_{Ly\alpha}$	z_{ISM}	$W_{Ly\alpha}$	q
20379	10.91919	-26.35526	24.12	24.61	24.38	2.778	2.772	7.57	0.6
15421	10.83720	-26.35773	25.55	24.32	23.75	2.962	2.935	6.65	0.5
19320	10.90407	-26.35851	99.00	25.56	23.96	3.290	3.284	8.77	0.6
14722	10.82571	-26.37016	25.09	22.05	24.25	2.909	2.922	30.44	0.5
14736	10.82621	-26.37643	25.06	22.17	24.29	3.693	3.682	13.41	0.5
19119	10.90031	-26.37582	25.15	24.82	23.29	2.739	2.731	10.38	0.7
14161	10.81635	-26.37893	24.32	19.65	24.42	2.885	2.921	-13.65	0.5
21546	10.93741	-26.37938	24.84	25.09	24.05	2.448	2.487	-13.10	0.5
16772	10.86199	-26.38984	99.00	25.79	24.85	3.242	3.234	7.97	0.6
22264	10.94700	-26.39323	23.04	23.42	21.86	2.756	2.739	10.83	0.5
15265	10.83504	-26.40688	25.52	24.78	24.70	2.871	2.852	7.10	0.5
14723	10.82592	-26.41199	24.29	22.01	24.26	2.209	2.201	14.12	0.7
19424	10.90577	-26.41610	24.49	24.85	24.05	2.404	2.410	-12.33	0.5
14779	10.82632	-26.41844	24.37	22.14	24.61	2.562	2.554	3.25	0.5
15223	10.83483	-26.42238	25.35	24.82	24.58	2.947	2.932	9.03	0.6
16852	10.86260	-26.42518	99.00	25.15	23.98	2.674	2.666	7.79	0.5
22378	10.94839	-26.42554	24.86	24.89	24.01	2.647	2.640	6.39	0.5
22525	10.95181	-26.42781	23.84	23.78	23.15	2.360	2.353	4.70	0.5

Table A.2: Spectroscopically confirmed LBGs in the J0124+0044 field.

ID	R.A.	Dec.	U	B	I	$z_{Ly\alpha}$	z_{ISM}	$W_{Ly\alpha}$	q
4046	21.24819	0.84664	25.02	24.65	23.28	2.452	2.298	4.69	0.5
4446	21.24224	0.83294	26.56	25.44	24.18	2.447	2.428	9.53	0.5
5735	21.22814	0.83037	26.64	25.62	22.85	2.720	2.724	3.44	0.5
5954	21.22512	0.82660	24.62	25.00	23.61	2.541	2.533	9.42	0.5
8462	21.19547	0.81757	24.86	25.15	23.76	2.481	2.463	4.33	0.5
8133	21.19925	0.81271	26.72	25.67	23.85	3.484	3.469	32.88	0.7
4104	21.24702	0.81367	26.01	25.20	24.03	2.947	2.939	92.23	0.6
8341	21.19703	0.80260	24.36	24.54	23.69	2.744	2.736	8.46	0.5
1130	21.28418	0.79742	24.95	25.26	23.47	3.211	3.203	8.36	0.5
8206	21.19758	0.79293	25.71	25.54	24.39	2.837	2.829	11.14	0.6
624	21.28984	0.79273	26.63	26.17	23.89	3.488	3.479	78.20	0.7
6158	21.22148	0.78776	25.40	24.98	24.12	2.967	2.956	3.52	0.5
5136	21.23368	0.77195	26.64	25.25	24.10	3.028	3.019	4.01	0.6

Table A.2 – continued from previous page

ID	R.A.	Dec.	U	B	I	$z_{Ly\alpha}$	z_{ISM}	$W_{Ly\alpha}$	q
679	21.28956	0.77360	26.63	25.90	22.78	2.907	2.902	8.03	0.5
27	21.29718	0.76922	24.94	24.91	24.34	2.549	2.536	64.28	0.5
3785	21.25195	0.98049	26.65	25.65	24.20	2.788	2.780	18.59	0.5
6817	21.21523	0.95354	25.07	25.35	24.01	2.439	2.435	4.94	0.6
47	21.29767	0.93569	24.70	24.99	24.30	2.646	2.653	-38.89	0.6
6234	21.22354	0.90622	26.64	25.48	22.03	2.739	2.731	9.56	0.5
14445	21.12044	0.99797	26.06	25.73	24.14	2.645	2.642	10.62	0.5
15616	21.10523	0.99500	24.69	25.01	23.56	3.130	3.117	5.52	0.5
20686	21.04127	0.98847	23.98	24.29	23.46	2.392	2.369	95.70	0.5
17949	21.07348	0.98463	25.16	24.95	23.56	3.240	3.232	12.94	0.5
17039	21.08512	0.97984	23.96	24.43	23.92	2.693	2.679	7.23	0.5
18793	21.06299	0.97041	25.52	25.23	24.13	2.419	2.411	4.95	0.7
18812	21.06283	0.96640	25.00	25.36	24.16	3.153	3.145	17.95	0.5
15800	21.10222	0.96688	24.68	24.96	23.97	2.758	2.787	-9.48	0.5
16992	21.08490	0.96220	25.79	25.25	24.21	3.063	3.055	40.40	0.8
12418	21.14684	0.96210	25.88	25.19	24.27	2.898	2.895	18.94	0.5
19497	21.05478	0.95919	26.62	25.14	23.98	2.352	2.344	141.34	0.5
17374	21.08046	0.95354	24.80	25.15	24.10	2.862	2.854	36.00	0.5
17586	21.07789	0.94464	25.80	25.65	24.03	2.992	2.984	7.97	0.5
21676	21.02810	0.94132	25.73	25.42	24.39	2.990	2.982	46.81	0.7
18525	21.06639	0.93240	26.50	25.95	23.74	3.298	3.290	1.92	0.5
18155	21.07055	0.92668	26.47	25.67	24.47	2.409	2.400	5.46	0.5
14436	21.12023	0.92409	26.71	26.35	24.45	2.992	2.984	10.34	0.6
19295	21.05804	0.91493	25.75	25.07	23.52	3.358	3.341	4.47	0.5
15665	21.10379	0.90012	26.28	25.40	24.17	2.543	2.556	-8.46	0.6
18777	21.06295	0.84902	25.46	24.88	23.68	2.717	2.718	-11.72	0.7
21697	21.02781	0.84475	26.56	25.68	24.27	2.512	2.499	14.47	0.5
17103	21.08353	0.84569	26.65	25.88	24.07	2.744	2.737	31.04	0.5
21167	21.03429	0.83829	25.83	26.11	24.29	3.280	3.271	17.63	0.5
13607	21.13052	0.82388	25.28	25.49	24.46	3.110	3.102	13.27	0.5
19964	21.04866	0.80326	26.65	25.83	24.47	2.982	2.974	7.71	0.6
12644	21.14380	0.79227	24.60	24.35	23.48	2.710	2.701	11.34	0.5
13131	21.13730	0.78406	25.42	25.33	23.93	2.621	2.632	-21.25	0.5
17582	21.07658	0.78012	24.69	25.18	24.39	2.517	2.506	-1.04	0.6
17847	21.07380	0.76915	25.74	25.16	23.87	3.079	3.071	4.00	0.6
14922	21.11310	0.76711	26.65	27.00	24.40	3.199	3.191	5.33	0.5
20523	21.04174	0.75889	24.38	24.73	24.11	2.999	2.991	5.28	0.5

Table A.2 – continued from previous page

ID	R.A.	Dec.	U	B	I	$z_{Ly\alpha}$	z_{ISM}	$W_{Ly\alpha}$	q
12468	21.14558	0.75955	26.32	26.01	24.02	3.645	3.639	25.16	0.7
18834	21.06274	0.75330	23.73	24.04	23.22	2.650	2.642	2.59	0.6
12963	21.13907	0.75214	26.51	25.64	23.99	2.836	2.827	5.60	0.6
15247	21.10851	0.74873	25.74	24.71	24.47	2.552	2.545	70.29	0.7
13968	21.12631	0.74401	23.92	24.32	23.55	2.671	2.662	10.30	0.6
22675	21.01615	0.85058	26.65	25.46	24.21	3.034	3.026	7.21	0.7
29322	20.93385	0.84525	25.23	25.45	23.71	2.912	2.904	5.26	0.5
30796	20.91748	0.84118	24.10	24.58	23.73	2.399	2.400	-0.62	0.8
25090	20.98727	0.83701	26.64	25.87	23.88	3.190	3.180	4.59	0.8
22232	21.02084	0.83350	26.47	25.56	24.34	3.394	3.382	14.33	0.5
21635	21.02964	0.83090	24.11	24.55	23.71	3.042	3.044	18.53	0.5
31176	20.91038	0.82517	24.59	24.62	24.31	2.938	2.930	4.82	0.6
24812	20.99039	0.82652	26.64	26.52	24.32	2.700	2.695	7.69	0.6
30310	20.92280	0.82177	26.55	25.46	22.92	3.463	3.458	2.99	0.7
26115	20.97395	0.80714	25.12	25.01	24.35	2.412	2.371	-18.63	0.6
22372	21.01938	0.80797	24.56	24.97	24.00	2.364	2.362	-8.59	0.5
26571	20.96818	0.80270	24.87	24.52	24.16	2.846	2.836	22.14	0.9
22510	21.01822	0.79629	26.52	25.94	23.72	3.776	3.773	7.92	0.5
22068	21.02403	0.79196	26.01	25.54	23.66	3.104	3.095	14.35	0.6
21647	21.02873	0.77009	25.10	25.25	24.07	2.139	2.135	75.63	0.5
31792	20.90258	0.76059	26.63	25.62	24.27	2.796	2.788	-7.28	0.5
26346	20.97158	0.76037	26.63	26.38	24.27	3.282	3.272	4.37	0.5
22967	21.01251	0.76101	26.03	25.47	24.16	2.852	2.844	16.28	0.7
29713	20.92848	0.75757	24.88	25.03	24.36	2.592	2.583	5.17	0.8
29106	20.93654	0.75313	24.25	24.47	23.67	2.576	2.567	3.56	0.5
24086	20.99920	0.75405	26.45	25.78	24.46	3.155	3.143	8.14	0.5
31212	20.91054	0.74652	25.78	25.25	23.17	2.998	2.990	-3.01	0.5
21906	21.02548	0.74698	25.21	25.11	24.19	2.403	2.393	6.87	0.5
26574	20.96807	0.74415	25.91	25.50	24.19	2.751	2.742	3.82	0.6
25636	20.98149	0.99091	26.65	25.29	22.40	3.482	3.474	-1.98	0.6
28584	20.94373	0.98637	26.06	25.31	23.79	2.644	2.627	5.72	0.7
23962	21.00146	0.98756	26.37	26.05	24.30	2.854	2.837	12.67	0.6
22759	21.01658	0.98283	24.44	24.67	23.78	2.586	2.587	3.92	0.5
25231	20.98567	0.97413	25.80	25.56	24.35	3.101	3.099	19.92	0.5
22713	21.01652	0.96449	24.47	24.80	24.33	3.292	3.283	6.77	0.5
31439	20.90785	0.96065	26.65	26.07	24.23	2.958	2.953	4.93	0.8
24145	20.99984	0.95951	26.53	25.53	23.94	2.867	2.849	19.54	0.5

Table A.2 – continued from previous page

ID	R.A.	Dec.	U	B	I	$z_{Ly\alpha}$	z_{ISM}	$W_{Ly\alpha}$	q
21958	21.02536	0.95407	24.98	25.44	24.18	3.118	3.110	5.75	0.7
22857	21.01474	0.95118	26.64	25.58	24.34	2.504	2.513	-12.85	0.5
29206	20.93583	0.94732	26.65	26.06	23.39	2.976	2.968	5.29	0.5
26054	20.97505	0.94744	26.64	27.51	24.46	2.961	2.955	7.42	0.5
31693	20.90525	0.94111	26.65	27.51	23.94	3.498	3.490	20.31	0.5
28658	20.94325	0.93440	25.29	24.77	23.75	2.766	2.749	36.71	0.8
21914	21.02589	0.93620	26.36	25.22	24.09	2.994	2.983	44.58	0.7
31828	20.90416	0.93132	26.64	25.74	23.58	2.742	2.744	27.71	0.5
23829	21.00300	0.92894	26.37	25.83	23.93	3.026	3.019	17.01	0.6
27422	20.95879	0.92385	24.30	24.78	24.06	2.440	2.432	14.86	0.5
22457	21.01935	0.92262	24.65	24.82	23.69	2.947	2.949	-9.83	0.5
25009	20.98859	0.91302	25.44	24.97	24.10	2.537	2.527	25.96	0.6
25187	20.98656	0.90251	25.82	25.42	24.16	3.077	3.069	6.26	0.5
28099	20.94993	0.89944	24.96	25.43	23.73	3.181	3.173	17.84	0.5
30854	20.91556	0.89623	25.94	25.52	24.22	3.091	3.092	12.30	0.5
29003	20.93768	0.89095	26.64	26.21	24.22	2.866	2.858	12.49	0.5
22315	21.02130	0.89119	26.28	25.27	23.12	2.923	2.911	21.39	0.5
28571	20.94450	0.98017	25.70	25.08	23.20	3.164	3.152	3.44	0.7
37726	20.82707	0.99833	25.91	25.50	24.12	2.484	2.439	-21.24	0.5
41332	20.77919	0.99532	26.64	25.77	24.48	3.389	3.371	9.61	0.5
34866	20.86275	0.99536	25.98	24.86	23.73	2.978	2.970	7.17	0.8
39255	20.80680	0.99100	25.33	25.03	24.01	2.510	2.513	-17.48	0.6
43706	20.74838	0.98266	24.77	25.25	23.95	2.522	2.523	-6.96	0.6
43193	20.75438	0.98006	25.45	25.75	24.22	2.411	2.392	-2.51	0.5
39720	20.80135	0.97984	25.18	24.71	23.48	2.715	2.698	2.54	0.5
39727	20.80045	0.97030	26.64	25.80	24.27	3.215	3.201	9.92	0.5
36846	20.83800	0.96695	26.38	25.46	23.45	2.572	2.557	3.06	0.6
43526	20.74999	0.96186	25.08	24.83	24.10	2.750	2.733	8.87	0.6
37993	20.82341	0.95909	26.64	26.52	24.15	3.666	3.658	22.13	0.6
39053	20.80948	0.95636	25.74	25.43	24.06	2.655	2.648	0.35	0.6
43244	20.75503	0.95111	24.28	24.46	22.51	2.897	2.888	1.67	0.6
34818	20.86294	0.93905	25.56	25.26	24.36	2.288	2.291	-42.99	0.5
43659	20.74866	0.93233	26.64	26.20	24.03	2.760	2.751	1.42	0.5
38254	20.81983	0.92775	24.36	24.85	23.61	2.438	2.421	5.58	0.5
41931	20.77193	0.92500	26.64	25.96	23.03	3.312	3.306	-4.64	0.5
37899	20.82485	0.92304	26.09	25.14	23.75	2.395	2.388	6.31	0.7
40222	20.79465	0.91327	24.56	24.87	23.93	2.241	2.233	8.99	0.5

Table A.2 – continued from previous page

ID	R.A.	Dec.	U	B	I	$z_{Ly\alpha}$	z_{ISM}	$W_{Ly\alpha}$	q
38701	20.81369	0.90598	26.46	25.78	24.13	2.873	2.862	4.81	0.6
34806	20.86364	0.89489	24.99	25.41	24.24	2.317	2.314	15.30	0.5
42671	20.76142	0.96604	24.18	24.64	24.03	2.488	2.479	5.50	0.5
36181	20.84554	0.85024	26.38	25.27	23.95	3.077	3.076	12.37	0.6
43318	20.75274	0.84578	24.15	24.53	23.64	2.655	2.647	2.89	0.5
43699	20.74752	0.84132	26.61	25.51	24.00	2.755	2.757	12.69	0.5
38196	20.81980	0.84045	24.48	24.89	24.46	2.244	2.238	41.39	0.6
42775	20.76039	0.82728	24.66	24.86	23.64	2.615	2.607	191.44	0.5
39187	20.80754	0.82766	26.64	25.43	24.00	3.186	3.178	4.09	0.5
40970	20.78369	0.82178	26.07	26.38	24.48	3.022	3.014	11.06	0.5
37565	20.82788	0.81179	26.64	26.93	24.38	3.392	3.364	6.27	0.6
36805	20.83662	0.80857	25.54	25.83	24.36	2.645	2.630	-18.57	0.5
36935	20.83562	0.79894	26.64	25.86	23.47	2.697	2.689	-6.19	0.6
43456	20.75089	0.79329	26.17	25.73	23.89	3.538	3.529	5.93	0.7
40501	20.79014	0.78741	25.90	25.37	23.43	2.741	2.737	4.37	0.5
34988	20.85962	0.77577	26.64	26.54	24.45	3.242	3.234	13.89	0.5
41014	20.78295	0.76130	24.51	24.94	24.39	2.252	2.250	-3.49	0.5
36724	20.83791	0.76143	26.64	26.01	24.16	3.423	3.412	91.11	0.7
42254	20.76686	0.75508	26.64	25.41	23.51	3.155	3.148	-5.85	0.5
40033	20.79558	0.74860	25.50	25.62	24.08	2.744	2.776	-11.24	0.5
40314	20.79294	0.74445	24.62	24.95	23.65	2.278	2.277	6.06	0.5
41507	20.77675	0.80097	25.53	25.08	24.26	2.707	2.699	13.99	0.5
41172	20.78176	0.83990	26.63	25.80	23.93	2.993	2.985	2.33	0.5
38776	20.81335	0.79003	24.54	24.94	23.66	2.651	2.641	7.14	0.5
26225	20.97172	0.59922	25.19	25.15	23.79	2.382	2.378	10.78	0.5
30562	20.91774	0.59636	25.81	25.29	23.66	3.451	3.442	61.51	0.8
26611	20.96665	0.59579	25.69	25.14	24.28	2.918	2.913	0.61	0.6
23107	21.01087	0.59578	25.48	24.99	23.11	2.682	2.674	5.41	0.5
29940	20.92477	0.59066	26.63	25.88	24.33	3.380	3.365	11.71	0.6
23092	21.01059	0.58684	25.02	25.48	24.05	2.983	2.975	8.82	0.6
23386	21.00656	0.58216	24.30	24.59	23.94	2.841	2.833	7.38	0.6
29409	20.93208	0.57739	26.63	26.60	23.91	2.386	2.377	8.74	0.5
23625	21.00336	0.55566	24.74	24.87	24.34	2.510	0.000	0.00	0.5
32020	20.89896	0.54877	25.92	25.15	24.38	2.746	2.737	240.72	0.8
27641	20.95325	0.55027	26.44	25.91	24.38	2.864	2.851	9.23	0.6
29607	20.92919	0.52889	25.53	24.79	23.80	2.991	2.983	182.21	0.5
32102	20.89845	0.52571	25.55	25.72	24.15	3.360	3.345	36.32	0.8

Table A.2 – continued from previous page

ID	R.A.	Dec.	U	B	I	$z_{Ly\alpha}$	z_{ISM}	$W_{Ly\alpha}$	q
26111	20.97285	0.51800	26.00	25.90	24.50	2.634	2.631	5.01	0.5
29263	20.93328	0.51209	26.64	27.50	23.12	2.776	2.774	19.37	0.5
22586	21.01677	0.49643	26.65	25.52	23.00	2.712	2.697	-19.70	0.6
28636	20.94094	0.49311	25.76	25.66	24.25	3.130	3.121	3.53	0.7
24759	20.99072	0.74193	26.06	25.58	24.35	2.876	2.866	12.27	0.8
31923	20.90111	0.72476	26.62	25.64	24.13	2.437	2.429	6.29	0.5
21601	21.02867	0.72428	26.64	25.79	24.07	2.999	2.983	9.39	0.8
23228	21.00901	0.72039	24.98	24.74	23.90	2.379	2.371	-26.67	0.8
23228	21.00901	0.72039	24.98	24.74	23.90	2.387	2.379	19.45	0.8
30556	20.91834	0.71318	24.42	24.78	24.04	2.431	2.420	-1.25	0.6
25718	20.97813	0.70622	25.55	25.18	24.23	3.428	3.421	6.68	0.7
31289	20.90855	0.70418	24.15	24.64	23.91	3.099	3.091	-2.17	0.5
26535	20.96864	0.69965	26.63	27.49	23.15	3.015	3.007	5.32	0.5
27297	20.95857	0.69256	26.50	26.08	24.17	3.060	3.047	33.33	0.7
31715	20.90347	0.68942	25.59	25.48	24.29	2.566	2.558	-5.10	0.5
27730	20.95299	0.68085	24.94	24.96	24.43	2.537	2.521	15.73	0.5
24274	20.99709	0.67871	25.35	25.13	23.87	3.099	3.085	19.89	0.7
23752	21.00406	0.66893	25.84	25.50	24.15	3.148	3.152	8.93	0.6
28861	20.93916	0.66534	25.01	25.01	24.05	3.110	3.102	100.86	0.8
29181	20.93526	0.65458	24.04	24.52	23.61	2.342	2.334	4.23	0.5
30999	20.91247	0.65172	26.30	25.53	23.61	3.392	3.386	9.04	0.7
30462	20.91898	0.63963	26.61	25.54	24.41	3.105	3.098	30.91	0.7
29160	20.93536	0.63419	25.51	25.16	23.66	2.849	2.843	6.78	0.6
36682	20.83899	0.74120	26.64	24.47	22.27	3.354	3.343	19.37	0.9
40679	20.78726	0.73087	26.64	25.47	24.05	2.971	2.960	-10.40	0.5
36545	20.84059	0.72277	26.32	24.89	23.35	3.433	3.427	19.95	0.9
38736	20.81306	0.71425	25.16	25.25	23.41	3.385	3.377	13.74	0.7
36685	20.83952	0.69843	26.64	25.63	22.19	3.083	3.075	5.96	0.5
35389	20.85508	0.69482	24.19	24.64	23.98	2.801	2.793	-20.51	0.5
42359	20.76415	0.68197	25.21	24.98	24.00	2.329	2.321	29.74	0.5
36197	20.84420	0.68200	25.88	26.03	24.26	2.786	2.787	23.68	0.6
38831	20.81093	0.66476	25.96	25.63	24.38	2.625	2.615	-6.43	0.5
42125	20.76863	0.66096	23.70	24.15	23.33	2.358	2.357	35.32	0.7
40069	20.79631	0.65315	26.47	25.55	22.87	2.594	2.586	-4.75	0.6
41550	20.77486	0.64157	25.90	25.44	24.28	2.691	2.670	14.61	0.6
37687	20.82631	0.64077	26.64	26.87	23.99	3.164	3.151	68.91	0.6
39951	20.79637	0.63819	26.34	25.58	24.45	2.731	2.723	111.14	0.8

Table A.2 – continued from previous page

ID	R.A.	Dec.	U	B	I	$z_{Ly\alpha}$	z_{ISM}	$W_{Ly\alpha}$	q
35591	20.85136	0.58146	26.63	25.30	24.12	2.423	2.395	16.50	0.5
36620	20.83781	0.55570	25.50	25.80	24.45	3.045	3.047	18.01	0.5
43493	20.75200	0.53115	24.89	24.48	22.90	2.712	2.701	14.21	0.9
43735	20.74588	0.52378	26.61	26.25	23.59	3.025	3.017	28.16	0.5
42028	20.76872	0.51620	24.38	24.79	23.57	2.488	2.465	7.30	0.7
36019	20.84651	0.51619	25.57	25.98	24.16	2.329	2.321	5.05	0.5
40405	20.79033	0.51338	26.43	25.09	23.70	2.711	2.704	7.35	0.9
36038	20.84539	0.49844	25.16	25.50	24.25	2.716	2.707	12.15	0.6
7419	21.20672	0.59067	26.65	25.75	23.79	3.731	3.724	9.15	0.5
7453	21.20593	0.57566	26.65	25.58	23.98	2.698	2.690	2.75	0.6
262	21.29342	0.57355	24.70	25.02	23.93	2.873	2.868	8.90	0.6
1931	21.27170	0.56938	26.65	26.37	23.89	2.725	2.709	14.57	0.5
3930	21.24804	0.56659	25.16	25.35	23.49	3.544	3.537	16.13	0.7
7938	21.20030	0.56300	26.21	25.52	23.52	2.749	2.771	-34.50	0.5
211	21.29395	0.56339	26.65	26.55	24.25	3.173	3.164	-12.37	0.7
4140	21.24528	0.55208	24.73	25.20	24.41	2.447	2.439	4.87	0.6
213	21.29389	0.54801	24.73	25.22	23.93	3.040	3.032	7.84	0.5
2016	21.27120	0.54343	25.00	25.39	24.13	2.584	2.576	12.23	0.5
2389	21.26594	0.54076	24.24	24.68	24.23	3.354	3.353	7.62	0.8
7774	21.20195	0.53395	26.65	25.28	23.91	2.740	2.727	4.08	0.5
3997	21.24738	0.53352	26.51	26.07	23.93	3.256	3.247	23.34	0.8
123	21.29542	0.52066	26.65	26.40	22.98	2.689	2.680	2.17	0.6
6944	21.21173	0.51290	25.98	25.44	23.59	3.238	3.230	8.01	0.5
6269	21.21936	0.49396	26.64	26.08	23.69	2.303	2.295	-13.27	0.8
7425	21.20606	0.49098	26.64	25.53	24.20	3.431	3.420	47.08	0.8
540	21.29050	0.57824	26.65	25.46	23.70	2.825	2.817	-7.96	0.5
3311	21.25608	0.59500	25.19	25.38	23.75	3.166	3.160	25.32	0.8
901	21.28569	0.73495	25.60	25.21	23.83	2.746	2.736	7.38	0.9
1357	21.27947	0.71275	26.63	26.52	24.39	3.349	3.352	60.52	0.6
6956	21.21213	0.70677	25.69	25.30	24.18	3.149	3.141	2.05	0.5
5853	21.22432	0.70013	26.65	26.21	24.42	2.990	2.982	9.18	0.5
7665	21.20371	0.69778	26.65	26.53	24.13	2.815	2.807	6.41	0.7
361	21.29249	0.68875	26.64	26.08	23.98	2.966	2.964	-4.20	0.6
6744	21.21545	0.67584	24.34	24.68	23.31	2.534	2.522	22.62	0.7
3186	21.25689	0.67321	25.48	25.01	24.32	2.293	2.293	-65.64	0.5
6618	21.21596	0.67027	25.42	25.21	24.08	2.713	2.726	-14.49	0.7
8270	21.19628	0.64206	25.21	25.17	24.36	2.931	2.923	15.28	0.6

Table A.2 – continued from previous page

ID	R.A.	Dec.	U	B	I	$z_{Ly\alpha}$	z_{ISM}	$W_{Ly\alpha}$	q
1154	21.28329	0.63491	25.98	25.50	23.45	2.759	2.781	-12.79	0.9
11711	21.15437	0.74707	26.66	27.52	24.45	2.373	2.376	2.05	0.5
14128	21.12384	0.72919	26.66	25.51	24.18	3.003	2.995	18.16	0.5
21601	21.02867	0.72428	26.64	25.79	24.07	2.883	2.865	5.01	0.9
16392	21.09226	0.71426	26.65	26.73	24.38	3.080	3.072	9.05	0.5
13806	21.12747	0.71038	25.53	25.32	24.48	2.413	2.424	-44.41	0.5
17767	21.07467	0.70647	26.22	25.29	24.03	2.861	2.889	-15.86	0.6
20177	21.04548	0.70054	25.45	25.93	24.15	3.396	3.388	8.63	0.6
15074	21.11045	0.70085	26.66	26.84	24.31	2.306	2.264	-97.27	0.5
11623	21.15554	0.69648	25.28	25.21	24.23	2.947	2.932	9.69	0.9
11783	21.15352	0.68849	26.77	25.56	24.08	2.811	2.803	-4.82	0.5
20703	21.03937	0.68043	26.46	25.37	23.83	3.206	3.198	5.11	0.8
19361	21.05466	0.67635	26.65	26.46	24.46	2.860	2.852	7.26	0.9
21065	21.03473	0.67277	26.64	26.24	24.20	2.558	2.548	17.60	0.6
21387	21.03103	0.67017	24.89	25.08	24.37	3.200	3.192	4.59	0.5
16335	21.09345	0.66029	26.65	25.29	23.71	2.905	2.932	-22.79	0.9
15252	21.10880	0.65753	25.96	25.48	23.59	2.625	2.617	8.42	0.5
20963	21.03667	0.65145	24.31	24.65	23.60	3.219	3.211	6.52	0.5
20295	21.04576	0.58894	25.40	24.53	22.86	3.097	3.088	16.93	0.5
15919	21.09886	0.58764	26.65	25.71	24.33	2.504	2.497	10.36	0.6
18994	21.05886	0.58503	25.35	25.10	24.20	2.662	2.665	-29.27	0.6
12340	21.14627	0.57138	25.78	25.28	24.16	2.854	2.847	48.33	0.5
17574	21.07662	0.56505	26.07	25.61	23.63	2.561	2.557	6.27	0.5
18038	21.06995	0.54290	25.63	25.32	24.35	3.012	3.003	3.78	0.5
12967	21.13823	0.53738	26.65	26.47	23.85	2.821	2.810	-4.37	0.6
12312	21.14571	0.51678	25.43	25.06	24.22	3.536	3.531	82.36	0.7
12326	21.14647	0.50980	23.58	23.99	23.55	2.270	2.262	4.92	0.9
15850	21.10009	0.49790	25.12	24.61	22.55	2.555	2.548	1.13	0.6
18051	21.07012	0.58174	24.99	25.28	24.06	2.933	2.925	10.65	0.5

Table A.3: Spectroscopically confirmed LBGs in the HE0940-1050 field.

ID	R.A.	Dec.	U	B	R	$z_{Ly\alpha}$	z_{ISM}	$W_{Ly\alpha}$	q
37087	145.65581	-11.15570	26.64	26.08	25.30	2.863	2.853	11.86	0.5
43741	145.57063	-11.16283	27.45	25.71	24.38	3.452	3.463	-8.47	0.7

Table A.3 – continued from previous page

ID	R.A.	Dec.	U	B	R	$z_{Ly\alpha}$	z_{ISM}	$W_{Ly\alpha}$	q
40674	145.61063	-11.16710	28.04	26.25	25.17	3.307	3.323	-8.71	0.6
44057	145.57085	-11.17309	27.01	26.06	25.08	3.030	3.041	-9.20	0.8
34849	145.68188	-11.17258	26.65	26.48	25.56	2.516	2.517	26.64	0.5
42432	145.59003	-11.18381	27.12	25.80	24.78	3.303	3.287	2.59	0.7
36552	145.66158	-11.19321	26.67	26.28	25.59	2.348	2.332	6.39	0.7
43278	145.57986	-11.21142	27.33	26.04	24.22	3.063	3.082	-29.42	0.9
34622	145.68459	-11.21394	25.82	25.16	24.07	2.882	2.886	-31.74	0.9
43226	145.58051	-11.21664	99.00	26.46	24.02	2.935	2.937	3.96	0.5
40313	145.61563	-11.23008	28.90	25.97	24.52	3.712	3.710	5.36	0.5
36284	145.66452	-11.23265	99.00	26.15	24.80	3.138	3.126	17.25	0.7
40072	145.61893	-11.23872	27.07	26.69	25.67	3.147	3.135	10.74	0.5
38821	145.63547	-11.24468	26.33	26.09	25.14	3.447	3.437	8.66	0.5
34901	145.68225	-11.26240	25.56	25.05	23.96	3.050	3.039	42.83	0.9
43662	145.57509	-11.21497	99.00	25.35	24.03	3.097	3.075	7.18	0.8
45279	145.55588	-11.20670	27.30	26.26	25.12	2.871	2.853	9.86	0.5
42132	145.59352	-11.17849	99.00	26.37	24.90	2.923	2.918	4.46	0.6
45718	145.55208	-11.18844	27.42	26.25	24.66	3.251	3.225	11.03	0.5
39522	145.62573	-11.22283	26.65	25.77	25.22	2.873	2.858	34.70	0.7
43417	145.57811	-11.22310	26.33	25.56	24.29	3.365	3.357	15.42	0.5
38173	145.64259	-11.16871	26.92	26.00	24.81	2.593	2.585	5.29	0.5
42026	145.59702	-11.16900	25.77	25.77	25.43	3.127	3.119	73.54	0.5
39442	145.62648	-11.15719	26.13	25.66	24.64	2.250	2.385	-92.28	0.6
42024	145.59367	-11.03725	26.35	26.02	25.01	3.343	3.353	14.20	0.5
35046	145.67842	-11.04684	24.74	24.56	23.74	2.230	2.240	-40.52	0.6
42074	145.59628	-11.06374	26.66	25.94	24.91	2.849	2.851	-9.82	0.5
36457	145.66216	-11.06332	25.65	24.86	23.76	2.580	2.582	3.73	0.6
35989	145.66769	-11.07044	26.93	26.18	24.80	2.427	2.417	7.59	0.6
39149	145.62982	-11.07409	25.58	24.78	23.82	2.926	2.917	20.20	0.9
38677	145.63658	-11.08511	27.43	26.89	25.86	2.912	2.907	124.41	0.6
39360	145.62718	-11.09662	26.48	25.62	24.81	2.420	2.408	4.45	0.5
41179	145.60474	-11.10846	24.99	24.93	24.09	3.328	3.329	4.38	0.5
41854	145.59662	-11.09485	25.45	24.93	24.24	2.819	2.363	5.55	0.6
39378	145.62686	-11.07945	25.87	25.66	25.28	2.153	2.146	3.51	0.5
39852	145.62093	-11.06633	23.86	24.17	23.41	2.432	2.431	-2.31	0.5
55811	145.42761	-11.00984	27.25	26.45	25.19	3.420	3.398	29.86	0.5
56780	145.41579	-11.02669	99.00	25.05	24.05	3.274	3.259	76.52	0.6
54602	145.44267	-11.03331	25.71	25.57	25.20	2.731	2.725	52.57	0.6

Table A.3 – continued from previous page

ID	R.A.	Dec.	U	B	R	$z_{Ly\alpha}$	z_{ISM}	$W_{Ly\alpha}$	q
49801	145.50139	-11.03228	26.42	25.99	25.18	2.691	2.677	6.74	0.5
52934	145.46275	-11.05044	26.09	25.30	24.90	2.831	2.829	30.82	0.7
53212	145.45927	-11.06307	24.85	24.69	24.07	2.302	2.292	8.18	0.5
58772	145.39320	-11.06807	25.46	25.37	24.89	2.359	2.362	123.66	0.7
57562	145.40773	-11.08358	99.00	25.33	23.36	3.254	3.243	3.59	0.5
58921	145.39156	-11.08795	25.00	25.00	24.40	2.539	2.534	20.03	0.5
50067	145.49809	-11.10139	26.49	25.90	25.31	2.608	2.586	2.97	0.6
59202	145.38828	-11.10403	26.71	26.54	25.63	2.726	2.707	84.07	0.6
58832	145.39920	-11.11250	26.83	25.67	24.41	3.298	3.278	23.39	0.8
52133	145.47253	-11.05234	26.87	25.90	24.33	2.912	2.909	-20.62	0.6
59318	145.38644	-11.09797	27.69	25.85	24.06	2.186	2.188	2.54	0.5
52539	145.46779	-11.10292	27.04	26.22	25.22	2.929	2.922	21.92	0.5
50178	145.49649	-11.08688	25.70	25.66	25.33	2.430	2.422	9.85	0.5
53411	145.45703	-11.15577	28.53	26.57	24.93	3.664	3.653	39.25	0.5
53910	145.45146	-11.15809	26.70	26.50	25.63	2.150	0.000	0.00	0.9
55612	145.43051	-11.16506	26.87	25.98	25.38	2.737	2.726	8.38	0.6
56219	145.42290	-11.18354	27.14	26.43	25.41	2.984	2.978	33.90	0.5
49797	145.50191	-11.19665	27.00	25.46	24.51	3.055	3.046	35.43	0.7
49707	145.50293	-11.19987	26.59	25.13	23.76	3.066	3.056	7.08	0.8
59631	145.38327	-11.20946	27.66	26.81	25.97	3.113	3.105	9.97	0.6
50986	145.48711	-11.20936	99.00	25.89	24.90	3.069	3.073	17.47	0.6
49935	145.50031	-11.21263	26.32	25.70	25.07	2.697	2.702	-15.49	0.7
55802	145.42839	-11.21521	25.81	25.71	24.85	3.060	2.560	11.97	0.5
55207	145.43591	-11.22004	26.28	26.06	25.40	2.584	2.576	3.70	0.5
53497	145.45631	-11.22981	27.07	25.67	24.78	2.986	2.983	9.94	0.7
50416	145.49376	-11.24001	27.27	26.28	24.72	2.972	2.953	12.76	0.5
55874	145.42725	-11.24345	25.36	24.69	23.51	3.124	3.108	3.18	0.7
48820	145.51321	-11.24635	25.92	25.65	24.79	2.856	2.848	22.95	0.6
58775	145.39374	-11.25290	25.98	25.34	25.09	3.081	3.073	8.01	0.5
56131	145.44160	-11.25095	26.73	25.94	24.90	2.948	2.938	11.54	0.6
57231	145.41150	-11.25819	29.26	24.97	23.91	3.120	3.148	-9.63	0.8
54054	145.44948	-11.15333	28.20	26.39	24.85	3.297	3.289	27.11	0.5
53584	145.45523	-11.25503	25.47	24.74	23.45	2.691	2.702	1.87	0.7
12749	145.88219	-11.16760	99.00	25.24	23.66	3.334	3.320	12.13	0.8
7203	145.93285	-11.17010	26.66	26.30	25.50	2.632	2.619	14.56	0.5
14336	145.86855	-11.18438	27.11	26.29	25.16	2.805	2.793	38.61	0.7
6794	145.93655	-11.18700	28.48	26.46	25.33	3.339	3.332	9.55	0.6

Table A.3 – continued from previous page

ID	R.A.	Dec.	U	B	R	$z_{Ly\alpha}$	z_{ISM}	$W_{Ly\alpha}$	q
9421	145.91171	-11.19270	99.00	26.05	24.73	2.677	2.668	84.35	0.6
3742	145.96521	-11.19773	25.45	24.80	23.54	2.952	2.985	-16.32	1.0
13574	145.87511	-11.20808	28.51	26.67	25.08	3.219	3.209	24.29	0.7
5918	145.94485	-11.20819	27.49	26.10	24.21	3.224	3.217	5.13	0.5
7672	145.92821	-11.21484	27.40	26.41	25.27	3.560	3.554	23.95	0.5
2133	145.98164	-11.21499	99.00	25.92	23.70	3.236	3.228	-7.51	0.7
2327	145.97937	-11.22647	26.00	25.75	24.90	2.630	2.622	9.40	0.5
8452	145.92084	-11.23759	26.04	25.22	24.14	2.878	2.877	52.75	0.6
8452	145.92084	-11.23759	26.04	25.22	24.14	2.877	2.905	-11.00	0.8
13688	145.88802	-11.25063	26.85	25.42	24.16	3.319	3.308	10.88	0.9
11663	145.89249	-11.25618	26.38	25.00	23.40	3.327	3.312	30.48	0.8
6441	145.94028	-11.26153	25.04	24.89	24.00	2.899	2.895	55.29	0.9
9035	145.91431	-11.01818	26.42	25.78	24.60	2.897	2.894	-5.98	0.7
10992	145.89771	-11.03633	99.00	26.34	25.38	3.249	3.240	13.17	0.6
11934	145.89102	-11.04179	26.81	25.56	24.27	2.801	2.841	-30.08	0.8
3031	145.97180	-11.04227	28.12	26.72	25.67	3.022	3.015	161.82	0.8
1973	145.98239	-11.04630	99.00	26.35	24.95	3.430	3.421	23.59	0.9
7560	145.92871	-11.05352	26.36	26.12	25.69	2.559	2.559	8.56	0.5
6290	145.94054	-11.05719	26.08	25.24	24.04	2.622	2.633	-14.35	0.7
4901	145.95363	-11.06703	26.14	25.92	25.04	2.796	2.784	30.68	0.9
8174	145.92268	-11.07316	25.36	25.30	24.61	2.336	2.321	5.77	0.7
2493	145.97728	-11.07493	27.41	25.95	24.73	2.930	2.947	-25.99	0.7
5868	145.94469	-11.07729	26.35	25.71	25.04	2.319	2.308	4.70	0.6
9774	145.90822	-11.08365	25.87	25.82	25.20	2.785	2.768	52.43	0.6
6358	145.93980	-11.09744	26.63	25.44	24.00	3.998	3.990	26.30	0.7
5017	145.95253	-11.10834	26.06	25.63	24.55	2.505	2.520	-6.75	0.7
1496	145.98763	-11.11422	25.88	24.88	24.01	3.004	2.993	19.30	0.9
5652	145.94691	-11.11631	25.64	25.57	24.74	2.761	2.752	3.03	0.7
14506	145.86639	-11.12030	26.47	25.90	24.95	2.775	2.771	23.99	0.9
5446	145.94873	-11.11892	26.51	26.12	25.33	2.316	2.302	5.07	0.5
4652	145.95564	-11.07916	26.12	25.53	24.81	2.777	2.770	24.30	0.9
10189	145.90472	-11.08007	25.51	25.43	24.61	2.226	2.215	4.31	0.5
15326	145.85899	-11.07553	27.04	26.43	25.75	3.183	3.170	58.08	0.7
9526	145.90973	-11.03993	24.94	23.82	22.46	3.293	3.290	-0.87	0.8
7570	145.92862	-11.04817	99.00	25.47	24.28	2.889	2.880	10.40	0.9
27170	145.75191	-11.02388	26.36	26.21	25.47	2.550	2.553	-20.54	0.6
22583	145.79105	-11.02465	99.00	26.02	24.68	3.513	3.501	5.12	0.5

Table A.3 – continued from previous page

ID	R.A.	Dec.	U	B	R	$z_{Ly\alpha}$	z_{ISM}	$W_{Ly\alpha}$	q
30185	145.72452	-11.03230	99.00	25.98	24.69	3.168	3.162	56.46	0.7
23915	145.78052	-11.02838	27.94	26.40	24.69	3.336	3.326	23.35	0.8
19535	145.81923	-11.03021	26.68	25.92	24.79	2.920	2.917	12.15	0.5
22087	145.79674	-11.03493	25.47	25.18	24.34	2.511	2.512	4.49	0.6
22687	145.79146	-11.04204	27.13	26.43	25.48	2.533	2.529	20.76	0.8
27997	145.74513	-11.04543	26.59	26.46	25.61	3.130	3.126	9.02	0.5
20926	145.80675	-11.05381	25.00	24.85	24.14	2.780	2.760	9.53	0.5
29824	145.72932	-11.05976	28.40	26.58	25.51	2.645	2.658	11.30	0.5
19686	145.81796	-11.05771	25.59	25.04	24.95	2.524	2.517	62.10	0.9
31121	145.71788	-11.06420	27.26	26.45	25.31	2.829	2.806	11.14	0.8
31030	145.71849	-11.06833	24.57	24.55	23.98	2.441	2.432	25.19	0.8
24596	145.77472	-11.06823	26.65	26.19	25.57	2.764	2.762	14.00	0.7
26118	145.76122	-11.07160	27.33	26.12	25.01	3.524	3.510	3.81	0.6
22889	145.78961	-11.07591	27.47	26.59	25.20	2.912	2.903	92.90	0.7
29608	145.73438	-11.07883	99.00	25.89	23.83	2.992	2.985	2.95	0.5
33127	145.69972	-11.08640	26.83	25.90	24.58	3.412	3.409	4.61	0.6
19730	145.81784	-11.08830	26.69	26.01	25.24	2.597	2.586	8.11	0.5
33158	145.69940	-11.09224	25.76	25.73	24.97	2.541	2.531	4.76	0.6
19458	145.82004	-11.09075	26.50	25.56	24.27	2.920	2.912	18.00	0.8
31500	145.71458	-11.09658	26.58	26.12	25.29	2.824	2.816	59.96	0.7
22156	145.79639	-11.09715	25.64	25.54	24.69	2.833	2.824	8.59	0.6
32389	145.70630	-11.10037	27.02	26.21	24.89	3.296	3.294	17.28	0.7
22967	145.78911	-11.10388	25.46	25.45	24.79	3.026	3.020	5.48	0.5
21262	145.80429	-11.11929	26.89	26.10	25.06	2.765	2.786	-21.91	0.6
34015	145.69165	-11.12484	26.31	25.30	24.21	2.934	2.953	-8.58	0.6
34365	145.68721	-11.05671	26.95	25.41	24.18	3.259	3.247	13.61	0.7
23492	145.78459	-11.16207	26.79	26.05	25.41	2.402	2.398	27.65	0.7
20240	145.81387	-11.16677	26.18	26.00	25.30	2.760	2.730	11.68	0.5
20970	145.80627	-11.17339	25.63	25.33	24.41	2.664	2.663	11.16	0.6
28657	145.74001	-11.17570	25.95	25.59	24.53	2.878	2.873	5.06	0.5
33532	145.69647	-11.18037	25.88	25.57	24.75	3.061	3.048	8.39	0.5
29787	145.73007	-11.18440	26.18	25.83	25.18	2.764	2.757	5.08	0.5
26363	145.75945	-11.19986	28.27	25.81	24.50	3.102	3.127	-7.78	0.8
29199	145.73515	-11.20442	27.13	25.35	24.01	3.005	3.022	-7.73	0.8
34424	145.68703	-11.22213	25.29	24.89	23.98	2.879	2.884	-39.63	0.9
22812	145.79083	-11.24072	99.00	26.01	24.93	2.840	2.805	-0.37	0.7
27525	145.74988	-11.24934	26.04	25.53	24.92	2.427	2.417	3.72	0.5

Table A.3 – continued from previous page

ID	R.A.	Dec.	U	B	R	$z_{Ly\alpha}$	z_{ISM}	$W_{Ly\alpha}$	q
20196	145.81441	-11.24969	99.00	25.59	23.77	3.278	3.296	-17.63	0.9
20540	145.81151	-11.25813	28.32	26.64	24.80	3.181	3.156	6.40	0.5
26988	145.75417	-11.26113	26.52	25.96	24.77	2.352	2.341	3.62	0.5
28486	145.74300	-11.26538	26.35	25.53	24.43	2.898	2.908	-10.00	0.9
27040	145.75377	-11.23924	25.14	24.67	23.73	3.001	2.989	22.63	0.9
22339	145.79510	-11.16460	99.00	25.18	23.53	2.721	2.719	3.52	0.5
11432	145.89340	-10.95265	26.24	25.58	25.37	3.405	3.402	12.00	0.5
10769	145.89920	-10.95696	25.98	25.71	25.08	2.754	2.746	207.58	0.7
15074	145.86082	-10.96324	23.99	23.84	23.10	2.247	2.242	6.19	0.5
10699	145.89990	-10.98449	28.44	26.03	24.60	3.155	3.148	16.99	0.8
6215	145.94106	-10.99385	28.69	27.42	25.91	3.391	3.384	6.45	0.6
5218	145.95010	-11.00072	27.40	26.02	24.79	3.008	2.997	105.96	0.7
6575	145.93756	-11.01023	25.06	24.74	24.13	2.862	2.855	38.15	0.8
9648	145.90796	-10.79547	26.69	26.13	25.65	2.960	2.956	7.28	0.7
13095	145.87775	-10.81413	24.39	24.35	23.44	2.296	2.270	0.00	0.5
13580	145.87366	-10.83527	26.25	25.90	24.76	0.000	0.000	0.00	0.6
8130	145.92223	-10.85222	26.72	26.03	25.33	2.835	2.838	14.82	0.5
11518	145.89191	-10.87342	26.52	25.24	23.42	3.549	3.541	8.17	0.6
8745	145.91644	-10.88614	25.78	25.21	23.66	2.916	2.908	2.90	0.5
22695	145.79044	-10.80167	26.44	26.16	25.05	2.776	2.773	42.34	0.5
30255	145.72424	-10.80941	26.00	25.33	24.28	2.859	2.852	32.09	0.6
20589	145.80922	-10.81147	25.85	25.69	24.32	3.379	3.379	22.97	0.6
27555	145.74802	-10.84418	26.03	24.96	24.61	3.081	3.074	28.54	0.5
33295	145.69722	-10.87789	24.64	24.55	24.02	2.272	2.269	-5.82	0.6
19465	145.81821	-10.87735	25.95	25.26	23.75	2.989	2.981	3.27	0.5
28733	145.73814	-10.88099	29.67	26.00	24.60	3.291	3.282	6.69	0.6
24376	145.77608	-10.88337	26.43	26.06	24.52	2.770	2.772	12.78	0.5
27519	145.74870	-10.92936	27.62	26.20	24.83	3.148	3.140	74.94	0.7
20297	145.81200	-10.92992	25.16	24.48	23.15	3.055	3.072	-9.11	0.9
27328	145.75012	-10.93331	25.36	25.12	24.02	2.688	2.678	1.28	0.8
20441	145.81085	-10.93631	28.33	26.35	24.99	3.178	3.168	82.90	0.7
27649	145.74738	-10.95093	27.21	25.54	23.86	3.509	3.501	18.10	0.5
31199	145.71666	-10.95356	26.52	26.31	25.67	2.601	2.593	55.63	0.6
22302	145.79408	-10.98409	26.99	25.20	23.53	2.780	2.772	4.16	0.5
33016	145.70023	-10.98642	99.00	25.18	24.06	3.224	3.216	56.42	0.9
27900	145.74568	-10.99052	26.20	26.15	24.89	2.818	2.805	-9.74	0.6
20777	145.80807	-10.98992	26.07	25.48	24.13	3.213	3.205	19.17	0.8

Table A.3 – continued from previous page

ID	R.A.	Dec.	U	B	R	$z_{Ly\alpha}$	z_{ISM}	$W_{Ly\alpha}$	q
25698	145.76447	-10.99345	25.84	25.02	23.70	2.910	2.920	-5.39	0.7
23915	145.78052	-11.02838	27.94	26.40	24.69	3.339	3.331	20.12	0.6
30185	145.72452	-11.03230	99.00	25.98	24.69	3.172	3.164	54.48	0.6

Table A.4: Spectroscopically confirmed LBGs in the J1201+0116 field.

ID	R.A.	Dec.	U	B	R	$z_{Ly\alpha}$	z_{ISM}	$W_{Ly\alpha}$	q
8387	180.68546	1.12263	99.00	26.09	24.96	2.455	2.448	4.11	0.5
13620	180.59245	1.11498	99.00	23.55	25.23	2.978	2.975	49.58	0.5
7214	180.70628	1.11474	99.00	26.00	24.12	2.623	2.615	35.25	0.6
9958	180.65779	1.10987	99.00	25.41	23.97	3.104	3.107	6.81	0.6
10533	180.64752	1.10010	99.00	25.83	24.43	3.010	3.005	7.49	0.5
11531	180.62871	1.09228	99.00	25.51	24.99	3.360	3.353	7.63	0.5
9092	180.67448	1.09362	99.00	23.92	24.22	2.669	2.665	-4.99	0.9
9557	180.66466	1.08926	99.00	26.47	24.38	2.456	2.450	5.15	0.6
8892	180.67726	1.08439	26.08	25.34	24.37	2.657	2.663	8.25	0.5
13737	180.58937	1.08074	99.00	25.05	23.72	2.470	2.468	5.29	0.7
9189	180.67113	1.07760	99.00	26.12	24.26	3.122	3.114	6.66	0.5
13865	180.58670	1.07022	99.00	26.43	24.80	2.459	2.454	10.94	0.5
13981	180.58554	1.06695	24.09	23.93	23.81	2.203	2.198	-50.43	0.8
11156	180.63707	1.06767	24.23	23.92	22.77	2.658	2.621	6.43	0.6
9107	180.67267	1.05844	99.00	26.12	24.35	2.585	2.583	20.80	0.8
11841	180.62317	1.05489	99.00	26.32	24.87	2.399	2.390	5.23	0.6
8482	180.68524	1.04881	99.00	24.17	24.32	2.203	2.203	-76.87	0.6
8223	180.68933	1.03946	24.08	24.11	24.86	2.290	2.281	4.25	0.5
11189	180.63557	1.03589	99.00	24.98	24.93	2.167	2.494	-95.80	0.7
13389	180.59750	1.27290	25.01	24.36	24.55	2.264	2.257	-23.55	0.7
12477	180.61516	1.26697	23.64	23.06	21.60	2.301	2.293	3.24	0.6
7663	180.69849	1.26563	25.54	24.32	24.43	2.320	2.313	3.54	0.5
11759	180.62411	1.25727	99.00	26.47	24.43	2.837	2.829	7.02	0.6
9968	180.65813	1.23888	99.00	25.11	24.95	2.783	2.775	13.80	0.7
12014	180.62030	1.22746	99.00	25.96	23.53	3.060	3.052	3.21	0.5
13647	180.59045	1.21929	99.00	25.81	24.37	2.628	2.618	12.11	0.5
12606	180.61008	1.19982	99.00	25.89	24.39	2.987	2.979	15.22	0.5
12903	180.60654	1.19755	24.42	23.93	22.71	2.582	2.573	0.41	0.5

Table A.4 – continued from previous page

ID	R.A.	Dec.	U	B	R	$z_{Ly\alpha}$	z_{ISM}	$W_{Ly\alpha}$	q
9915	180.65839	1.19081	99.00	25.06	22.74	3.310	3.298	3.17	0.5
9657	180.66412	1.18277	99.00	24.76	23.24	3.103	3.104	6.35	0.5
18836	180.50099	1.28040	99.00	26.28	24.02	3.077	3.069	2.96	0.5
20724	180.47240	1.26493	99.00	25.93	23.82	2.674	2.664	-23.76	0.5
20044	180.48337	1.25353	99.00	24.39	24.86	2.293	2.282	20.69	0.7
18866	180.50156	1.24829	25.37	24.39	24.31	2.414	2.406	212.89	1.0
20047	180.48749	1.23422	24.11	24.07	24.09	2.402	2.391	29.82	0.8
21065	180.46736	1.22388	99.00	24.63	24.75	2.759	2.746	8.24	0.5
23719	180.42552	1.20425	23.79	23.58	22.44	3.182	3.179	37.02	0.5
22299	180.44804	1.20153	99.00	23.72	24.95	2.624	2.616	81.39	0.5
20525	180.47511	1.19858	99.00	24.93	24.74	2.731	2.716	20.90	0.6
20448	180.47807	1.18088	23.89	24.00	22.92	3.132	3.129	2.52	0.5
16786	180.53291	1.13439	25.21	25.26	23.98	2.653	2.634	6.62	0.6
21422	180.46062	1.11141	99.00	26.05	25.11	2.366	2.365	15.76	0.5
18868	180.50081	1.09373	99.00	26.15	25.13	2.424	2.415	15.15	0.6
20158	180.48102	1.08985	99.00	26.39	25.17	2.729	2.721	20.95	0.7
20665	180.47356	1.08164	99.00	24.80	23.96	2.879	2.881	4.37	0.6
19946	180.48676	1.07833	24.70	23.71	23.37	2.795	2.780	6.23	0.9
19790	180.48700	1.04713	99.00	25.17	24.33	2.726	2.718	4.45	0.5
18441	180.50865	1.03946	24.43	24.11	22.65	3.008	3.006	-9.68	0.9
22327	180.44608	1.03421	24.31	24.44	25.02	2.443	2.443	-77.29	0.9
27127	180.37404	1.11383	25.24	25.37	24.65	2.510	2.501	8.51	0.5
24094	180.41873	1.10982	99.00	25.22	23.17	2.515	2.521	-142.80	0.6
26356	180.38487	1.10284	99.00	25.75	24.75	2.487	2.486	11.33	0.5
25580	180.39676	1.09933	99.00	25.73	23.82	2.705	2.716	2.59	0.5
27994	180.36162	1.08979	23.32	23.47	23.38	2.445	2.437	3.43	0.5
30400	180.32297	1.08503	99.00	25.30	23.93	3.090	3.082	15.91	0.9
24787	180.40961	1.08585	25.73	24.70	24.89	3.157	3.154	144.37	0.5
24787	180.40961	1.08585	25.73	24.70	24.89	2.671	2.664	23.03	0.5
28271	180.35625	1.08040	26.11	24.54	22.80	2.581	2.565	63.34	0.5
23264	180.43086	1.07950	99.00	25.73	24.13	2.995	2.987	5.79	0.5
26167	180.38773	1.07568	99.00	25.95	24.10	2.876	2.869	4.01	0.6
26210	180.38745	1.03376	99.00	26.17	24.00	3.255	3.249	4.23	0.6
25242	180.40323	1.27553	25.49	24.46	23.65	2.689	2.697	3.18	0.6
29527	180.33664	1.26597	25.60	24.75	23.72	2.514	2.508	-0.00	0.9
23504	180.42694	1.25778	99.00	25.77	23.75	2.763	2.780	-8.81	0.9
30912	180.31531	1.23445	25.39	25.02	23.75	2.420	2.404	-87.44	0.9

Table A.4 – continued from previous page

ID	R.A.	Dec.	U	B	R	$z_{Ly\alpha}$	z_{ISM}	$W_{Ly\alpha}$	q
27523	180.36671	1.23120	99.00	26.10	24.08	2.635	2.630	-7.10	0.5
26241	180.38638	1.21052	99.00	26.02	24.43	2.515	2.509	7.77	0.8
28143	180.35721	1.18147	24.95	24.90	25.04	2.407	2.400	31.96	0.9
23669	180.42506	1.17567	24.90	24.99	24.59	2.424	2.416	19.20	0.8
36287	180.22818	1.26704	99.00	26.41	24.17	2.941	2.931	21.69	0.6
35763	180.23700	1.25951	99.00	25.46	23.86	2.642	2.628	40.52	0.7
35763	180.23700	1.25951	99.00	25.46	23.86	2.843	2.836	8.55	0.7
35362	180.24283	1.25534	99.00	26.38	24.17	2.680	2.672	11.59	0.5
39367	180.17619	1.24229	99.00	23.43	21.58	3.455	3.453	15.62	0.6
34383	180.26085	1.22097	99.00	23.51	23.07	2.652	2.651	7.54	0.6
41021	180.14955	1.21540	24.67	24.85	24.14	3.252	3.246	-12.28	0.5
39114	180.17999	1.21238	99.00	25.82	23.57	3.010	2.997	-0.25	0.8
36609	180.22629	1.17694	99.00	23.10	23.45	3.002	2.993	0.77	0.7
39813	180.16916	1.13478	24.26	24.13	24.33	2.676	2.667	39.31	0.7
36339	180.22815	1.12990	99.00	24.92	24.37	2.818	2.833	-17.92	0.6
40522	180.15956	1.10510	24.51	22.70	22.22	2.397	2.391	18.05	0.9
37346	180.21030	1.10012	99.00	26.33	24.21	2.533	2.527	98.98	0.6
40141	180.16240	1.09099	99.00	25.54	23.58	3.364	3.349	5.61	0.7
36474	180.22556	1.08737	99.00	25.85	24.36	2.999	2.992	17.88	0.5
39489	180.17444	1.02745	24.20	23.67	23.37	2.841	2.830	4.89	0.9
26873	180.37680	1.36915	99.00	25.22	24.82	2.309	2.302	10.55	0.5
23973	180.42007	1.35777	99.00	25.62	25.07	2.435	2.434	1.78	0.5
30019	180.32867	1.34890	99.00	25.15	24.01	2.948	2.939	292.28	0.5
23357	180.42902	1.35138	99.00	25.75	24.82	2.530	2.529	14.46	0.6
25995	180.39198	1.34662	24.99	23.88	22.75	2.648	2.661	-6.24	0.9
26147	180.38814	1.33561	99.00	25.08	24.21	2.769	2.772	-2.98	0.5
26003	180.39116	1.30336	24.87	24.29	23.76	3.144	3.134	2.93	0.8
25684	180.39474	1.29799	99.00	25.99	24.86	2.447	2.433	-74.90	0.7
23134	180.43309	1.29214	99.00	24.82	24.60	2.492	2.485	15.21	0.6
30189	180.32709	1.28931	99.00	24.28	25.15	2.863	2.841	4.81	0.5
23710	180.42618	1.28667	24.41	23.99	23.19	2.219	2.227	-70.73	0.9
30663	180.31856	1.52612	99.00	26.15	24.73	2.690	2.695	28.51	0.5
29465	180.33716	1.52179	99.00	24.43	23.07	2.563	2.577	-79.47	0.9
24049	180.41949	1.48425	99.00	24.99	23.72	2.575	2.567	13.71	0.5
28939	180.34499	1.48095	99.00	24.86	23.69	2.222	2.218	-89.99	0.9
29795	180.33499	1.44433	24.70	23.45	24.54	2.398	2.397	6.65	0.5
23415	180.42909	1.44552	25.53	24.87	23.74	3.016	3.008	-1.69	0.5

Table A.4 – continued from previous page

ID	R.A.	Dec.	U	B	R	$z_{Ly\alpha}$	z_{ISM}	$W_{Ly\alpha}$	q
25516	180.39760	1.43936	99.00	25.71	24.41	3.184	3.176	9.85	0.5
30635	180.32097	1.43440	24.95	23.91	23.69	3.159	3.157	78.43	0.6
27414	180.36855	1.43477	99.00	25.53	23.41	2.497	2.486	-97.07	0.8
38500	180.18964	1.52494	99.00	26.42	24.56	2.682	2.689	26.62	0.6
37776	180.20262	1.49669	24.89	25.09	25.16	2.438	2.439	4.35	0.5
34504	180.25739	1.48616	99.00	26.08	24.98	2.193	2.184	-68.93	0.8
41209	180.14876	1.47552	99.00	23.85	23.45	2.561	2.559	-2.24	0.5
41209	180.14876	1.47552	99.00	23.85	23.45	2.916	2.909	180.67	1.0
37038	180.21700	1.47384	99.00	25.00	23.56	3.375	3.367	25.53	0.5
41448	180.14468	1.46127	99.00	25.92	24.52	2.585	2.577	7.27	0.5
37389	180.20967	1.45598	99.00	25.92	23.62	2.582	2.568	7.47	0.6
38295	180.19374	1.45212	99.00	25.48	24.60	2.920	2.906	71.08	0.6
37195	180.21313	1.43519	99.00	26.08	25.20	2.400	2.393	9.93	0.5
37602	180.20618	1.43250	99.00	25.22	23.73	2.936	2.921	18.59	0.9
37320	180.21159	1.42260	99.00	24.81	24.27	2.506	2.500	148.71	0.6
34226	180.26318	1.38015	99.00	24.05	23.48	2.999	3.025	-15.79	0.9
40384	180.15849	1.36590	99.00	25.44	24.08	2.688	2.683	-5.46	0.5
41343	180.14661	1.34488	24.22	24.38	23.67	2.184	2.185	2.34	0.8
35731	180.23755	1.34697	99.00	25.43	24.21	2.727	2.739	1.50	0.5
34514	180.25757	1.34204	99.00	25.20	24.35	3.029	3.018	6.27	0.9
40909	180.15117	1.33536	99.00	25.64	23.54	2.668	2.698	-22.85	0.9
34785	180.25241	1.33434	99.00	25.78	23.77	3.122	3.115	10.96	0.5
35208	180.24521	1.32110	99.00	25.88	24.05	2.491	2.472	4.06	0.6
35965	180.23396	1.30604	99.00	25.43	24.32	2.014	0.000	0.00	0.7
35089	180.24748	1.27992	25.03	24.85	23.71	2.306	2.295	-97.36	0.8
8142	180.69080	1.37854	99.00	24.43	22.95	2.796	2.788	4.69	0.5
8866	180.67862	1.33923	24.25	23.51	22.44	2.581	2.573	1.95	0.5
8583	180.68530	1.29473	23.57	23.02	22.21	2.730	2.728	-5.09	0.5
9770	180.66484	1.29197	25.14	23.30	24.10	2.808	2.804	39.58	0.8
13630	180.59055	1.28944	24.29	24.45	24.10	2.416	2.426	-14.66	0.5
13631	180.59088	1.28248	99.00	24.51	23.28	2.511	2.501	5.05	0.6
13947	180.58537	1.50767	99.00	25.48	23.36	3.141	3.168	-8.88	0.9
9086	180.67265	1.50865	99.00	26.16	24.51	2.935	2.927	11.65	0.7
12983	180.60336	1.50106	99.00	25.71	23.62	3.211	3.203	25.39	0.8
9481	180.66582	1.47181	99.00	25.37	24.10	3.074	3.062	14.47	0.8
10161	180.65440	1.45013	25.20	25.39	24.26	2.388	2.379	4.35	0.9
12569	180.61272	1.44715	24.34	23.59	22.55	3.273	3.266	10.05	0.5

Table A.4 – continued from previous page

ID	R.A.	Dec.	U	B	R	$z_{Ly\alpha}$	z_{ISM}	$W_{Ly\alpha}$	q
18334	180.50916	1.51599	99.00	25.54	24.28	2.757	2.749	24.84	0.8
16929	180.53108	1.50276	24.76	24.08	23.76	2.377	2.389	-7.68	0.8
24687	180.41248	1.46414	24.38	24.08	23.07	2.674	2.664	24.22	0.7
17173	180.52803	1.42294	24.91	23.90	22.80	2.868	2.860	6.60	0.7
18301	180.50949	1.38403	99.00	25.26	23.38	2.796	2.788	9.23	0.5
24024	180.42000	1.38012	99.00	25.41	25.19	2.542	2.533	6.69	0.5
23823	180.42249	1.37265	99.00	25.51	23.80	2.839	2.830	3.42	0.7
20502	180.47556	1.36503	99.00	24.76	24.22	2.782	2.790	4.01	0.5
18053	180.51405	1.35810	99.00	24.48	24.78	2.802	2.795	10.78	0.7
23357	180.42902	1.35138	99.00	25.75	24.85	2.303	2.295	3.96	0.7
24516	180.41393	1.34276	99.00	25.17	23.64	2.983	2.975	46.86	0.6
21866	180.45401	1.33845	99.00	25.23	24.14	2.967	2.970	-9.40	0.8
22235	180.44673	1.31315	99.00	25.40	23.11	3.263	3.252	14.33	0.9
18894	180.50053	1.30921	99.00	24.89	23.54	2.995	2.987	2.56	0.5
17047	180.53040	1.30535	23.55	23.57	23.59	3.089	3.095	-0.23	0.6
17280	180.52670	1.30011	24.41	24.58	23.50	2.429	2.422	2.79	0.5
20866	180.47141	1.29279	24.74	24.38	22.86	2.615	2.605	-10.89	0.5
22122	180.44904	1.28768	25.76	25.17	23.65	2.988	2.972	11.11	0.5
19034	180.49837	1.27432	99.00	25.26	23.65	2.904	2.896	20.27	0.5

Table A.5: Spectroscopically confirmed LBGs in the PKS2126-158 field.

ID	R.A.	Dec.	U	B	R	$z_{Ly\alpha}$	z_{ISM}	$W_{Ly\alpha}$	q
3524	322.63715	-15.54523	25.96	25.31	24.64	2.863	2.853	54.20	0.9
7643	322.59445	-15.55206	99.00	26.22	23.84	3.014	3.003	2.82	0.5
7770	322.59314	-15.55498	99.00	26.29	24.43	2.987	2.978	5.11	0.5
12507	322.54324	-15.56101	26.98	25.78	24.70	2.522	2.520	-23.35	0.5
11654	322.55185	-15.56398	99.00	25.99	24.59	2.922	2.925	9.91	0.6
11396	322.55756	-15.57283	99.00	25.48	23.65	3.510	3.500	2.01	0.6
5318	322.61819	-15.57495	27.70	26.02	24.69	2.716	2.707	5.16	0.5
6350	322.60754	-15.57820	99.00	25.63	24.44	3.322	3.306	3.33	0.5
9995	322.56885	-15.58733	27.05	25.79	24.42	2.776	2.767	3.82	0.5
14224	322.53381	-15.59719	26.68	25.92	24.62	2.944	2.934	5.29	0.5
7071	322.60043	-15.60133	26.54	25.84	24.78	2.886	2.877	11.46	0.6
3945	322.63284	-15.61267	99.00	25.82	24.51	3.358	3.352	30.23	0.9

Table A.5 – continued from previous page

ID	R.A.	Dec.	U	B	R	$z_{Ly\alpha}$	z_{ISM}	$W_{Ly\alpha}$	q
9303	322.57623	-15.62325	25.77	25.42	24.43	3.272	3.260	10.21	0.6
10415	322.56485	-15.63057	24.71	24.67	23.96	2.664	2.678	-5.73	0.8
10384	322.56540	-15.63333	27.82	26.39	25.01	0.000	0.000	0.00	0.5
14246	322.52502	-15.55386	26.75	25.88	24.74	2.356	2.347	3.23	0.5
5415	322.61710	-15.59904	99.00	26.09	24.79	3.349	3.340	5.09	0.5
8123	322.58899	-15.58851	27.64	25.90	24.24	3.073	3.067	2.90	0.5
8225	322.59073	-15.65312	25.35	25.21	24.54	2.584	2.572	15.75	0.6
12277	322.54462	-15.40161	99.00	26.31	24.51	2.971	2.962	4.93	0.6
13317	322.53403	-15.40478	99.00	25.68	24.21	3.487	3.462	1.70	0.5
14465	322.52170	-15.41483	27.37	25.25	23.83	3.363	3.361	15.87	0.5
5920	322.61066	-15.41073	25.48	24.89	23.67	2.643	2.654	-25.04	0.9
3288	322.63895	-15.44228	26.14	25.53	24.84	2.391	2.385	7.97	0.5
9615	322.57236	-15.44821	26.11	25.82	25.08	2.244	2.235	23.89	0.5
5139	322.61942	-15.45830	99.00	26.25	24.80	3.318	3.320	-27.66	0.7
7409	322.59622	-15.46897	27.17	25.93	24.77	2.980	2.969	15.06	0.8
2693	322.64523	-15.47160	25.85	25.60	25.08	2.424	2.409	10.72	0.5
3711	322.63464	-15.47875	25.64	25.52	24.83	2.220	2.200	7.95	0.5
8938	322.57944	-15.49688	26.11	25.15	23.75	2.932	2.929	-1.69	0.5
29290	322.36996	-15.39829	99.00	25.90	23.97	3.193	3.193	-11.19	0.7
23746	322.42902	-15.40453	26.69	25.90	25.05	3.209	3.201	6.49	0.6
18866	322.47855	-15.41042	27.39	26.02	24.95	2.719	2.702	13.08	0.5
29991	322.36334	-15.41727	99.00	25.07	22.91	3.269	3.280	-3.09	0.6
19498	322.47226	-15.41459	99.00	26.09	25.11	2.777	2.753	17.45	0.5
30329	322.35983	-15.42164	99.00	26.24	23.98	2.634	2.624	5.64	0.5
18954	322.47794	-15.42636	26.53	25.67	24.48	3.053	3.046	19.67	0.7
27018	322.39426	-15.43122	99.00	26.03	24.30	3.489	3.483	-0.90	0.8
21838	322.44870	-15.43110	99.00	25.33	23.24	3.205	3.194	3.77	0.5
24846	322.41461	-15.43414	26.10	25.54	24.44	2.846	2.828	16.61	0.5
30958	322.36267	-15.44157	99.00	25.59	23.20	3.284	3.293	-1.87	0.6
21275	322.45505	-15.44229	99.00	26.81	24.77	3.434	3.427	-8.43	0.5
31469	322.34735	-15.45539	28.24	26.03	24.29	3.205	3.196	16.82	0.7
27023	322.39493	-15.45314	25.72	25.66	24.96	2.865	2.863	24.10	0.5
28947	322.37448	-15.46800	99.00	26.09	24.85	3.123	3.125	3.09	0.6
20250	322.46506	-15.47555	24.92	24.84	24.43	2.554	2.543	17.97	0.5
29782	322.36630	-15.48330	26.56	25.76	24.71	2.507	2.499	15.28	0.5
23469	322.43228	-15.48613	25.23	25.23	24.59	2.660	2.651	13.45	0.9
30768	322.35532	-15.48920	99.00	26.46	24.10	2.888	2.880	4.92	0.5

Table A.5 – continued from previous page

ID	R.A.	Dec.	U	B	R	$z_{Ly\alpha}$	z_{ISM}	$W_{Ly\alpha}$	q
27285	322.39194	-15.49594	99.00	26.43	23.98	2.975	2.975	3.68	0.5
20526	322.46188	-15.39293	25.38	24.45	24.27	2.966	2.951	6.04	0.5
28012	322.38394	-15.49669	99.00	26.06	23.82	2.500	2.503	7728.61	0.5
24825	322.41858	-15.55192	25.52	24.83	23.63	2.898	2.881	8.62	0.7
31116	322.35196	-15.57087	26.02	25.18	24.56	2.609	2.608	5.15	0.6
19850	322.46973	-15.56908	26.48	26.06	25.04	3.261	3.251	2.51	0.5
24356	322.42365	-15.58137	25.05	24.84	24.08	2.428	2.435	5.03	0.5
22794	322.44006	-15.58423	26.90	25.69	24.21	3.202	3.207	-3.76	0.5
30004	322.36423	-15.58817	99.00	26.22	24.49	3.176	3.174	-8.55	0.5
22523	322.44266	-15.58714	27.22	26.36	25.10	3.562	3.556	77.37	0.8
26828	322.39819	-15.59599	28.94	26.74	25.00	3.045	3.027	-13.20	0.6
31403	322.34503	-15.60544	99.00	25.85	23.38	3.994	3.985	6.60	0.5
19523	322.46909	-15.60783	25.68	25.49	24.72	3.060	3.051	6.00	0.6
21672	322.45142	-15.61200	26.34	25.59	24.75	2.253	2.251	15.90	0.6
20047	322.46786	-15.61511	26.55	25.66	24.81	2.967	2.956	10.82	0.8
25843	322.40686	-15.62155	26.88	25.43	23.66	3.094	3.074	11.43	0.5
21058	322.45825	-15.62153	25.18	24.77	25.03	2.749	2.753	8.30	0.6
24065	322.42697	-15.63185	28.08	25.45	24.57	3.279	3.276	4.80	0.8
27964	322.38776	-15.64225	26.39	25.73	24.62	2.867	2.867	-14.02	0.7
23673	322.43088	-15.64512	99.00	25.67	23.99	2.866	2.858	2.49	0.5
24631	322.42087	-15.64917	26.15	25.69	24.68	2.473	2.463	17.31	0.5
29404	322.37048	-15.59736	26.23	25.72	24.74	2.763	2.756	8.73	0.5
25114	322.41562	-15.56421	99.00	26.09	24.63	3.233	3.226	69.73	0.8
31129	322.35132	-15.56016	26.31	25.18	23.80	3.206	3.228	-11.54	0.5
42171	322.23911	-15.55313	26.24	25.25	24.23	2.882	2.872	22.41	0.6
32562	322.33652	-15.55115	26.25	25.41	24.45	3.011	2.998	5.55	0.5
42541	322.23544	-15.55638	27.05	26.14	24.88	3.194	3.181	13.22	0.7
32763	322.33487	-15.58259	26.88	25.53	25.15	3.357	3.358	11.12	0.6
41705	322.24197	-15.64538	25.58	25.49	24.78	2.828	2.821	20.40	0.5
37087	322.29196	-15.64626	25.98	25.29	24.16	3.392	3.400	-2.12	0.5
32566	322.33701	-15.64517	27.04	26.03	25.20	2.887	2.878	7.45	0.5
36296	322.29929	-15.65220	25.10	24.83	24.13	2.935	2.924	5.90	0.5
44193	322.21790	-15.54477	27.84	25.39	23.94	3.365	3.361	7.01	0.8
38638	322.27603	-15.61686	25.33	25.28	24.45	2.829	2.816	4.38	0.9
33440	322.32812	-15.64190	26.18	25.69	24.75	2.839	2.828	5.65	0.5
43840	322.22165	-15.63124	26.98	25.38	23.68	3.331	3.329	19.98	0.6
40283	322.25885	-15.63317	99.00	26.31	24.79	2.936	2.932	14.55	0.6

Table A.5 – continued from previous page

ID	R.A.	Dec.	U	B	R	$z_{Ly\alpha}$	z_{ISM}	$W_{Ly\alpha}$	q
42413	322.23666	-15.58493	25.84	25.41	24.48	3.347	3.333	25.38	0.8
33679	322.32431	-15.56209	25.16	25.13	24.86	3.219	3.214	15.82	0.5
33938	322.32199	-15.56326	24.68	24.63	23.89	2.782	2.783	15.85	0.9
32909	322.33270	-15.54509	26.81	25.60	25.00	2.441	2.431	151.63	0.5
35544	322.30637	-15.54242	26.29	25.83	24.98	3.001	2.989	4.37	0.7
44321	322.21698	-15.64997	26.88	25.86	25.13	3.229	3.228	165.41	0.9
43939	322.22018	-15.40242	99.00	25.90	24.04	3.642	3.632	10.26	0.7
37158	322.29031	-15.41085	99.00	26.28	25.12	2.744	2.718	14.28	0.5
33775	322.32312	-15.41443	99.00	25.76	24.51	3.313	3.307	8.32	0.9
37097	322.30334	-15.41830	27.08	25.79	25.22	3.523	3.517	9.97	0.5
31943	322.34204	-15.41838	99.00	25.75	24.68	3.370	3.362	13.79	0.6
43949	322.22034	-15.44211	26.73	25.99	24.86	2.815	2.806	6.45	0.5
33905	322.32135	-15.45825	25.61	25.41	24.94	2.419	2.412	3.14	0.5
37414	322.28897	-15.47075	26.46	24.90	24.11	3.016	3.004	5.99	0.9
41943	322.24139	-15.47750	24.79	24.49	23.82	2.731	2.720	7.68	0.9
42871	322.23154	-15.48356	26.88	26.26	25.01	3.390	3.381	4.14	0.7
34376	322.31717	-15.48406	27.26	26.23	24.89	2.580	2.580	3.71	0.6
40818	322.25308	-15.49688	26.62	25.68	24.46	2.838	2.832	1.49	0.5
32866	322.33310	-15.42630	26.46	25.09	24.59	3.020	3.011	7.83	0.9
44636	322.21231	-15.45405	25.59	25.48	24.83	2.668	2.666	-14.00	0.6
31547	322.34674	-15.47432	99.00	26.18	24.52	3.452	3.439	3.03	0.5
33701	322.32437	-15.50336	26.28	25.32	24.12	3.261	3.271	-2.96	0.5
32063	322.34085	-15.40027	26.09	25.39	24.65	2.658	2.651	-2.67	0.7
53037	322.12045	-15.39598	99.00	26.16	24.49	3.020	3.009	2.65	0.7
59775	322.04276	-15.40489	24.58	22.67	23.74	3.096	3.076	6.32	0.7
49843	322.15521	-15.40426	24.68	24.61	24.42	2.961	2.939	10.79	0.5
58079	322.06317	-15.41576	26.52	25.53	24.65	2.819	2.813	6.08	0.5
59821	322.04193	-15.42625	23.72	23.21	24.13	2.770	2.758	4.38	0.5
53848	322.11179	-15.42593	26.03	25.94	25.11	2.420	2.411	7.94	0.5
58559	322.05850	-15.42926	99.00	26.19	25.29	3.035	3.015	33.36	0.9
50663	322.14694	-15.42978	25.73	25.64	25.00	2.628	2.613	10.81	0.9
58462	322.05817	-15.43332	25.76	25.53	24.80	2.454	2.450	6.89	0.5
57863	322.06567	-15.43720	99.00	25.71	24.54	3.155	3.146	15.55	0.9
53665	322.11368	-15.43594	27.64	25.79	24.54	2.564	2.559	4.05	0.6
51050	322.14215	-15.43923	99.00	25.85	24.06	3.146	3.167	-17.35	0.9
59189	322.05011	-15.44374	25.67	24.88	25.00	3.032	3.017	3.99	0.5
52554	322.12564	-15.44239	99.00	26.17	24.56	3.239	3.232	2.60	0.6

Table A.5 – continued from previous page

ID	R.A.	Dec.	U	B	R	$z_{Ly\alpha}$	z_{ISM}	$W_{Ly\alpha}$	q
50454	322.14902	-15.44636	99.00	26.02	24.76	3.201	3.192	40.04	0.8
50823	322.14499	-15.45099	26.51	25.16	23.86	3.205	3.189	3.97	0.8
59168	322.05002	-15.45532	99.00	25.12	24.13	2.758	2.746	0.24	0.6
49156	322.16351	-15.45469	25.80	25.46	24.65	2.607	2.585	0.16	0.7
59893	322.04160	-15.45775	25.42	23.84	24.86	2.715	2.706	5.48	0.5
59758	322.04330	-15.46923	24.37	23.09	23.99	2.769	2.762	2.83	0.6
52234	322.12915	-15.47465	26.49	25.81	24.69	2.726	2.717	3.99	0.5
59457	322.04715	-15.48986	24.36	23.99	23.78	2.604	2.580	4.61	0.7
60255	322.03662	-15.48263	26.46	20.20	24.71	2.690	2.674	3.78	0.5
55319	322.09558	-15.55055	25.31	25.29	24.53	2.708	2.715	-14.99	0.8
49656	322.15790	-15.54921	25.33	25.30	24.69	2.957	2.948	6.75	0.7
57232	322.07330	-15.55824	24.99	24.97	24.47	2.733	2.723	19.62	0.9
49859	322.15567	-15.55794	24.59	24.44	23.54	2.611	2.604	46.68	0.8
52051	322.13181	-15.58404	25.78	25.36	24.69	3.010	3.002	14.74	0.5
50249	322.15179	-15.58762	25.90	25.57	24.80	2.895	2.891	12.97	0.7
51334	322.13968	-15.59411	25.44	24.90	24.18	2.937	2.947	4.36	0.5
56341	322.08353	-15.59870	26.36	25.32	24.33	2.716	2.699	2.59	0.6
59108	322.05402	-15.60294	27.22	26.17	24.98	3.118	3.098	20.52	0.9
48958	322.16650	-15.61919	25.89	25.29	24.12	3.011	2.995	4.19	0.8
56314	322.08411	-15.63599	99.00	25.92	24.17	3.448	3.446	4.70	0.5
57503	322.07083	-15.63957	99.00	26.23	25.12	3.354	3.343	3.46	0.5
12408	322.54550	-15.80990	25.09	25.04	24.76	2.313	2.306	15.97	0.5
13496	322.53467	-15.82843	99.00	26.11	24.70	3.128	3.118	6.89	0.6
8685	322.58151	-15.82657	25.62	25.07	24.62	2.684	2.676	49.64	0.8
8645	322.58478	-15.83536	27.13	25.88	24.48	2.576	2.568	4.50	0.5
1784	322.65701	-15.86274	26.98	25.70	24.96	3.339	3.334	22.06	0.5
5152	322.62192	-15.87683	25.10	25.08	24.74	3.026	3.012	6.60	0.5
12518	322.54578	-15.90629	26.36	25.26	23.86	3.518	3.510	42.05	0.7
13357	322.53659	-15.91196	99.00	25.79	24.42	3.005	2.993	10.69	0.5
5189	322.62131	-15.91318	25.08	24.49	23.37	2.938	2.930	10.93	0.9
11738	322.55170	-15.66321	99.00	25.92	24.37	3.558	3.550	73.04	0.8
10305	322.56503	-15.67015	25.50	25.40	24.70	2.687	2.677	15.99	0.6
7941	322.59155	-15.68360	24.86	24.64	23.83	2.802	2.789	4.35	0.5
7126	322.60056	-15.69026	26.68	25.89	24.69	3.154	3.146	16.97	0.7
10533	322.56415	-15.69808	27.69	26.21	24.75	3.274	3.267	12.08	0.6
4410	322.62845	-15.70112	25.04	24.31	24.20	2.952	2.944	103.93	0.8
4348	322.62952	-15.74726	26.72	25.74	25.08	3.127	3.117	32.99	0.7

Table A.5 – continued from previous page

ID	R.A.	Dec.	U	B	R	$z_{Ly\alpha}$	z_{ISM}	$W_{Ly\alpha}$	q
2663	322.64722	-15.75775	99.00	25.66	24.65	3.149	3.141	6.94	0.5
12298	322.54248	-15.76110	99.00	25.47	23.33	3.313	3.305	5.79	0.5
6785	322.60355	-15.76309	28.01	24.81	23.18	3.219	3.212	3.15	0.7
13925	322.52975	-15.77072	99.00	25.64	23.85	3.347	3.340	4.68	0.5
1709	322.65677	-15.70650	25.69	25.12	24.42	2.698	2.691	14.88	0.5
7744	322.59439	-15.73487	25.37	25.03	24.02	3.024	3.016	12.85	0.5
7345	322.59277	-15.74206	26.92	25.42	23.94	3.285	3.272	-1.92	0.5
26524	322.40140	-15.66114	27.34	25.71	24.86	3.278	3.274	34.81	0.6
27468	322.39105	-15.66790	26.16	25.43	25.14	2.471	2.474	21.22	0.6
23772	322.43011	-15.70283	99.00	26.42	23.93	3.121	3.114	23.35	0.6
30828	322.35611	-15.73381	25.93	25.19	24.40	2.891	2.891	75.05	0.5
22784	322.44110	-15.74820	26.44	25.76	24.59	2.816	2.826	9.61	0.5
29851	322.36697	-15.81833	26.94	25.35	24.07	3.121	3.114	-3.42	0.5
20605	322.46368	-15.82084	99.00	26.28	24.65	3.281	3.268	16.80	0.5
22068	322.44879	-15.82706	99.00	26.24	24.53	3.553	3.544	12.64	0.5
24645	322.42184	-15.82949	26.11	24.88	23.50	2.859	2.852	9.76	0.7
23390	322.43494	-15.83295	99.00	25.61	23.97	3.160	3.152	-17.67	0.5
26068	322.40656	-15.84201	25.67	25.32	25.14	2.871	2.866	93.89	0.7
19043	322.47946	-15.84264	99.00	26.06	25.05	3.645	3.642	198.74	0.6
19243	322.47742	-15.86837	25.17	25.05	24.53	2.620	2.612	40.72	0.7
23038	322.43893	-15.88486	26.45	24.85	23.14	2.680	2.673	3.12	0.6
29408	322.37180	-15.89048	99.00	25.85	24.76	3.055	3.050	57.86	0.5
31751	322.34641	-15.87332	26.72	24.99	23.57	3.396	3.388	3.54	0.5
32396	322.33862	-15.82658	26.13	25.94	25.02	3.334	3.326	37.55	0.5
43131	322.22989	-15.84035	26.55	24.79	23.46	3.162	3.152	5.15	0.7
40128	322.26117	-15.84313	99.00	26.38	25.01	3.420	3.401	30.64	0.5
36480	322.29834	-15.84591	99.00	25.35	23.82	3.255	3.232	-3.80	0.5
43741	322.22403	-15.85791	26.65	25.78	24.57	2.943	2.939	10.18	0.5
44705	322.21371	-15.86539	99.00	26.35	24.32	3.329	3.324	3.56	0.5
44772	322.21298	-15.88773	99.00	26.17	24.56	3.542	3.526	2.52	0.6
32839	322.33560	-15.88902	26.55	26.06	25.19	3.035	3.031	5.12	0.5
44438	322.21677	-15.89227	99.00	25.93	24.36	3.754	3.755	19.16	0.9
43747	322.22400	-15.89972	26.55	25.58	24.80	2.741	2.732	4.67	0.5
44488	322.21616	-15.90553	27.95	26.56	25.28	3.459	3.480	32.63	0.5
36673	322.29688	-15.90755	99.00	25.36	24.11	3.180	3.173	20.50	0.9
40459	322.25784	-15.80418	25.52	25.16	25.01	2.666	2.659	58.70	0.8
41282	322.25018	-15.91454	26.38	25.77	24.74	3.333	3.328	2.41	0.5

Table A.5 – continued from previous page

ID	R.A.	Dec.	U	B	R	$z_{Ly\alpha}$	z_{ISM}	$W_{Ly\alpha}$	q
31737	322.34644	-15.85642	26.09	25.38	24.05	3.055	3.046	23.34	0.9
33016	322.33347	-15.81071	26.93	25.89	24.94	2.816	2.795	4.66	0.7
43941	322.22131	-15.66129	26.55	26.04	25.14	3.272	3.276	9.89	0.5
39995	322.26181	-15.66099	27.06	25.80	25.15	2.851	2.859	13.40	0.5
37542	322.28732	-15.66799	27.30	26.00	24.67	2.862	2.846	6.16	0.5
36836	322.29453	-15.67427	25.43	25.19	25.25	2.489	2.481	7.50	0.7
32688	322.33591	-15.68613	25.53	25.34	24.65	2.936	2.926	17.34	0.5
41368	322.24835	-15.72107	99.00	25.33	23.54	2.706	2.698	5.75	0.6
31617	322.34711	-15.74848	25.55	25.34	24.60	2.824	2.813	6.99	0.5
32989	322.33337	-15.75275	25.90	25.54	24.94	2.901	2.894	17.98	0.7
35395	322.30896	-15.75608	26.13	25.51	24.89	2.563	2.569	11.78	0.5
44048	322.22058	-15.76176	25.30	25.28	24.59	2.858	2.850	9.72	0.5
34629	322.31558	-15.75908	24.71	24.59	23.88	2.882	2.862	21.81	0.9
56645	322.08054	-15.67080	26.66	25.60	24.57	3.563	3.555	81.33	0.5
49434	322.16229	-15.66870	25.38	24.86	23.71	2.722	2.729	-3.30	0.5
55648	322.09204	-15.67406	25.40	25.02	24.60	2.841	2.823	8.95	0.5
51910	322.13361	-15.67627	99.00	26.45	24.00	3.312	3.305	2.73	0.5
59625	322.04553	-15.68550	27.70	25.20	23.31	2.808	2.802	2.95	0.5
55100	322.09863	-15.69350	27.17	26.02	24.61	3.146	3.137	92.15	0.7
51326	322.14038	-15.69843	26.72	25.84	24.52	3.190	3.179	2.20	0.5
57201	322.07391	-15.70315	27.93	25.96	24.73	3.365	3.346	19.30	0.9
49524	322.16037	-15.70434	26.05	25.69	24.64	2.897	2.890	28.37	0.8
48443	322.17203	-15.72093	25.95	25.07	23.65	2.935	2.939	4.49	0.6
55565	322.09338	-15.73161	25.68	25.59	24.89	2.255	2.245	2.76	0.6
49023	322.16623	-15.72775	24.96	24.95	24.62	2.252	2.243	-77.72	0.6
53658	322.11554	-15.73493	25.45	25.17	24.85	3.224	3.216	4.02	0.5
52620	322.12610	-15.74565	99.00	25.79	24.59	3.161	3.148	9.00	0.7
51890	322.13412	-15.75128	99.00	25.91	24.73	3.316	3.309	13.85	0.6
60172	322.03870	-15.68444	26.25	25.31	24.65	3.141	3.130	3.77	0.5
50986	322.14380	-15.67691	26.27	25.25	23.74	2.891	2.881	14.30	0.6
59035	322.05325	-15.80477	99.00	26.24	24.27	3.467	3.463	4.51	0.5
52425	322.12845	-15.80969	25.78	25.38	24.29	2.753	2.741	8.41	0.5
52134	322.13214	-15.83053	99.00	25.58	24.48	3.404	3.407	13.42	0.6
48874	322.16812	-15.83297	99.00	26.27	24.55	3.359	3.346	9.49	0.5
48739	322.16962	-15.84361	25.81	24.99	23.79	3.056	3.050	4.61	0.5
52247	322.13037	-15.85009	25.92	24.80	24.00	3.076	3.068	363.90	0.8
56289	322.08521	-15.87030	99.00	25.76	23.38	3.524	3.513	1.11	0.5

Table A.5 – continued from previous page

ID	R.A.	Dec.	U	B	R	$z_{Ly\alpha}$	z_{ISM}	$W_{Ly\alpha}$	q
58322	322.06155	-15.88611	99.00	26.32	25.08	3.160	3.158	64.61	0.9
56544	322.08261	-15.90301	26.37	25.71	24.90	2.426	2.416	5.03	0.5
49410	322.16220	-15.90290	27.62	25.61	23.77	3.479	3.455	1.96	0.5
54698	322.10333	-15.91016	25.56	24.72	23.69	3.112	3.104	78.88	0.8
50250	322.15802	-15.87136	24.56	24.32	23.49	2.907	2.896	14.67	0.9
50120	322.15408	-15.89321	99.00	26.21	23.92	3.922	3.914	20.45	0.6
56598	322.08182	-15.90446	99.00	26.11	24.07	3.278	3.290	-9.61	0.7
57342	322.07346	-15.88756	99.00	25.46	23.14	3.291	3.284	-5.25	0.5
57854	322.06708	-15.87994	24.18	24.10	23.51	2.693	2.686	-2.19	0.6

Table A.6: QSOs at $z > 2$ observed during the VLT VIMOS LBG Survey

ID	R.A.	Dec.	R	z
VLT_HE0940_30758	145.7211304	-11.0823317	24.728	3.7880
VLT_J1201_41502	180.1444702	+01.2551187	24.180	2.6180
VLT_J1201_28697	180.3492889	+01.3543601	24.300	2.7290
VLT_J1201_34026	180.2698517	+01.3705031	22.830	2.9145
VLT_J1201_14132	180.5821991	+01.4263303	23.040	2.5339
VLT_J1201_24709	180.4125214	+01.2927353	21.580	3.7289
VLT_PKS2126_42279	322.2389832	-15.7310381	24.865	2.3054
VLT_PKS2126_59238	322.0506287	-15.7591658	22.789	3.6413
VLT_PKS2126_58456	322.0610962	-15.8940449	22.664	3.1684
VLT_Q0042_20390	10.91676040	-26.0939198	21.530	2.1980
VLT_Q0042_41581	11.20168020	-26.2154408	24.220	2.9940

APPENDIX B

QSOs OBSERVED WITH AAOMEGA

Table B.1: QSOs observed in our AAOmega QSO Survey at $z > 2$ in our targeted field around the bright QSO Q0042-2627.

ID	R.A.	Dec.	Mag	z
WHO91_0046-267	12.2027083333	-26.4511388	19.74	3.52
WHO91_0043-265	11.3769583333	-26.2858888	18.34	3.44
WHO91_0042-267	11.2972083333	-26.4307500	19.71	2.81
LBQS_0042-2657	11.3315416667	-26.6808055	18.70	2.898
WHO91_0042-269	11.2176666667	-26.6692530	18.29	3.33
WHO91_0042-266	11.1488333333	-26.3833888	19.46	2.98
LBQS_0041-2658	11.024375	-26.7012222	18.62	2.457
LBQS_0041-2707	10.966	-26.8579444	17.95	2.786
004347.060-263305.00	10.9460833333	-26.5513888	99.00	2.95
LBQS_0041-2638	10.9282916667	-26.3695000	18.27	3.053
LBQS_0042-2627	11.1414583333	-26.1888611	18.47	3.289
LBQS_0041-2607	10.995	-25.8543611	17.15	2.501
WHO91_0043-259	11.5402916667	-25.6464444	19.06	3.31
WHO91_0043-261	11.5647916667	-25.8342500	19.55	3.11

Table B.2: QSOs observed in our AAOmega QSO Survey at $z > 2$ in our targeted field around the bright QSO J0124+0044.

ID	R.A.	Dec.	Mag	z
str82_012715+001828	21.8132708	+0.30802222	21.56	2.27
nbc_012714+001650	21.8110583	+0.28064444	20.19	2.50
str82_012730+001525	21.8753291	+0.25713611	21.35	2.70
str82_012421+002158	21.0895583	+0.36620000	21.82	2.95
SDSS_J012650.71+000933.3	21.7113041	+0.15926388	20.86	3.43

Table B.2 – continued from previous page

ID	R.A.	Dec.	Mag	z
SDSS_J012642.91+000239.0	21.6788125	+0.04418055	19.74	3.23
nbc_012617-000421	21.5746083	-0.07262222	20.70	2.77
SDSS_J012658.10-001202.4	21.7421208	-0.20068333	20.77	2.76
012614-001215	21.5615416	-0.20420277	21.46	2.32
str82_012514-000342	21.3101583	-0.06173333	20.99	2.99
012530-001351	21.3787250	-0.23106388	20.62	2.66
str82_012528-002431	21.3677166	-0.40886666	21.28	2.39
str82_012459-001600	21.2483750	-0.26684722	21.02	3.15
str82_012429-000344	21.1228208	-0.06239722	22.00	3.37
nbc_012433-000335	21.1399333	-0.05989722	21.05	3.00
nbc_012426-001708	21.1093666	-0.28559444	21.18	2.67
nbc_012428-003835	21.1200583	-0.64320833	21.33	2.21
str82_012355-001853	20.9831041	-0.31483611	20.47	3.13
nbc_012348-001538	20.9519500	-0.26076944	21.07	2.88
str82_012217-002520	20.5728458	-0.42235833	21.22	2.48
nbc_012314-000534	20.8083500	-0.09287777	20.46	2.54
SDSS_J012114.86-001637.3	20.3119291	-0.27705277	19.22	2.39
str82_012200-000308	20.5012958	-0.05236111	21.47	2.23
SDSS_J012226.76+000327.5	20.6115208	+0.05764166	19.74	2.48
str82_012145-000208	20.4397041	-0.03571944	21.87	2.60
str82_012040-000947	20.1693166	-0.16320833	21.89	2.31
str82_012229+000849	20.6232416	+0.14697222	21.80	3.12
SDSS_J012039.47-000239.4	20.1644750	-0.04428611	19.52	2.51
SDSS_J012058.06+000205.0	20.2419416	+0.03473055	20.47	2.96
SDSS_J012019.99+000735.5	20.0833125	+0.12656944	19.96	4.10
str82_012101+002102	20.2565833	+0.35072777	20.49	2.37
str82_012232+002321	20.6342333	+0.38921388	21.64	2.24
nbc_012028+004141	20.1172958	+0.69497500	20.59	2.97
SDSS_J012052.64+004315.5	20.2193375	+0.72099444	19.42	2.30
nbc_012146+004645	20.4449041	+0.77923611	20.80	2.32
012229+004039	20.6214875	+0.67770277	21.40	2.60
str82_012203+010728	20.5131375	+1.12448333	21.45	2.65
str82_012244+010604	20.6856250	+1.10121944	21.62	2.76
SDSS_J012255.42+010315.3	20.7309208	+1.05427222	20.83	3.51

Table B.2 – continued from previous page

ID	R.A.	Dec.	Mag	z
nbc_012351+005958	20.9625000	+0.99961111	21.49	2.59
SDSS_J0124+0044	21.0157375	+0.74241666	17.88	3.84
str82_012523+004918	21.3497375	+0.82183611	21.93	2.46
nbc_012552+005827	21.4678541	+0.97433888	21.32	3.01
nbc_012549+005250	21.4543125	+0.88078888	19.83	2.99
str82_012434+002834	21.1455208	+0.47625277	21.95	2.65
str82_012635+004531	21.6484958	+0.75888333	21.01	2.62
nbc_012702+003707	21.7617750	+0.61871666	20.34	2.51
SDSS_J012714.39+003249.6	21.8099750	+0.54712500	20.52	2.39
nbc_012558+002707	21.4953666	+0.45210833	20.19	2.40
SDSS_J012753.69+002516.4	21.9737416	+0.42123611	20.67	2.46

Table B.3: QSOs observed in our AAOmega QSO Survey at $z > 2$ in our targeted field around the bright QSO HE0940-1050.

ID	R.A.	Dec.	Mag	z
HE0940-1050	145.726654	-11.0736112	16.60	3.054
TS0159	146.381166	-11.3015833	19.90	2.37
MC068682	146.001570	-11.4590833	18.66	2.58
MC028494	146.191679	-11.5380305	21.68	3.00
MC077364	146.032133	-11.4422694	19.92	2.86
MC135005	145.881637	-11.3303666	21.33	2.61
MC065102	145.956633	-11.4668777	20.70	3.48
TS0357	146.003916	-11.7993055	19.49	2.90
MC071514	145.719941	-11.4521222	20.82	3.16
TS0417	145.685000	-11.3607500	19.64	2.96
TS0365	145.603041	-12.0396944	19.40	2.85
MC056290	145.534150	-11.4824083	20.98	2.47
TS0195	145.526666	-11.5409166	18.70	2.92
MC114481	145.583633	-11.3710722	21.49	2.81
MC027451	145.375520	-11.5407583	20.79	3.00
TS0139	145.376083	-11.1712500	18.86	2.10
MC211341	145.221970	-11.1853472	20.37	2.47

Table B.3 – continued from previous page

ID	R.A.	Dec.	Mag	z
MC243273	145.457841	-11.1214027	21.79	2.84
TS0316	144.986750	-11.1896111	19.45	2.81
HE0936-1043	144.722929	-10.9544000	17.89	2.455
VLT0052	145.649958	-11.0784805	20.61	2.08
TS0292	145.627291	-10.8141111	19.05	2.33
VLT0032	145.809916	-10.6889666	20.55	2.01
TS0294	145.875166	-10.8329722	19.87	2.22
WWz2.760	145.850966	-10.8924416	21.40	2.76
TS0396	145.929125	-10.8754444	19.58	3.02
MC394567	146.033920	-10.8444305	20.75	2.68
MC358148	145.990266	-10.9097638	20.82	3.00
MC285696	146.152129	-11.0382111	21.84	2.90
TS0108	146.135916	-11.0132777	18.55	2.40

Table B.4: QSOs observed in our AAOmega QSO Survey at $z > 2$ in our targeted field around the bright QSO J1201+0116.

ID	R.A.	Dec.	Mag	z
2QZ_J120210.5+011543	180.543975	+1.262294	19.85	2.5
2QZ_J120222.6+010119	180.594500	+1.022250	20.16	2.28
120220.057+002242.06	180.583570	+0.378350	17.57	2.58
2QZ_J120148.0+002000	180.450170	+0.333563	20.38	2.83
SDSS_J120138.56+010336.1	180.410683	+1.060061	20.07	3.83
2QZ_J120117.1+010045	180.321308	+1.012775	20.06	2.38
120001.292+003432.69	180.005383	+0.575747	19.97	3.36
2QZ_J115948.5+003203	179.952525	+0.534525	22.09	2.27
2QZ_J115949.8+004329	179.957666	+0.724900	19.99	2.71
SDSS_J120144.36+011611.5	180.434870	+1.269902	17.38	3.23
115840.064+014335.24	179.666933	+1.726455	21.08	2.98
SDSS_J115923.69+015224.2	179.848758	+1.873327	20.10	2.44
2QZ_J120055.7+013430	180.232395	+1.575222	20.59	2.51
SDSS_J120045.05+013953.3	180.187754	+1.664783	19.17	2.23
120244.717+020528.49	180.686320	+2.091247	20.28	3.54

Table B.4 – continued from previous page

ID	R.A.	Dec.	Mag	z
2QZ_J120311.2+015209	180.797066	+1.869427	20.25	2.27
120150.102+011855.99	180.458758	+1.315552	20.77	2.24
120408.37+014507.5	181.034904	+1.752091	20.74	2.3
2QZ_J120529.7+012326	181.373850	+1.390633	20.52	2.51

Table B.5: QSOs observed in our AAOmega QSO Survey at $z > 2$ in our targeted field around the bright QSO PKS2126-158.

ID	R.A.	Dec.	Mag	z
212628.800-155008.50	321.62000	-15.835694	20.67	2.83
COSMOS011142	322.93398	-15.962897	18.36	3.9
213141.420-160231.50	322.92258	-16.042083	18.18	2.14
213054.400-160540.40	322.72666	-16.094555	19.81	2.56
212904.900-160249.00	322.27041	-16.046944	19.23	2.94
212719.000-161001.10	321.82916	-16.166972	19.72	2.54
COSMOS018166	321.44190	-15.670472	19.25	1.09
HB892126-158	322.30062	-15.644694	17.3	3.268
212658.460-150839.80	321.74358	-15.144388	20.24	2.19
212732.200-151026.60	321.88416	-15.174055	19.84	2.29
HB892126-150	322.19008	-14.832333	19.3	2.2
J21291-1524B	322.29520	-15.406583	20.3	2.14
212916.600-144542.60	322.31916	-14.761833	20.04	2.28
COSMOS030286	322.34201	-15.114780	18.62	2.39
J21301-1533	322.53108	-15.555805	21.9	2.56
213201.800-153256.40	323.0075	-15.549000	17.8	2.74